Maritime Moving Target Detection, Tracking and Geocoding Using Range-Compressed Airborne Radar Data

Zur Erlangung des akademischen Grades eines

DOKTORS DER INGENIEURWISSENSCHAFTEN (Dr.-Ing.)

von der KIT-Fakultät für
Elektrotechnik und Informationstechnik
des Karlsruher Instituts für Technologie (KIT)

genehmigte

DISSERTATION

von

M.Tech Sushil Kumar Joshi
geb. in Haldwani, Uttarakhand, Indien

Tag der mündlichen Prüfung: 04.07.2022

Hauptreferent: Prof. Dr.-Ing. Marwan Younis
Korreferent: Hon.-Prof. Dr. rer. nat. Michael Eineder

To my dearest maa

Acknowledgement

During my doctoral research work at DLR's Microwaves and Radar Institute, I have received help and support of many people. I express my heartfelt thanks to:

My supervisor Dr. Stefan V. Baumgartner for sharing his in-depth knowledge on radar data processing and moving targets, for having regular discussions, and for his constant guidance, support and motivation throughout my research work.

My department head Prof. Dr. Gerhard Krieger for supporting my work and for providing his valuable feedback and suggestions on my journal and conference publications.

My advisor Prof. Dr. Marwan Younis for allowing me to carry out the research work in his team and for helping me enroll as a PhD student at the KIT-IHE institute.

Institute director Prof. Dr. Alberto Moreira for supporting my stay at the institute and for holding PhD status meetings with me.

My co-advisor Prof. Dr. Michael Eineder and the professors from KIT for evaluating my thesis and for being in my defense examination committee.

DAAD organization for funding my research work at DLR from the beginning.

My department secretary Mrs. Sibylle Radzuweit for helping me with all the administrative works at the institute.

My former officemate Dr. André B.C. da Silva for assisting me in my initial days in Germany and for having discussions on ground moving targets.

Dr. Jaya Shradha Fowdur from DLR Neustrelitz for helping me in understanding the fundamentals of tracking.

Colleagues from DLR for conducting several flight campaigns and providing the experimental radar data for my investigations.

My friends from DLR for accompanying me during the lunch breaks and for making occasional excursions with me over the weekends.

My friend Petar and his family for their pleasant company outside the workplace.

And finally, my family for being there with me at all times, especially my mother who always encouraged me to be optimistic and move forward even in the toughest situations.

Oberpfaffenhofen, July 2022

Sushil Kumar Joshi

Zusammenfassung

Eine regelmäßige und großflächige überwachung des Schiffsverkehrs gewinnt zunehmend an Bedeutung, vor allem auch um maritime Gefahrenlagen und illegale Aktivitäten rechtzeitig zu erkennen. Heutzutage werden dafür überwiegend das automatische Identifikationssystem (AIS) und stationäre Radarstationen an den Küsten eingesetzt. Luft- und weltraumgestützte Radarsensoren, die unabhängig vom Wetter und Tageslicht Daten liefern, können die vorgenannten Systeme sehr gut ergänzen. So können sie beispielsweise Schiffe detektieren, die nicht mit AIS-Transpondern ausgestattet sind oder die sich außerhalb der Reichweite der stationären AIS- und Radarstationen befinden. Luftgestützte Radarsensoren ermöglichen eine quasi-kontinuierliche Beobachtung von räumlich begrenzten Gebieten. Im Gegensatz dazu bieten weltraumgestützte Radare eine große räumliche Abdeckung, haben aber den Nachteil einer geringeren temporalen Abdeckung.

In dieser Dissertation wird ein umfassendes Konzept für die Verarbeitung von Radardaten für die Schiffsverkehr-überwachung mit luftgestützten Radarsensoren vorgestellt. Die Hauptkomponenten dieses Konzepts sind die Detektion, das Tracking, die Geokodierung, die Bildgebung und die Fusion mit AIS-Daten. Im Rahmen der Dissertation wurden neuartige Algorithmen für die ersten drei Komponenten entwickelt. Die Algorithmen sind so aufgebaut, dass sie sich prinzipiell für zukünftige Echtzeitanwendungen eignen, die eine Verarbeitung an Bord der Radarplattform erfordern. Darüber hinaus eignen sich die Algorithmen auch für beliebige, nicht-lineare Flugpfade der Radarplattform. Sie sind auch robust gegenüber Lagewinkeländerungen, die während der Datenerfassung aufgrund von Luftturbulenzen jederzeit auftreten können.

Die für die Untersuchungen verwendeten Daten sind ausschließlich entfernungskomprimierte Radardaten. Da das Signal-Rausch-Verhältnis von Flugzeugradar-Daten im Allgemeinen sehr hoch ist, benötigen die neuentwickelten Algorithmen keine vollständig fokussierten Radarbilder. Dies reduziert die Gesamtverarbeitungszeit erheblich und ebnet den Weg für zukünftige Echtzeitanwendungen.

Der entwickelte neuartige Schiffsdetektor arbeitet direkt im Entfernungs-Doppler-Bereich mit sehr kurzen kohärenten Verarbeitungsintervallen (CPIs) der entfernungskomprimierten Radardaten. Aufgrund der sehr kurzen CPIs werden die detektierten Ziele im Dopplerbereich fokussiert abgebildet. Wenn sich die Schiffe zusätzlich mit einer bestimmten Radialgeschwindigkeit bewegen, werden ihre Signale aus dem Clutter-Bereich hinausgeschoben. Dies erhöht das Verhältnis von Signal- zu Clutter-Energie und verbessert somit die Detektierbarkeit. Die Genauigkeit der Detektion hängt stark von der Qualität der von der Meeresoberfläche rückgestreuten Radardaten ab, die für die Schätzung der Clutter-Statistik verwendet werden. Diese wird benötigt, um einen Detektions-Schwellenwert für eine konstante Fehlalarmrate (CFAR) abzuleiten und die Anzahl der Fehlalarme niedrig zu halten. Daher umfasst der vorgeschlagene Detektor auch eine neuartige Methode zur

automatischen Extraktion von Trainingsdaten für die Statistikschätzung sowie geeignete Ozean-Clutter-Modelle. Da es sich bei Schiffen um ausgedehnte Ziele handelt, die in hochauflösenden Radardaten mehr als eine Auflösungszelle belegen, werden nach der Detektion mehrere von einem Ziel stammende Pixel zu einem physischen Objekten zusammengefasst, das dann in aufeinanderfolgenden CPIs mit Hilfe eines Bewegungsmodells und eines neuen Mehrzielverfolgungs-Algorithmus (Multi-Target Tracking) getrackt wird. Während des Trackings werden falsche Zielspuren und Geisterzielspuren automatisch erkannt und durch ein leistungsfähiges datenbankbasiertes Track-Management-System terminiert.

Die Zielspuren im Entfernungs-Doppler-Bereich werden geokodiert bzw. auf den Boden projiziert, nachdem die Einfallswinkel (DOA) aller Track-Punkte geschätzt wurden. Es werden verschiedene Methoden zur Schätzung der DOA-Winkel für ausgedehnte Ziele vorgeschlagen und anhand von echten Radardaten, die Signale von echten Schiffen beinhalten, bewertet.

Abstract

Frequent ship monitoring can not only facilitate a broad insight of sea traffic situation but may also deliver timely information about myriad maritime threats. Prominent state-of-the art sensors that are used for this task are primarily the automatic identification system (AIS) and coastal radars. Air- and spaceborne radars, which have all-weather and day-night acquisition capabilities, can supplement these systems by detecting ships that are not equipped with AIS transponders or which are too far away from coastal AIS and radar stations. Airborne radars allow for shorter revisits and longer observation times at the cost of limited spatial coverage. On the contrary, spaceborne radars provide large spatial coverage with the disadvantage of longer revisit times.

This doctoral thesis presents a comprehensive maritime surveillance radar data processing concept for airborne radar sensors. The major components of this concept are the detection, the tracking, the geocoding, the imaging and the fusion with AIS data. Novel algorithms for the first three components are developed in the framework of this doctoral thesis. The algorithms are structured in a way that they are suitable for future real-time applications requiring onboard processing. In addition, the algorithms are applicable to arbitrarily flown nonlinear fight tracks and are robust against attitude angle changes occurring during data acquisition due to air turbulence.

The data used for the investigations are range-compressed (RC) radar data. Since for a well-designed airborne radar, the signal-to-noise ratio in RC data is generally sufficiently high, there is no need to use fully focused synthetic aperture radar (SAR) images. This reduces the overall processing time significantly and paves the way for future real-time monitoring systems.

The developed novel target detector operates directly in range-Doppler domain on very short coherent processing intervals (CPI) of the RC data. Due to the short CPIs the targets appear focused in Doppler domain. If they are additionally moving with a certain line-of-sight (LOS) velocity, their signals are shifted out of the clutter region, thus improving their detectability due to an increased signal-to-clutter plus noise ratio. The accuracy of the target detection relies strongly on the quality of the radar data backscattered by the ocean surface, which are used for estimating the ocean clutter statistics needed for deriving a constant false alarm rate (CFAR) detection threshold and keeping the number of false alarms at a low level. Therefore, the proposed detector includes a novel automatic ocean training data extraction method and suitable sea clutter models.

Furthermore, since ships are extended targets occupying more than one resolution cell in high resolution radar data, after detection several target-originated pixels are clustered to physical objects, which are then tracked over successive CPIs using a novel range-Doppler-based target motion model and a multi-target tracking algorithm. During

tracking false or ghost target tracks are automatically recognized and terminated by an incorporated powerful database-based track management system. The obtained target tracks in range-Doppler domain are geocoded and projected to ground, respectively, after estimating the direction-of-arrival (DOA) angles of all track points. Different methods for estimating the DOA angles for extended targets are proposed and evaluated using real radar data containing real moving ships.

Measurement data acquired with DLR's F-SAR and DBFSAR airborne radar sensors provide the proof of concept for all the novel algorithms presented in this doctoral thesis.

Contents

Acronyms and Symbols

Constants

π	Pi (ratio of circle's circumference to its diameter)	3.14159265359
c_0	speed of light in vacuum	2.99792458×10^8[m/s]

Mathematical Notations and Symbols

j	imaginary unit j=$\sqrt{-1}$
arg min	argument of the minimum
arg max	argument of the maximum
exp[·]	exponential function
rect[·]	rectangular operation
$\mathbb{C}$	set of complex numbers
$\mathbb{R}$	set of real numbers
$\forall$	for all
$\in$	element of
$*$	convolution
$\approx$	approximately equal
$\triangleq$	equal by definition
$(\cdot\|\cdot)$	conditioning (for probabilities, estimates or covariances)
$\|\cdot\|$	absolute value (or magnitude) of a quantity
$(\cdot)^{\mathrm{T}}$	transposition of the vector and the matrix
$(\cdot)^{\mathrm{H}}$	complex conjugate transposition of the vector and the matrix
$\sum_k a_{\mathrm{k}}$	sum and the summands a_{k}
$\langle\cdot\rangle$	mean operator
median$(\cdot)$	median operator
$\Gamma(\cdot)$	gamma function
$p(\cdot)$	probability density function of a random variable
$\bar{a}$	mean value of a
$\hat{a}$	estimated or predicted value of a

$\tilde{a}$	difference betweeen the true and the estimated value of a
$\dot{f}(x)$	first-order derivative
$\ddot{f}(x)$	second-order derivative
$K(\cdot)$	modified Bessel function of second kind
arctan	inverse tangent function
$\sin(\theta)$	sine function
$\cos(\theta)$	cosine function
$\tan(\theta)$	tangent function

Acronyms

ACA	average complex amplitude
AIS	automatic identification system
ATI	along-track interferometry
CA	constant acceleration
CCDF	complementary cumulative distribution function
CCM	clutter covariance matrix
CFAR	constant false alarm rate
CMP	cluster center corresponding to the maximum peak
CNR	clutter-to-noise ratio
COBB	center of the bounding box of the cluster
COG	center of gravity
CPI	coherent processing interval
CPU	central processing unit
CV	constant velocity
dB	decibel
DBFSAR	digital beamforming synthetic aperture radar
DBSCAN	density-based spatial clustering of applications with noise
DEM	digital elevation model
DLR	German Aerospace Center

DOA	direction-of-arrival
DOF	degrees of freedom
DPCA	displaced phase center antenna
DST	Defence Science and Technology
EDPCA	extended displaced phase center antenna
EEZ	exclusive economic zone
ENU	east-north-up
FARR	false alarm rate ratio
FFT	fast Fourier transform
FHR	Fraunhofer Institute for High Frequency Physics and Radar Techniques
F-SAR	flugzeug-synthetic aperture radar
GMTI	ground moving target indication
GNN	global nearest neighbour
GOSPA	generalized optimal sub-pattern assignment
GPS	global positioning system
GPU	graphical processing unit
HAP	high-altitude platform
HAPS	high-altitude pseudo satellite
HFSWR	high-frequency surface-wave radar
IMU	inertial measurement unit
ISAR	inverse synthetic aperture radar
ISTAP	inverse space-time adaptive processing
JPDAF	joint probabilistic data association filter
KA	K-class A distribution
KF	Kalman filter
LFM	linear frequency modulation
LOS	line-of-sight

LRIT	long range identification and tracking
LTE	long term evolution
MAA	maximum of the absolute amplitude
MAD	median absolute deviation
MMSI	maritime mobile service identity
MoM	method of moments
MTI	moving target indication
MTT	multi-target tracking
MV	mean and variance
NEES	normalized (state) estimation error squared
NIS	normalized innovation squared
NLLSQ	non-linear least squares
NNCG	nearest neighbor to the center of gravity
OS-CFAR	order-statistic constant false alarm rate
OSPA	optimal sub-pattern assignment
OTHR	over-the-horizon radar
PAMIR	phased array multi-functional imaging radar
PDF	probability density function
PF	predicted flag
PFA	probability of false alarm
PP	prediction percentage
PRF	pulse repetition frequency
RADAR	radio detection and ranging
RAR	real aperture radar
RC	range-compressed
RCMC	range cell migration correction
RCS	radar cross section

RMSE	root mean square error
ROI	region of interest
RPM	revolutions per minute
RX	receive
SAR	synthetic aperture radar
S-AIS	satellite-based automatic identification system
SCNR	signal-to-clutter-plus-noise ratio
SG	Savitzky-Golay filter
SNR	signal-to-noise ratio
SOG	speed over ground
SQL	structured query language
STAP	space-time adaptive processing
SWMF	stationary world matched filtering
TanDEM-X	TerraSAR-X add-on for digital elevation measurement
TB	terabytes
TS-CFAR	truncated statistics constant false alarm rate
TX	transmit
UTM	universal transverse mercator
VMS	vessel monitoring system
VTS	vessel traffic services
WGS84	world geodetic system 1984
3MD	tri-modal discrete texture

Lower Case Letters

a	moving target acceleration magnitude
a_{d}	discrete texture intensity level in 3MD model
a_{dop}	target acceleration in the range-Doppler domain
a_{s}	coeffcient covering the free-space attenuation, reflectivity and two-way antenna pattern weighting
a_{r}	target's acceleration in the range-time domain
a_{x}	moving target along-track acceleration
a_{y}	moving target across-track acceleration
b	scale parameter of the K-distribution
b_{L}	lower bound of chi-square test at a certain significance level α
b_{r}	scale parameter of the K-Rayleigh distribution
b_{U}	upper bound of chi-square test at a certain significance level α
c_{d}	weighting of discrete texture intensity level of 3MD model
d_{M}	Mahalanobis distance metric
d_{min}	minimum Mahalanobis distance
$\boldsymbol{d}(u)$	beamforming vector or DOA angle vector
$\boldsymbol{e}_{\mathrm{x}}, \boldsymbol{e}_{\mathrm{y}}, \boldsymbol{e}_{\mathrm{z}}$	vectors for converting the target position from local to global coordinates
f	factor for setting the target pre-detection threshold
$f_{\mathrm{a,st}}$	Doppler frequency of a stationary target
f_{a}	Doppler frequency of a moving target
f_{am}	measured Doppler frequency position of the target cluster
f_{r}	range sampling frequency
$f_{\mathrm{cl}}[r,t]$	clutter Doppler centroid as a function of range and azimuth time
f_{DC}	Doppler frequency shift or Doppler centroid
f_{NNCG}	Doppler frequency of the NNCG pixel
h	platform height above ground
$h(t)$	reference function in time domain
h_{t}	difference between the platform and the target height
h_{m}	histogram bin in least square fitting for sea clutter modeling
$k_{0.75}$	scale factor representing the 0.75 quantile of the standard Gaussian distribution
k_{r}	linear FM rate (or chirp slope)
k_{a}	Doppler slope or Doppler rate of the moving target signal
$k_{\mathrm{a,st}}$	Doppler slope or Doppler rate of the stationary target signal
k_{als}	CPI at which Doppler aliasing occurs

l	dimension of the measurement states or the degrees of freedom in chi-square-based hypothesis testing
$\boldsymbol{m}(k)$	radar measurement vector at CPI k
n	dimension of the target states in the range-Doppler domain
n_{det}	total number of false positive target pixels in a radar data patch
n_{min}	minimum number of pixel-based detections needed to form a cluster using DBSCAN
n_{r}	total number of range bins of a radar data patch
n_{tot}	total number of pixels in a radar data patch
q	quadratic Doppler coefficient
r	slant range between TX/RX antenna phase center and the target on the ground
r_0	slant range of a stationary point-like target at t=0 (or antenna beam center)
r_{10}	slant range between the antenna and the moving target at t=0
$r(f_{\mathrm{a}})$	target range as a function of Doppler frequency
r_{t}	measured slant range of the target
$r_{\mathrm{t,g}}$	ground range of the target
$r_{\mathrm{t,ref}}$	reference slant range of the target
r_{st}	slant range of a stationary target
r_{m}	measured slant range position of the target cluster
r_{NNCG}	range of the NNCG pixel
$s(t)$	uncompressed input signal in time domain
$s_{\mathrm{out}}(t)$	compressed signal in time domain or the impulse response function
$s_{\mathrm{RX}}(\tau)$	received single-channel pulse waveform in radio frequency band
$s_{\mathrm{RX,b}}(\tau)$	received single-channel pulse waveform in baseband
$s_{\mathrm{TX}}(\tau)$	transmitted single-channel pulse waveform in radio frequency band
$s_{\mathrm{TX,b}}(\tau)$	transmitted single-channel pulse waveform in baseband
t	azimuth time or slow time
t_{k}	absolute center time of the CPI k
t_{olp}	azimuth time at which the moving target range histories overlap
u_{r}	initial velocity of the target in the range-time domain
$u(t)$	directional cosine as a function of slow time
v_0	absolute target velocity on the ground
v_{dop}	target velocity in the range-Doppler domain
v_{p}	platform velocity in azimuth

v_{r0}	line-of-sight velocity of the target at t=0
$v_{\mathrm{r,max}}$	maximum unambiguous target's radial velocity
$v_{\mathrm{r,min}}$	minimum detectable LOS velocity of the target
v_{x0}	moving target along-track velocity at t=0
v_{y0}	moving target across-track velocity at t=0
(x, y, z)	coordinate system whose x-axis is parallel to the aircraft's azimuth direction
x_0	x-position of the target at t=0
x_{m}	position of the antenna phase center in azimuth with respect to the array origin
$(x_{\mathrm{p}}, y_{\mathrm{p}}, z_{\mathrm{p}})$	platform position in (x, y, z) coordinate system
$\boldsymbol{x}_{\mathrm{p}}$	platform position vector in (x, y, z) coordinate system
$\boldsymbol{x}_{\mathrm{p,UTM}}$	platform position vector in UTM coordinate system
$\boldsymbol{x}_{\mathrm{rd}}(k)$	target kinematics in the range-Doppler domain at CPI k
x_{s}	modified speckle mean of the K-Rayleigh distribution
$(x_{\mathrm{t}}, y_{\mathrm{t}}, z_{\mathrm{t}})$	target position in (x, y, z) coordinate system
$\boldsymbol{x}_{\mathrm{t}}$	target position vector in (x, y, z) coordinate system
$(x_{\mathrm{UTM}}, y_{\mathrm{UTM}}, z_{\mathrm{UTM}})$	ENU or UTM coordinate system
$\boldsymbol{x}_{\mathrm{t,UTM}}$	target position vector in UTM coordinate system
y_0	y-position of the target at t=0
z	complex amplitude pixel in the range-time domain
z_0	z-position of the target at t=0

Capital Letters

A	look direction of the antenna (1 is for right-looking and -1 is for left-looking antenna)
$A(r)$	average amplitude profile as a function of range
$\hat{A}_{\mathrm{DS}}(f_{\mathrm{a}})$	estimated average Doppler spectrum
$A_{\mathrm{med}}(r)$	one-dimensional moving median of $A(r)$
A_{s}	coeffcient that comprises the refectivity of the scatterer
B_{c}	clutter bandwidth in the Doppler domain
B_{r}	chirp bandwidth
C	clutter signal
D	number of discrete scatterers in 3MD model
$\boldsymbol{D}(k)$	innovation (or residual) matrix
$D_{\mathrm{r}}(u)$	receive antenna characteristics as a function of directional cosine

$D_{\mathrm{t}}(u)$	transmit antenna characteristics as a function of directional cosine
$\boldsymbol{F}$	state transition matrix in Kalman filter
H_0	null hypothesis
H_1	alternative hypothesis
$\boldsymbol{H}$	output transition matrix (or observation matrix)
I	backscatter intensity in the Doppler domain
$\boldsymbol{I}$	identity matrix
$\boldsymbol{K}(k)$	Kalman gain
L	effective number of looks
L_{a}	antenna length in azimuth direction
M	number of receving antennas in a multichannel radar system
N	number of azimuth samples or addtive white Gaussian noise
N_{CPI}	number of consecutive azimuth samples within a CPI
$N_{\mathrm{CPI,DS}}$	utilizable azimuth samples in a CPI for a certain Doppler bin size
$N_{\mathrm{CPI,SR}}$	utilizable azimuth samples in a CPI without performing RCMC
N_{pred}	number of CPIs where the target positions are only "predicted"
N_{L}	total extracted track length in terms of total number of CPIs
N_{vm}	validated measurements within the gating region of a track
$P(r, f_{\mathrm{a}})$	power sectral density
$P_{\mathrm{CN}}(r, f_{\mathrm{a}})$	power sectral density after clutter normalization
$\mathrm{PFA}_{\mathrm{est}}$	estimated or measured false alarm rate
$\mathrm{PFA}_{\mathrm{set}}$	desired false alarm rate
$\boldsymbol{P}(k)$	target state covariance matrix at CPI k
$\boldsymbol{Q}$	process (or system) noise covariance matrix
R	total number of range samples used for target pre-detection
$\boldsymbol{R}$	measurement noise covariance matrix
$\boldsymbol{R}_{\mathbf{W}}$	clutter covariance matrix
S	moving target signal
$S(f_{\mathrm{a}})$	target signal as a function of Doppler frequency
$\boldsymbol{S}(k)$	innovation covariance matrix
T_{CPI}	time duration (or the integration time) of a CPI
$T_{\mathrm{CPI,DS}}$	integration time corresponding to a certain Doppler bin size
T_{SA}	synthetic aperture time
$Z(r, f_{\mathrm{a}})$	single-channel data in the range-Doppler domain
$\boldsymbol{Z}(r, f_{\mathrm{a}})$	multichannel data in the range-Doppler domain
$Z_{\mathrm{cs}}(r, f_{\mathrm{a}})$	clutter suppressed data in the range-Doppler domain
$Z_{\mathrm{sum}}(r, f_{\mathrm{a}})$	sum-channel data in the range-Doppler domain
$\boldsymbol{Z}_{\mathrm{t}}(r, f_{\mathrm{a}})$	target's multichannel data vector in the range-Doppler domain

$\boldsymbol{Z}_{\mathrm{t,ACA}}(r, f_{\mathrm{a}})$	average complex amplitude target pixel
$\boldsymbol{Z}_{\mathrm{t,MAA}}(r, f_{\mathrm{a}})$	maximum of the absolute amplitude target pixel
$\boldsymbol{Z}_{\mathrm{t,norm}}(r, f_{\mathrm{a}})$	normalized complex amplitude target pixel
$\boldsymbol{Z}_{\mathrm{t,NNCG}}(r, f_{\mathrm{a}})$	complex target amplitude at the NNCG of the cluster
$\boldsymbol{Z}_{\mathrm{t,set}}(r, f_{\mathrm{a}})$	clustered multichannel target data vector in a single CPI

Greek Symbols

α	unknown parameters of a distrbution function or the significance level in a hypothesis testing
α_{p}	aircraft's course angle measured with respect to the UTM Easting
α_{t}	target moving direction with respect to its along-track motion
α_{wn}	factor accounting for the losses due to windowing in matched filtering
$\delta_{\mathrm{az,RAR}}$	azimuth resolution of RAR
$\delta_{\mathrm{az,SAR}}$	azimuth resolution of SAR
δ_{cr}	cross-range resolution of the image
δf_{a}	Doppler bandwidth or Doppler frequency spread
$\delta_{\mathrm{g,raw}}$	ground range resolution of the radar image
$\delta_{\mathrm{r,raw}}$	slant range resolution using single frequency waveform
δ_{r}	slant range resolution after pulse compression using LFM waveform
Δ	mulitplicative texture component of the K-distribution
$\Delta\psi_{\mathrm{DOA}}$	DOA angle difference between the measured and the reference DOA angles
Δf_{a}	Doppler bin size of the range-Doppler image
$\Delta f_{\mathrm{thres}}$	width of the rectangular search window along Doppler
$\Delta r_{\mathrm{thres}}$	length of the rectangular search window along range
Δr	slant range spacing
Δt	time difference between two successive target positions on the ground
Δx	azimuth displacement of the moving target in SAR image
Δx_{az}	difference between measured and true azimuth position of the target
Δx_{r}	azimuth position difference between the radar and the target on the ground
Δx_{g}	distance moved by the target in along-track in a given time interval
Δt_{rc}	time interval where the range cell migration do not cross one slant range spacing
Δt_{mng}	time interval used in track management
Δy_{g}	distance moved by the target in across-track in a given time interval

Δy_r	ground range distance between the radar and the target
ϵ_c	radius used in DBSCAN for expanding the clusters
ϵ_NIS	normalized innovation squared
η	target detection threshold based on CFAR
$\tilde{\eta}$	threshold error between the data and the model CCDF at a specific CCDF value
η_data	threshold obtained from the data at a specific CCDF value
η_model	threshold obtained from the model at a specific CCDF value
$\eta_\mathrm{pre}(r)$	range-dependent target pre-detection threshold
θ_D	depression angle
θ_3dB	one-way 3 dB antenna azimuth beamwidth
θ_i	incidence angle
θ_roll	roll angle
θ_pitch	pitch angle
θ_yaw	yaw angle
λ	radar wavelength
μ	mean of the data
ν	shape parameter of the K-distribution
ν_r	shape parameter of the the K-Rayleigh distribution
ρ_c	normalized clutter variance in 3MD model
ρ_n	normalized noise variance in 3MD model or thermal noise in the K-Rayleigh distribution
ρ_r	extra Rayleigh component in the K-Rayleigh distribution
σ	standard deviation
σ_DOA	standard deviation in the measured DOA angles of an extended target in a single CPI
σ_p0^2	parameter used for the initialization of the state covariance matrix
$\sigma(r)$	standard deviation as a function of range for target pre-detection
τ	range time or fast time
τ_p	pulse duration
χ^2	chi-square distribution
$\psi_\mathrm{DOA,ar}$	DOA angle with respect to the antenna array axis
$\psi_\mathrm{DOA,az}$	DOA angle with respect to the aircraft's azimuth axis
$\psi_\mathrm{DOA,az,g}$	ground projection of the DOA angle with respect to the aircraft's azimuth axis
$\psi_\mathrm{DOA,ref}$	reference DOA angle computed using the reference target range

Superscripts and Subscripts

k	CPI number
m	index of the RX channel
p	relates to the platform
RX	receive
t	relates to the target
TX	transmit
UTM	relates to global UTM coordinate system

1 Introduction

1.1 Background

Maritime transport is considered as the backbone of global trade and the world economy. Despite having new modes of transport, they are responsible for carrying 90% of the world's merchandise. Without maritime transport, large scale goods exchange necessary to sustain the global society would not be possible. As of January 2021, there are around 55,000 merchant ships active in international trade [1].

With ever increasing sea traffic volumes, several maritime threats, for instance, terrorism, piracy, human smuggling, illegal migration, arms or drugs supply, overfishing and marine pollution have also escalated over the past few decades [2–4]. To cope with these threats and to ensure the safety and security on the oceans, maritime surveillance systems are deployed across the globe [5–7]. They facilitate a comprehensive insight into sea traffic conditions and enhance maritime situational awareness. European Commission defines the maritime surveillance as "*the effective understanding of all activities carried out at sea that could impact the security, safety, economy or environment of the European Union and its Member States*" [8]. In the next section some state-of-the-art maritime surveillance systems which are dominating the maritime world and are currently operating worldwide are discussed.

1.2 State-of-the-Art Maritime Surveillance Systems

Popular maritime surveillance systems are VTS (vessel traffic services) [9], LRIT (long-range identification and tracking) [10], VMS (vessel monitoring system) [11], AIS (automatic identification system) [12], marine radars (radio detection and ranging) [13] and HFSW-OTHR (high-frequency surface-wave over-the-horizon radar) [14]. In this section, AIS, marine radars and HFSW-OTHR are briefly discussed.

The AIS transceivers on the ships transmit and receive the ship-related messages and allow vessels to exchange navigational data with one another and also with the shore and the satellites that are equipped with onboard AIS receivers. There are two types of AIS: terrestrial (or vessel-based) and satellite-based (S-AIS). Terrestrial-based AIS allow for ship-to-ship and ship-to-shore communication. In S-AIS the messages are exchanged not only between the AIS equipped ships, but also with the low-orbit satellites [15]. With S-AIS it is possible to achieve global AIS coverage by monitoring vessels which are well beyond the reach of terrestrial-based AIS.

One major disadvantage common to both the terrestrial and the S-AIS is that, for detecting a ship, its AIS receiver must be turned on [16]. Vessels with illegal activities, e.g.,

fishing in protected areas, can conceal their location by turning off their AIS transponders. Marine radars can detect such vessels as long as the vessels are good reflectors and are within the line-of-sight (LOS) of the radar.

Marine radars are ship-borne or vessel-based radars that operate at X- (8-12 GHz) and S-band (2-4 GHz) frequency region of the electromagnetic spectrum. They assist in collision avoidance and safe navigation at sea by detecting other ships and land obstacles [17]. Some excellent works related to ship monitoring using marine radars can be found in [18–22].

Marine radars, however, have their own set of limitations. First, the structure of the ship (eg., masts, derricks and funnels) and the objects on the ship can cause so-called blind and shadow sectors. The targets lying in these sectors are shielded and as a result, they do not appear on the radarscope. Furthermore, marine radars have limited range visibility (between 24 and 40 nautical miles) due to the Earth's curvature and the radar elevation [13, 23].

Ground-based coastal radars are more comprehensive, large scale and cost-efficient long-range (around 96 nautical miles) maritime surveillance systems. They are responsible for protecting the coastlines from several sea threats [24]. Despite having the long-ranging capability due to their installations on higher altitude areas such as hills, their surveillance area generally is limited to regions along the coast. Therefore, ships on open sea, far away from the coast cannot be detected by the coastal radars.

HFSW-OTHR can overcome the limitations of both marine and coastal radars by transmitting shortwave radio frequency (3-30 MHz) that reaches the target beyond the horizon (up to 200 nautical miles) by refracting off the ionosphere [25,26]. It has both long-range tracking and real-time monitoring capability [27, 28]. However, the infrastructural requirements of these systems are very high which makes them a very expensive investment [24].

The aforementioned limitations of currently operating maritime surveillance systems have encouraged the need for the development of space and air-based radars for ship monitoring.

1.3 Airborne Radar-based Maritime Surveillance

Radars that are flying at high altitudes have the ability to detect and monitor ships that are not equipped with the AIS transceivers and are out of the LOS of the marine radars. The operating frequencies of the high-flying radar sensors can penetrate through the clouds, fog and rain, and their active systems allow them to operate even during night times. Airborne radars, in contrast to the spaceborne radar systems, can collect data with shorter revisits and longer observation times on the land and the ocean surface, at the cost of limited spatial coverage.

Compared to the stationary ground-based maritime surveillance radars, with airborne radars, the targets are observed and tracked differently. In the following some key differences are detailed:

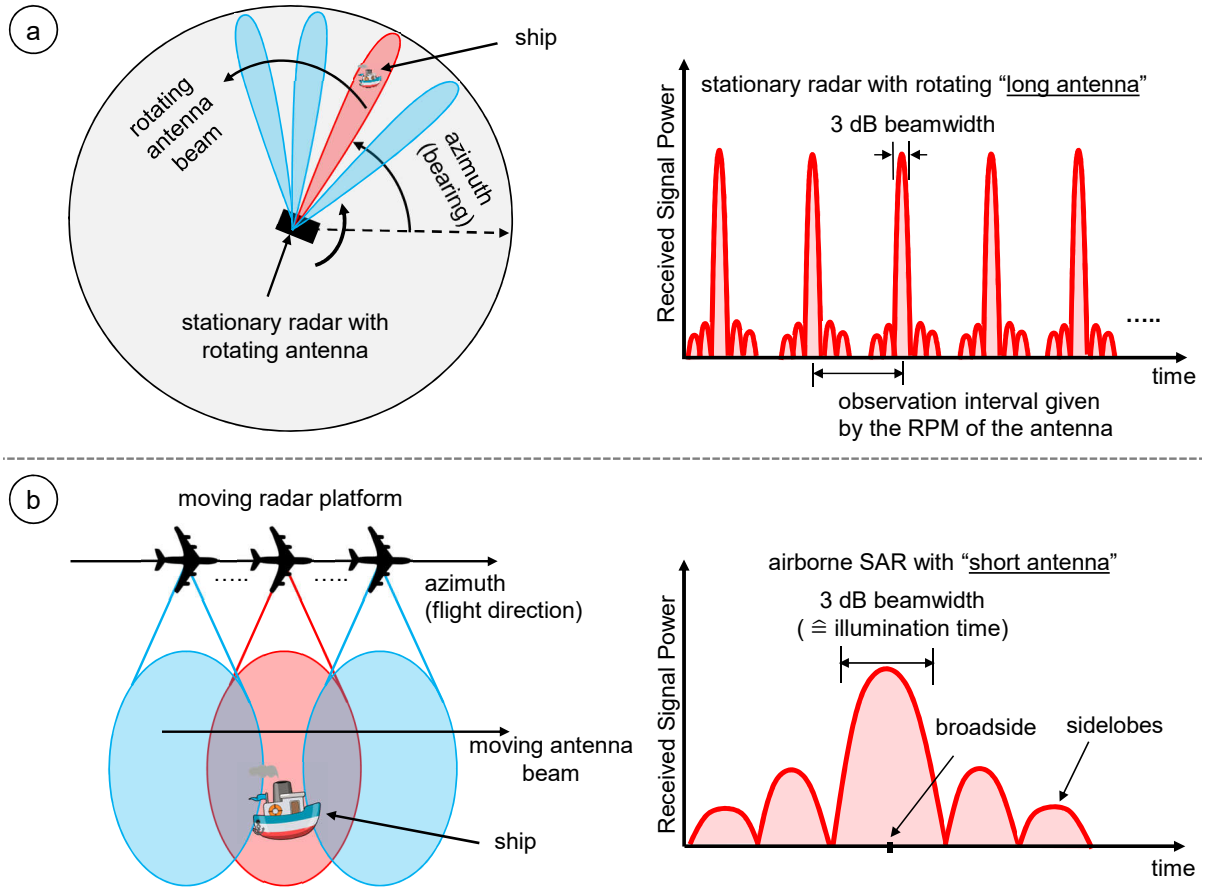

Figure 1.1: Acquisition geometries and the received signal powers of (a) stationary ground-based radar with rotating or electronically steerable long antenna and (b) air-based radar with short and non-steerable antenna. The 3 dB antenna beams and targets within the beams are shown in the figure.

- A stationary ground radar shown in Figure 1.1(a) uses a large rotating antenna and transmits a very narrow horizontal antenna beam. For a typical ground-based radar system, its antenna rotates at 24-45 RPM (revolutions per minute), resulting in one complete scan occurring at every 1.3-2.5 s [13]. The narrow antenna beam (in the order of less than 1°) allow these radars to measure the bearing (angular position) of the target very precisely [23].
- On the other hand, as shown in Figure 1.1(b), the airborne radar uses a relatively short antenna with a wide antenna beam. The target is detected and tracked as long as it is illuminated by the antenna beam that moves by itself at the speed of the aircraft. Note that the antenna in the shown example is non-steerable, has a wide beamwidth and is typically designed for synthetic aperture radar (SAR) systems. In SAR systems short antennas are used for obtaining high azimuth resolution since the achievable azimuth resolution after SAR focusing is half the antenna length (cf. Section 2.3).

Different beamwidths of the ground and air-based radar sensors, as shown in Figure 1.1, are due to their different antenna lengths along the azimuth direction. The relationship

between the antenna length L_{a} and one-way 3 dB beamwidth $\theta_{3\mathrm{dB}}$ of a planar antenna with rectangular aperture can be expressed as [29]

$$\theta_{3\mathrm{dB}} \approx 0.886 \cdot \frac{\lambda}{L_{\mathrm{a}}}, \tag{1.1}$$

where λ is the radar wavelength. From (1.1) it is clear that long antennas radiate narrow and highly directional beams. With such beams, high angular resolution and thus, high target position accuracy can be achieved by the radar. However, if the antenna is non-steerable, the narrow beam illuminates the target for a short amount of time. Therefore, the antenna length requires a trade-off: it should be short enough for increasing the illumination time on the target and long enough for radiating directive beams in order to improve the target location accuracy.

Airborne radar-based surveillance systems employ pulse-Doppler radars for detecting and locating the moving targets [30]. Pulse-Doppler radars are also the basis of modern day SAR systems. Although, SAR is a well-established imaging technique and have been widely used for earth remote sensing [31, 32], it is originally designed for imaging the stationary world and the moving targets in SAR images appear defocused and dislocated from their original geographical positions (cf. Section 2.5.3) [33]. This happens due to the different Doppler frequencies of the moving objects in comparison to the stationary objects. Therefore, instead of using conventional SAR processing, pulse-Doppler radar-based MTI (moving target indication) techniques are exploited for detecting and monitoring the moving targets [34].

With pulse-Doppler MTI radars the Doppler frequency shift produced by the moving target are used to estimate the target's LOS (or radial) velocity. The Doppler frequency shift f_{DC} of the moving target is expressed as [30]

$$f_{\mathrm{DC}} = \frac{-2}{\lambda} \cdot v_{\mathrm{r0}}, \tag{1.2}$$

where v_{r0} is the target's LOS velocity. The above equation shows that after measuring the Doppler frequency shift, the LOS velocity of the moving target can be estimated.

Some state-of-the-art airborne SAR systems that are used for the maritime surveillance activities are F-SAR [35] and DBFSAR [36] operated by the Microwaves and Radar institute of DLR (German Aerospace Center), PAMIR from FHR (Fraunhofer Institute for High Frequency Physics and Radar Techniques) [37, 38] and Ingara airborne radar developed by DST (Defence Science and Technology Organization), Australia [39, 40]. There are also some spaceborne radar systems with MTI capabilities such as the German X-band satellites TerraSAR-X and TanDEM-X [41–43], Canadian C-band RADARSAT-2 satellite [44, 45] and the X-band COSMO-Skymed satellite from Italy [46, 47].

An example of a high resolution ISAR (inverse SAR) image of a ship using DLR's DBFSAR airborne radar system is shown in Figure 1.2. The ship name is HAM 316, which is a dredger of dimensions 129 m x 22 m (cf. Table B.3 in page 152).

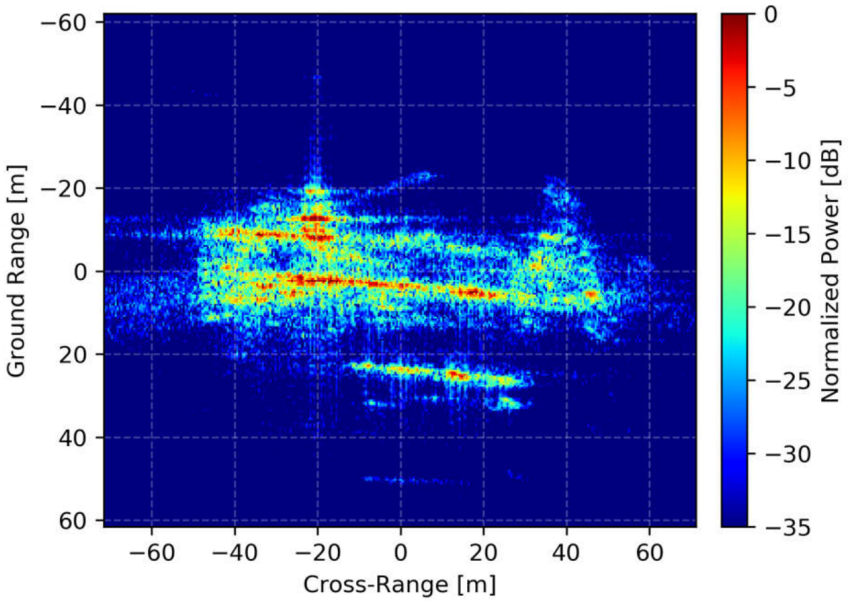

Figure 1.2: High resolution ISAR image of ship HAM 316 obtained using the DLR's DBFSAR airborne radar system [36].

1.4 Main Objectives and Thesis Contributions

Airborne radars carry immense potential for supplementing the existing state-of-the-art maritime surveillance systems. However, there is no substantial research work published in the open literature that describes a comprehensive and complete operational ship surveillance approach using moving airborne radar platforms. The available algorithms for such platforms were originally designed for monitoring road vehicles with limited range-resolution [48]. For monitoring extended targets like ships, additional efforts are needed.

The requirements in the context of maritime moving target monitoring using airborne radar sensors that shall be addressed in this thesis are:

1. Onboard processing concept for achieving real-time or near real-time target monitoring capability.
2. Developing algorithms in a way that they are also suitable for arbitrarily flown (nonlinear) flight tracks.
3. Detecting ships of low radar cross section (RCS) in the presence of moving background clutter.
4. Tracking and track management of multiple extended targets in dense multi-target scenarios.
5. Estimating the actual geographical positions of the tracked targets.

Considering the aforementioned objectives, this thesis presents a novel maritime surveillance processing chain using airborne radar sensors. A high-level flowchart of the air-based ship monitoring is illustrated in Figure 1.3. As can be seen in the figure, the major

blocks of the processing flowchart are: (i) detection and clustering for finding extended targets in the data; (ii) multi-target tracking (MTT) for extracting individual target tracks; (iii) ground projection for visualizing the target tracks on the ground; (iv) ship data patch extraction for saving the data downlink capacity; (v) ISAR imaging for generating high resolution radar image sequences of the targets (cf. Figure 1.2) using the extracted data patches, and (vi) AIS fusion. Novel algorithms for the first three components are developed in the frame of this doctoral thesis. For ISAR imaging an already available algorithm is used [49]. AIS fusion is the future work, however, AIS data are used in this thesis for validation purposes.

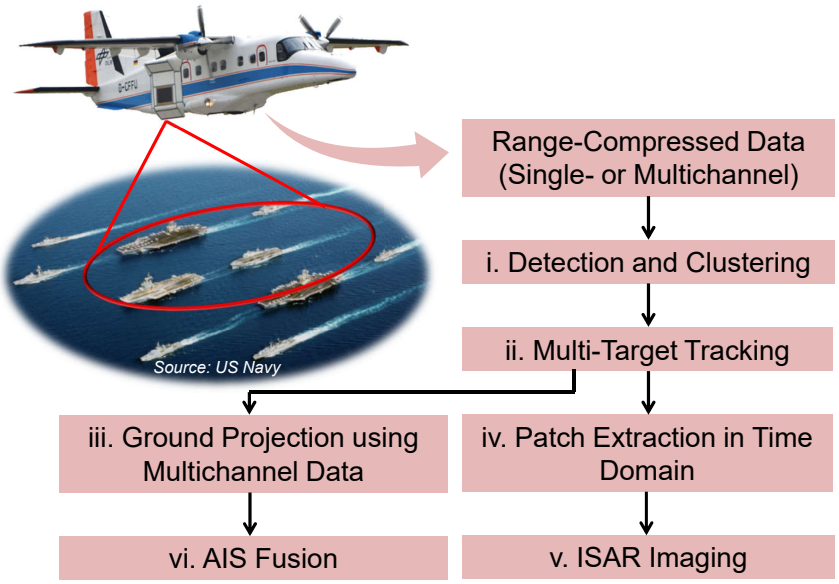

Figure 1.3: High-level processing flowchart of the proposed radar-based ship monitoring concept using an airborne radar sensor.

As an input to the proposed airborne radar-based maritime surveillance chain, instead of using fully focused SAR images, as traditionally used when it comes to ship detection using spaceborne SAR [50,51], range-compressed (RC) data (either single or multichannel data) are used [52]. This is because for a well-designed airborne radar, signal-to-noise-ratio (SNR) in most cases is sufficiently large. For instance, DLR's F-SAR system has a peak power of approximately 2 kW which leads to sufficient high SNR values of RC data for altitudes up to 6 km above ground [49]. Therefore, there is not a need to implement conventional time-consuming SAR focusing techniques (cf. Section 2.3.1). This saves overall processing time and paves the way for future real-time capability.

Novelties and major contributions of the thesis in the field of maritime surveillance using airborne radar sensors are as follows:

- A novel range-Doppler-based constant false alarm rate (CFAR) ship detection algorithm with automatic training data extraction using single-channel RC airborne radar data (cf. Chapter 3). The algorithm has the following components:

  - A novel target pre-detection module running in time domain that excludes bright peaks and spiky clutter from the data for avoiding estimation biases;
  - Clutter normalization in the Doppler domain for extracting reliable ocean clutter training samples; and
  - Ocean clutter modeling and statistics estimation using CFAR-based stochastic distribution functions followed by the target detection threshold computation.

- A novel target motion model for tracking targets in the range-Doppler domain. The motion model is incorporated into the conventional Kalman filter (KF) [53] framework for recursively estimating the kinematics (eg., position, velocity and acceleration) of the targets in the Doppler domain (cf. Chapter 4).
- A novel range-Doppler-based tracking and track management algorithm for tracking multiple extended targets (cf. Chapter 5). The algorithm has the following components:
  - An SQLite [54] database structure written in Python as the core of the overall MTT system;
  - A powerful track management scheme that is running simultaneously within the tracker for automatically updating the confirmed tracks and terminating the false or ghost targets;
  - Fast and efficient data association module for doing MTT; and
  - Doppler aliasing block for extracting the target's true range and Doppler history by recognizing and correcting the Doppler back-folding.
- Novel methods for estimating the direction-of-arrival (DOA) angle of extended targets using multichannel RC airborne radar data. Estimated DOA angles of the extended targets are used for computing their actual geographical positions. The target ground position estimates using different methods are validated with the simultaneously acquired AIS-based ground truth data (cf. Chapter 6).

The structure of the proposed methods is chosen in such a way that, real-time capability can be achieved after an efficient implementation of the algorithms in a parallelized way on a multicore or multiprocessor computer, taking also into account graphical processing units (GPUs).

Furthermore, it is worth mention here that a major motivation to develop airborne radar-based maritime surveillance chain is to integrate it in future high-altitude platforms (HAP) or high-altitude pseudo satellites (HAPS). These platforms are expected to have a much longer endurance than conventional aircraft. They will be flying in the stratosphere for several days, weeks, months or even years. With radars integrated in such platforms, a continuous monitoring of hotspots like exclusive economic zone (EEZ) and larger regions of interest in the order of several hundred to several thousand square kilometers is feasible [52, 55]. An example of a future HAPS in a circular flight track configuration is illustrated in Figure 1.4.

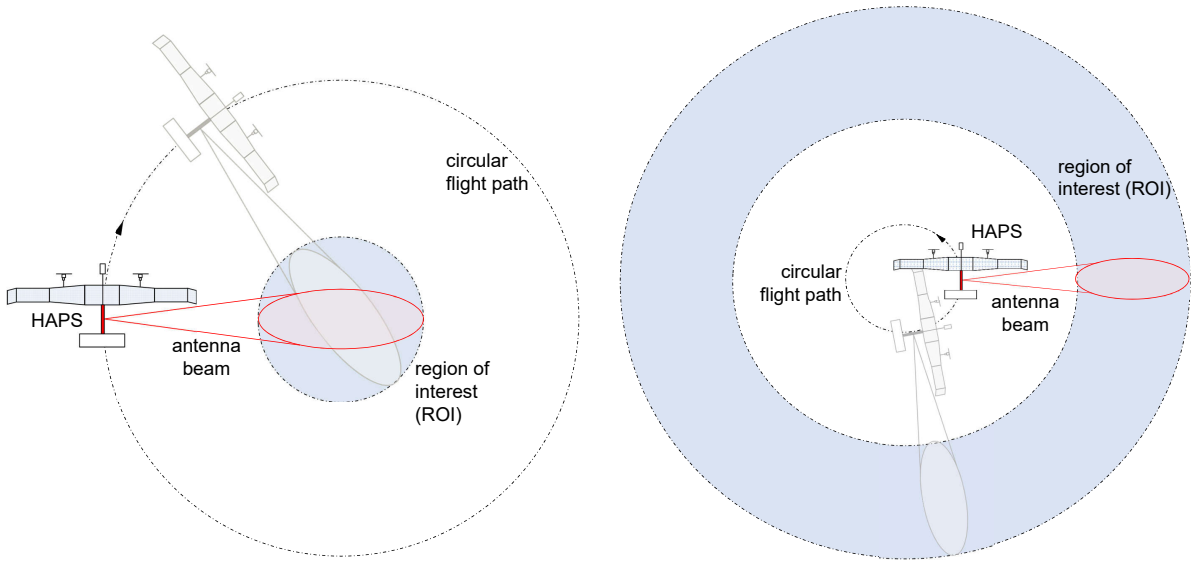

Figure 1.4: Observing a region of interest (ROI) using HAPS flying in a circle. The HAPS antenna beam on the left illuminate a ROI over the entire aspect angle of 360° whereas on the right an annulus is repeatedly monitored [52].

1.5 Structure of the Thesis

This thesis is organized into seven chapters addressing different aspects of the proposed air-based maritime surveillance. The outline of the remaining chapter is as follows:

In **Chapter 2**, the acquisition geometry of airborne radar and its working principle are discussed. Furthermore, details related to the range-Doppler processing of the radar data and its benefits in the context of moving target are presented.

A range-Doppler-based CFAR ship detection algorithm using single-channel RC airborne radar data is presented in **Chapter 3**. The chapter proposes a novel automatic training data extraction procedure for robust ocean statistics estimation and later, for an accurate target detection threshold computation.

A KF-based target motion model for tracking targets in the range-Doppler domain is introduced in **Chapter 4**. The outcomes of the proposed motion model are used as an input to the MTT algorithm. In **Chapter 5**, an efficient MTT and track management algorithm in the range-Doppler domain is discussed. The MTT framework has several components and each component is explained in detail in the chapter.

Chapter 6 presents multichannel RC radar data processing and geocoding techniques for projecting the radar-based target detections to the ground. In the chapter different methods for computing the geographical position of extended targets are proposed. The obtained target ground position estimates are compared with the simultaneously acquired AIS data for validation purposes.

At the end of every chapter experimental results from real measurement airborne radar data are presented to prove the concept. Finally, **Chapter 7** concludes the thesis with a summary and discussion. It also presents an outlook and recommendations for the future research on radar-based ground moving target monitoring systems and techniques.

2 Airborne Radar and Moving Targets

In this chapter the principle of airborne radar is explained and the concepts of real and synthetic aperture radar (SAR) are briefly reviewed. Different types of real-world target motions and single- and multichannel moving target signal models are presented in the chapter. The effects of moving targets in SAR imagery are also briefly discussed. Finally, the concept of range-Doppler processing in the context of moving target signals is presented.

2.1 Acquisition Geometry

This section presents the acquisition geometry and the working principle of airborne radar and introduces some common radar terminologies. For simplifying the explanation two main assumptions are considered in this section. First, it is assumed that the airborne radar is flying in a straight line over the flat Earth surface. Second, the acquisition mode of the airborne radar is stripmap mode, i.e., the radar has a side-looking acquisition geometry and as the radar platform moves, the antenna beam pointing direction is fixed. The acquisition geometry of the moving airborne radar is illustrated in Figure 2.1.

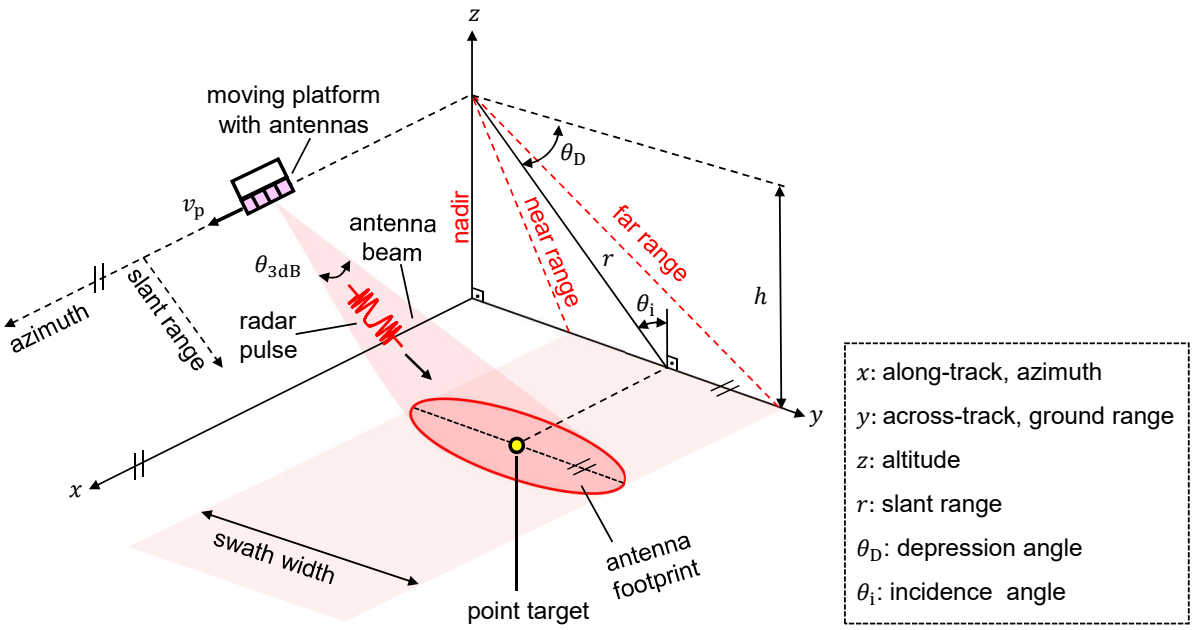

Figure 2.1: Airborne radar acquisition geometry. The radar in the shown figure is left-looking with respect to the flight path.

As shown in Figure 2.1, the platform carrying the radar sensor moves parallel along the x-axis with a constant velocity (CV) v_p and at a constant height h. The radar system mounted on the moving airborne platform has a side-looking geometry and the antenna is tilted downward by the depression angle θ_D, measured from the horizontal plane at the location of the platform. The moving direction of the radar is known as the azimuth direction and the radar LOS direction is known as the slant range direction.

The antenna beam that moves at the speed of the aircraft illuminates an area on ground with a certain swath width, referred to as antenna footprint. The point in the swath nearest to the nadir point of the radar platform is called the near range and the farthest point from the nadir is known as the far range. The incidence angle θ_i, which is the angle between the radar beam and the ground surface, increases from near range to far range.

The radar while moving in the along-track direction coherently sends a train of pulses in its LOS direction at a certain pulse repetition frequency (PRF). The PRF is generally fixed during a single acquisition, and it ranges from a few hundreds to a few thousand Hertz for airborne and spaceborne radar systems, respectively.

2.2 Real Aperture Radar

Real aperture radar (RAR) is a side-looking radar which emits the antenna beam in the slant range direction orthogonal to the aircraft's azimuth direction as shown in Figure 2.1. The transmitted beam then interacts with the ground objects and only a portion of the transmitted signal energy is collected by the receiving antenna (same as the transmit antenna for a monostatic radar or a different one for a bi- or multistatic radar).

The received radar echoes from the ground objects arrive at the antenna at different times, depending on their slant ranges or LOS distances from the antenna. As the aircraft moves forward and more pulses are transmitted, the associated received echoes from the target are written into the successive rows and finally, a two-dimensional reflectivity map of the imaged swath is generated [31].

The azimuth resolution of a RAR is determined by the 3 dB azimuth beamwidth of the antenna and is approximated as [32]

$$\delta_\mathrm{az,RAR} \approx \theta_\mathrm{3dB} \cdot r \approx 0.886 \cdot \frac{\lambda\, r}{L_\mathrm{a}}, \tag{2.1}$$

where r is the slant range of the target (cf. Figure 2.1). From this equation it is clear that as the target's slant range increases, the azimuth resolution of the RAR degrades. In order to improve the azimuth resolution, long antennas are needed. A discussion on enhancing the azimuth resolution using long antennas is given in Section 2.3.

The slant range resolution (ability to distinguish two or more targets at different slant ranges) $\delta_\mathrm{r,raw}$ is generally determined by the pulse duration τ_p and is given as

$$\delta_{\mathrm{r,raw}} = \frac{\mathrm{c}_0\,\tau_\mathrm{p}}{2}, \tag{2.2}$$

where c_0 is the speed of light in vacuum. The ground range resolution (projection of slant range resolution on the ground) $\delta_{\mathrm{g,raw}}$ is written as

$$\delta_{\mathrm{g,raw}} = \frac{\delta_\mathrm{r}}{\sin\theta_\mathrm{i}}. \tag{2.3}$$

For an exemplary airborne radar system where $\tau_\mathrm{p} = 5\mu\mathrm{s}$, the achieved slant range resolution according to (2.2) is 750 m. To increase the slant range resolution, short transmit pulses are necessary. However, for sending short pulses, high transmit power is needed so that received radar echoes have sufficient signal-to-noise-ratio (SNR). To overcome this limitations, pulse compression techniques are used.

2.2.1 Pulse Compression

Pulse compression techniques also known as "matched filtering", employing linear frequency modulated (LFM) signals known as "Chirp" signals are applied in the slant range direction for improving the slant range resolution of the radar and also the SNR of the targets embedded in additive white Gaussian noise. It allows the radar system to achieve the resolution of a short pulse and the energy of a long pulse. With pulse compression along range, the slant range resolution can be improved up to a few meters or even centimeters [56].

Pulse compression is performed by convolving an uncompressed received input signal $s(t)$ with a proper reference function $h(t)$. The pulse compressed signal $s_\mathrm{out}(t)$ is given as

$$s_\mathrm{out}(t) = s(t) * h(t) = \int_{-\infty}^{\infty} s(\tau)h(t-\tau)d\tau, \tag{2.4}$$

where $*$ denotes convolution. The reference function $h(t)$ is the time-reversed complex conjugate of the expected input signal $s(t)$.

After applying the matched filtering, the range resolution δ_r for an LFM transmitted pulse is given by [31]

$$\delta_\mathrm{r} = \alpha_\mathrm{wn} \cdot \frac{\mathrm{c}_0}{2B_\mathrm{r}}, \tag{2.5}$$

where B_r is the chirp bandwidth and α_wn accounts for the losses due to windowing, e.g., $\alpha_\mathrm{wn} \cong 0.89$ for a rectangular window. This equation suggests that large chirp bandwidths should be used for achieving high slant range resolution.

An example after performing pulse compression in slant range direction is shown in Figure 2.2 bottom left.

2.3 Synthetic Aperture Radar

Synthetic aperture radars (SAR) are used for overcoming the azimuth resolution limitations of RAR systems. The principle of SAR was first discovered by Carl Atwood Wiley in the 1950s [57]. Similar to conventional RAR, SAR is also a pulsed radar mounted on a moving platform as shown in Figure 2.1. In the case of SAR, forward radar platform motion and the coherent integration of the received radar echoes along the aircraft's azimuth direction are exploited for synthesizing a long synthetic antenna aperture and, hence, for improving the azimuth resolution [32].

For SAR systems, the azimuth resolution $\delta_{\mathrm{az,SAR}}$ as a function of the integration time or coherent processing intervals (CPI) is expressed as

$$\delta_{\mathrm{az,SAR}} \approx \frac{\lambda\, r}{2\, v_{\mathrm{p}}\, T_{\mathrm{CPI}}}, \tag{2.6}$$

where T_{CPI} is the coherent integration time . From the above equation it is clear that the azimuth resolution of SAR can be increased by increasing T_{CPI}. If T_{CPI} is the complete synthetic aperture time (= total illumination time of the radar) determined by the antenna footprint in azimuth direction, the best achievable azimuth resolution of SAR is given by [31]

$$\delta_{\mathrm{az,SAR}} \approx \frac{L_{\mathrm{a}}}{2}. \tag{2.7}$$

According to this equation, in contrast to RAR (cf. (2.1)), the azimuth resolution of SAR is range-independent and depends only on the actual azimuth antenna length. Therefore, even with spaceborne SAR systems it is possible to acquire SAR images with high azimuth resolution, provided, the antenna length is small enough so that a wider azimuth beam and thus, an increased coherent integration time can be achieved.

2.3.1 SAR Image Generation

SAR processing or SAR image generation is regarded, particularly among GMTI (ground moving target indication) community, as "Stationary World Matched Filtering (SWMF)". A simplified flowchart of SAR processing for a single stationary point-like target is shown in Figure 2.2. The steps of SAR image generation is described as follows:

1. Range compression: Pulse compression is performed along the range direction of the raw radar data (cf. bottom left of Figure 2.2).
2. Range cell migration correction (RCMC): The curvature of the target range history is corrected (cf. bottom right of Figure 2.2) [31].
3. Azimuth compression: Pulse compression is performed along the azimuth direction (cf. top right of Figure 2.2).

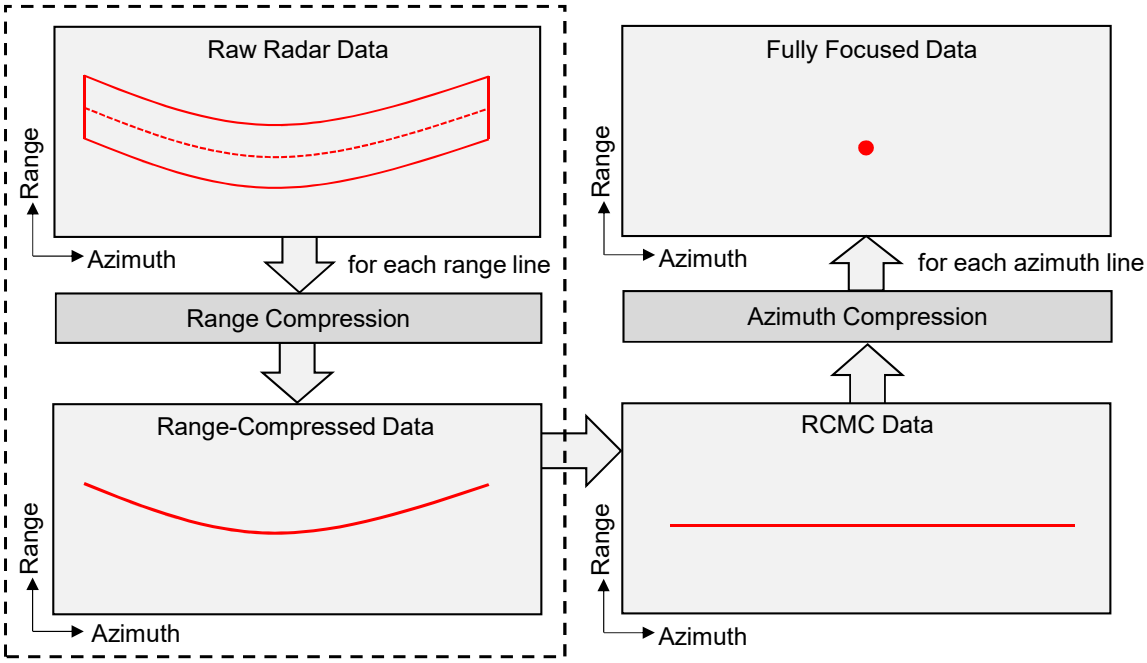

Figure 2.2: Simplified processing steps for generating a fully-focused SAR image of a single non-moving point-like target. The dashed rectangular block shown in the figure is only needed for the proposed air-based maritime surveillance (cf. Figure 1.3).

After performing sequentially the aforementioned steps, a fully focused SAR image can be obtained [31].

2.4 Real-World Target Motions

Treating radar as a range measuring sensor, it generates a unique range history for each target in the scene. Compared to stationary targets, moving targets have different range histories due to their motions. Appropriate modeling of target motion is essential for developing detection and motion parameter estimation algorithms. In this section two types of real-world target motions, in particular ship motions, are discussed. In the first type of ship motion, a model considering the linear motion of the ship moving with constant acceleration (CA) on the ocean surface is presented. In the second type, an overview on ship motions that arises due to the interaction between the vessel and the moving ocean surface are provided.

2.4.1 Linear Motion with Constant Acceleration Model

Assume a target is moving with CA on the ground in the x-y plane at a constant altitude z_t. Its CA-based motion w.r.t. time (in Cartesian coordinates) is given as

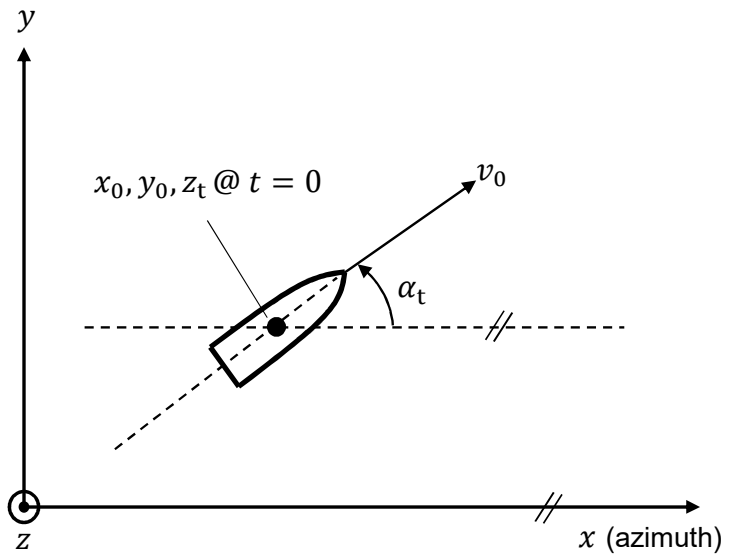

Figure 2.3: Moving target position at time t=0 in Cartesian coordinates. The target's absolute velocity v_0 and moving direction α_t are shown in the figure.

$$x_t(t) = x_0 + \underbrace{v_0 \cos \alpha_t}_{=v_{x0}} t + \frac{1}{2} a \cos \alpha_t t^2 \tag{2.8}$$

$$y_t(t) = y_0 + \underbrace{v_0 \sin \alpha_t}_{=v_{y0}} t + \frac{1}{2} a \sin \alpha_t t^2, \tag{2.9}$$

$$z_t(t) = z_0, \tag{2.10}$$

where x_0, y_0 and z_0 are the positions of the target at time $t = 0$ as shown in Figure 2.3. The terms α_t, v_0 and a are the moving or the heading direction w.r.t the target's along-track motion, absolute velocity and acceleration, respectively. The magnitudes of the velocity and acceleration can be expressed as

$$v_0 = \sqrt{{v_{x0}}^2 + {v_{y0}}^2} \tag{2.11}$$

$$a = \sqrt{{a_x}^2 + {a_y}^2}, \tag{2.12}$$

where $v_{x0} = v_0 \cos \alpha_t$ and $v_{y0} = v_0 \sin \alpha_t$ are the along-track and across-track velocity components at time $t = 0$, respectively and a_x and a_y are the along-track and across-track acceleration components, respectively.

The target range $r(t)$ measured by the airborne radar for a CA-based target motion on the ground (cf. Figure 2.4 top) is expressed as

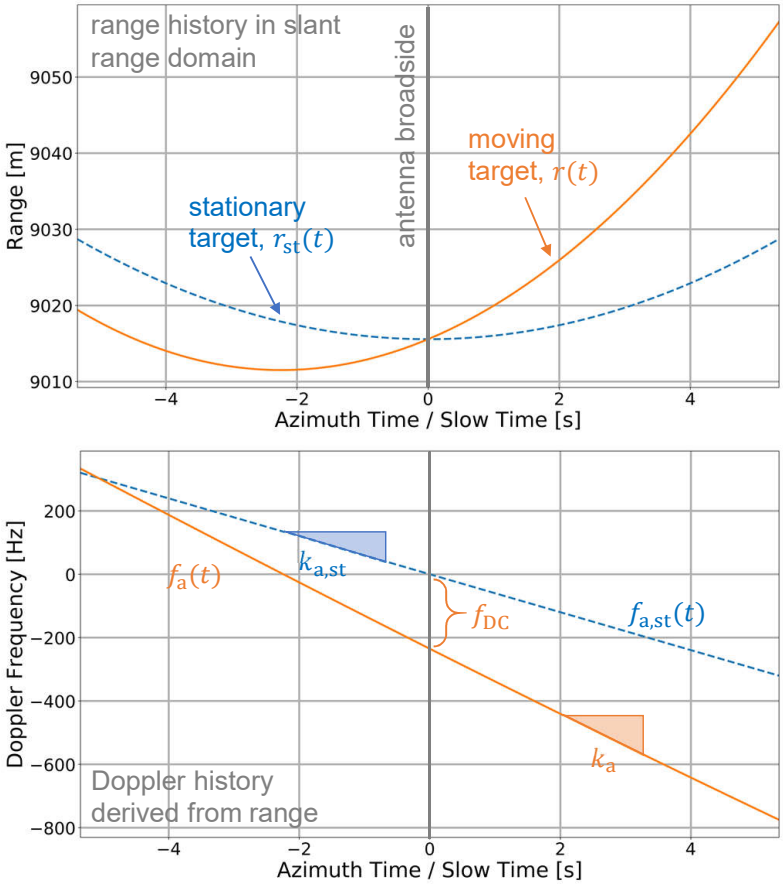

Figure 2.4: Top: Example range histories of a CA-based moving point target (orange curve) and a stationary point target (dashed blue curve) in slant range/azimuth time domain. The stationary point target is shown only for the comparison purposes. Bottom: Their corresponding Doppler frequency histories. Simulation parameters of the moving target: $v_\mathrm{p} = 91$ m/s, $x_0 = 0$ m, $y_0 = 3000$ m, $v_0 = 5$ m/s, $a = 1$ m/s^2, $\alpha_\mathrm{t} = 60°$, z_t=0 m, $z_\mathrm{p} = 5000$ m and $\lambda = 0.0306$ m.

$$r(t) = \sqrt{\left(x_0 + v_{\mathrm{x}0}t + \frac{1}{2}a_\mathrm{x}t^2 - v_\mathrm{p}t\right)^2 + \left(y_0 + v_{\mathrm{y}0}t + \frac{1}{2}a_\mathrm{y}t^2\right)^2 + (z_\mathrm{t} - z_\mathrm{p})^2}. \tag{2.13}$$

The above range equation is true, without the loss of generality, only when:

- the platform is moving linearly with CV and flying at a constant altitude, and
- at $t = 0$ the platform is directly above the origin of the Cartesian coordinate system whose x-axis is parallel to the aircraft's flight direction.

The moving target instantaneous Doppler frequency $f_\mathrm{a}(t)$ as shown in Figure 2.4 bottom due to azimuth time-dependent range change can be written as

$$f_\mathrm{a}(t) = \frac{-2}{\lambda}\frac{dr(t)}{dt}. \tag{2.14}$$

Using (2.13) and (2.14), the first-order Taylor series approximation of the Doppler frequency (cf. Figure 2.4 bottom) can be written as

$$f_{\mathrm{a}}(t) \approx f_{\mathrm{DC}} + k_{\mathrm{a}} t + q t^2, \tag{2.15}$$

where f_{DC}, k_{a} and q denote the Doppler shift, the Doppler slope and the quadratic Doppler coefficient, respectively. The terms f_{DC}, k_{a} and q are mathematically expressed as [58]

$$f_{\mathrm{DC}} \approx \frac{-2}{\lambda r_{10}} \{ y_0 v_{\mathrm{y0}} + x_0 (v_{\mathrm{x0}} - v_{\mathrm{p}}) \} \tag{2.16}$$

$$k_{\mathrm{a}} \approx \frac{-2}{\lambda r_{10}} \left\{ (v_{\mathrm{x0}} - v_{\mathrm{p}})^2 + v_{\mathrm{y0}}^2 \left(1 - \frac{y_0^2}{r_{10}^2} \right) + y_0 a_{\mathrm{y}} \right\} \tag{2.17}$$

$$q \approx \frac{-3}{\lambda r_{10}} \left\{ a_{\mathrm{x}} (v_{\mathrm{x0}} - v_{\mathrm{p}}) + v_{\mathrm{y0}} a_{\mathrm{y}} \left(1 - \frac{y_0^2}{r_{10}^2} \right) \right\}, \tag{2.18}$$

where the term r_{10} is the range between the radar and the target at $t = 0$ (antenna broadside). Using (2.16), (2.17) and (2.18) in (2.13) and after some mathematics, the range history of a target moving with CA on ground can now be approximated using Doppler parameters in the following way

$$r(t) \approx r_{10} - \frac{\lambda}{2} f_{\mathrm{DC}} t - \frac{\lambda}{4} k_{\mathrm{a}} t^2 - \frac{\lambda}{6} q t^3. \tag{2.19}$$

For a non-moving target, as shown by the dashed blue curve in Figure 2.4, its slant range $r_{\mathrm{st}}(t)$ and Doppler history $f_{\mathrm{a,st}}(t)$ are approximated as

$$r_{\mathrm{st}}(t) \approx r_0 - \frac{\lambda}{4} k_{\mathrm{a,st}} t^2 \approx r_0 + \frac{v_{\mathrm{p}}^2}{2 r_0} t^2 \tag{2.20}$$

$$f_{\mathrm{a,st}}(t) \approx k_{\mathrm{a,st}} t \approx \frac{-2 v_{\mathrm{p}}^2}{\lambda r_0} t, \tag{2.21}$$

where r_0 is the minimum range of the stationary target at t=0 and $k_{\mathrm{a,st}}$ is its Doppler slope. Note that in contrast to r_0, the range position r_{10} of a moving target in (2.19) is not the minimum range since due to target motion its minimum range is not at the antenna broadside.

2.4.2 Oscillatory Linear and Angular motions

Wave-induced ship motions influence not only the quality of high resolution ISAR imaging but also play an important role in detection, clustering and geocoding since the scattering and, hence, the center of gravity of the ship may change significantly due to these motions.

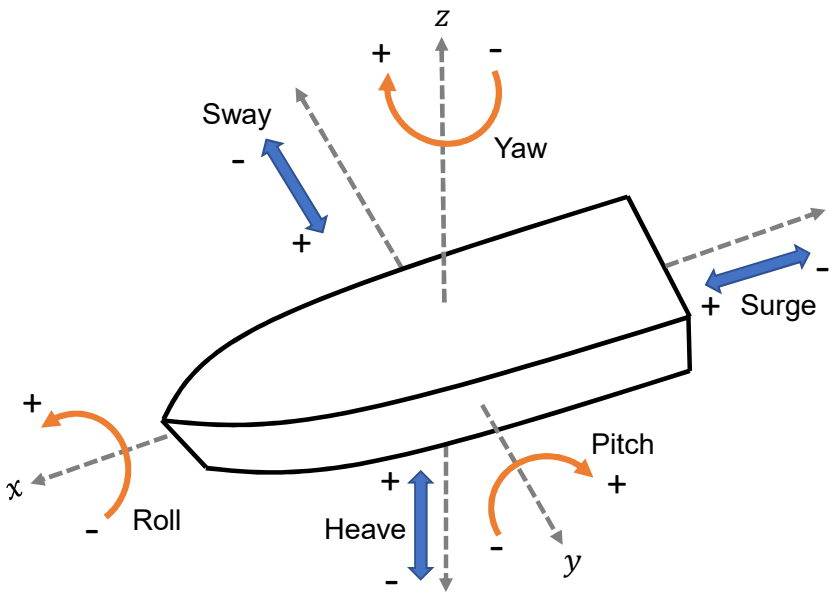

Figure 2.5: Ship and its six different oscillatory motions with the sign conventions.

While moving on the ocean surface, a ship exhibit six degrees of freedom (DOF) associated with six types of motions. They are the roll, pitch, yaw, surge, sway and heave as shown in Figure 2.5. Roll, pitch and yaw are the oscillatory angular motions whereas, surge, sway and heave are the oscillatory linear motions of the ship [59]. The main factor that drives these motions is the waves on the sea surface. These waves after interacting with the vessels induce all kinds of different oscillatory motions. The most important ones are the roll, pitch and yaw, and among them, roll and pitch are the most significant.

The magnitude of the roll angle depends on the sea state and the beam of the ship. In case of high sea states and small beam the roll angle can go up to several tens of degree. The maximum pitch angle depends on the sea state and the ship lengths. For longer ships the pitch angles are smaller [59].

2.5 Point Target Signal Models

Since in this doctoral thesis radar data based on both single and multiple receiving channels are investigated for monitoring ground moving targets (cf. Figure 1.3 top), target signal models based on single and multichannel radar data are discussed in the next two

sections. The presented signal models are applicable to both stationary targets and moving targets.

2.5.1 Single-Channel Signal Model

One single pulse transmitted in range direction by the airborne radar is expressed as

$$s_{\mathrm{TX}}(\tau) = s_{\mathrm{TX,b}}(\tau) \cdot \exp\left[\mathrm{j}\frac{2\pi}{\lambda}c_0\tau\right], \tag{2.22}$$

where TX stands for transmit, $s_{\mathrm{TX,b}}(\tau)$ is the pulse waveform in baseband, $\exp[\cdot]$ is the exponential term, j is the imaginary unit and τ is the range time, also known as fast time.

In most airborne radar systems $s_{\mathrm{TX,b}}(\tau)$ is the LFM pulse waveform, also known as "range chirp". This waveform is used for obtaining better range resolution after applying pulse compression techniques, as discussed in Section 2.2.1. The transmitted chirp in baseband can be expressed as

$$s_{\mathrm{TX,b}}(\tau) = \exp(\mathrm{j}\pi k_{\mathrm{r}}\tau^2) \cdot \mathrm{rect}\left[\frac{\tau}{\tau_{\mathrm{p}}}\right], \tag{2.23}$$

where $\mathrm{rect}[\cdot]$ is the rectangular function and $k_{\mathrm{r}} = B_{\mathrm{r}}/\tau_{\mathrm{p}}$ is the linear FM rate or chirp slope expressed in hertz per second.

The target's echo signal received by the same antenna (= monostatic case) can be expressed as

$$s_{\mathrm{RX}}(\tau) = a_{\mathrm{s}} \cdot s_{\mathrm{TX}}\left(\tau - \frac{2r(\tau)}{c_0}\right), \tag{2.24}$$

where RX stands for receive and the coefficient a_{s} covers the free-space attenuation, the backscattering coefficient and the two-way antenna pattern weighting. In the equation, the received echo from the target is a delayed and attenuated copy of the transmitted signal.

The extracted received signal in baseband after using a phase preserving quadrature demodulator can be written in two-dimensional form as

$$s_{\mathrm{RX,b}}(\tau, t) = a_{\mathrm{s}} \cdot s_{\mathrm{TX}}\left(\tau - \frac{2r(\tau)}{c_0}\right) \cdot \exp\left[-\mathrm{j}\frac{4\pi}{\lambda}r(t)\right]. \tag{2.25}$$

The factor of 2 in $s_{\mathrm{TX}}(\cdot)$ is due to the two-way range measurement of the radar system. The exponential term in the equation represents the phase difference between the transmitted and the received signal.

For GMTI applications, the azimuth signal is most relevant. From (2.25) the single-channel target azimuth signal is obtained as

$$s(t) = a_{\mathrm{s}} \cdot \exp\left[-\mathrm{j}\frac{4\pi}{\lambda} r(t) \right] \cdot \mathrm{rect}\left[\frac{t}{T_{\mathrm{SA}}} \right], \tag{2.26}$$

where rect[·] limits the duration of target illumination to the synthetic aperture or coherent integration time T_{SA}.

2.5.2 Multichannel Signal Model

In this section a target signal model using multiple receiving antennas is introduced and briefly discussed. The multichannel signal model is used for estimating the direction-of-arrival (DOA) angle of the detected target (cf. Figure 2.6). With the known DOA angle of the target and the aircraft navigation parameters, the target can directly be mapped to ground for obtaining its actual geographical coordinates via a geocoding operation (cf. Chapter 6). A multichannel radar system consisting of M number of receiving channels is depicted in Figure 2.6.

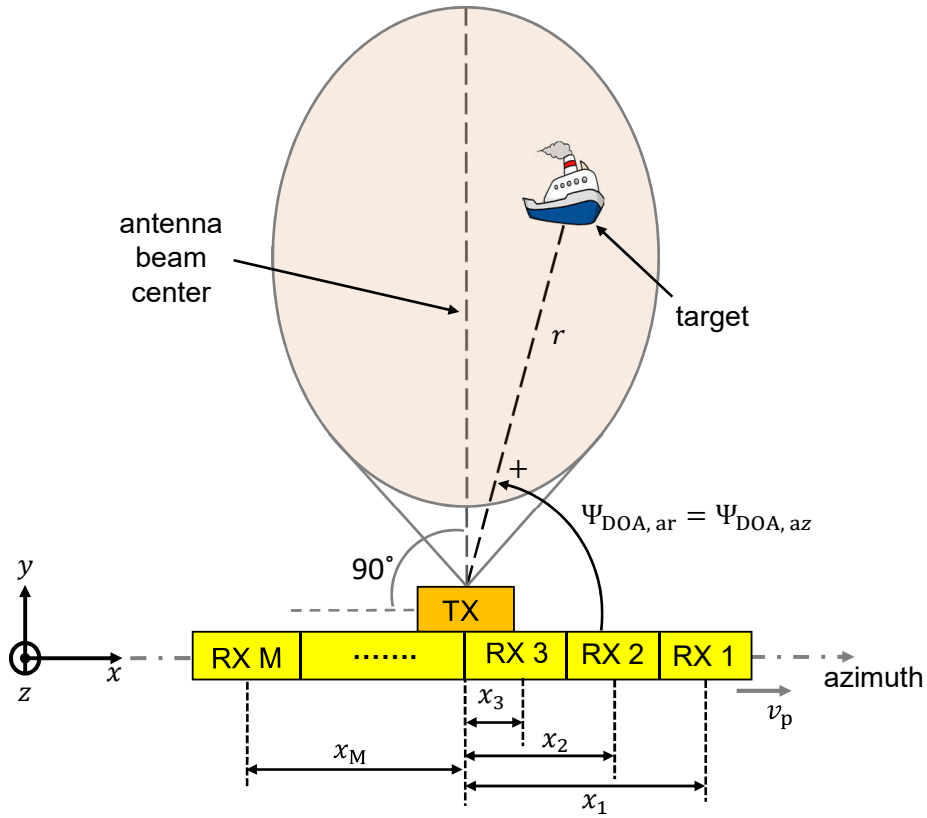

Figure 2.6: Multichannel radar system consisting of one TX antenna and M uniformly distributed RX antennas. The antenna array in the shown figure is left-looking with respect to the flight's azimuth direction.

The multichannel target signal model in its time continuous form can be expressed as [60]

$$
\begin{aligned}
s(t) &= A_{\mathrm{s}} \cdot e^{-j\frac{4\pi}{\lambda}r(t)} D_{\mathrm{t}}(u(t)) \begin{bmatrix} D_{\mathrm{r},1}(u(t))e^{j\frac{2\pi}{\lambda}u(t)x_1} \\ D_{\mathrm{r},2}(u(t))e^{j\frac{2\pi}{\lambda}u(t)x_2} \\ \vdots \\ D_{\mathrm{r,M}}(u(t))e^{j\frac{2\pi}{\lambda}u(t)x_{\mathrm{M}}} \end{bmatrix} \\
&= A_{\mathrm{s}} \cdot e^{-j\frac{4\pi}{\lambda}r(t)} \boldsymbol{d}(u(t)) \in \mathbb{C}^{M\times 1}.
\end{aligned} \tag{2.27}
$$

Note that the single-channel target signal model expressed with (2.26) is one row of the multichannel signal model shown in (2.27). The term A_{s} in (2.27) comprises the reflectivity of the scatterer, $D_{\mathrm{t}}(u)$ and $D_{\mathrm{r,M}}(u)$ are the transmit and receive characteristics of the m^{th} RX channel, x_{m} is the position of the antenna center position in azimuth direction with respect to the array origin and $u(t) = \cos\psi_{\mathrm{DOA,ar}}$ is the directional cosine where $\psi_{\mathrm{DOA,ar}}$ is the DOA angle measured with respect to the antenna array axis (cf. Figure 2.6). The term $\psi_{\mathrm{DOA,az}}$ is the DOA angle measured with respect to the aircraft's azimuth direction and ideally, for a non-tilted array, $\psi_{\mathrm{DOA,az}} = \psi_{\mathrm{DOA,ar}}$. However, in practice, due to atmospheric turbulence the array may be tilted so that $\psi_{\mathrm{DOA,ar}} \neq \psi_{\mathrm{DOA,az}}$. In this case additional calibration is needed (cf. Section 6.6) [61]. The vector $\boldsymbol{d}$ is known as the beamforming vector or DOA angle vector.

The multichannel signal model discussed in this section is primarily used in the space-time adaptive processing (STAP) techniques [62]. STAP is an efficient multichannel processing technique that is used for suppressing the clutter and enhancing the target detectability. It can additionally be used for estimating the target's LOS velocity (cf. Chapter 6).

2.5.3 SAR and Moving Targets

In focused SAR images moving targets often appear blurred and displaced from their actual geographical positions. This is because SAR is originally designed for imaging stationary targets and it is not adapted for the imaging of moving targets.

When the moving target has either an along-track velocity or across-track acceleration, there is a Doppler slope change of the moving target with respect to the stationary target (cf. Figure 2.4 bottom where $k_{\mathrm{a}} \neq k_{\mathrm{a,st}}$). After azimuth compression, the offset $k_{\mathrm{a}} - k_{\mathrm{a,st}}$ causes a quadratic phase error in time domain that results in defocusing of moving targets in azimuth direction, causing decreased peak amplitude and peak SCNR (signal-to-clutter-plus-noise ratio) and thus, lower detection probability [33].

For targets that are moving with across-track velocity there is a Doppler frequency shift f_{DC} and a slight variation in the Doppler slope k_{a}. The major effect seen in SAR images is the target dislocation in azimuth direction [33]. For illustrating the azimuth displacement problem of moving targets in fully focused SAR images, an example is shown in Figure 2.7.

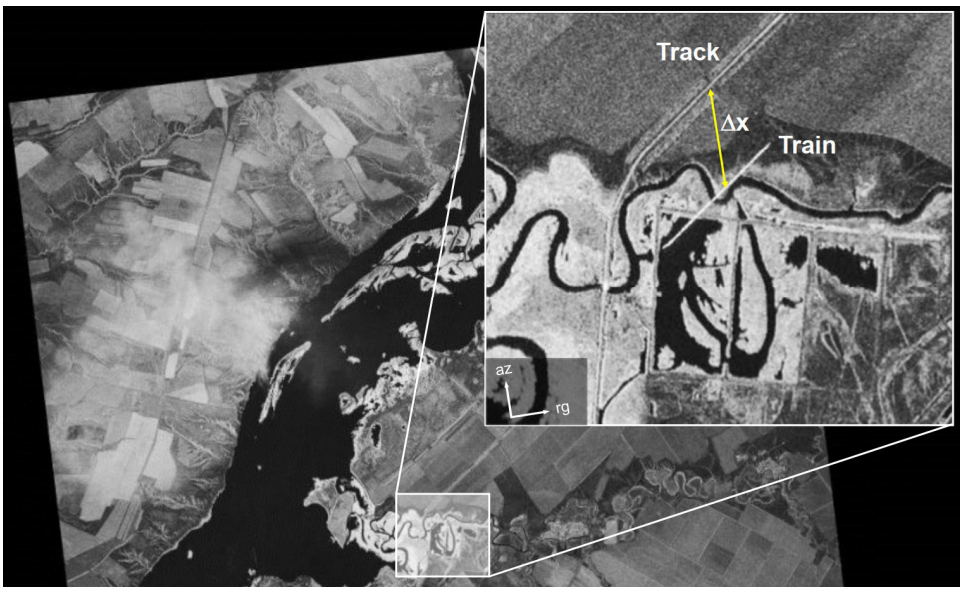

Figure 2.7: TerraSAR-X image of the region near Wolgograd, Russia. In the zoomed part of the image, a train displaced in azimuth direction from its original rail track is clearly visible [34].

In the figure a moving train is displaced from its original rail track on the ground along azimuth direction of the moving radar platform. For a non-tilted acquisition geometry, the azimuth displacement Δx can be approximated as [34]

$$\Delta x \approx -\frac{y_0}{v_\mathrm{p}} v_{\mathrm{y}0}. \tag{2.28}$$

According to this equation the azimuth displacement of a moving target is proportional to its across-track velocity. For instance, if $v_{\mathrm{y}0} = 50$ km/h, $v_\mathrm{p} = 91$ m/s, and $y_0 = 3000$ m, the azimuth displacement of the target is in the order of 500 m.

Furthermore, targets accelerating in along-track direction change the quadratic Doppler coefficient q which bends the Doppler history of the target. After azimuth compression, the focused target has reduced peak amplitude and also the impulse response function has asymmetric sidelobes [34].

The aforementioned moving target effects on SAR imagery are generally more severe in airborne SAR than in spaceborne SAR due to the lower platform speeds and longer integration times [33]. One desirable data for monitoring moving targets using airborne platforms is the RC radar data. Such data are very attractive from the viewpoint that they are generally acquired with sufficient SNR. Therefore, short integration times can be used so that the moving target signal appears focused without performing additional time-consuming RCMC and SAR imaging techniques (cf. Figure 2.2).

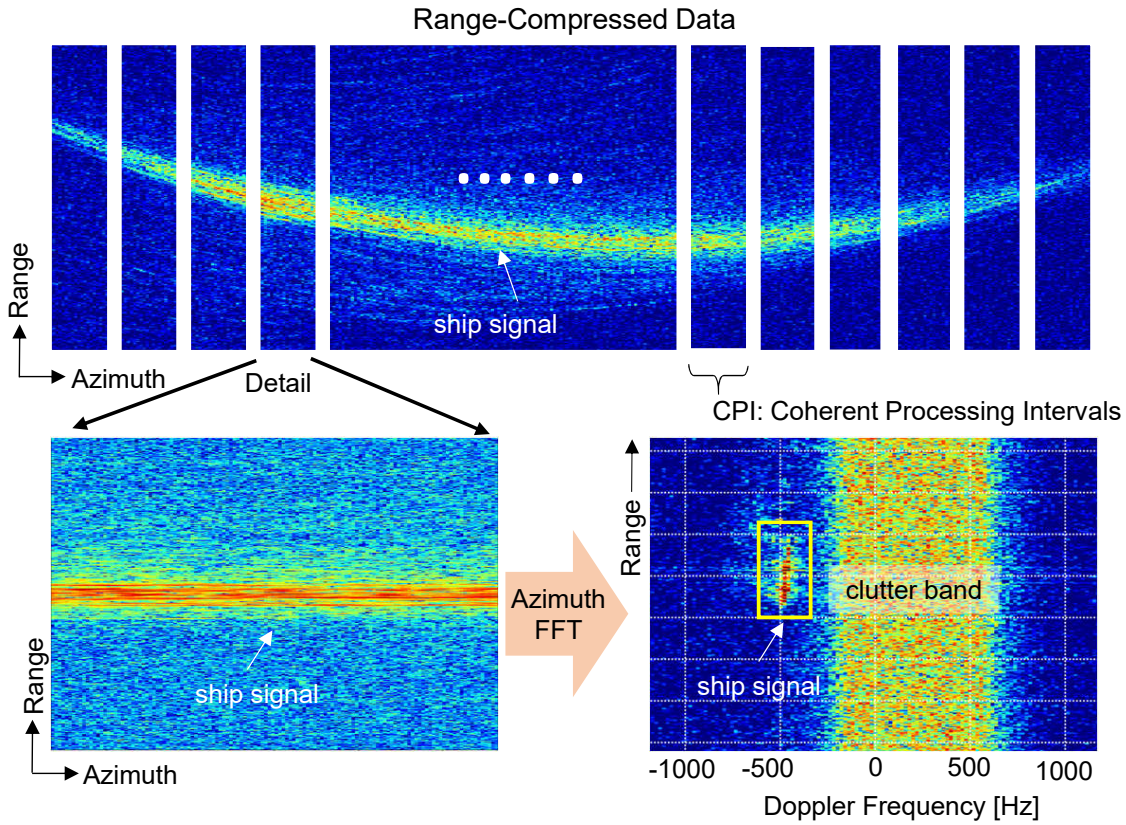

Figure 2.8: Illustration of the range-Doppler processing for detecting moving targets in RC radar data. Top: Real RC X-band HH polarized F-SAR radar data acquired using only one receiving channel. The range history of a single real ship target can be seen in the figure. The RC data are partitioned into smaller CPIs along azimuth. Bottom left: Detailed view of one extracted CPI in time domain. Bottom right: Range-Doppler image of the extracted CPI after applying an azimuth FFT. The ship signal shifted to the exo-clutter region can clearly be seen.

2.6 Moving Targets in Range-Doppler Domain

Moving target signals are processed in the range-Doppler domain of the RC radar data. For generating the range-Doppler images, RC data are initially partitioned along the aircraft's azimuth direction into smaller data patches, known as CPI. Individual CPIs are transformed into the range-Doppler domain via azimuth FFT (fast Fourier transform). An example is shown in Figure 2.8.

As shown in Figure 2.8 bottom right, the ship signal appears focused in range-Doppler image. This is because the signal phase is linear since only a few number of azimuth samples within a CPI and hence, a very short integration time is used. Criterion to select optimum number of azimuth samples within a CPI are presented in Section 2.7.

The moving target signal $S(f_\mathrm{a})$ in the range-Doppler domain as a function of Doppler frequency can be approximated as [34]

$$S(f_\mathrm{a}) \approx \exp\left[\mathrm{j}\pi \frac{1}{k_\mathrm{a}} f_\mathrm{a}^2\right], \tag{2.29}$$

and its range history as a function of Doppler frequency after using (2.13) and (2.15) is approximated as [34, 63]

$$r(f_\mathrm{a}) \approx r_{10} + \left(\frac{-\lambda f_\mathrm{DC}}{2k_\mathrm{a}}\right)(f_\mathrm{a} - f_\mathrm{DC}) + \frac{1}{2}\left(\frac{-\lambda}{2k_\mathrm{a}}\right)(f_\mathrm{a} - f_\mathrm{DC})^2. \tag{2.30}$$

Substituting $\tilde{f}_\mathrm{a} = f_\mathrm{a} - f_\mathrm{DC}$, (2.30) is further written as

$$r(f_\mathrm{a}) \approx r_{10} + v_\mathrm{dop}\tilde{f}_\mathrm{a} + \frac{1}{2}a_\mathrm{dop}\tilde{f}_\mathrm{a}^{\,2}, \tag{2.31}$$

where v_dop and a_dop can be considered as the velocity and the acceleration of the moving target in the Doppler domain, respectively. Equation (2.31) is depicted in Figure 2.9 bottom where the quadratic behavior of the range histories of three simulated moving point targets can be seen as a function of the Doppler frequency.

Reasons for using the range-Doppler domain for target detection and also for target tracking are:

1. **Moving ships in exo-clutter region**: Ships moving with certain LOS velocities are shifted to different Doppler frequencies (cf. (1.2)). When the Doppler shift is larger than half the clutter bandwidth, i.e., $|f_\mathrm{DC}| > B_\mathrm{c}/2$ where B_c is the clutter bandwidth, the target is shifted to the exo-clutter region (cf. Figure 2.8, bottom right). In this region, generally a target detection is possible due to increased SCNR values.

2. **Compression gain**: Due to the coherent integration of a certain number of samples along azimuth, a compression gain in the order of $10\log_{10}N_\mathrm{CPI}$, where N_CPI is the number of consecutive azimuth samples within a CPI, can be achieved, causing an increased target signal power in the Doppler domain. That means targets even of low RCS, not detectable in the time domain, can principally be detected in the Doppler domain.

3. **Moving targets are separated in Doppler**: Overlapping moving target signals in the time domain are separated in the Doppler domain if they are moving with different LOS velocities. This is because the targets moving with different LOS velocities are shifted to different Doppler frequencies (cf. (1.2)).

   An example is shown in Figure 2.9 where three simulated moving targets with different absolute velocities on ground and heading directions are shown. From Figure 2.9 top it can be seen that Target_0 and Target_2 are crossing each other at azimuth time $t_\mathrm{olp,0}$. At this azimuth time, these two targets are separated in the Doppler domain (cf. Figure 2.9 bottom). Similarly, Target_0 and Target_1 that are crossing each other at azimuth time $t_\mathrm{olp,1}$ are also separated in the Doppler domain due to their different Doppler frequency shifts. Therefore, it can be said that when there are multiple targets in dense maritime scenarios, tracking in range-Doppler domain is very advantageous.

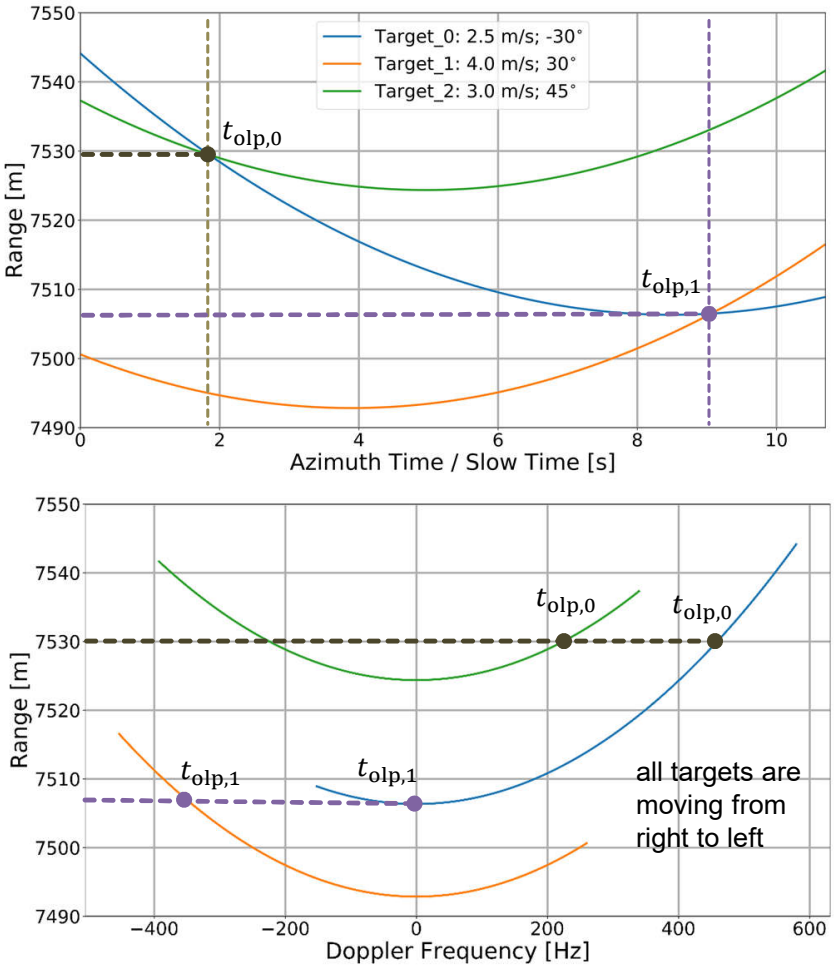

Figure 2.9: Three simulated moving targets shown in both range/azimuth time (top) and range-Doppler domain (bottom). In the legend their absolute velocities v_0 on ground and their moving directions α_t are listed. Used simulation parameters: $v_p = 91$ m/s, $z_p = 5000$ m and $\lambda = 0.0306$ m.

The aforementioned benefits of range-Doppler domain clearly make it a suitable choice for detecting and tracking multiple moving targets even in single-channel RC radar data.

2.7 Optimum CPI selection

Appropriate CPI length is one of the key parameters in range-Doppler-based moving target signal processing. This is because when the CPI is too long, the target signal migrates from one resolution cell to another resolution cell, causing range/Doppler cell migration effects and target defocusing. On the other hand, when the CPI is too small, the cross-range (or azimuth) resolution is decreased (cf. (2.6)), thereby reducing the quality of range-Doppler images. In this section two criterion for optimal CPI selection are discussed. The first criteria is based on the slant range sample spacing and it gives maximum number of utilizable azimuth samples that can be used without the need for RCMC. The second criteria is discussed in terms of Doppler spacing and it ensures linear phase and, hence, a focused target signal in Doppler domain without the need of additional phase

compensation. For simplicity, a stationary point target is assumed for explaining the criterion. Figure 2.10 shows the slant range and Doppler frequency history of the stationary point target.

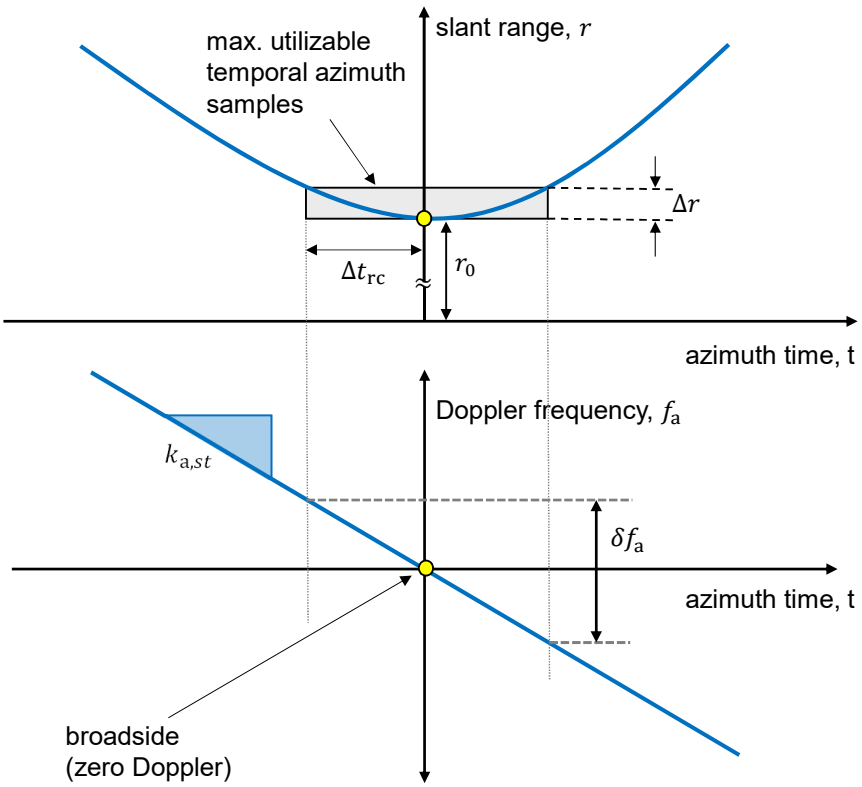

Figure 2.10: Slant range (top) and Doppler frequency (bottom) history of a stationary point target [64].

In the figure the maximum number of utilizable azimuth samples of the target signal is shown. The target azimuth samples are within one slant range spacing of the radar data. The slant range spacing Δr is given by

$$\Delta r = \frac{c_0}{2 f_r}, \tag{2.32}$$

where f_r is the range sampling frequency. The number of utilizable azimuth samples $N_{\mathrm{CPI,SR}}$ that can be considered within a CPI without doing RCMC can be expressed as [58]

$$N_{\mathrm{CPI,SR}} = 2\,\mathrm{PRF}\,|\Delta t_{rc}|, \tag{2.33}$$

where Δt_{rc} is the time interval where the range cell migration of the target do not cross one slant range sample spacing, as shown in Figure 2.10 top. For a stationary point target Δt_{rc} can be approximated as

$$\Delta t_{\mathrm{rc}} \approx \sqrt{\frac{r_0\, c_0}{v_{\mathrm{p}}^2\, f_{\mathrm{r}}}}. \tag{2.34}$$

Considering typical F-SAR/DBFSAR system parameters with PRF = 3000 Hz, $v_{\mathrm{p}} = 91$ m/s, $r_0 = 3000$ m and $f_{\mathrm{r}} = 500$ MHz, $N_{\mathrm{CPI,SR}}$ is calculated as 2797. That means $N_{\mathrm{CPI,SR}}$ for this particular system parameter must be less than 2797. Note here that for moving targets, depending on their velocities and moving directions, $N_{\mathrm{CPI,SR}}$ can vary [58].

After calculating the $N_{\mathrm{CPI,SR}}$ limit based on first criteria, the number of samples per CPI should also the satisfy the second criteria:

$$\Delta f_{\mathrm{a}} \geq \delta f_{\mathrm{a}}, \tag{2.35}$$

where Δf_{a} is the Doppler bin size and δf_{a} is the Doppler bandwidth or the Doppler frequency spread of the target signal (cf. Figure 2.10 bottom). The Doppler bin size is given as

$$\Delta f_{\mathrm{a}} = \frac{1}{T_{\mathrm{CPI,DS}}} = \frac{\mathrm{PRF}}{N_{\mathrm{CPI,DS}}}, \tag{2.36}$$

where $N_{\mathrm{CPI,DS}}$ is the number of azimuth samples for a certain Doppler bin size and $T_{\mathrm{CPI,DS}}$ is its corresponding integration time. The Doppler bandwidth can be expressed as

$$\delta f_{\mathrm{a}} \approx |k_{\mathrm{a,st}}|\, T_{\mathrm{CPI,DS}} \approx \left|\frac{-2v_{\mathrm{p}}^2}{\lambda r_0}\right| T_{\mathrm{CPI,DS}}. \tag{2.37}$$

Using (2.35) and after rearranging (2.36) and (2.37), $N_{\mathrm{CPI,DS}}$ can be expressed as

$$N_{\mathrm{CPI,DS}} \leq \sqrt{\left|\frac{\lambda r_0}{-2v_{\mathrm{p}}^2}\right| \mathrm{PRF}^2}. \tag{2.38}$$

Finally, the N_{CPI} that shall be used for range-Doppler processing of moving targets is decided based on the following expression

$$N_{\mathrm{CPI}} \leq \min(N_{\mathrm{CPI,DS}}, N_{\mathrm{CPI,SR}}). \tag{2.39}$$

Considering again typical F-SAR/DBFSAR acquisition parameters, $N_{\mathrm{CPI,DS}}$ is calculated as 224. In this doctoral thesis $N_{\mathrm{CPI}} = 128$ is used for all investigations. The selected N_{CPI} not only satisfies the right-hand-side expression of (2.39) but it is also a power of 2 which is needed for an efficient FFT processing.

3 Ship Detection using Single-Channel Range-Compressed Data

This chapter proposes a novel ship detection algorithm using RC airborne radar data. The proposed algorithm is designed keeping in mind future real-time requirements and arbitrarily flown nonlinear flight tracks. A constant false alarm rate (CFAR)-based target detection threshold is computed in the range-Doppler domain using suitable stochastic sea clutter models. In order to determine a robust detection threshold, the ocean statistics have to be described accurately. Bright target peaks in the background ocean data bias the statistics and lead to an erroneous threshold. Therefore, an automatic ocean training data extraction procedure is presented in this chapter. It includes (1) a novel target pre-detection module that removes the bright peaks from the data in the time domain, (2) clutter normalization in the Doppler domain using the remaining ocean training samples, (3) ocean statistics estimation and finally, (4) detection threshold computation. Various sea clutter models are investigated and analyzed in this chapter for finding the most suitable models for the RC data. The robustness and the applicability of the proposed method is validated using real radar data from DLR's airborne F-SAR system acquired using linear and circular flight tracks.

The methodology and the results provided in this chapter I have published in the journal paper [65] and the conference papers [66–69].

3.1 Structure of the Algorithm

Target detection is carried out in the range-Doppler domain of the RC radar data. It was already shown in (1.2) and discussed in Section 2.6 that in the Doppler domain ships moving with sufficiently high LOS velocities appear out of the clutter region (cf. Figure 2.8 bottom right), thus improving their detectability.

The minimum detectable LOS velocity $v_{\mathrm{r,min}}$ of the ship using a single-channel radar can be expressed as [52]

$$|v_{\mathrm{r,min}}| \approx \frac{\lambda}{4} \cdot B_{\mathrm{c}} \approx 0.886 \cdot \frac{\lambda v_{\mathrm{p}}}{2L_{\mathrm{a}}}. \tag{3.1}$$

For a typical airborne radar with $\lambda = 0.0306$ m, $v_{\mathrm{p}} = 91$m/s and $L_{\mathrm{a}} = 0.3$ m, $v_{\mathrm{r,min}}$ is calculated as 4.1 m/s. Note that the computed lower bound of $v_{\mathrm{r,min}}$ can be increased in case of high sea states since extreme ocean currents will increase the clutter bandwidth.

The major processing steps of the proposed algorithm for ship detection in the range-Doppler domain using the RC data can be summarized as:

1. Extraction of a small data block from the RC radar data in the time domain.
2. Transformation of the data block to the range-Doppler domain via azimuth FFT.
3. Normalization over Doppler for achieving a "flat" spectrum (cf. Section 3.3.2).
4. Estimation of the ocean clutter statistics using various distribution functions (cf. Section 3.4).
5. Computation of a CFAR detection threshold based on the estimated ocean clutter statistics (cf. Section 3.4).

3.2 Algorithm Block Diagram

Figure 3.1 shows the detailed block diagram of the proposed methodology for ship detection in the range-Doppler domain using single-channel RC radar data as input. Apart from the single-channel, the sum-channel or the clutter-suppressed channel data obtained, e.g., after applying the STAP technique on RC multi-channel data, can principally be used. However, the focus of this chapter in on target detection using single-channel radar data only.

In Figure 3.1, the RC radar data (top) are initially divided into "green" regions, where each green region is further partitioned along range into "red" sub-regions. Each red sub-region consists of a group of "blue" data blocks where each data block is a CPI that consists of a certain number of consecutive azimuth samples.

First, an average amplitude profile over azimuth is estimated for a red sub-region (labeled with (1) in Figure 3.1). A trend along range is derived after performing median filtering (2). Then, for each blue data block, this median filtered range trend is used for performing range de-trending (3). This is important for normalizing the range varying amplitude of the data to a constant value (4). After range de-trending, each data block or each CPI is transformed into the range-Doppler domain by performing an azimuth FFT (5).

From the "target pre-detection" module (6), the azimuth lines corresponding to "potential targets" at certain range positions are detected and excluded in the range-Doppler domain for each data block of the red sub-region (7). More details on the significance of target pre-detection and the proposed method are presented in Section 3.3.1. Afterwards, an average Doppler spectrum without target signals is estimated using all data blocks (8).

Normalization over Doppler (9) is performed individually for each "red" group of data blocks using the estimated average Doppler spectrum (10). As a result, a normalized Doppler spectrum is obtained (11). More details on the average Doppler spectrum estimation and normalization are given in Section 3.3.2. The normalized target-free data are used as training data to estimate the local ocean clutter statistics (12). By using the estimated statistics from the sea clutter model and by setting a desired probability of false alarm (PFA) (acceptable probability limit to incorrectly label a background pixel or an ocean sample as target), a CFAR detection threshold is computed (13).

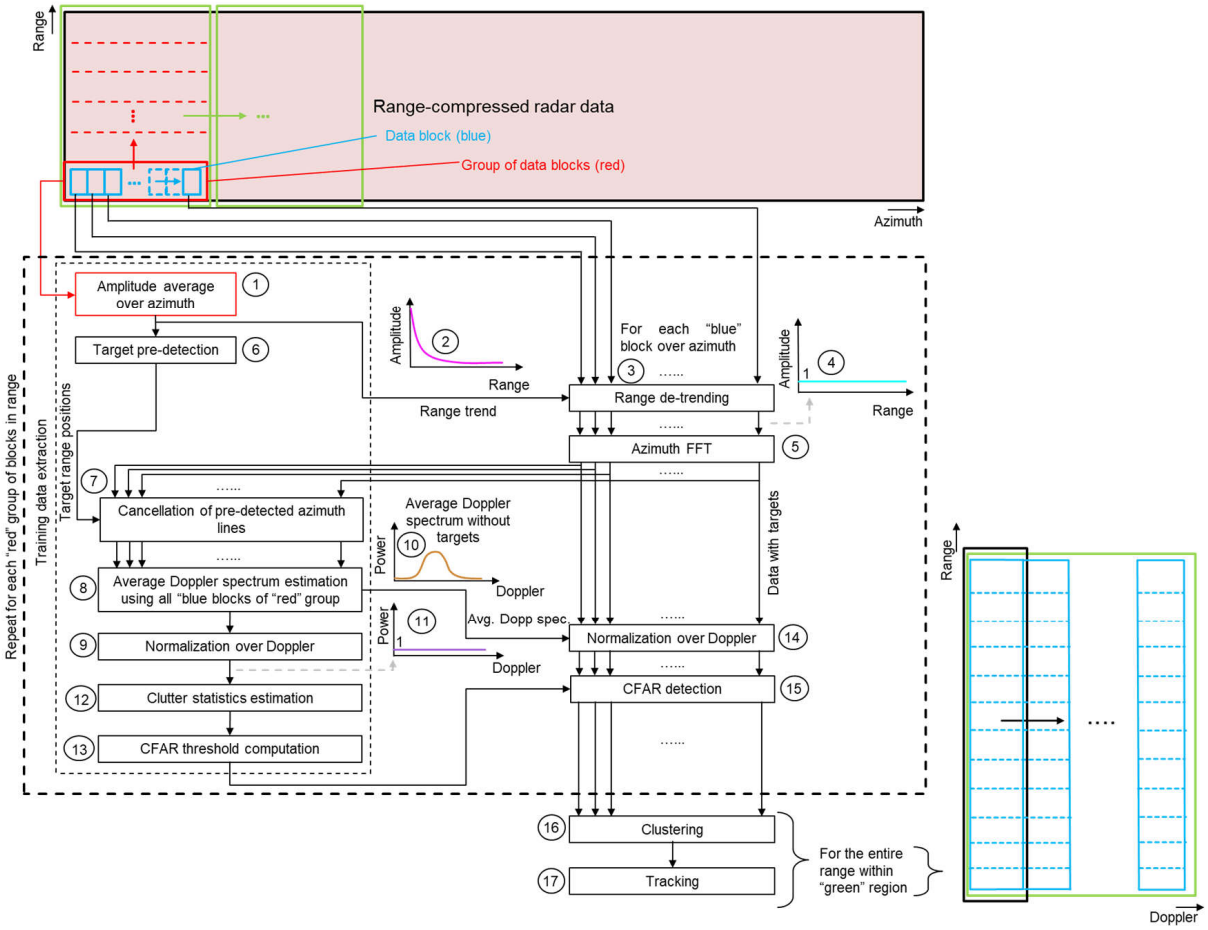

Figure 3.1: Block diagram of the proposed target detection algorithm which uses RC airborne radar data as input. The individual blocks and processing steps are numbered from 1 to 17 and are discussed in detail in this section.

The average Doppler power spectrum (10) which was estimated before, is further used to normalize the "original" "blue" range-Doppler data blocks (14). The CFAR threshold is then applied individually to each of these data blocks to detect the ship pixels (15). This procedure is repeated until all "red" groups of data blocks along range (i.e., within the "green" region at the top of Figure 3.1) are covered.

Finally, clustering (16) is performed using all the available detections along the complete range of the scene within a CPI (cf. black box in Figure 3.1 bottom right). The computed cluster centroids in each "black" data block are then used for "Tracking"(17). Details related to the clustering and the tracking algorithms are presented in Chapter 4 and Chapter 5, respectively.

3.3 Training Data Selection

An appropriate selection of ocean training data and sea clutter statistics estimation lead to an accurate computation of the detection threshold. In reality, training samples within a given ROI may be contaminated by target peaks and high clutter peaks. A typical

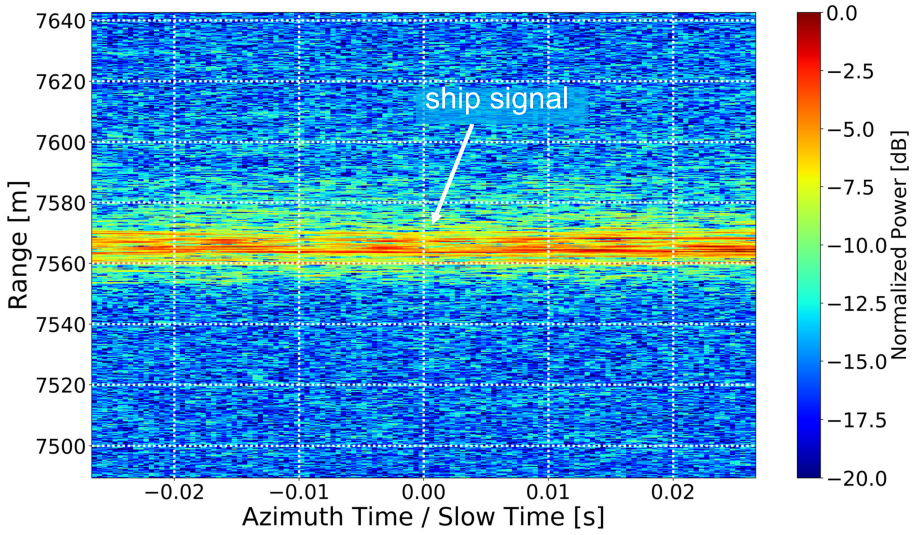

Figure 3.2: Patch of HH polarization X-band RC F-SAR radar data containing a ship target (at a range of approx. 7570 m). For visualization purposes, the data were normalized to the maximum power.

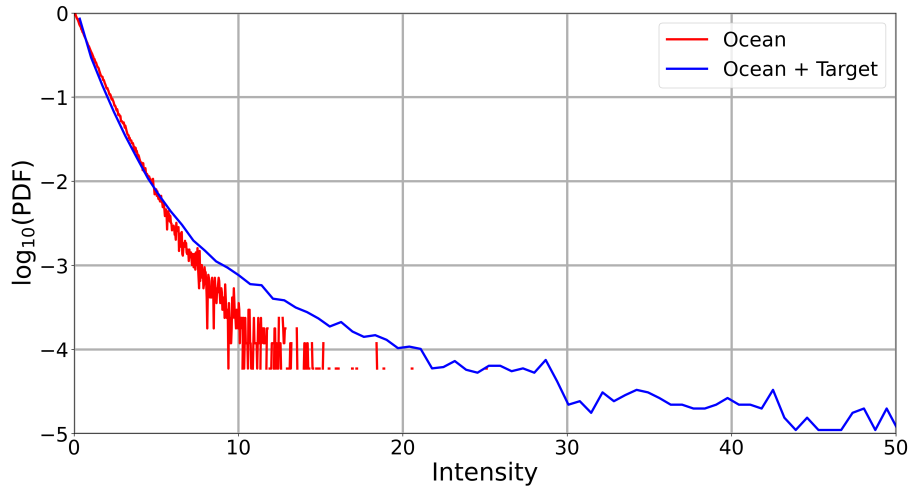

Figure 3.3: Logarithmic plot of the PDFs of the ocean only (red) and ocean with a ship signal (blue) are shown. For visualization purposes, the intensity axis is truncated as the maximum intensity due to ship is around 600.

example of the presence of a bright ship signal in the RC radar data in time domain is shown in Figure 3.2.

To understand the effects of ocean clutter contamination due to bright targets, a logarithmic plot of the probability density functions (PDFs) of "ocean only" and "ocean with the bright ship signal" is shown in Figure 3.3. In the figure it is shown how the presence of the target and other high peaks in the background clutter skews the histogram to extremely high intensity values (blue). Such high intensities can severely degrade the performance of clutter models. The CFAR detection threshold may be raised to a very high value which lowers the probability of detection. In the literature, such effects are termed as "capture effects". Other complications in the modeling of sea clutter arise due to the

presence of high clutter peaks that causes sudden transition and shift in the background intensity values. These effects are known as "clutter edge effects" [70].

An example of ship detection results using the K-distribution-based sea clutter model (cf. Section 3.4.2) without excluding bright targets and high clutter peaks from the data is shown in Figure 3.4(b). It can be seen in the figure that the ship is not properly detected (see also Figure 3.17 for comparison). This is because the bright targets and spiky ocean clutter were included in the ocean statistics estimation which increased the CFAR detection threshold. From the figure it is now clear that in order to maximize the target detectability, the bright peaks in the radar data must be removed in advance.

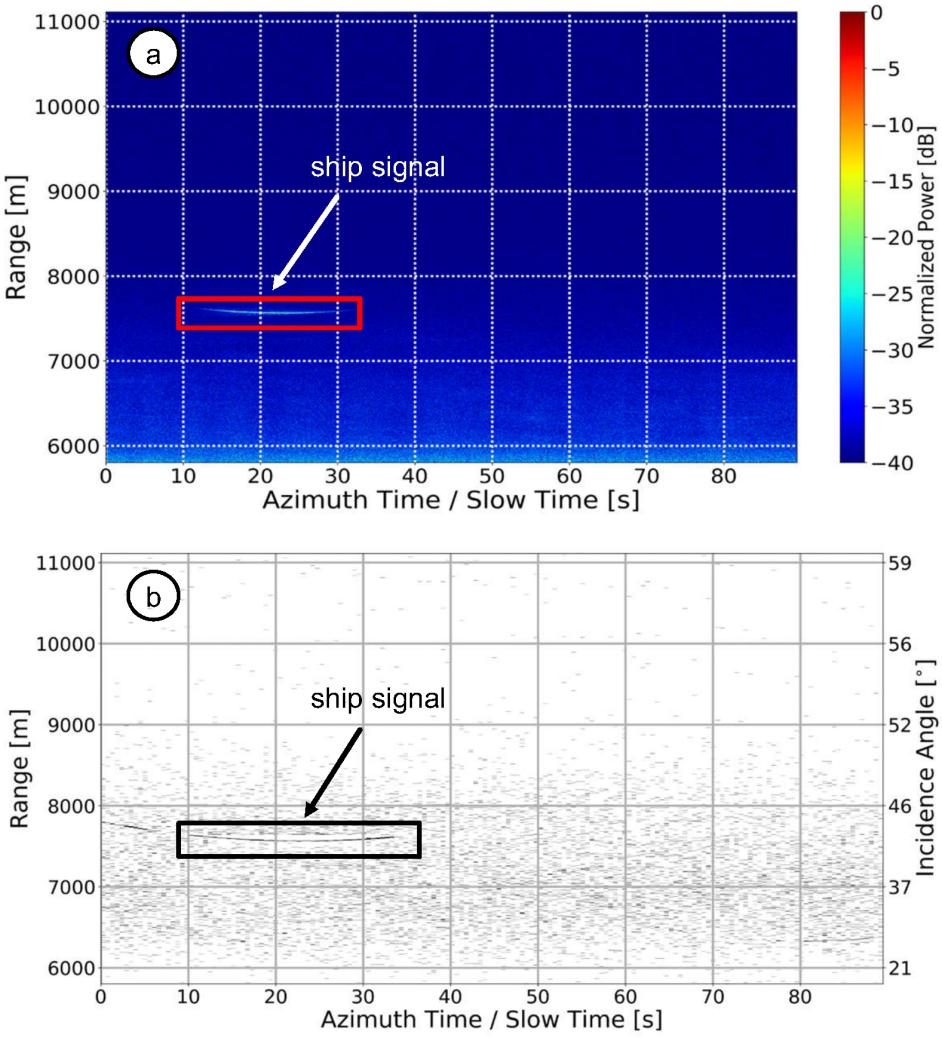

Figure 3.4: (a) Real RC X-band HH polarized F-SAR radar data acquired during a linear flight track (cf. Section B.1.1 in page 148). The ship signal is indicated in the figure. (b) K-distribution-based binary ship detection map without applying any kind of target pre-detection. Poorly detected ship signal and high clutter peaks (in near ranges) can be seen in the figure.

Several versions of CFAR detectors were developed in the past to improve the target detection performance by eliminating these outliers. Order-statistic CFAR (OS-CFAR),

trimmed CFAR, censored mean level detector and iterative censoring are some of the state-of-the-art methods used for removing the interfering targets. Despite showing relatively good performance in homogeneous scenarios, these techniques either have limited performance in heterogeneous environments or require wise choice of the parameters or are computationally ineffective [71–74]. More recently, a new algorithm based on truncated statistics CFAR (TS-CFAR) was developed in [75] where the threshold is estimated from the truncated distribution functions. TS-CFAR has been shown as a very effective way to eliminate the outliers and estimate a robust threshold. Although being a powerful method, the truncation depth has first to be fixed to a certain value and the truncated statistical distribution functions have to be derived afterwards. Fixing the truncation depth is difficult and deriving the truncated version of the sophisticated sea clutter models is both complex and time-consuming.

All these aforementioned developments and their associated limitations led to propose a simple, robust and effective method to pre-detect the potential targets with real-time capability. In the following, the target pre-detection method in the time domain is explained in detail.

3.3.1 Target Pre-Detection

The proposed target pre-detection method is based on deriving an adaptive threshold in the time domain which varies along range. Such a threshold is needed because the backscatter received by the radar system is range-dependent. The proposed target pre-detection algorithm contains the following major steps:

1. RC radar data extraction in the time domain (cf. green region in Figure 3.1).
2. Incoherent summation over azimuth.
3. Range-dependent adaptive threshold computation.
4. Target peak detection and cancellation.

For an incoherent summation over azimuth consider a set of complex amplitude pixels z spanning over N azimuth samples and R range bins of the scene (cf. green region from Figure 3.1). The average amplitude profile $A(r)$ for $r = 1, 2, 3, ...R$ of the extracted RC data is given as

$$A(r) = \frac{1}{N} \sum_{n=1}^{N} |z(r, n)|. \tag{3.2}$$

Figure 3.5 shows $A(r)$ which is plotted for different polarization channels of an F-SAR data patch which is free of any ship targets.

It can be seen in Figure 3.5 that the amplitude variation is a function of range (or incidence angle). High radar backscatter was received at low incidence angles, the amplitude decreases as the incidence angle increases. The intensity of the backscatter was found highest in HH channel and lowest in HV channel. It is now clear that for detecting

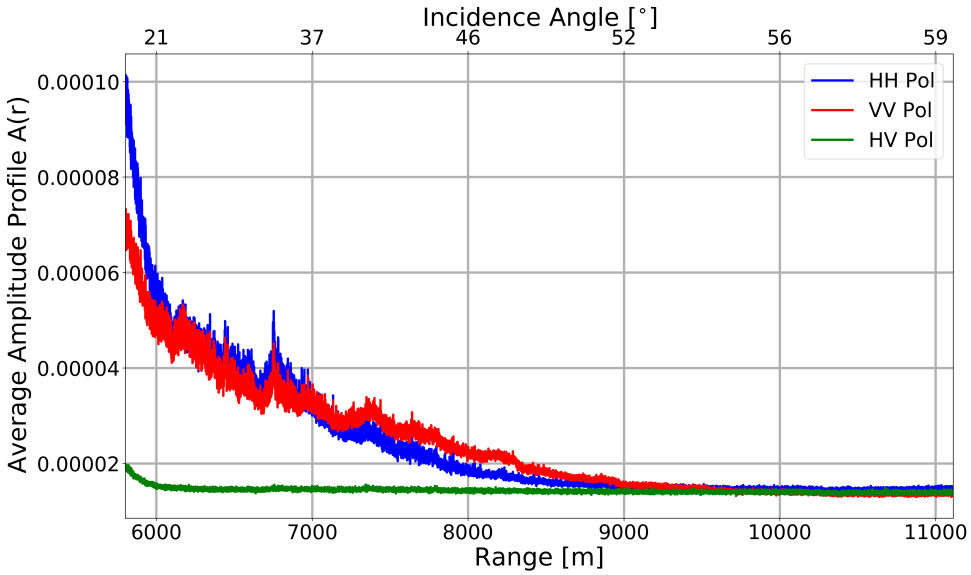

Figure 3.5: Amplitude over range profile of the sea backscatter in HH, VV and HV polarization channels of RC F-SAR X-band radar data.

potential targets at any range, the pre-detection threshold has to be adaptive along range. Therefore, the pre-detection threshold $\eta_{\text{pre}}(r)$ is defined as a function of range, i.e., $\eta_{\text{pre}}(r) = f(r)$ where r is the range.

Referring again to (3.2), the samples are incoherently added along azimuth and an average amplitude for each range is computed. Applying a moving average filter to $A(r)$ will not be an effective step to cancel the target peaks. These peaks might be extremely high which could significantly alter the center mean computed from the samples within the moving window. Instead, a one-dimensional moving median filter of a certain window size is applied because the median is more robust and less sensitive to such outliers. The median $A_{\text{med}}(r)$ of $A(r)$ is written as

$$A_{\text{med}}(r) = \text{median}(A(r)). \tag{3.3}$$

Instead of using the standard deviation around the mean to compute a pre-detection threshold, the median absolute deviation (MAD) is used. Compared to the standard deviation computed from the mean, the MAD is a more robust estimator to measure the statistical dispersion and it is resilient to the outliers present in the data [76]. The $\text{MAD}(r)$ is given as

$$\text{MAD}(r) = \text{median}(|A(r) - A_{\text{med}}(r)|). \tag{3.4}$$

The $\text{MAD}(r)$ is then used to estimate the standard deviation $\sigma(r)$ defined as

$$\sigma(r) = k_{0.75} \cdot \text{MAD}(r), \tag{3.5}$$

where $k_{0.75}$ is a scale factor with $k_{0.75} \approx 1.4826$ representing the 0.75 quantile of the standard Gaussian distribution.

The standard deviation $\sigma(r)$ is further smoothened by applying a Savitzky-Golay (SG) filter [77] with the window size being the same as the one used in median filtering. This filter performs a moving polynomial fit to the data in order to further reduce the noise without greatly affecting the signal. The SG filter becomes a simple moving average filter when the polynomial order is zero. Unlike the moving average filter, which along with the noise also removes the high frequency component of the signal, the SG filter of a certain polynomial order is able to preserve these components in the data. There are no general guidelines to choose an appropriate parameter for the SG filter. However, a polynomial order of two is a good compromise which leads to reasonable results for the F-SAR data.

The final mathematical expression for the adaptive pre-detection threshold $\eta_{\text{pre}}(r)$ can be written as

$$\eta_{\text{pre}}(r) = A_{\text{med}}(r) + f \cdot \text{SG}(\sigma(r)), \tag{3.6}$$

where $f > 1$ is a factor used to determine the decision criterion to set the pre-detection threshold. Figure 3.6 shows the influence of different factors f on the outlier detection.

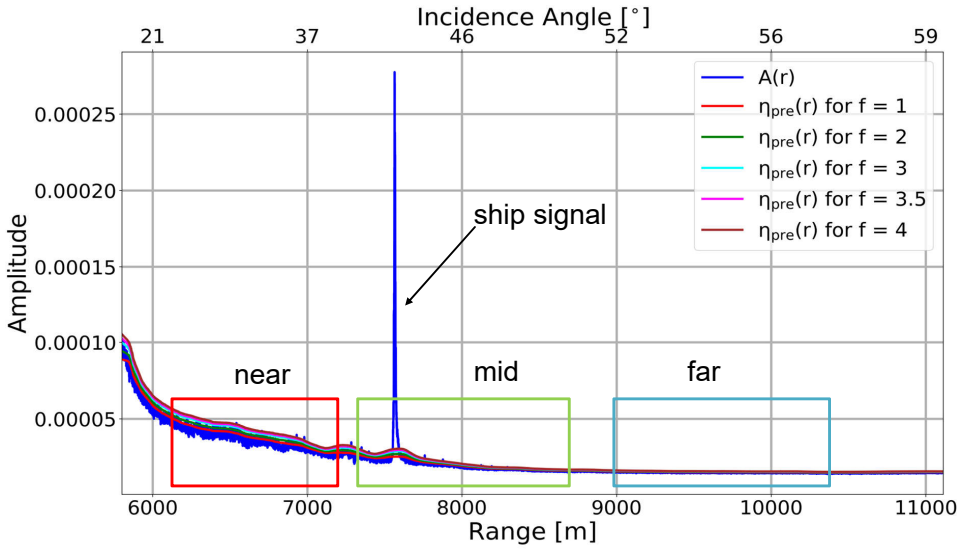

Figure 3.6: Average amplitude profile with range-dependent pre-detection thresholds. A high target peak (= ship) is present at a range of approximately 7500 m. The effectiveness of the MAD-based pre-detection is evaluated in three different zones; near (red), mid (green) and far range (blue). Details are shown in Figure 3.7.

From Figures 3.6 and 3.7 it is noticed that the pre-detection threshold is not only able to detect target peaks but also other high clutter peaks. However, a threshold based on a setting of $f = 1$ or 2 would cancel most of the peaks which might have originated from the ocean. The goal of target pre-detection is to cancel only the bright targets and

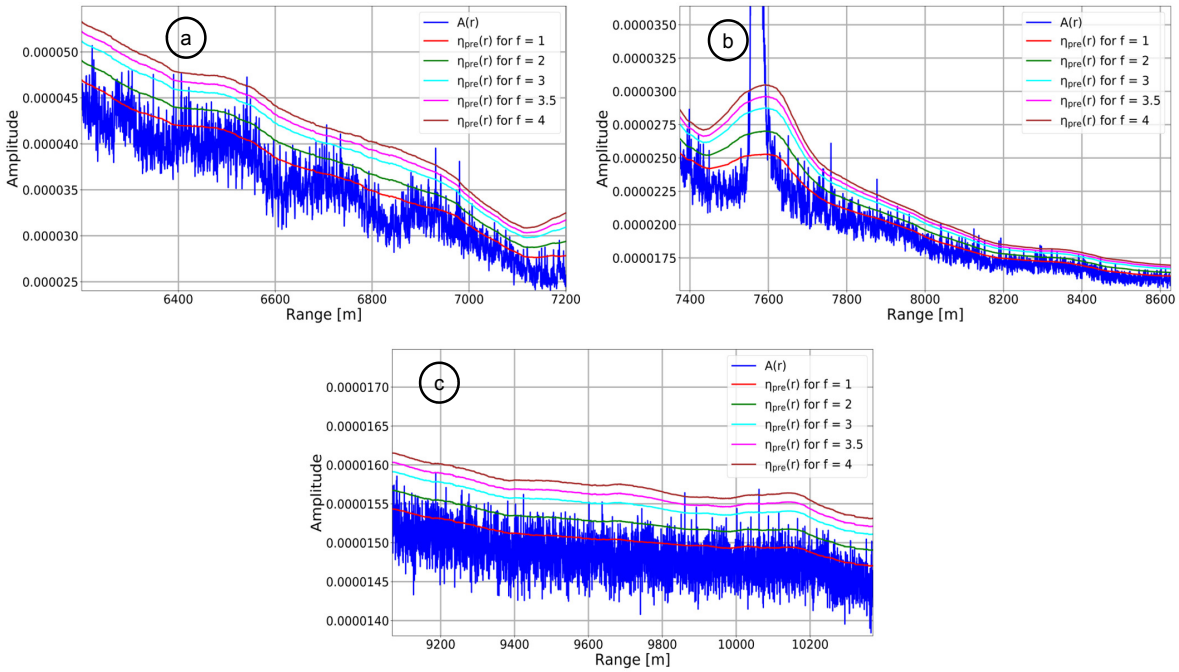

Figure 3.7: Details of the pre-detection thresholds computed for different factors f in (a) near (b) mid and (c) far ranges.

high clutter peaks. Therefore, the best value for f has to be found empirically. For the F-SAR X-band HH data it was found that a value of $f = 3.5$ or 4 effectively detects the outliers.

To demonstrate the effectiveness of the proposed pre-detection algorithm, it is applied to a real X-band HH polarized RC data in the time domain (cf. Figure 3.4(a)). For this particular case, the suitable window size of the median filter was set to 625. For an F-SAR range sample spacing of 0.3 m, this value corresponds to an approximately 188 m slant range distance. It is recommended that the window size of the median filter should be in the order of the maximum expected slant range length of the ships to be pre-detected. This ensures proper peak detection capability. The binary pre-detection map of the bright targets and outliers after applying the proposed pre-detection algorithm is shown in Figure 3.8.

To further illustrate the robustness of the proposed pre-detection algorithm, the ratio of the actual (or measured) false alarm rate $\mathrm{PFA}_{\mathrm{est}}$ and the desired false alarm rate $\mathrm{PFA}_{\mathrm{set}}$ before and after target pre-detection and cancellation was computed. The measured false alarm rate is computed as

$$\mathrm{PFA}_{\mathrm{est}} = \frac{n_{\mathrm{det}}}{n_{\mathrm{tot}}}, \tag{3.7}$$

where n_{det} is the total number of obtained detections assuming that the evaluated data patch contains no ship targets, and n_{tot} is the total number of samples contained in the same data patch. A K-distribution-based sea clutter model was used for determining n_{det} at a desired false alarm rate of $\mathrm{PFA}_{\mathrm{set}} = 10^{-6}$. In the optimum case, when the data

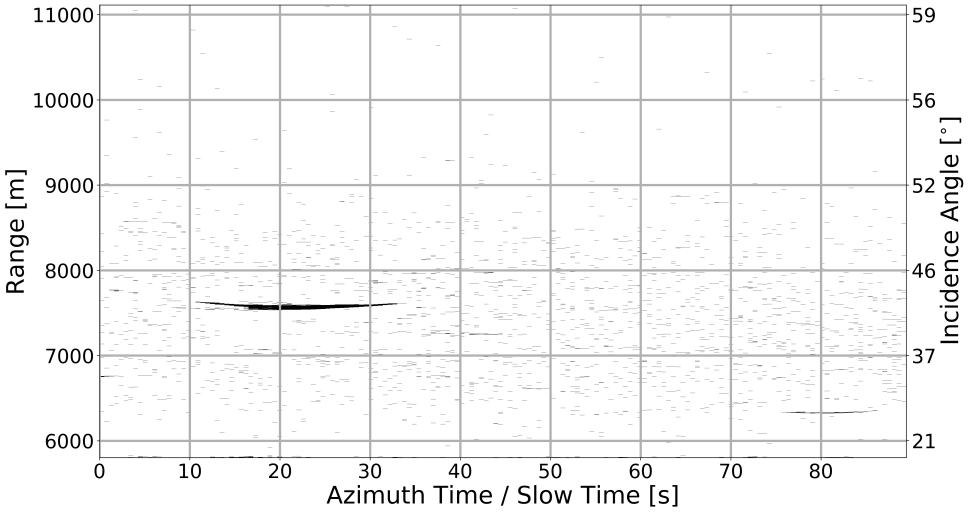

Figure 3.8: Binary detection map after applying the proposed pre-detection algorithm to the RC radar data shown in Figure 3.4(a). The pre-detected ship signal (left) as well as spiky clutter peaks can clearly be seen.

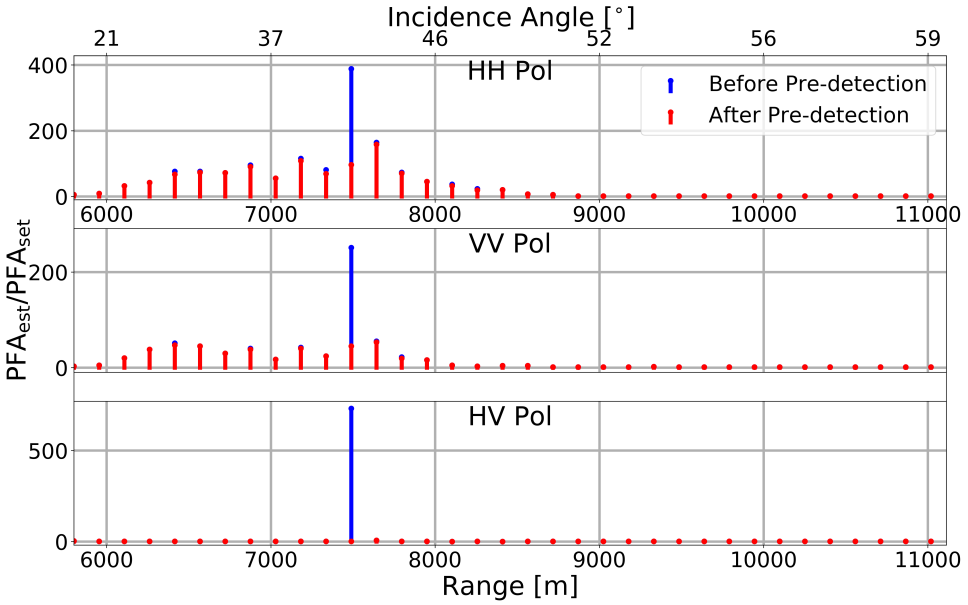

Figure 3.9: Ratio of the measured and set false alarm rates over range for X-band HH (top), VV (middle) and HV (bottom) polarizations before (blue) and after (red) pre-detection and target cancellation. Note that a ship target is present at around 42° incidence angle.

contain no ships and no spiky clutter, the ratio $\mathrm{PFA_{est}}/\mathrm{PFA_{set}}$ should be one. Practically this cannot be achieved, since there is always a slight difference between the chosen ocean clutter model and the actual ocean clutter statistics.

From the data shown in Figure 3.4(a) its HH, VV and HV polarization channels were chosen for the evaluation. The measured ratios $\mathrm{PFA_{est}}/\mathrm{PFA_{set}}$ for all channels are shown in Figure 3.9. The higher the ratio the worse is the detection performance.

As observed in Figure 3.9, irrespective of the polarization channels, the presence of a target severely degrades the estimated false alarm rate. After applying the proposed

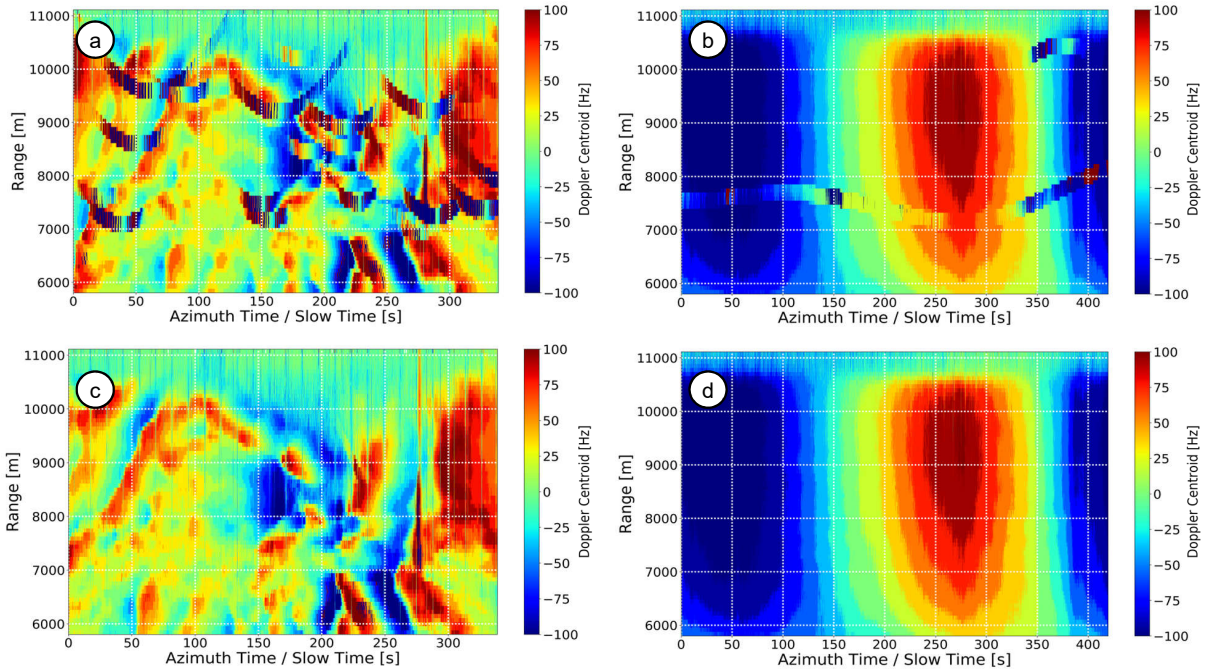

Figure 3.10: Doppler centroid maps estimated from F-SAR L-band HH polarized RC data acquired using (a) linear and (b) circular flight tracks. The ship range histories in both (a) and (b) can be clearly seen. (c, d) Doppler centroid maps re-estimated after canceling the potential targets using the proposed pre-detection algorithm.

pre-detection algorithm which also cancels the target, the actual false alarm rate around the target region gets drastically improved. However, the ratio is still higher in the near and mid ranges of the HH and VV channels. This is due to the fact that the K-distribution generally is not well suited for the RC F-SAR data. A further explanation and discussion on the proper selection of the optimum sea clutter model is given later in Section 3.4.

In addition to this, the Doppler centroid maps of the data are also generated to further examine the potential of the pre-detection algorithm. The Doppler centroid is estimated from the data using the energy balance algorithm proposed in [78]. A moving window of 512 range samples and 128 azimuth samples was used for estimating the Doppler centroid and was applied on RC F-SAR L-band data acquired using linear and circular flight tracks. Details about the acquired radar data are given in Section B.1.1 (cf. page 148). The results are shown in Figure 3.10.

It can clearly be seen in the second row of Figure 3.10 that the bright target signals contained in the first row, were canceled after applying the proposed pre-detection module. Note that the Doppler centroid variations in Figure 3.10(c) are due to the presence of sandbanks in the Wadden Sea area which lies in the southeastern part of the North Sea close to the town Cuxhaven. The ocean surface is very heterogeneous in this area. This is confirmed by comparing its corresponding RC data and the fully focused Pauli image with an optical Google Earth image (cf. Figure 3.11)

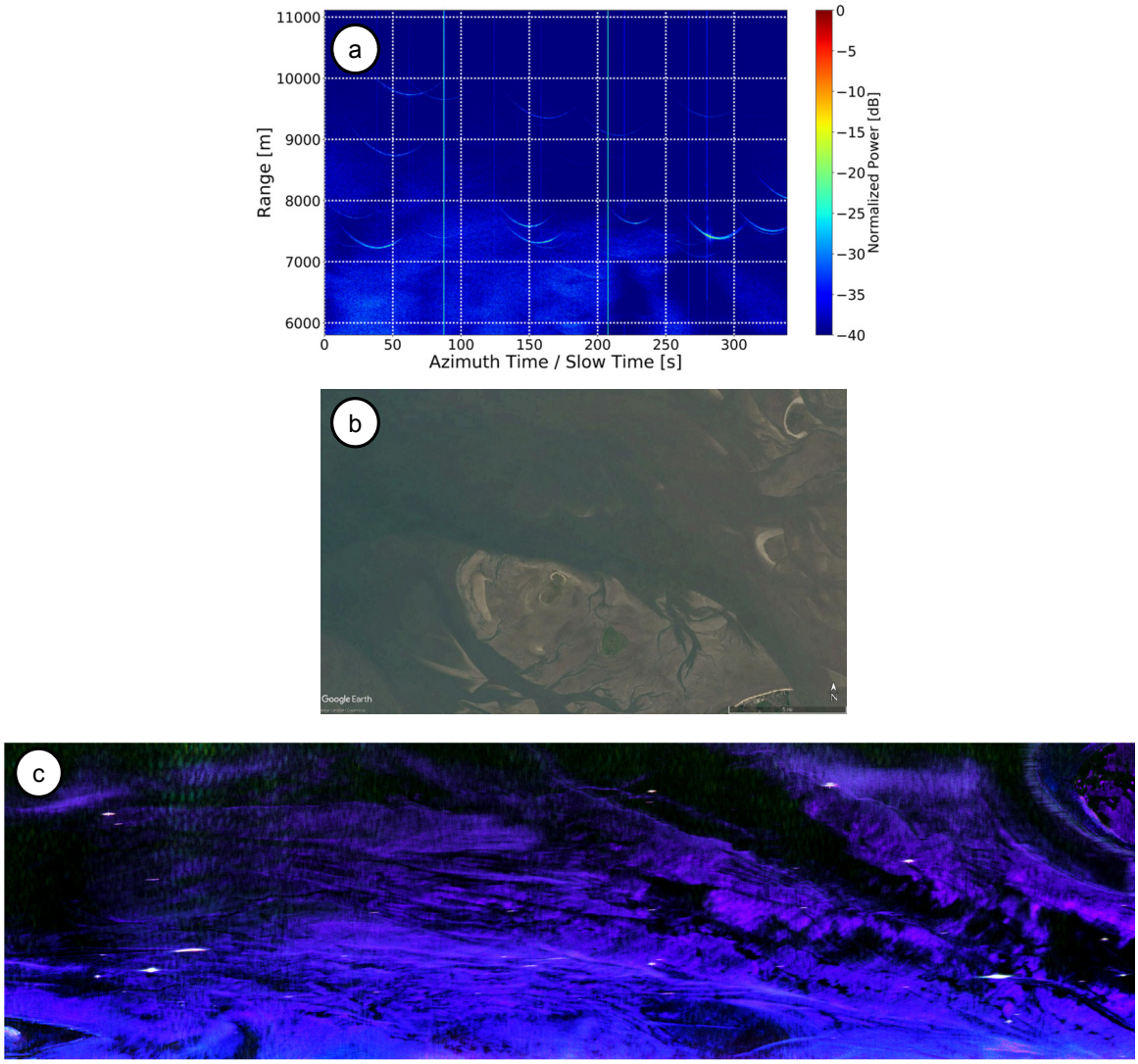

Figure 3.11: (a) RC airborne radar data, (b) Google Earth image and (c) Pauli image corresponding to Figure 3.10(a). Sandbanks are clearly visible in the Google Earth image. The bright spots in the Pauli image are strong scatterers, e.g., buoys or ships.

3.3.2 Clutter Normalization

With the proposed target pre-detection algorithm running in the time domain, potential targets are well detected and removed leaving behind the "ocean only" training data. These clean data can directly be used to determine a single CFAR threshold using standard sea clutter models. However, the steps of CFAR threshold computation cannot be applied one to one in the Doppler domain, as conventionally applied in the time domain, because the training sample amplitude varies along the Doppler frequency as shown by the red curve in Figure 3.12(a).

If no whitening of the Doppler spectra is performed and if it is directly used as the training data, then the CFAR threshold has to be estimated for each Doppler bin independently. Computing such a threshold for each Doppler bin comes with higher computa-

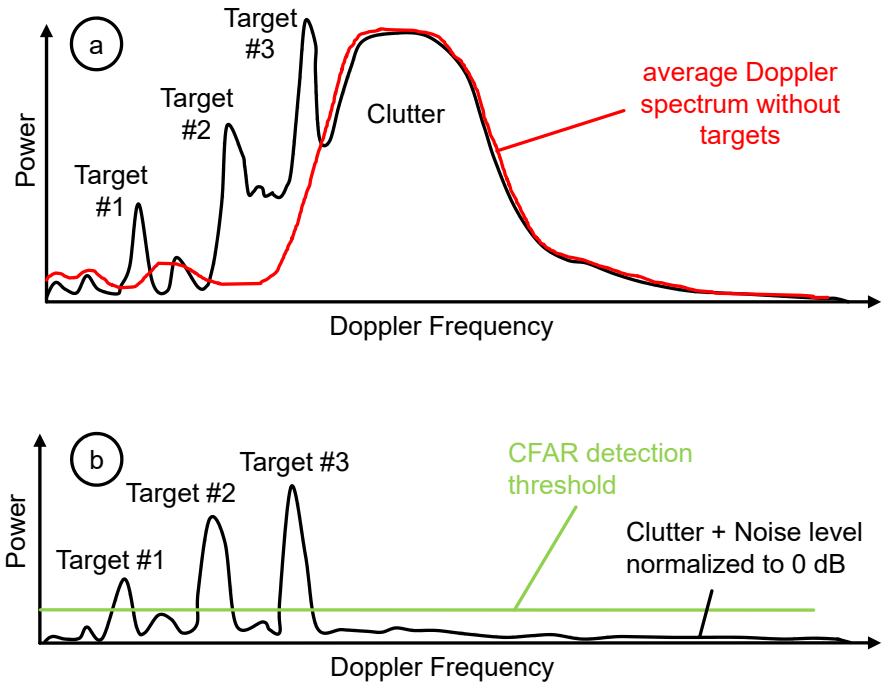

Figure 3.12: Illustration of the average Doppler spectrum of a range-Doppler image containing clutter and ship targets (a) before and (b) after normalization over Doppler. The red curve in (a) is the average Doppler profile estimated without considering the targets. The green line in (b) is the CFAR-based detection threshold computed based on clutter-plus-noise level.

tional cost. The idea is to derive a single Doppler frequency independent threshold which is achieved by normalizing the clutter and noise power to 0 dB (cf. Figure 3.12(b)).

For the normalization, consider a data block in the Doppler domain consisting of $\mathrm{n_r}$ range samples and a certain number of Doppler bins. The clutter normalization is based on the estimation of the average spectra $\hat{A}_{\mathrm{DS}}(f_{\mathrm{a}})$ (cf. red curve in Figure 3.12(a)) which can be expressed as [79, 80]

$$\hat{A}_{\mathrm{DS}}(f_{\mathrm{a}}) = \frac{1}{n_{\mathrm{r}}} \sum_{k=1}^{n_{\mathrm{r}}} |Z(r_{\mathrm{k}}, f_{\mathrm{a}})|^2, \tag{3.8}$$

where $Z(r, f_{\mathrm{a}})$ is the frequency domain representation of the time domain signal $z(r, n)$ (cf. (3.2)). For simplicity, $|Z(r, f_{\mathrm{a}})|^2 = P(r, f_{\mathrm{a}})$, which is known as power spectral density or Doppler spectrum of the data $Z(r, f_{\mathrm{a}})$. The clutter normalized power spectral density $P_{\mathrm{CN}}(r, f_{\mathrm{a}})$ can be written as

$$P_{\mathrm{CN}}(r, f_{\mathrm{a}}) = \frac{P(r, f_{\mathrm{a}})}{\hat{A}_{\mathrm{DS}}(f_{\mathrm{a}})}. \tag{3.9}$$

Upon estimating $\hat{A}_{\mathrm{DS}}(f_{\mathrm{a}})$ with (3.8) for each Doppler bin and by using (3.9) the clutter and noise are scaled to 0 dB. An example of clutter normalization is shown in Figure 3.13(b).

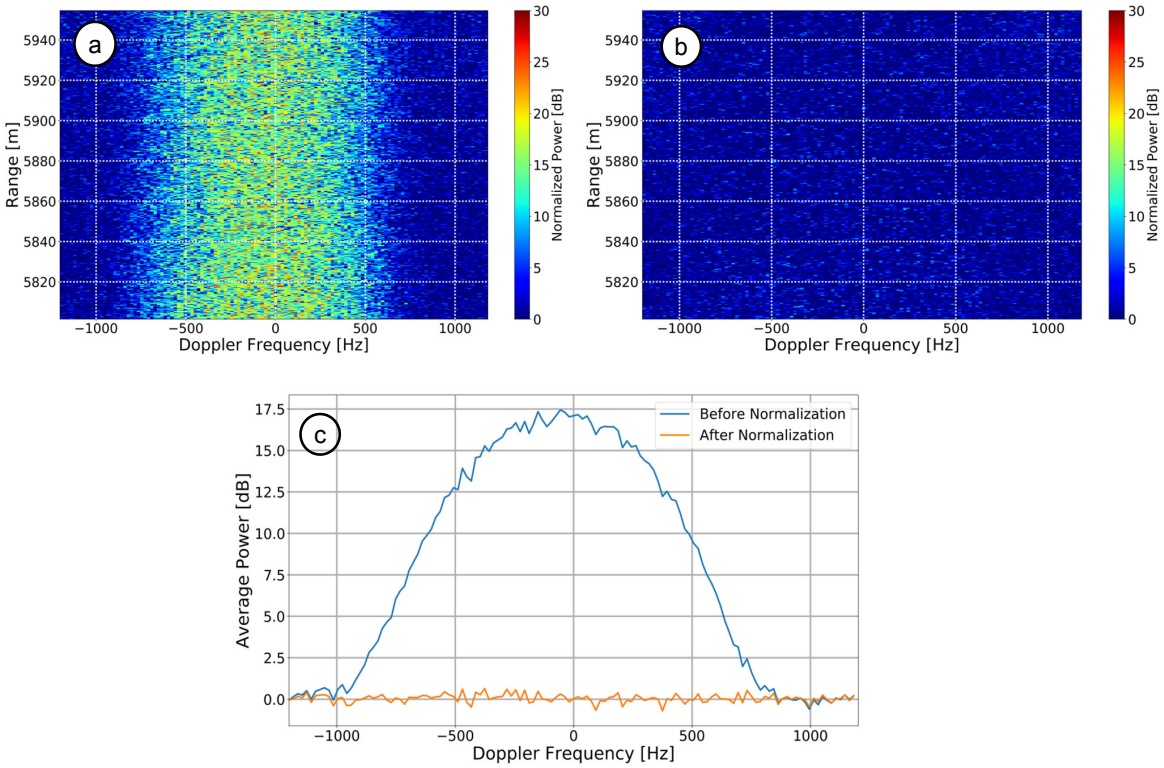

Figure 3.13: Range-Doppler image of a target-free image patch (a) before and (b) after clutter normalization. The normalized average power profiles of (a) and (b) are shown in (c).

Table 3.1: Measured target SCNR before and after clutter normalization.

Range-Doppler Image	Target SCNR [dB]
1. Before normalization (Figure 3.14(a))	24.02
2. After normalization but without pre-detection (Figure 3.14(c))	14.2
3. After normalization with exclusion of pre-detected targets in training data (Figure 3.14(e))	23.08

The data in Figure 3.13(b) are the training data used for estimating the ocean clutter statistics. However, when the range-Doppler image additionally contains a ship signal, which may be the case if no target pre-detection is carried out, the clutter normalization causes target self-whitening as shown in Figure 3.14(b)(c).

To examine this negative and unwanted target self-whitening effects, the target SCNRs are estimated for Figure 3.14(a)(c) and (e) and are listed in Table 3.1. From the table it is clear that the proper estimation of average Doppler spectrum to perform normalization over Doppler maintains the target SCNR. However, if the high peaks are not removed beforehand using pre-detection, then after normalization the target SCNR is severely degraded ($\approx$ 10 dB in this case). Therefore, it is essential to apply the proposed pre-detection and target cancellation algorithm before estimating the average Doppler spectrum used for clutter normalization.

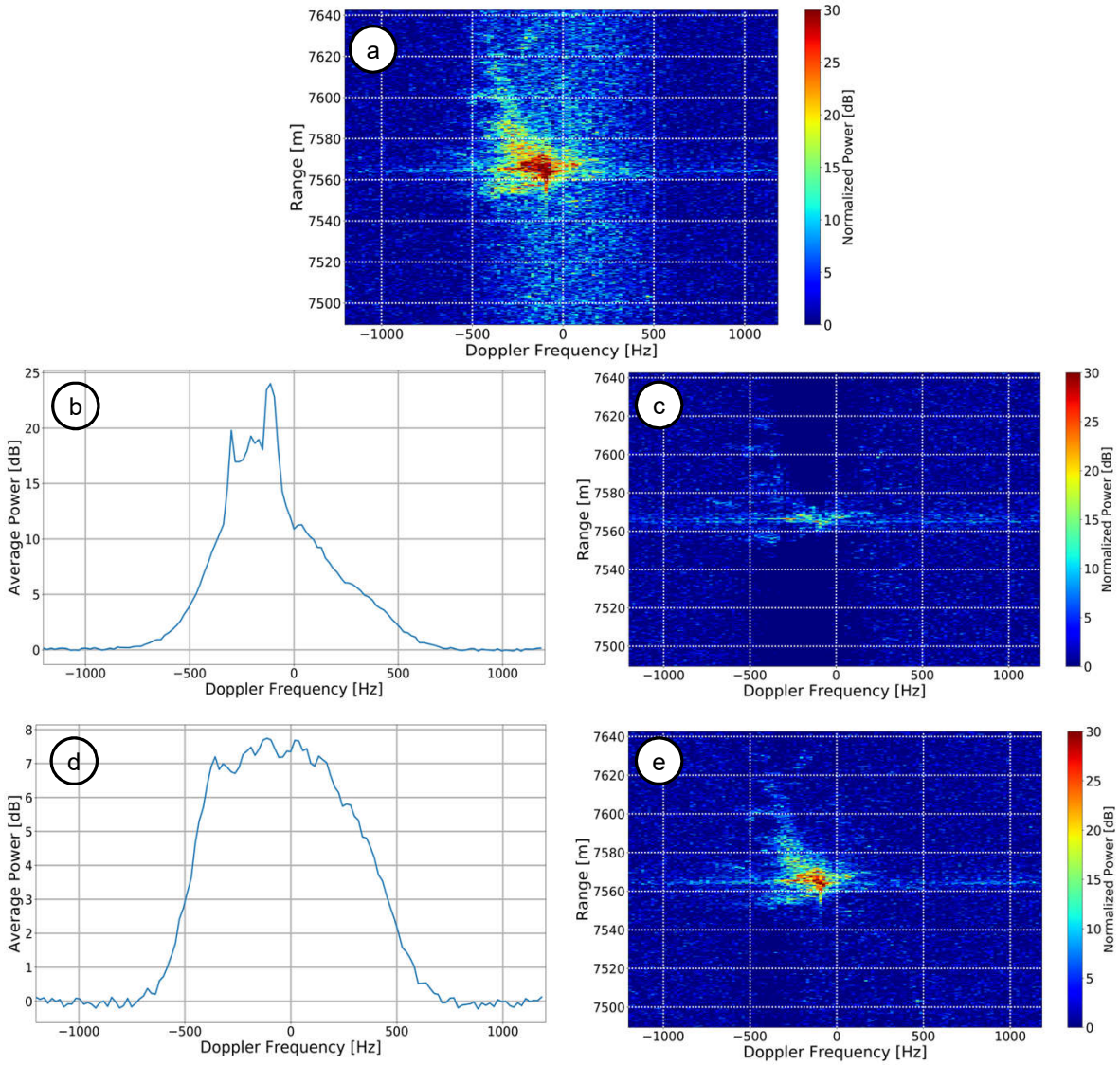

Figure 3.14: Data containing a ship target: (a) range-Doppler image before clutter normalization, (b) average Doppler spectrum estimated without using pre-detection for removing the target from (a), (c) normalized image after using the average Doppler spectrum from (b), (d) target-free estimation of average power spectrum after using pre-detection algorithm, (e) normalized image after using (d).

3.3.3 Importance of Training Data Update

Training data update is an important step because of two main reasons. The first reason is due to the change of the Doppler centroid over range and azimuth time. Atmospheric disturbances cause variations in the aircraft's Euler angles (roll, pitch and yaw) and these variations change the Doppler centroid of the data. In the special case of a non-moving ocean surface, i.e., in case of stationary clutter, the clutter Doppler centroid $f_{\mathrm{cl}}[r,t]$ is given as [81]

$$\begin{aligned} f_{\mathrm{cl}}[r,t] = &\frac{2\cdot v_{\mathrm{p}}}{\lambda}[\cos(\theta_{\mathrm{i}}[r]+\theta_{\mathrm{roll}}[t])\tan(\theta_{\mathrm{pitch}}[t])+ \\ &\sin(\theta_{\mathrm{i}}[r]+\theta_{\mathrm{roll}}[t])\tan(\theta_{\mathrm{yaw}}[t])], \end{aligned} \tag{3.10}$$

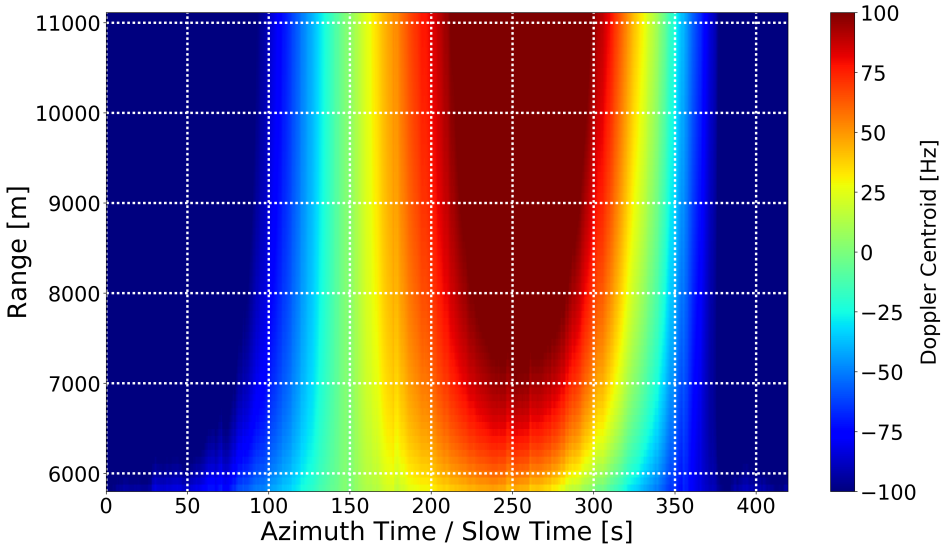

Figure 3.15: Clutter Doppler centroid map computed by using the measured aircraft Euler angles for a circular flight carried out with F-SAR (details about the flight are given in Section B.1.1 in page 148).

where θ_{roll}, θ_{pitch} and θ_{yaw} are the roll, pitch and yaw angles of the radar antenna mounted on the aircraft, respectively.

For a non-moving ocean surface, the computed clutter Doppler centroid using (3.10) is shown in Figure 3.15 for a real circular flight of F-SAR. For computation, the Euler angles (roll, pitch and yaw angles) obtained from the aircraft inertial measurement unit and corrected by taking into account the antenna lever arms are used. The Doppler centroid map shown in Figure 3.15 matches quiet well with the one computed using the data (cf. Figure 3.10(d)). The observable difference is among others given by the fact that the ocean surface moves itself.

From Figure 3.10(d) and Figure 3.15 it is clear that due to the change of the clutter Doppler centroid along range and azimuth time, a regular update of training data in range-Doppler is essential.

The second reason is due to the varying motion of the ocean surface. With a moving ocean surface, the clutter statistics tend to change significantly over range and time. To show this behavior, the texture (or shape) parameter of the K-distribution (cf. Section 3.4.2) is estimated. The variation of the texture along range and azimuth time is shown in Figure 3.16 for X-band HH polarized data acquired during a linear and circular flight. Lower values of texture indicate spiky clutter and higher values indicate Rayleigh-like characteristics of the clutter intensity.

From Figure 3.16 it can clearly be observed that the K-distribution-based texture parameter varies along range and azimuth time. Significant changes are observed along range whereas, along the azimuth the variation tends to follow a sinusoidal pattern which may be aligned with the wind direction [82]. Therefore, to consider these changes accurately, the training data need to be updated frequently in order to obtain bias-free local sea clutter statistics [83].

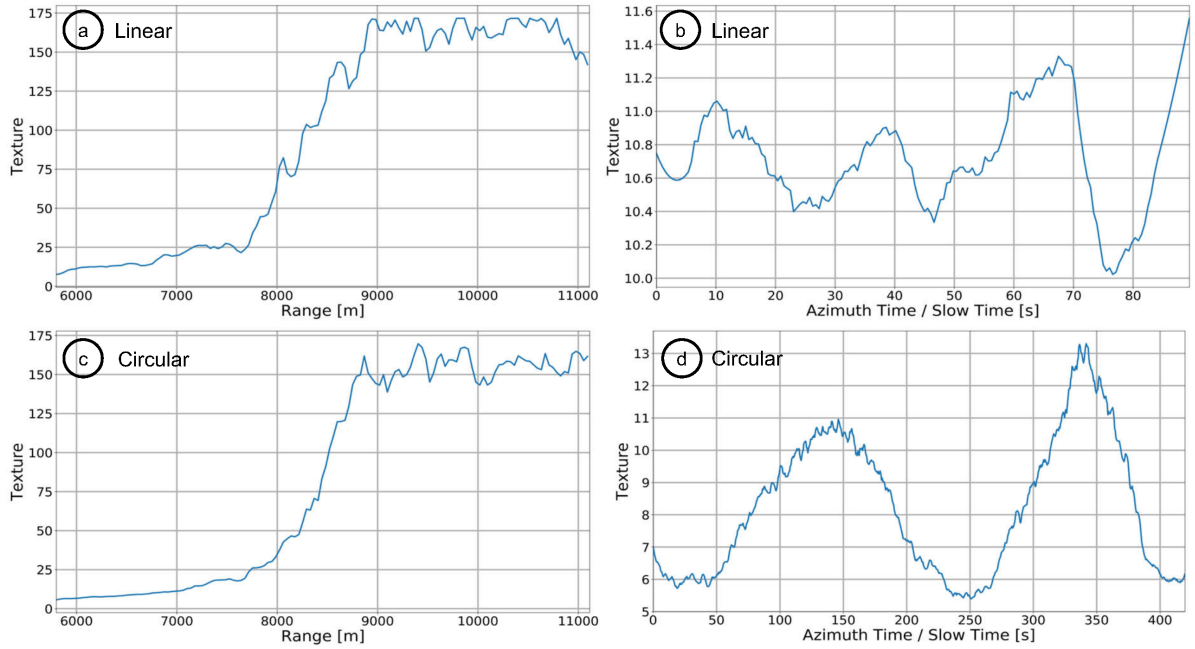

Figure 3.16: Estimated texture parameter of the K-distribution along (a),(c) range and (b),(d) azimuth using real F-SAR radar data acquired during a linear and circular flight.

3.4 Clutter Statistics and Target Detection

After target pre-detection and clutter normalization, the next step is to derive an appropriate target detection threshold in the range-Doppler domain using target-free ocean training data. In the next sections CFAR-based target detection principle is briefly explained followed by various distribution functions used for sea clutter modeling.

3.4.1 Detection Principle

CFAR-based detection algorithms are pixel-based. Therefore, for a given complex amplitude pixel Z in the Doppler domain with or without normalization, there exist two hypothesis H_0 and H_1 [62]

$$H_0 : Z = C + N \qquad \text{Moving target is absent} \tag{3.11}$$

$$H_1 : Z = C + N + S \qquad \text{Moving target is present,} \tag{3.12}$$

where C, N and S are the clutter, noise and target signals, respectively.

The sea clutter models discussed in this section are formulated based on the normalized backscattered intensity in the Doppler domain, therefore, for simplicity, $P_{\mathrm{CN}}(r, f_{\mathrm{a}}) = I$ is written (cf. (3.9)). Once a PDF $p(I)$ is chosen to model the ocean backscattered

intensity and the sea clutter parameters are estimated using the selected model, the PFA is calculated by using

$$\mathrm{PFA} = \int_{\eta}^{\infty} p(I)dI. \tag{3.13}$$

where η is the target detection threshold. After setting the PFA to a fixed value, the target detection threshold is computed using the above equation. Pixel intensity values above threshold η are declared as moving target pixels.

3.4.2 K-Distribution

Equations (3.11) and (3.12) are applicable only when the clutter amplitude is Rayleigh distributed (= homogeneous clutter) [84,85]. However, in the case of relatively low grazing angles (10° - 50°) and high resolution systems, the clutter returns are often spiky and they no longer follow Rayleigh distribution [82]. To address this problem, an additional independent random variable called texture Δ is introduced. This leads to the following expression

$$Z = \Delta \cdot C + N + S. \tag{3.14}$$

The introduction of the texture component leads to the product or compound clutter models. One of the most popular and widely used compound models is the K-distribution. It is a comprehensive representation of a Gamma distributed texture over Rayleigh distributed homogeneous clutter. For L number of looks, it is represented as [86, 87]

$$p(I, \nu, b, L) = \frac{2\Gamma(\nu)^{-1}}{\Gamma(L)}(Lb)^{\frac{L+\nu}{2}} I^{\frac{L+\nu-2}{2}} K_{\nu-\mathrm{L}}(2\sqrt{LbI}), \tag{3.15}$$

where ν, b, $\Gamma(\cdot)$ and $K(\cdot)$ are the shape, scale, gamma function and the modified Bessel function of the second kind of order $\nu - L$, respectively. The scale parameter b is related to the mean μ of the data as $b = \frac{\nu}{\mu}$.

The shape parameter ν, also known as texture, mainly controls the shape of the K-distribution. The range of ν is $[0.1, \infty]$, where for $\nu = \infty$, the PDF reduces to a Rayleigh distribution. Lower values of ν represents spiky clutter (cf. near ranges in Figure 3.16(a)(c)).

The PFA of the K-distribution obtained after using (3.13) can be expressed as [85]

$$\mathrm{PFA}(\eta) = 2\sum_{l=0}^{L-1} \frac{(\nu L)^{\frac{\nu+l}{2}}}{\Gamma(l+1)\Gamma(\nu)} \eta^{\frac{\nu+l}{2}} K_{\nu-1}(2\sqrt{\nu L\eta}). \tag{3.16}$$

There are in total three unknowns of K-distribution: shape (ν), scale ($\frac{\nu}{\mu}$) and number of looks (L) to be determined to fit the distribution.

Method of Moments (MoM)

One way to estimate μ and ν of the K-distribution is to use the first and second moments of the data. This method is referred to as MV (mean and variance), contrast-based or V-statistic. The equations are [88]

$$\hat{\mu} = \langle I \rangle, \tag{3.17}$$

$$\left(1 + \frac{1}{\hat{\nu}}\right)\left(1 + \frac{1}{L}\right) = \frac{\langle I^2 \rangle}{\langle I \rangle^2}, \tag{3.18}$$

where $\langle \cdot \rangle$ is the expectation operator. The number of looks L is either known or can be estimated using the ratio of the square of the mean and the standard deviation [89]. Knowing the number of looks L and the estimated mean $\hat{\mu}$, the shape parameter $\hat{\nu}$ can be computed using (3.18).

It is found that the V-statistic works quiet well in most of the cases and is therefore preferred for estimating the parameters of K-distribution. Another estimator proposed in [90] is referred as X-statistic, which is computationally faster and gives a more straightforward solution than other estimators. The mathematical expression for the X-statistic is

$$\left(\frac{1}{\hat{\nu}} + \frac{1}{L}\right) = \frac{\langle I \cdot \log I \rangle}{\langle I \rangle} - \langle \log I \rangle. \tag{3.19}$$

Nonlinear Least Squares Method (NLLSQ)

The parameters of K-distribution can also be estimated by using the NLLSQ method. The NLLSQ method uses the Levenberg-Marquardt algorithm [91] to find the local minima of a function by expressing the function as a sum of the squares of the difference between the proposed PDF and the data PDF. The minimization function is expressed as

$$\arg\min_{\alpha} \left(\sum_{m=1}^{M} p(I, \alpha) - h_{\mathrm{m}} \right)^2, \tag{3.20}$$

where $p(I, \alpha)$ is the distribution function having α unknown parameters and h_{m} is the m^{th} histogram bin of the normalized distribution.

3.4.3 Chi-Square Distribution

The chi-square (χ^2) distribution is one of the models that is used when the K-distribution fit fails because the estimated shape parameter $\hat{\nu}$ of K-distribution gives negative values, especially in case of highly homogeneous training samples [92].

The χ^2 distribution function with two degrees of freedom (DOF) is represented as [93]

$$p(I, \sigma, L) = \frac{I^{L-1}}{2^L \sigma^{2L} \Gamma(L)} \exp\left(\frac{-I}{2\sigma^2}\right), I \geq 0. \tag{3.21}$$

The number of unknowns of this distribution is 2: the number of looks L and the standard deviation σ.

The PFA as a function of the threshold η can be written as

$$\mathrm{PFA}(\eta) = \frac{1}{\Gamma(L)} \Gamma\left(L, \frac{\eta}{2\sigma^2}\right). \tag{3.22}$$

For a single look, the threshold becomes $\eta = -2\sigma^2 \ln(\mathrm{PFA})$. The parameters in this case are estimated using the NLLSQ method (cf. Section 3.4.2).

3.4.4 Tri-Modal Discrete (3MD) Texture Model

A new model called tri-modal discrete texture model (3MD) was recently proposed for detecting moving targets with a very low PFA [85,94,95]. The model was mainly invented for detecting ships in fully focused spaceborne SAR data. It is based on the idea of the statistical modeling of the sea texture in a discrete form. The PDF of the 3MD model for L number of looks can be written as

$$p(I, \odot, L, \rho_\mathrm{c}) = \frac{L^L}{\Gamma(L)} I^{L-1} \sum_{d=1}^{D} c_\mathrm{d} \frac{\exp\left(-\frac{LI}{\rho_\mathrm{c} a_\mathrm{d}^2 + \rho_\mathrm{n}}\right)}{(\rho_\mathrm{c} a_\mathrm{d}^2 + \rho_\mathrm{n})^L}, \tag{3.23}$$

where $\odot = [c_\mathrm{d}, a_\mathrm{d}]$, D corresponds to the number of discrete scatterers in a single pixel. The variables ρ_c and ρ_n are the normalized clutter and noise variances, respectively, whose sum is unity. The parameters a_d and c_d are the d^{th} discrete texture intensity level and their corresponding relative weightings, respectively, where $\sum_{d=1}^{D} c_\mathrm{d} = 1, c_\mathrm{d} > 0$.

The PFA as a function of the threshold η is given by [85]

$$\mathrm{PFA}(\eta) = \sum_{d=1}^{D} c_\mathrm{d} \frac{\Gamma\left(L, \frac{L\eta}{\rho_\mathrm{c} a_\mathrm{d}^2 + \rho_\mathrm{n}}\right)}{\Gamma(L)}. \tag{3.24}$$

The value of D after testing even highly heterogeneous sea state was found to be 3 [94]. Therefore, for the 3MD clutter model there are eight unknown parameters: $\odot = [c_\mathrm{d}, a_\mathrm{d}]$ (six unknowns, three for each), ρ_c and L. In the frame of this doctoral thesis, these unknowns are estimated using the NLLSQ method (cf. Section 3.4.2).

It has to be noted that different estimation methods may lead to different results, especially for very low false alarm rates. For future systems, Christoph Gierull recommends to use the method of moments proposed in [95] as the preferred estimation method [personal email conversation]. The recommended method shall be investigated in future for the RC radar data in the range-Doppler domain.

3.4.5 K-Rayleigh Distribution

The presence of non-Bragg scattering components in the ocean surface, better known as discrete sea spikes, is the main reason why the K-distribution fit fails even when the thermal noise in the data is taken into account [96]. An example of ship detection using the K-distribution applied on the RC F-SAR X-band HH polarized data is shown in Figure 3.17. In the figure the detection map is obtained using the methodology described in Section 3.2 at a desired of PFA $= 10^{-6}$. Only for the visualization purposes, the detections are projected back to the time domain. As shown in the figure due to the high intensities of the sea spikes, they are often confused with the target, giving rise to a very high number of false detections.

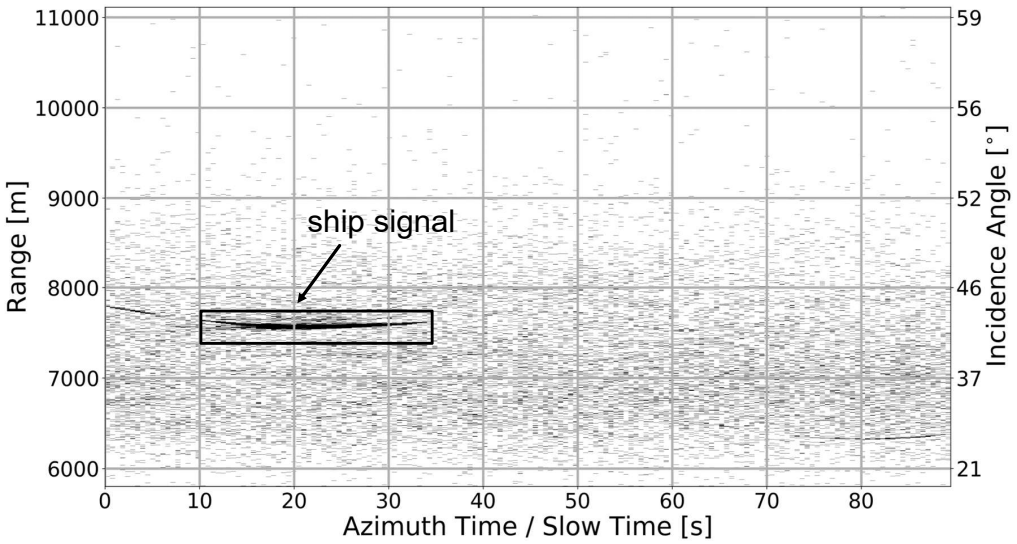

Figure 3.17: Binary detection map based on the K-distribution obtained from the real RC airborne radar data shown in Figure 3.4(a). The detected ship signal (left) and high sea clutter spikes in near ranges can clearly be observed.

In recent studies, KA (K-class A), KK and Pareto distribution models, along with their adaptations to consider thermal noise were proposed and investigated to model these sea

spikes. However, these models have many unknowns and require a prior knowledge of the thermal noise [96].

The K-Rayleigh distribution function is one of the recently proposed distribution functions that models sea spikes as an extra Rayleigh component which is typically not captured by the K or even the K+Noise (K+N) distributions. The PDF of the K-Rayleigh distribution has no closed form solution and is given as [96]

$$p(I|\nu_{\mathrm{r}}, b_{\mathrm{r}}, \rho_{\mathrm{r}} + \rho_{\mathrm{n}}) = \frac{b_{\mathrm{r}}^{\nu_{\mathrm{r}}}}{\Gamma(\nu_{\mathrm{r}})} \int_0^{\infty} \frac{x_{\mathrm{s}}^{\nu_{\mathrm{r}}-1}}{x_{\mathrm{s}} + \rho_{\mathrm{r}} + \rho_{\mathrm{n}}} \exp\left(- \frac{I}{x_{\mathrm{s}} + \rho_{\mathrm{r}} + \rho_{\mathrm{n}}} - b_{\mathrm{r}} x_{\mathrm{s}} \right) dx_{\mathrm{s}}, \quad (3.25)$$

where ν_{r}, b_{r} are the shape and scale parameters of the K-Rayleigh distribution, respectively. The sum $x_{\mathrm{s}} + \rho_{\mathrm{r}}$ is the total speckle mean; where x_{s} and ρ_{r} are the modified speckle mean and the extra Rayleigh component which is modeled like the thermal noise ρ_{n}. If $\rho_{\mathrm{r}} = 0$, it takes the form of the K+N distribution. Furthermore, as shown in (3.25) there are three unknowns in the K-Rayleigh distribution and they are computed by solving the following set of equations [96]

$$\hat{\nu_{\mathrm{r}}} = \frac{18\big(\langle I^2 \rangle - 2\langle I \rangle^2\big)^3}{\big(12\langle I \rangle^3 - 9\langle I^2 \rangle \langle I \rangle + \langle I^3 \rangle\big)^2}, \quad (3.26)$$

$$\hat{\rho}_{\mathrm{r+n}} = \langle I \rangle - \sqrt{\frac{\hat{\nu}_{\mathrm{r}}}{2}\big(\langle I^2 \rangle - 2\langle I \rangle^2\big)}, \quad (3.27)$$

$$\hat{b}_{\mathrm{r}} = \frac{\hat{\nu}_{\mathrm{r}}}{\langle I \rangle - \hat{\rho}_{\mathrm{r+n}}}. \quad (3.28)$$

The term $\hat{\rho}_{\mathrm{r+n}} = \rho_{\mathrm{r}} + \rho_{\mathrm{n}}$, where the Rayleigh offset ρ_{r} and the thermal noise ρ_{n} are estimated as a single parameter using (3.27). Even when the thermal noise is not known, all the parameters needed to fit the data can be well estimated using the above equations.

The PFA and hence, the detection threshold in this case is computed numerically using (3.13). A comparison between the detections obtained from the K- and the K-Rayleigh distribution functions is shown in Figure 3.18. In the figure it is clearly visible that the threshold computed using the K-Rayleigh distribution function is much higher compared to the K-distribution. As a consequence, the number of false alarms is significantly decreased but also could be the number of true detections.

3.5 Experimental Results and Discussion

In this section the performance of various clutter models discussed in Section 3.4 are evaluated using linearly and circularly acquired single-channel RC airborne radar data from F-SAR radar system. The acquired radar data and the flight experiments are described

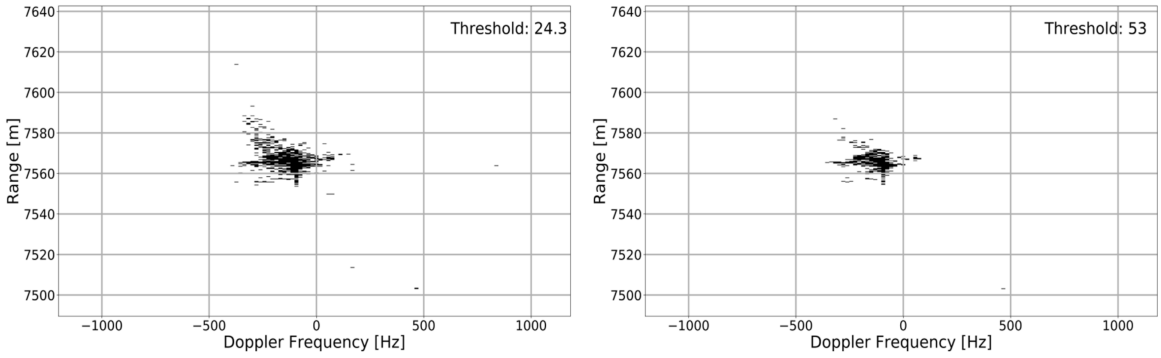

Figure 3.18: Binary detection map in the range-Doppler domain using K-distribution (left) and K-Rayleigh distribution (right). The thresholds estimated in both the cases are shown on the top right of both figures. Real X-band HH pol F-SAR data were used as an input. The detection maps were generated using 128 azimuth and 512 range samples and the desired false alarm rate was set to PFA $= 10^{-6}$.

in Section B.1.1 (cf. page 148) and the acquisition and system parameters are listed in Table B.1 (cf. page 150).

3.5.1 Clutter Model Fitting

To test the clutter models fitting the acquired radar data are first partitioned into three regions: (a) near range (10° - 30° incidence angle), (b) mid-range (30° - 50°) and (c) far range (> 50°). Since the backscatter changes over the incidence angle (cf. Figure 3.5), it is important to segment the data for a detailed investigation and understanding of the chosen models.

The image patches, each from the near, mid and far ranges of the linear and circular data, were independently chosen from each other to evaluate the models behavior. The RC data patch used for the investigations has 1280 azimuth samples and 512 range samples (cf. the red region shown at the top in Figure 3.1). Figures 3.19 and 3.20 show the fit between the measured data PDF and the PDFs provided from different sea clutter models.

From Figure 3.19(a)(b) and Figure 3.20(a)(b) it can be observed that in near and mid-range the K-distribution, the chi-square distribution and the 3MD model fit only for the intensity values of up to 2.5 and 4, respectively. In contrast, the K-Rayleigh distribution is able to fit well in the near and mid-range for both linear and circular data. Due to the presence of spiky clutter the data histogram is more skewed in the mid-range compared to the near range. The K-Rayleigh distribution is able to model this skewness by estimating an extremely low texture value of 0.04 (cf. Figure 3.19(b)) and 0.09 (cf. Figure 3.20(b)), respectively. When the K-distribution is used instead of the preferred K-Rayleigh, then the V-statistics rather than the X-statistics and the NLLSQ shall be used for parameter estimation, since it leads to the best K-distribution performance in both near and mid ranges.

In the far range however, only the K-distribution parameters estimated using the NLLSQ method, the chi-square and the 3MD model fit well. Others do not fit because the

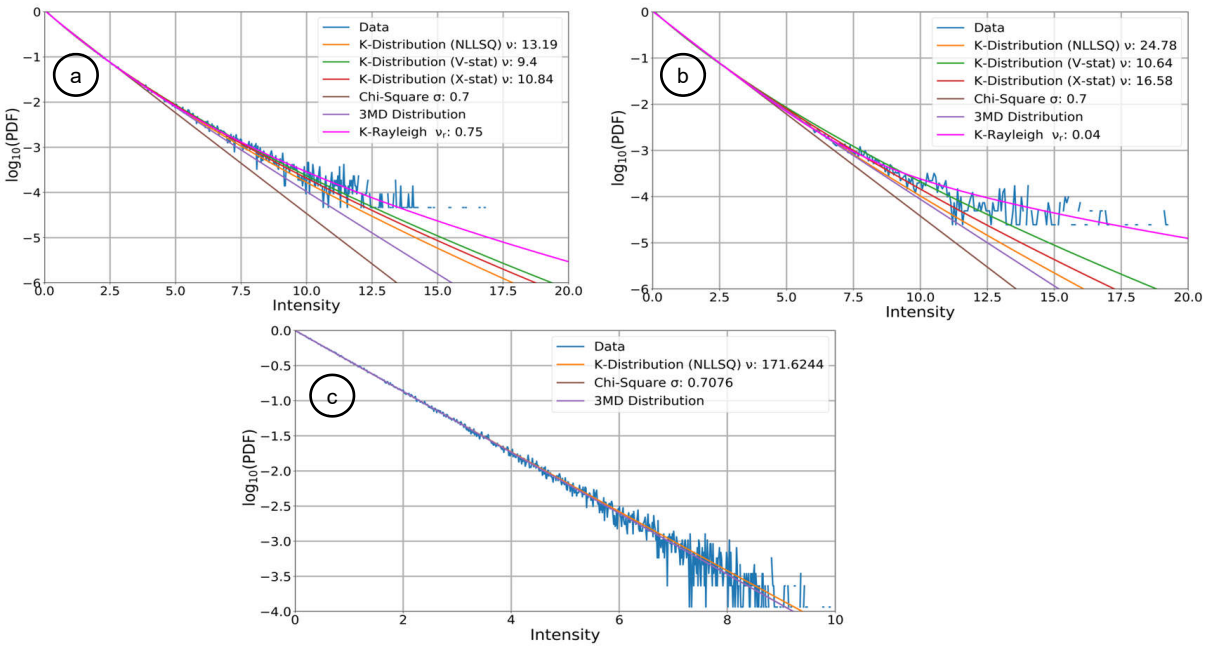

Figure 3.19: Logarithmic PDFs of different distribution functions plotted for (a) near (b) mid and (c) far range using the data acquired during the linear flight track. Google Earth view of the flight track is shown in Figure B.3(b) (cf. page 149). The estimated parameters corresponding to different distribution functions are shown in the legends of the plots, apart from the 3MD model since it has 8 unknowns.

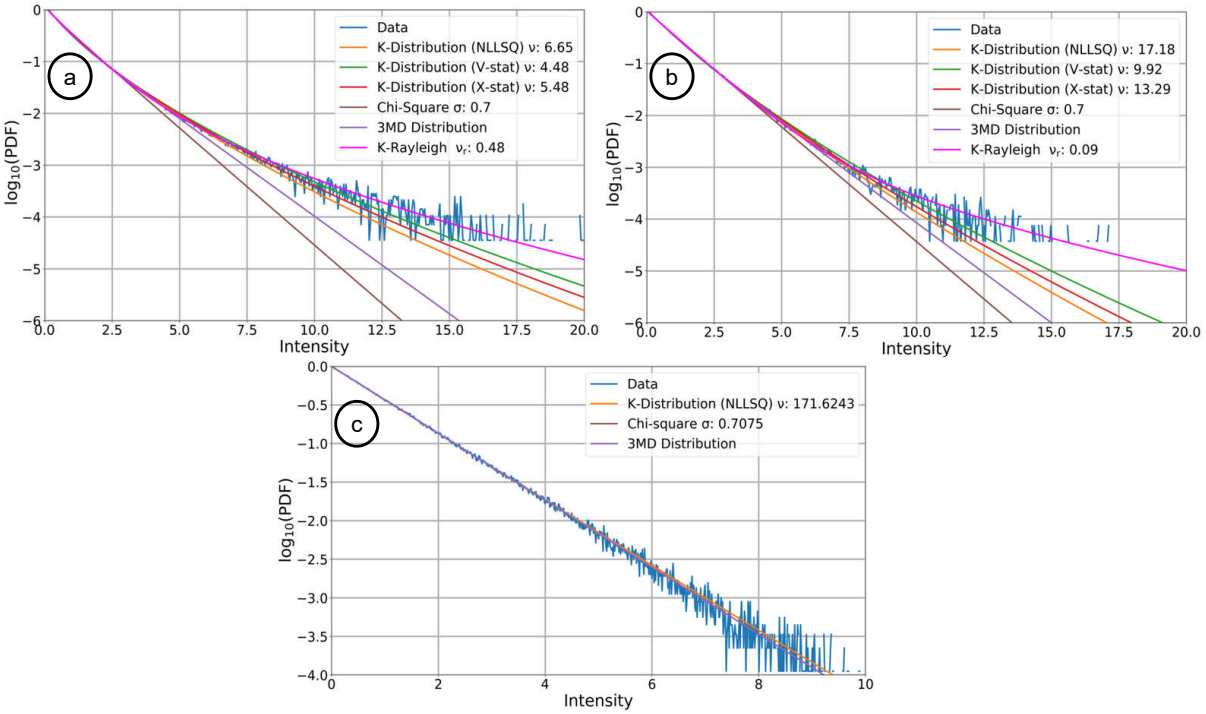

Figure 3.20: Logarithmic PDFs of different distribution functions plotted for (a) near (b) mid and (c) far range using the data acquired during the circular flight track. Google Earth view of the flight track is shown in Figure B.3(c) (cf. page 149). The estimated parameters corresponding to different distribution functions are shown in the legends of the plots.

estimated parameters have negative values. This is because the NLLSQ-based methods fits the data histogram in a least square sense, whereas the MoM doesn't have optimal properties [97]. Another reason why they do not fit in far range is because, due to the long range and shallow incidence angle, the clutter power in far range is comparable to the noise power, as shown in Figure 3.21.

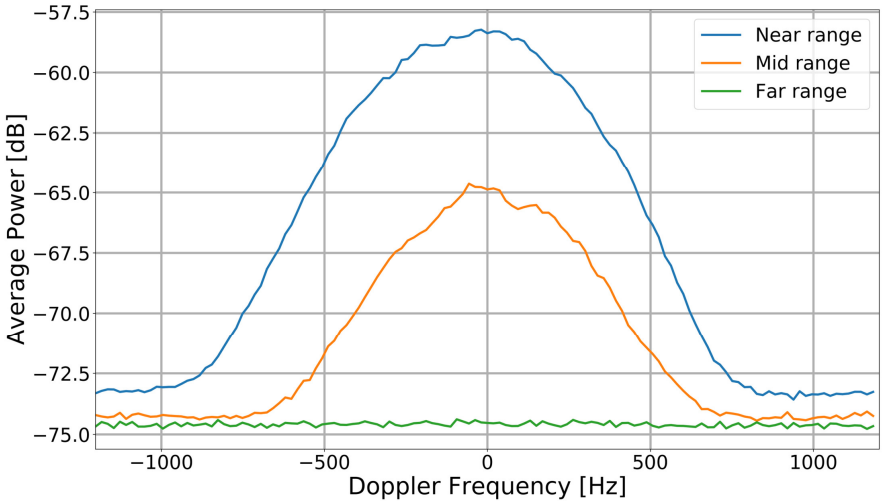

Figure 3.21: Average Doppler spectrum of real RC radar data estimated in near, mid and far range. The ambiguities cause a variation in the average power in the noise region of the spectrum.

From Figure 3.21 it is clear that due to high incidence angle, the backscatter power received in far range is very low. It can also be said that in far range the intensities are more Rayleigh distributed. This is evident from Figure 3.19(c) and Figure 3.20(c) where the texture value from the K-distribution estimated using the NLLSQ method in both the data is approximately 171. Such a high value implies Rayleigh distributed statistics [96].

Furthermore, the complementary cumulative distribution function (CCDF) computed from the estimated data PDF and the CCDFs computed from different clutter models are also plotted. Plotting such functions is important due to their relationship with the detection threshold. In the literature the CCDF is also known as PFA [96]. The logarithmic CCDF plots of the radar data acquired using linear and circular flights are shown in Figure 3.22 and Figure 3.23, respectively.

It can be observed from Figure 3.22(a)(b) and Figure 3.23(a)(b) (near and mid ranges) that the CCDF from the K-Rayleigh distribution align very well with the estimated data CCDF. In contrast in Figure 3.22(c) and Figure 3.23(c) (far range), the CCDF from the K-Distribution using NLLSQ for parameter estimation, the chi-square and the 3MD model fit very well with the data CCDF. The reason why other models don't fit in far range can again be explained in terms of low clutter-to-noise ratio (CNR) and Rayleigh distributed characteristics.

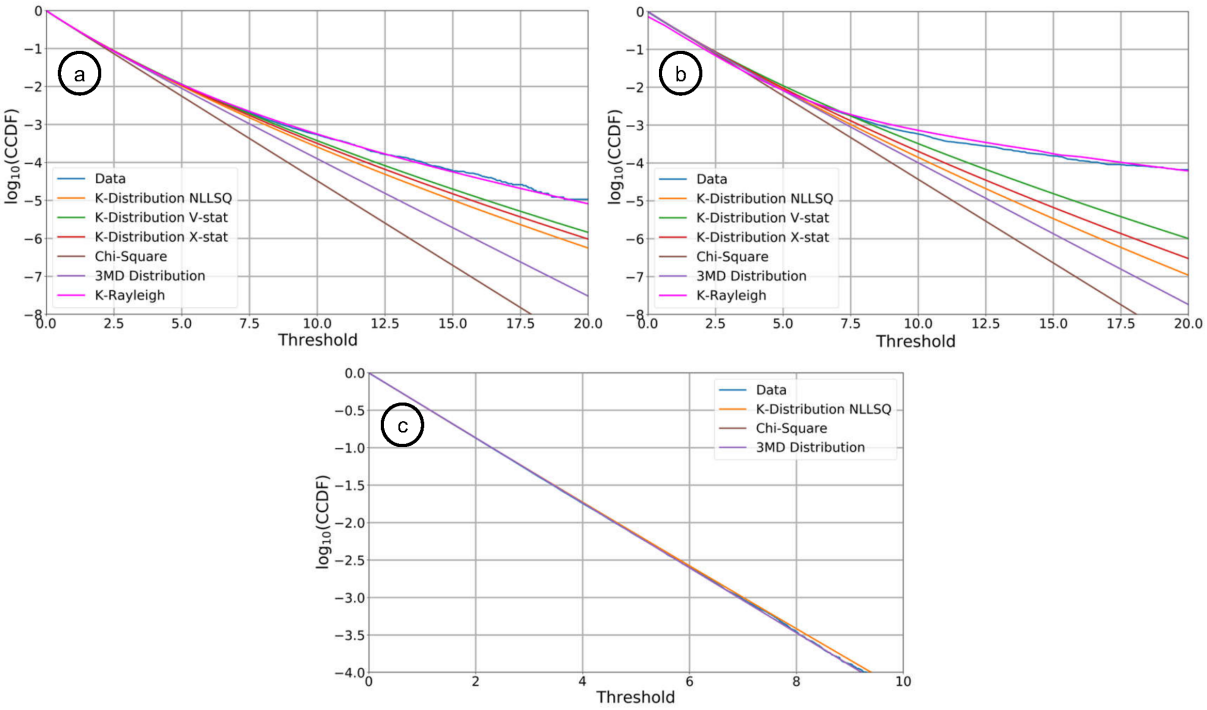

Figure 3.22: Logarithmic CCDFs of different distribution functions plotted for (a) near (b) mid and (c) far range. These plots are generated from the same data used for generating the plots shown in Figure 3.19.

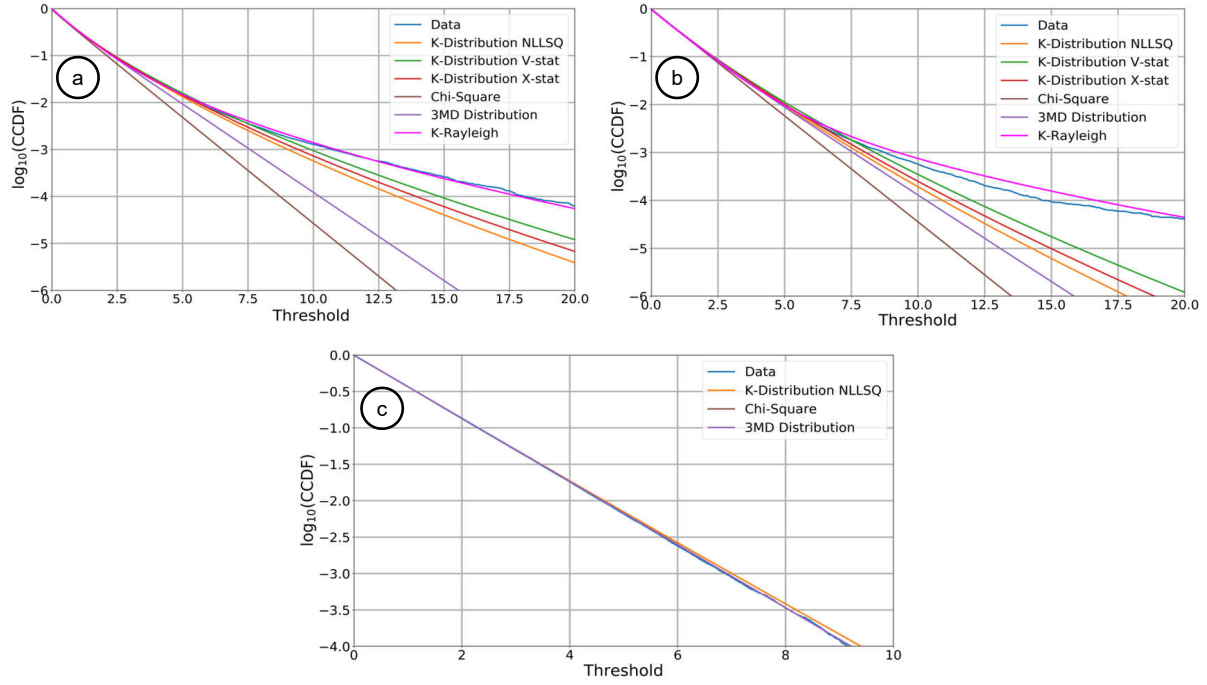

Figure 3.23: Logarithmic CCDFs of different distribution functions plotted for (a) near (b) mid and (c) far range. These plots are generated from the same data used for generating the plots shown in Figure 3.20.

3.5.2 Performance Assessment

In this section methods for evaluating the accuracy of the investigated clutter models are presented. Two error matrices are used for the assessment purposes: threshold error at a fixed CCDF value and false alarm rate ratio (FARR) at a fixed $\mathrm{PFA}_{\mathrm{set}} = 10^{-6}$. Based on these error matrices, suitable clutter models are selected which are later used for generating final ship detection results in the RC radar data.

Threshold Error

In order to know which models give the best results the actual threshold errors are estimated. The threshold error is computed by calculating the absolute difference between the thresholds estimated from the data CCDF and the model CCDF at a certain CCDF value in the tail region of the histogram as shown in Figure 3.24.

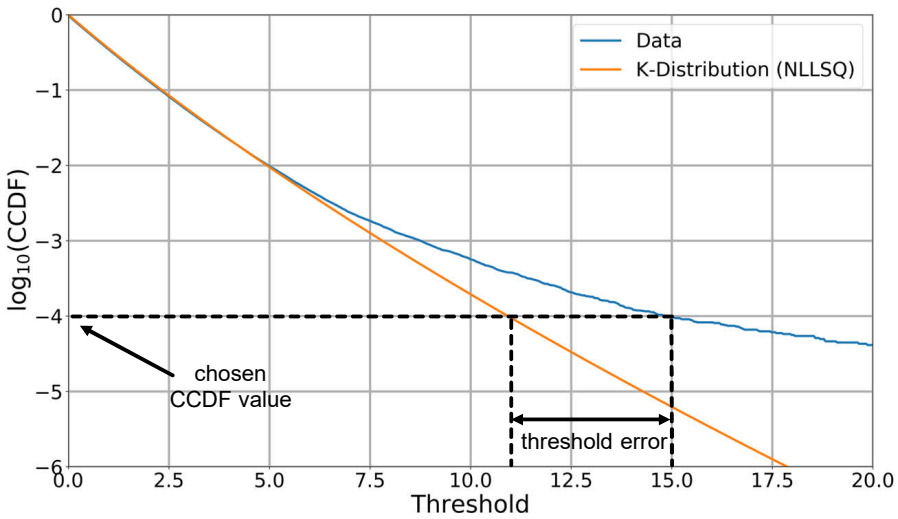

Figure 3.24: Threshold error computation using logarithmic CCDF plots from the data and the K-Distribution NLLSQ method against the threshold. Threshold error and the chosen CCDF value are marked in the figure.

The threshold error $\tilde{\eta}$ is written as

$$\tilde{\eta} = |\eta_{\mathrm{data}} - \eta_{\mathrm{model}}|_{\mathrm{CCDF}=10^{-4}} \tag{3.29}$$

where η_{data} and η_{model} are the thresholds obtained from the data and the clutter model at a specific CCDF value, respectively. The threshold error is computed in the tail region because of two reasons: bright ship target signals lie mostly in that region and the tail region is the region where most of the mismatch between reality and models occurs.

The threshold errors (in log scale) computed using different distribution functions for near, mid and far ranges as well as for linear and circular data are shown in Table 3.2 and Table 3.3, respectively.

Table 3.2: Estimated threshold errors for different clutter models of the acquired F-SAR data with linear flight track.

Clutter Models	Near Range	Mid-Range	Far Range	
	CCDF (= PFA)			
	10^{-4}	10^{-4}	10^{-4}	10^{-5}
K-NLLSQ	3.97	8.01	-10.34	-2.16
K-Vstat	2.41	6.89	-	
K-Xstat	3.23	7.61	-	
Chi-square	6.98	8.87	-10.34	-4.98
3MD	5.62	8.27	-10.34	-5.17
K-Rayleigh	-5.79	-0.26	-	

Table 3.3: Estimated threshold errors for different clutter models of the acquired F-SAR data with circular flight track.

Clutter Models	Near Range	Mid-Range	Far Range
	CCDF(= PFA)		
	10^{-4}	10^{-4}	10^{-4}
K-NLLSQ	6.89	6.02	-5.86
K-Vstat	5.19	4.6	-
K-Xstat	6.19	5.49	-
Chi-square	9.7	7.73	-11.65
3MD	8.94	6.94	-10.86
K-Rayleigh	-6.68	2.27	-

From Table 3.2 and Table 3.3 it can be seen that the threshold error is minimum in case of K-Rayleigh distribution and maximum in case of chi-square distribution in near and mid-range. In circular data for far range the chi-square distribution gives the minimum error.

In far range of linearly acquired data (cf. Table 3.2, right) the computed threshold errors are the same for CCDF $= 10^{-4}$ for the K-NLLSQ, chi-square and 3MD model. Therefore, the threshold errors were additionally computed for CCDF $= 10^{-5}$ and it is found that the 3MD gives minimum error in far range of linear data.

FARR

To further quantify the suitability of the clutter models FARRs are also evaluated for different ranges. The FARR is computed as the ratio of estimated false rate (cf. (3.7)) to the set false alarm rate where the latter is set as 10^{-6}. It has to be noted that for estimating the false alarm rate all the bright targets have first to be excluded from the scene for avoiding biases. This can be done using the proposed pre-detection method (cf. Section 3.3.1). The obtained results from all the clutter models using linearly and circularly acquired data are shown in Table 3.4 and Table 3.5, respectively.

Table 3.4: FARR for the linearly acquired F-SAR radar data for a set false alarm rate of 10^{-6}.

Clutter Models	Near Range	Mid-Range	Far Range
K-NLLSQ	80.5	112.1	3.08
K-Vstat	35.1	57.1	-
K-Xstat	56.9	86.8	-
Chi-square	277.4	242.9	2.43
3MD	149.2	135.9	1.56
K-Rayleigh	1.31	1.68	-

Table 3.5: FARR for circularly acquired F-SAR radar data for a set false alarm rate of 10^{-6}.

Clutter Models	Near Range	Mid-Range	Far Range
K-NLLSQ	63.3	74.6	12.2
K-Vstat	30.6	38.9	-
K-Xstat	46.9	55.9	-
Chi-square	422.4	234.9	9.43
3MD	257.9	154.9	7.73
K-Rayleigh	2.03	2.08	-

From Tables 3.4 and 3.5 it can be concluded that the K-Rayleigh distribution gives the least FARR in near and mid ranges, whereas the chi-square gives the highest error. In far range the 3MD, chi-square and K-NLLSQ match well with the set false alarm rate.

Based on the analyses presented in this section, it can be concluded that for near and mid ranges ($15° - 50°$ incidence angle) the K-Rayleigh distribution function is the best suitable choice, whereas for the far range ($> 50°$ incidence angle), the 3MD model or the chi-square is the preferred choice. This recommendation is valid for all the RC X-band

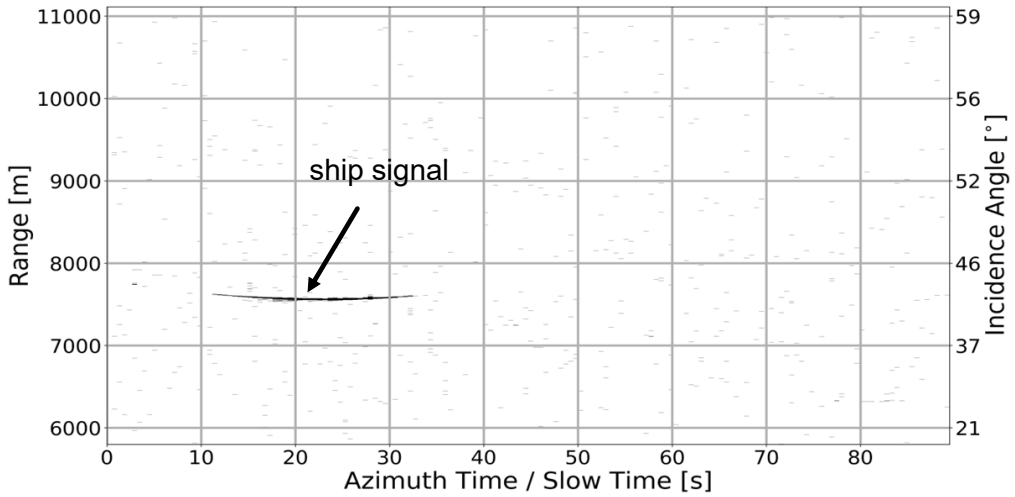

Figure 3.25: Binary detection map shown in the time domain after applying CFAR-based ship detection in the range-Doppler domain. The corresponding RC data was already shown in Figure 3.4(a). K-Rayleigh distribution function was used in the near and mid ranges, and the 3MD model was used in the far range of the data. The desired false alarm rate was set to $\mathrm{PFA}_{\mathrm{set}} = 10^{-6}$. The ship signal is clearly visible in the binary detection map.

HH polarized airborne radar data used for the investigations and the current sea state conditions during data acquisitions.

It has to be further noted that the detection rate of the proposed CFAR detector is not evaluated. This is because the vessel size is larger than the spatial resolution of the image which gives several pixel-based detections for a single vessel (cf. Figure 3.18). Thus, even with the ground truth information the number of "true" detections belonging to a vessel cannot be determined reliably. Therefore, it is difficult when not even impossible to accurately measure the probability of detection using data containing real ships. Even if the detected pixels would be (manually) clustered to a single physical object, it is important to set an appropriate detection criterion to consider it as a "true" detection. Therefore, this kind of "object-based" detection and the derived "object-based" detection rate so far cannot be compared with the established "pixel-based" probability of detection used in any CFAR detection framework [98, 99].

3.5.3 Detection Results

This section of the chapter provides the detection results obtained after the analyses performed in Sections 3.5.1 and 3.5.2.

The K-Rayleigh distribution function is used in the near and mid ranges and the 3MD model is used in the far range of the data. The detection threshold is estimated based on a desired false alarm rate of 10^{-6}. The binary ship detection maps of the linearly acquired real X-band F-SAR radar data and circularly acquired real X- and L-band F-SAR radar data are shown in Figures 3.25, 3.26(b) and Figure 3.27(b), respectively. The equations that are finally used to generate the detection results are (3.6), (3.9), (3.13), (3.24) and (3.25).

In Figure 3.26(a) the ship signal is not completely visible over the entire observation time. There are some gaps. This is because the F-SAR X-band 3 dB azimuth antenna beamwidth in the order of 8° is rather small. Since the antenna also cannot be steered electronically or mechanically, during a circular flight with a ship moving in the circle center, the cross-wind may cause a significant yaw angle so that the ship is not always illuminated. In contrast to the X-band, the L-band 3 dB azimuth antenna beamwidth is in the order of 18° so that the ship signal is always visible in the data as shown in Figure 3.27. The 3 dB azimuth antenna beamwidths for both X- and L-band F-SAR radar systems are given in Table B.1(cf. page 150).

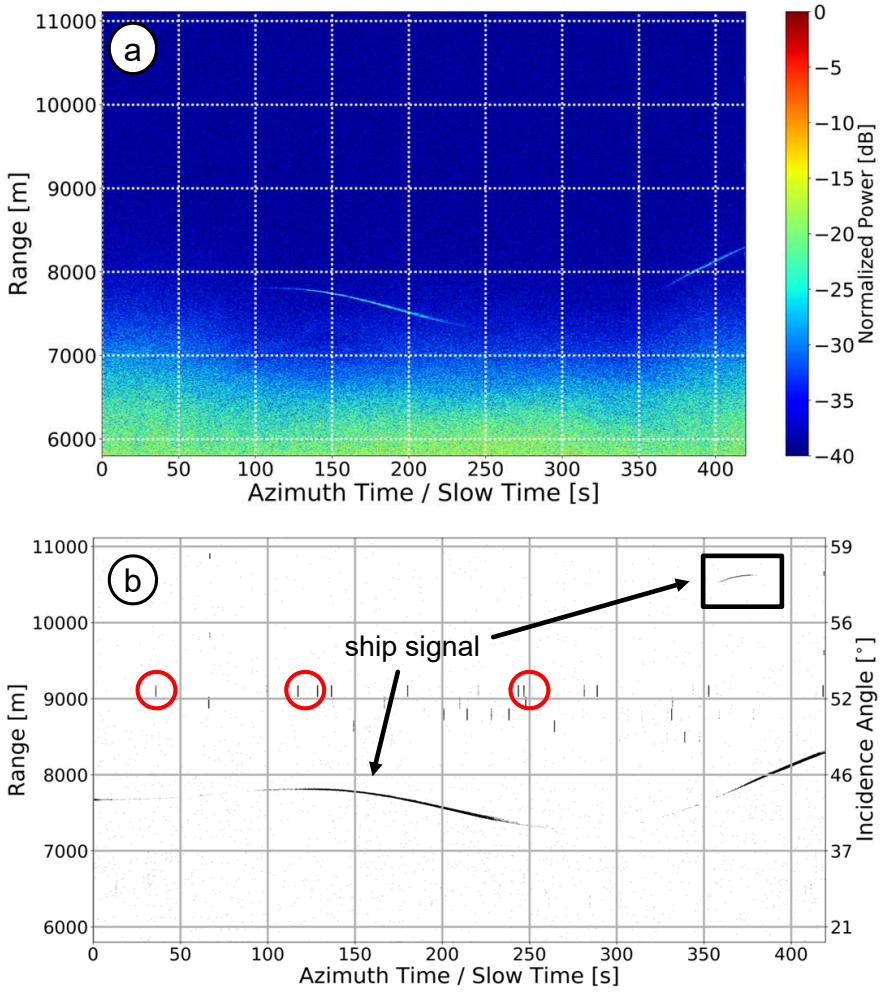

Figure 3.26: (a) Circularly acquired real single-channel HH polarized RC X-band F-SAR radar data. (b) Corresponding binary detection map shown in the time domain after applying CFAR-based ship detection in the range-Doppler domain. K-Rayleigh distribution was used in the near and mid ranges, and the 3MD model was used in the far range of the data. The desired false alarm rate was set to $\mathrm{PFA}_{\mathrm{set}} = 10^{-6}$. The detections marked by the red circles are due to the interfering signals from a ground surveillance radar located close to the test site (for visualization purposes not all of the interfering signals are marked).

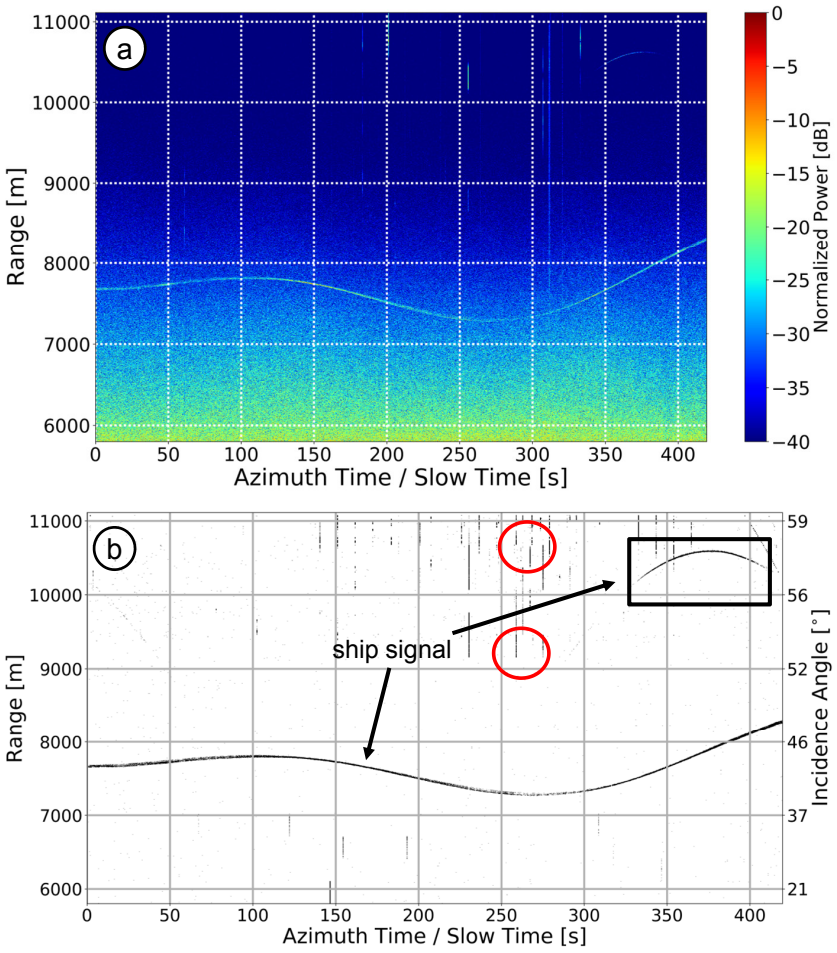

Figure 3.27: (a) Circularly acquired real single-channel HH polarized RC L-band F-SAR radar data. (b) Binary detection map shown in the time domain after applying CFAR-based ship detection in the range-Doppler domain. K-Rayleigh distribution was used in the near and mid ranges, and the 3MD model was used in the far range of the data. The desired false alarm rate was set to $\mathrm{PFA}_{\mathrm{set}} = 10^{-6}$. The detections marked by the red circles are due to the interfering signals from a ground surveillance radar located close to the test site (for visualization purposes not all of the interfering signals are marked).

To summarize, the performance of the proposed CFAR ship detection algorithm mainly depends on two factors: the target pre-detection threshold (cf. Section 3.3.1) and the accuracy of the clutter model. Inappropriate estimation of the target pre-detection threshold in the time domain may prevent target cancellation and can directly impact the average Doppler spectrum, and, hence, the normalization (cf. Figure 3.14(c)) and degrade the performance of the clutter models. Therefore, the parameters for computing the target pre-detection threshold should be carefully selected for obtaining later a valid CFAR threshold in the Doppler domain. Additionally, an appropriate selection of the clutter model also plays a key role to improve the target detection by minimizing the detection threshold amplitude error and the FARR (Section 3.5.2). It is recommended to use the K-Rayleigh distribution in the near and mid ranges because of the numerous discrete sea spikes present in the data at those ranges. For the far range where less sea spikes are

observable in the experimental data, the clutter intensity is more Rayleigh distributed so a chi-square or 3MD model is recommended.

One potential third factor which may negatively influence the performance of the proposed algorithm is the sea state, although not investigated in this doctoral thesis due to a lack of appropriate data. Especially in the case of high sea state, i.e., if the pixels corresponding to the vessel have similar statistics and intensity as the surrounding clutter, it may happen that the vessel is not detectable, especially not in the time or imaging domain. However, high sea state does not prevent the vessel detection if it is properly illuminated by the radar (i.e., if the illumination is not prevented by high sea waves) and, if the LOS component is large enough so that the corresponding echo signal is shifted to the exo-clutter region (cf. (1.2) and Figure 2.8 bottom right).

3.5.4 Processing Time Evaluation

This section evaluates the processing time of the proposed ship detection algorithm. The detection algorithm for evaluation is written in the Python programming language and it is processed on a 32-core 2.10 GHz Intel(R) Xeon(R) Gold 6130 CPU (central processing unit) which is shared with several users and running tasks. The detection algorithm is composed of several different blocks as shown in Figure 3.1. Time needed to process individual block is provided in this section.

For every individual block of the detector its mean processing time is calculated. For this, each block is executed hundred times and after hundred consecutive runs, the obtained processing times are averaged. After having the mean processing times of all the blocks, the most time-consuming blocks of the detector are determined, so that the overall detector can be optimized for the future onboard processing.

The radar data patch used for calculating the processing time is extracted from the data shown in Figure 3.4(a). The data patch contains 1280 azimuth samples and 512 range samples (cf. the red region shown at the top in Figure 3.1). The results are shown in Table 3.6. The table includes the processing time results of all the major blocks of the detection processing chain except the blocks (12) and (13) which are the clutter statistics estimation and threshold computation blocks, respectively (cf. Figure 3.1). This is because for computing clutter statistics estimation and thresholds this doctoral thesis considers not one but several sea clutter models and the processing time of each clutter model varies depending on their complexities. Therefore, for these two blocks, their processing times for different sea clutter models are shown separately in Table 3.7.

From Table 3.6 and Table 3.7 it can be seen that amplitude average and the K-Rayleigh-based statistics estimation and threshold computation are the most time consuming blocks of the proposed ship detection algorithm, respectively. The former is time-consuming because it involves computations like incoherent summation of azimuth samples along azimuth followed by an averaging operation based on the methodology described in Section 3.3.1.

Table 3.6: Processing time calculated for each block of the proposed ship detection algorithm shown in Figure 3.1. The value in bold is the most time-consuming process. The data patch consisting of 1280 azimuth and 512 range samples was considered.

Major blocks of the CFAR-based detection algorithm	Block number as per Figure 3.1	Calculated processing time [s]
Amplitude average	**1**	**2.85e-02**
Range detrending	3	3.85e-03
Azimuth FFT	5	7.51e-03
Target pre-detection	6	4.32e-05
Target azimuth lines exclusion	7	2.28e-04
Average Doppler spectrum estimation	8	4.87e-05
Normalization over Doppler without target	9	7.72e-04
Normalization over Doppler with target	14	9.64e-04
CFAR detection	15	5.72e-03

Table 3.7: Processing time calculated for the investigated sea clutter models. The results are generated using the same data which are used in Table 3.6. The values in bold correspond to the most time-consuming sea clutter model.

Clutter Models	Calculated processing time [s]	
	Clutter statistics estimation (12)	CFAR threshold computation (13)
K-NLLSQ	3.29e-02	8.39e-03
K-Vstat	5.69e-02	7.95e-03
K-Xstat	3.21e-03	7.87e-03
Chi-square	1.87e-02	2.71e-03
3MD	1.94e-02	4.26e-03
K-Rayleigh	**7.39e-02**	**0.35136**

The bottleneck of the proposed ship detector is the threshold computation using the K-Rayleigh distribution function as clearly can be seen in Table 3.7. This is because K-Rayleigh distribution has no closed-form solution for computing the threshold and the threshold is computed iteratively using numerical integration (cf. (3.13)).

Using Table 3.6 and Table 3.7 the total processing time needed to execute the red sub-region shown in Figure 3.1 using the K-Rayleigh-based sea clutter model (best model in near and mid ranges based on the analyses in Section 3.5.2) is approximately calculated as 0.5 s. Furthermore, the processing time required by the green region (including all the range samples) in Figure 3.1 can be calculated by multiplying the time needed by the red sub-region with the total number of red sub-regions available within the green region.

As an example, consider a typical scene size of 30 km^2 (3 km in ground range and 10 km in azimuth). With the given F-SAR system parameters, an area of 30 km^2 corresponds to approximately 260×10^3 azimuth samples ($\approx$ 106 s of total acquisition time) and 6×10^3

range samples. Keeping in mind the processing time of 0.5 s which is required for target detection in a data patch of 1280 azimuth and 512 range samples, the overall processing time needed for detecting targets in 30 km^2 ground area is approximately calculated as 20 minutes, which is nearly 11 times more than the total radar acquisition time. Note that no multiprocessing is implemented so far since this was not the focus of the PhD topic. With multiprocessing it is expected that the computation time will significantly improve as more than two processors will simultaneously be involved to process the program.

3.6 Chapter Summary

This chapter proposed a novel CFAR-based ship detection processing chain using RC airborne radar data. The major component of the proposed processing chain is the automatic training data selection approach. It includes a novel target pre-detection module used for successfully canceling the outliers, i.e., spiky clutter peaks and strong ship signals from the training data. This ensures a proper fit of suitable sea clutter models, and consequently an accurate CFAR threshold computation. A proper fit of the sea clutter models and an accurate CFAR threshold computation are essential for keeping the threshold errors and false alarm rate errors at a low level.

Various sea clutter models were thoroughly investigated in terms of threshold errors and false alarm rate ratios using the experimental single-channel RC radar data acquired with DLR's airborne sensor F-SAR during linear and circular flight tracks. Many X-band radar data with HH polarization and a range bandwidth of 384 MHz were used for these investigations. It was found that as a sea clutter model the K-distribution (regardless of any parameter estimation method) is generally not a good choice, especially not for near ($15° - 30°$ incidence angle) and mid ranges ($30° - 50°$). The chi-square and the 3MD model lead to extremely high threshold and false alarm rate errors in the near and mid ranges but perform very well in the far range ($> 50°$ incidence angle), which, for the F-SAR system, is dominated by thermal noise. In contrast, the K-Rayleigh distribution results in the smallest false alarm rate errors and threshold errors in the near and mid-ranges but were found unsuitable for the far range.

Therefore, in terms of suitable sea clutter models, it is recommended to use the K-Rayleigh distribution function for lower incidence angle ranges ($15° - 50°$) and the 3MD model or the chi-square model for higher incidence angles ($> 50°$). It has also to be pointed out that for the investigations presented in this chapter, mainly X-band radar data acquired during two F-SAR flight campaigns each lasting only a few hours have been used. During that short time frame it can be expected that the sea state has not changed significantly. Therefore, the investigation of the influence of the sea state on the sea clutter model performance cannot be made. This is an open topic for the future. Further investigations using linearly and circularly acquired radar data at different sea states are recommended. However, to the best of my knowledge, so far, such an extensive data set, which would allow for more sophisticated investigations, does not exist.

Furthermore, it has to be mentioned here that the proposed algorithm is mainly foreseen for airborne radar but not for spaceborne radar-based vessel detection. The major

reason is that the algorithm only uses a relatively small CPI for the azimuth FFT and the ship detection. This generally is too small for obtaining a sufficiently high peak SNR required for successful spaceborne-based vessel detection. In contrast, for the airborne case, a short integration time in the order of a few milliseconds, and hence, a small number of azimuth samples is sufficient for obtaining high enough peak SNR values. Therefore, for the spaceborne radars, either single-channel algorithms optimized for fully focused SAR images [100] or more sophisticated multi-channel algorithms, for instance, the powerful Extended Displaced Phase Center Antenna (EDPCA) or Inverse STAP (ISTAP) algorithms [101], should be used.

4 Motion Model and Kalman Filter in Range-Doppler

This chapter proposes a target motion model for tracking ships in the range-Doppler domain. Since ships are extended targets in high resolution data, extracted centroids of the ships are tracked using the motion model. The motion model is integrated into the framework of the Kalman Filter (KF) for fast and accurate target position and motion parameter estimation. In addition to that, the KF is also used for predicting the target position in the absence of its corresponding detection. By predicting the missed target positions in the data larger gaps in the target trajectory can be bridged and the track loss can be prevented. The robustness of the proposed range-Doppler-based target motion model is validated using real ships in real experimental RC airborne radar data acquired using DLR's F-SAR radar system.

Some parts of the results and discussions provided in this chapter I have published in the peer-reviewed journal paper [63].

4.1 Clustering

Ships are generally extended targets occupying more than a single resolution cell in high resolution data (cf. Figure 3.18). Therefore, after obtaining multiple pixel-based detections from a single ship (cf. Chapter 3), clustering is applied to group these detections as a single "physical object". For clustering, a standard DBSCAN (density-based spatial clustering of applications with noise) algorithm [102] is used. It is able to form clusters of arbitrary shape. The basic principle of the DBSCAN algorithm is illustrated in Figure 4.1.

As shown in Figure 4.1, given a set of points, the DBSCAN algorithm starts with an arbitrary point a. Point a is considered as a core point and it forms a cluster if there are at least $n_{\min}$ (minimum points) of points (including a) within a radius of ϵ_{c}. Every reachable point from point a belongs to the same cluster. For instance, point b is directly reachable from point a because it is within distance ϵ_{c} from point a. Point c is also reachable from point a via a chain of other core points. The edge of the cluster is defined by the reachable non-core points, also known as the border points. The non-reachable points are considered as outliers or noise [102]. The parameters $n_{\min}$ and ϵ_{c} are data-dependent and they are defined by the user.

4.1.1 Clustering in Range-Doppler Geometry

The distance or the radius ϵ_{c} shown in Figure 4.1 is set based on the Euclidean distance. The Euclidean distance metric can only be used when the image axes have the same unit. However, in a range-Doppler image, the y-axis corresponds to the slant range (in meters)

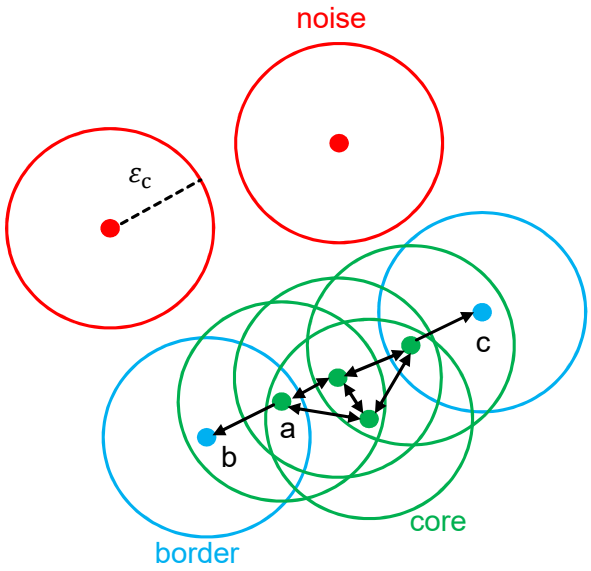

Figure 4.1: Principle of the DBSCAN algorithm. The green, blue and red points in the figure correspond to the core, border and noise points, respectively.

and the x-axis corresponds to the Doppler frequency (in Hertz). Therefore, to be able to use the Euclidean distance metric and, hence, the DBSCAN algorithm, the detected pixel dimensions are mapped to the ground geometry where both x- and y-axes have the same unit (both are in meters). For this, the slant ranges of the detected pixels are first converted to ground range using the following expression

$$r_{\mathrm{t,g}} = r_{\mathrm{t}} \sin \theta_{\mathrm{i}}, \tag{4.1}$$

where $r_{\mathrm{t,g}}$ and r_{t} are the ground range and the slant range of the target, respectively. Then, the target's Doppler frequency bins (which are spaced in Hz) are mapped to meters (= cross-range coordinates) using the approximation shown in (2.6).

After doing these necessary conversions, DBSCAN-based clustering algorithm is then implemented. After clustering, the clustered cross-range/ground-range coordinates of the ship are projected back to Doppler frequency/slant range coordinates for doing target tracking in the range-Doppler domain.

An example of the clustering applied on a real X-band HH polarized F-SAR radar data is shown in Figure 4.2(b). In the figure the clustered ship signal and its corresponding bounding box is shown. The bounding box is generated by using the nearest and farthest Doppler and range positions of the cluster with some guard zones. The user-defined clustering parameter n_{min} and ϵ_{c} in this case are chosen as 4 and 35 m, respectively. There is no automatic way to determine these parameters, however, as a rule of thumb, n_{min} is chosen as two times the data dimensionality (2 is the dimension of the data in this case) [102] and ϵ_{c} is set based on the familiarity with the data set, e.g., the expected ship size and the range resolution.

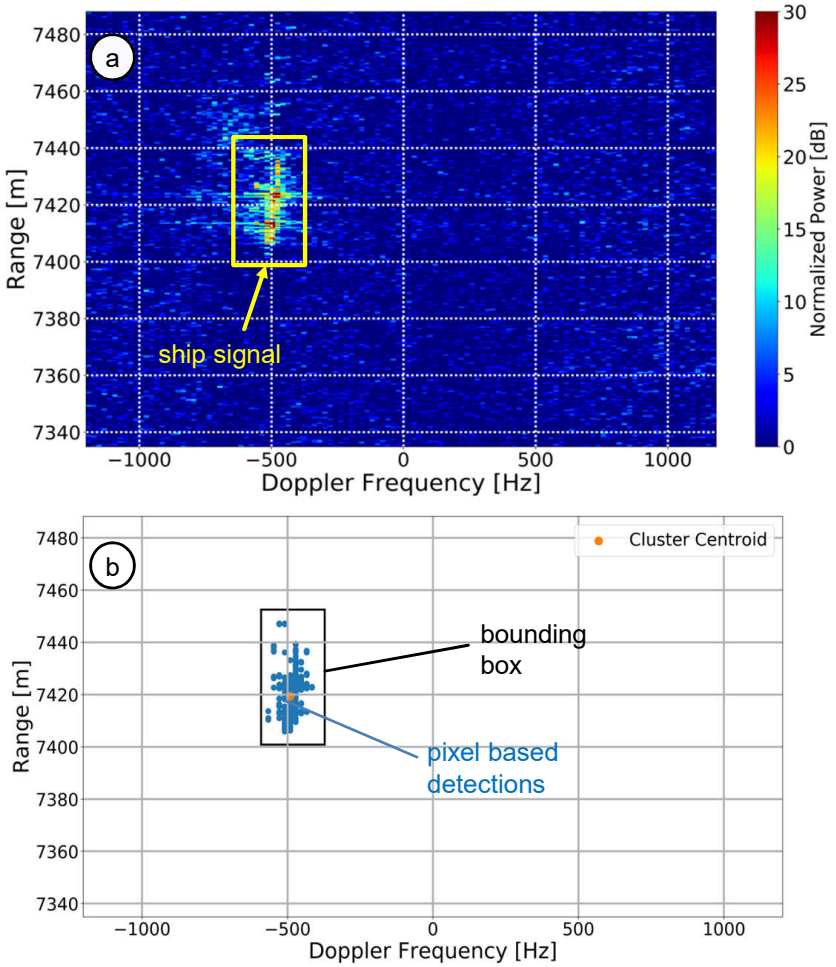

Figure 4.2: (a) Real X-band HH polarized RC F-SAR radar data in the range-Doppler domain for a specific azimuth time. The ship signal is shown within the yellow box. (b) The clustered ship signal with its centroid (orange dot) and the bounding box.

4.1.2 Cluster Center Estimation

To perform tracking the center of the clustered ship, i.e., its Doppler frequency and range position is to be estimated and tracked at successive times. For this, three different methods namely center of the bounding box (COBB), center corresponding to the maximum peak (CMP) and center of gravity (COG) have been investigated.

As an example, Figure 4.3 shows the estimated cluster range position at each azimuth time using the CMP-based method. The estimated range positions of the target are plotted together with the reference range positions. To get the reference range, first of all, the range positions are estimated at each azimuth time using all aforementioned cluster center estimation methods. The estimated positions using these methods are then averaged at each time and a higher order polynomial is fitted to the averaged range position. Such a method to get the reference range position is chosen because the single true position of an extended target in a high resolution data cannot be known accurately because of the ship dimensions.

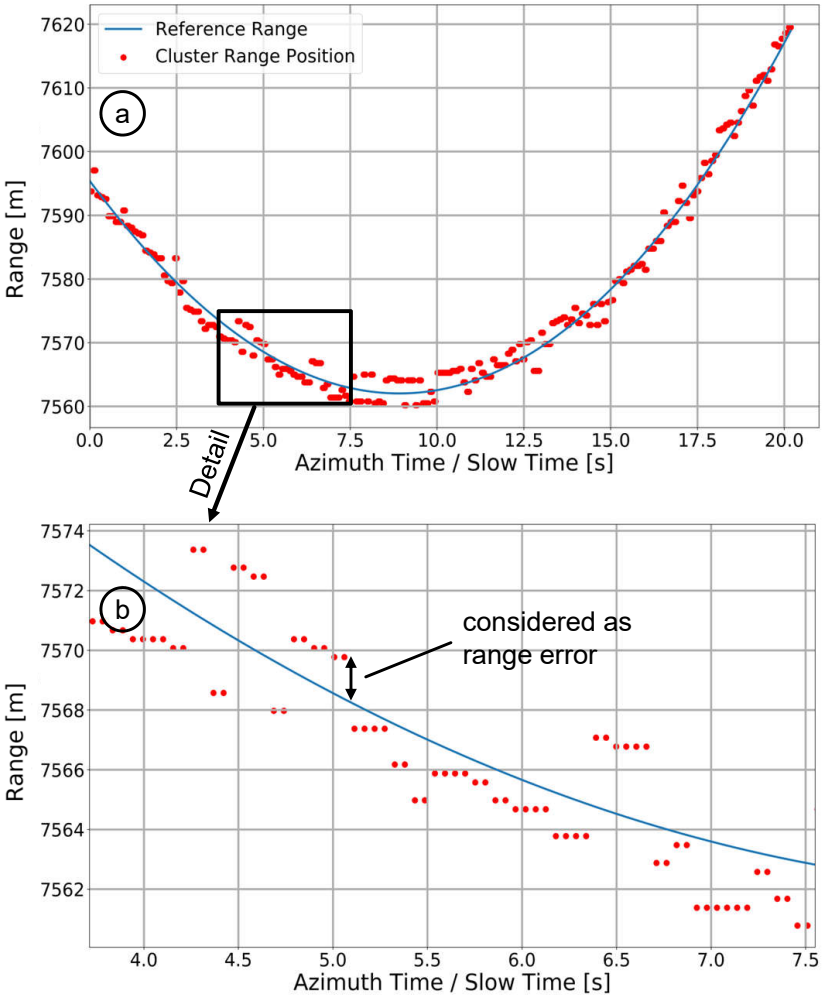

Figure 4.3: (a) CMP-based estimates of the range position (red dots) and the reference range (blue) over azimuth time of a real ship signal. The radar data for generating these results were acquired with F-SAR along a linear flight track (cf. Section B.1 in page 147). (b) Zoom in detail to highlight the error in the estimated range position.

As observed in Figure 4.3(b), the cluster range position (red dots) estimated using CMP-based method is highly unstable and deviates from the reference range (blue). The reason is the signal amplitude fluctuations over azimuth time. Therefore, it is necessary to do a performance evaluation of all three cluster center estimation methods in order to select a suitable cluster center for tracking, eg., the center that is less fluctuating and/or closest to the reference position.

Figure 4.4 shows the mean error and standard deviation plots of the cluster range positions estimated using the methods: COBB, CMP and COG. In the figure it can clearly be seen that the COG gives the minimum error followed by the COBB and the CMP. Therefore, COG is the first choice for estimating the cluster center to be used for extended target tracking. It is pointed out here that for the investigated airborne radar data and for all ships, COG was found to be more stable.

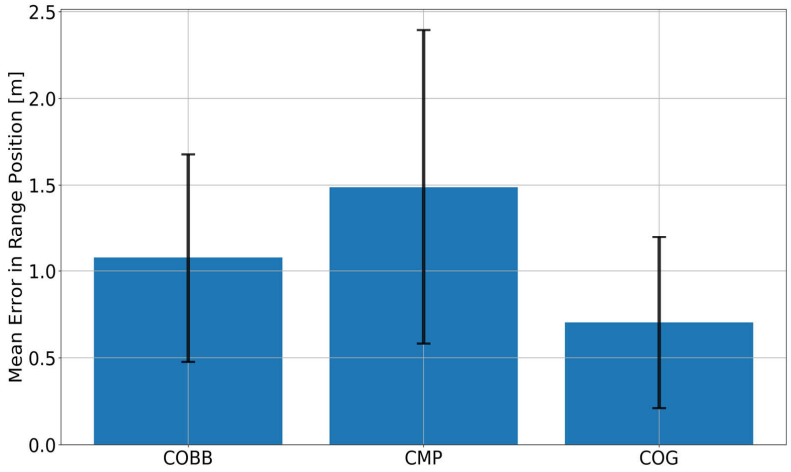

Figure 4.4: Mean error in range (blue) and standard deviation (black error bar) of the cluster range positions estimated using COBB, CMP and COG methods.

4.2 Target Motion Model and Radar Measurements

The detected ships, i.e., the cluster centers at each CPI are tracked by using a target motion model. In this section a state-space target motion model and radar measurements for tracking targets in the range-Doppler domain are described. The former is used for predicting the target position and the latter is used for updating the predicted position. Tracking can still be performed without using any motion model. This is valid only when the targets are detected at every time step and the time steps are relatively small so that the target moves not more than its size. However, without a motion model, gaps due to missing detections cannot be bridged. The ability of the motion model to fill the gaps in the detections are explained in Section 4.3.4.

4.2.1 State-Space Motion Model

For a target moving with constant acceleration (CA) on the ground, as shown in (2.8) and (2.9), its Doppler frequency and slant range positions, which are assumed to evolve in time can be modeled by (2.15) and (2.19), respectively. Due to short integration times assumption the Doppler quadratic coefficient q in these equations can be ignored and they can be rewritten as

$$f_{\mathrm{a}}(t) \approx f_{\mathrm{DC}} + k_{\mathrm{a}} t \tag{4.2}$$

and

$$r(t) \approx r_{10} - \frac{\lambda}{2} f_{\mathrm{DC}} t - \frac{\lambda}{4} k_{\mathrm{a}} t^2. \tag{4.3}$$

For simplicity (4.3) is written as

$$r(t) \approx r_{10} + u_{\mathrm{r}} t + \frac{1}{2} a_{\mathrm{r}} t^2, \tag{4.4}$$

where u_{r} and a_{r} can be considered as the initial range velocity and acceleration components of the target and have values of $-\frac{\lambda}{2} f_{\mathrm{DC}}$ and $-\frac{\lambda}{2} k_{\mathrm{a}}$, respectively.

Using (4.2) and (4.3), the target kinematics for tracking targets in range-Doppler can be expressed by the state vector $\boldsymbol{x}_{\mathrm{rd}}(t_{\mathrm{k}}) \in \mathbb{R}^n$ which is defined as

$$\boldsymbol{x}_{\mathrm{rd}}(t_{\mathrm{k}}) \triangleq [f_{\mathrm{a}}(t_{\mathrm{k}})\ \dot{f}_{\mathrm{a}}(t_{\mathrm{k}})\ r(t_{\mathrm{k}})\ \dot{r}(t_{\mathrm{k}})\ \ddot{r}(t_{\mathrm{k}})]^{\mathrm{T}} \tag{4.5}$$

where $[\cdot]^{\mathrm{T}}$ is the transpose operator, t_{k} is the absolute center time of the CPI k and the symbol $\triangleq$ is the definition sign. The estimates $f_{\mathrm{a}}(t_{\mathrm{k}})$ and $\dot{f}_{\mathrm{a}}(t_{\mathrm{k}})$ are the Doppler frequency and its first-order derivative (cf. (4.2)), and $r(t_{\mathrm{k}})$, $\dot{r}(t_{\mathrm{k}})$ and $\ddot{r}(t_{\mathrm{k}})$ are the range and its first- and second-order derivatives (cf. (4.3)), respectively.

The components of the target state vector shown in (4.5) are written as

$$\dot{f}_{\mathrm{a}}(t_{\mathrm{k}}) = k_{\mathrm{a}} \tag{4.6}$$

$$\dot{r}(t_{\mathrm{k}}) = -\frac{\lambda}{2}(f_{\mathrm{DC}} + k_{\mathrm{a}}.t_{\mathrm{k}}) \tag{4.7}$$

$$\ddot{r}(t_{\mathrm{k}}) = -\frac{\lambda}{2} k_{\mathrm{a}}. \tag{4.8}$$

To estimate the target kinematics shown in (4.5), the target's Doppler frequency and range can be approximated by CV and CA motion models (cf. (4.2) and (4.3)), respectively. For the range history, a CV-based motion model can also be used by assuming that the range is piece-wise linear between two adjacent CPIs. For this, the quadratic term in the right-hand-side of (4.3) can be ignored.

4.2.2 Radar Measurements

After defining the target motion model in range-Doppler, radar measurements for updating the target states in (4.5) are defined in this section. The received radar measurements in this case are the cluster centers, i.e., the Doppler frequencies and the range positions (cf. Section 4.1.2). The two-dimensional target measurement vector $\boldsymbol{m}(t_{\mathrm{k}}) \in \mathbb{R}^l$ is defined as

$$\boldsymbol{m}(t_{\mathrm{k}}) \triangleq [f_{\mathrm{am}}(t_{\mathrm{k}})\ r_{\mathrm{m}}(t_{\mathrm{k}})]^{\mathrm{T}}, \tag{4.9}$$

where f_{am} and r_{m} are the measured Doppler frequency and slant range position of the detected target.

4.3 Kalman Filter

The (CV+CA)-based target state space motion model and the radar measurements discussed in the previous section are incorporated within the framework of the KF. The KF is considered to be computationally fast since it uses the current measurement, the estimated state and its uncertainty from the previous time step in order to estimate the true state at the current time step.

4.3.1 Algorithm

The KF works in three stages: In the first stage, also known as the *initialization stage*, the initial state mean estimate $\hat{\boldsymbol{x}}_{\mathrm{rd}}(0|0)$ (estimate of the state at time $k = 0$ conditioned on the measurements up to time $k = 0$) and the initial posteriori error covariance $\boldsymbol{P}(0|0)$ of the state are set up. It is assumed here that $\hat{\boldsymbol{x}}_{\mathrm{rd}}(0|0)$ is the first detected position of the target, i.e., $\hat{\boldsymbol{x}}_{\mathrm{rd}}(0|0) = \boldsymbol{m}(0)$ because the true position of the target at $k = 0$ cannot be known in advance. Initialization of the error covariance matrix of the target state is explained in Section 4.3.2.

In the *prediction stage* the target states are predicted by using a motion model which is described in Section 4.2. The standard KF equations for the prediction stage are

$$\hat{\boldsymbol{x}}_{\mathrm{rd}}(k|k-1) = \boldsymbol{F}\hat{\boldsymbol{x}}_{\mathrm{rd}}(k-1|k-1) \tag{4.10}$$

$$\boldsymbol{P}(k|k-1) = \boldsymbol{F}\boldsymbol{P}(k-1|k-1)\boldsymbol{F}^{\mathrm{T}} + \boldsymbol{Q}, \tag{4.11}$$

where $\hat{\boldsymbol{x}}_{\mathrm{rd}}(k|k-1)$ is the predicted state at CPI k given all measurements up to CPI $k-1$. The matrices $\boldsymbol{P}(k|k-1)$ and $\boldsymbol{Q}$ are the $n \times n$ covariance matrices of the predicted state and the process noise, respectively. Here n is the dimension of the target state vector (cf. (4.5) where $n = 5$).

The state transition model $\boldsymbol{F}$ applied to the previous state $\hat{\boldsymbol{x}}(k-1|k-1)$ to predict $\hat{\boldsymbol{x}}_{\mathrm{rd}}(k|k-1)$ is written as

$$\boldsymbol{F} = \begin{bmatrix} 1 & T_{\mathrm{CPI}} & 0 & 0 & 0 \\ 0 & 1 & 0 & 0 & 0 \\ 0 & 0 & 0 & 1 & T_{\mathrm{CPI}} \\ 0 & 0 & 0 & 0 & 1 \end{bmatrix}, \tag{4.12}$$

where T_{CPI} is the time interval corresponding to one CPI. In the last stage, i.e., in the *correction stage*, the predicted state and the covariance matrix from (4.10) and (4.11) are corrected based on the received noisy measurements (cluster centers from (4.9)). The updated state $\hat{\boldsymbol{x}}_{\mathrm{rd}}(k|k)$ and the covariance matrix $\boldsymbol{P}(k|k)$ then becomes

$$\hat{\boldsymbol{x}}_{\mathrm{rd}}(k|k) = \hat{\boldsymbol{x}}_{\mathrm{rd}}(k|k-1) + \boldsymbol{K}(k)\boldsymbol{D}(k) \tag{4.13}$$

$$\boldsymbol{P}(k|k) = (\boldsymbol{I} - \boldsymbol{K}(k)\boldsymbol{H})\boldsymbol{P}(k|k-1), \tag{4.14}$$

where $\boldsymbol{I}$ is the identity matrix, $\boldsymbol{K}(k)$ is the Kalman gain and $\boldsymbol{D}(k)$ is the innovation (or the residual) which are expressed as

$$\boldsymbol{K}(k) = \boldsymbol{P}(k|k-1)\boldsymbol{H}^{\mathrm{T}}\boldsymbol{S}(k)^{-1} \tag{4.15}$$

$$\boldsymbol{D}(k) = \boldsymbol{m}(k) - \hat{\boldsymbol{m}}(k|k-1), \tag{4.16}$$

where $\hat{\boldsymbol{m}}(k|k-1) = \boldsymbol{H}\hat{\boldsymbol{x}}_{\mathrm{rd}}(k|k-1)$. The matrix $\boldsymbol{H}$ is the $l \times n$ observation matrix that maps the state-space to the measurement-space. Here l is the the dimension of the measurement state vector (cf. (4.9) where l=2). The matrix $\boldsymbol{S}(k)$ in (4.15), commonly known as the measurement prediction covariance matrix or innovation covariance matrix, is written as

$$\boldsymbol{S}(k) = \boldsymbol{H}\boldsymbol{P}(k|k)\boldsymbol{H}^{\mathrm{T}} + \boldsymbol{R}, \tag{4.17}$$

where $\boldsymbol{R}$ is the $l \times l$ measurement noise covariance matrix. The significance of the matrix $\boldsymbol{S}(k)$ and the innovation $\boldsymbol{D}(k)$ in terms of multi-target tracking are explained in Chapter 5.

4.3.2 Initialization of Kalman Filter Matrices

Kalman filtering requires the initialization of the $\boldsymbol{P}(0|0)$, $\boldsymbol{R}$ and $\boldsymbol{Q}$ matrices. They are set offline based on either simulated or already available real experimental data and are kept constant throughout the filtering process. This is because the online estimation of these matrices is difficult as it is not possible to observe the process that is being estimated. However, a fairly good approximation of $\boldsymbol{R}$ can be made by using the cluster centers themselves.

In the next sections some plausible initialization values of $\boldsymbol{R}$, $\boldsymbol{P}(0|0)$ and $\boldsymbol{Q}$ matrices are given. To initialize these matrices three linearly acquired real X-band HH polarized experimental RC data were investigated. Each data take had a real single controlled moving ship. The specifications of the data (e.g. wavelength, PRF etc.) are listed in Table B.1 (cf. page 150) and details about the flight experiments are given in Section B.1.1 (cf. page 148). Additional details of the radar data and the ships in the data are given in Table 4.1. It is mentioned here that these three acquisitions were found sufficient to retrieve suitable initialization parameters of the KF.

Table 4.1: Details of the real airborne radar data takes used for the initialization of KF matrices. The data were acquired using linear F-SAR flight tracks.

Data Takes	Flight Moving Direction w.r.t. Ship Motion	Ship Dimension [m]	Ship Illumination Time [s]
Data Take I	0°	66 × 11	18.3
Data Take II	45°	66 × 11	15.4
Data Take III	0°	66 × 11	19.8

Initialization of R matrix

The $\boldsymbol{R}$ matrix is a diagonal matrix that stores the variance of the deviations between the received measurements and the true measurements (cf. Table 4.2). The received measurements are the cluster centers that were computed at each CPI using the methodology shown in Section 4.1. The true measurements are assumed as the higher order polynomial fitting to the received noisy measurements. This is because the true position of the ship cannot be known precisely due to the bias caused by the ship size.

After having at each time instant the true and the received measurements from the ship, the variances are computed over azimuth. Figure 4.5 shows the standard deviation plot of the measured Doppler and range positions of the ship in data take I (cf. Table 4.1).

As shown in Figure 4.5 the uncertainties for both Doppler and range vary significantly over time. This is mainly because of the unstable estimated cluster centers. The factors that contribute to the instability of the cluster centers are the ship extents (cf. Table 4.1), their amplitude fluctuations in the data and the Doppler and range bin sizes which for the investigated F-SAR data are approximately 20 Hz and 0.3 m, respectively. In order to set the initials for the $\boldsymbol{R}$ matrix the mean standard deviations in Doppler and range are computed using the results shown in Figure 4.5. The obtained values are then squared to get the mean variances which are listed in Table 4.2 for three different data takes.

Table 4.2: Estimated $\boldsymbol{R}$ matrix for data takes I-III. First and second values of the diagonal matrix correspond to the variances in Doppler and range, respectively.

Data	Estimated $\boldsymbol{R}$ (covariance matrix)
Data Take I	diag(186,0.68)
Data Take II	diag(312.3,2.26)
Data Take III	diag(213.5,0.5)

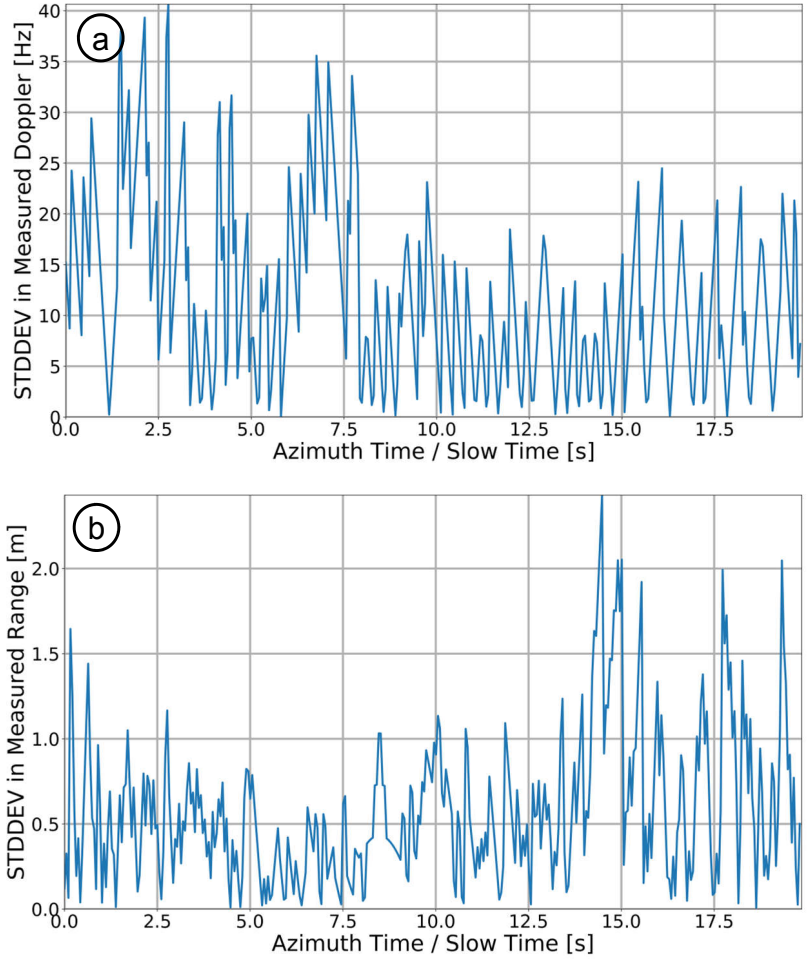

Figure 4.5: Standard deviation plots over azimuth for the (a) measured Doppler and (b) range positions of a real ship signal in data take III.

Using Table 4.2 as reference the initial values of the $\boldsymbol{R}$ matrix are set as diag(350,5). The initialization is however, data dependent and is usually recommended to be set higher as the obtained estimates.

Initialization of $\boldsymbol{P}(0|0)$ matrix

The initialization of $\boldsymbol{P}(0|0)$ is based on the knowledge about the initialization error. If it is assumed that the initial state is far from its true state, then $\boldsymbol{P}(0|0)$ should be set higher. It is also assumed that there is no information about the typical values of $\boldsymbol{P}(0|0)$ and therefore, $\boldsymbol{P}(0|0) = \sigma_{\mathrm{p0}}^2 \boldsymbol{I}_{\mathrm{n}}$. The term σ_{p0}^2 is now the only tuning parameter for $\boldsymbol{P}(0|0)$. Figure 4.6 shows how different initializations of σ_{p0}^2 affects the trajectory of a real moving ship.

In Figure 4.6 it is observed with lower initialization values (i.e., $\boldsymbol{P}(0|0) = 0.01\boldsymbol{I}_5$), the predictions are more reliable at the beginning. As a result, the cluster centers are ignored and larger errors are observed. Therefore, $\boldsymbol{P}(0|0) = 1000\boldsymbol{I}_5$ is set in order to avoid the discrepancies at the beginning of the estimation. Although it is fixed initially, with more

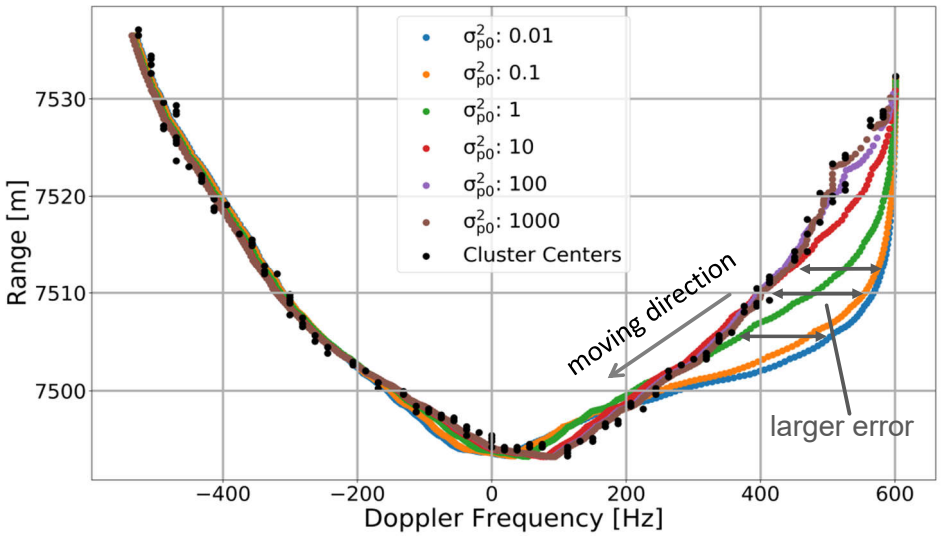

Figure 4.6: KF-based trajectory reconstruction of a real moving ship present in data take I (cf. Table 4.1). The noisy cluster centers can be seen in the figure. The ship tracks is shown in the range-Doppler domain using different initialization values of σ^2_{p0}.

successive measurements, the position estimates converge quickly and the influence of $\boldsymbol{P}(0|0)$ soon becomes negligible. This can clearly be observed in Figure 4.6 where the position estimates obtained for different initialization values of σ^2_{p0} are similar after -200 Hz Doppler frequency.

Initialization of Q matrix

The $\boldsymbol{Q}$ matrix represents the expected uncertainties in the state equations. The uncertainties are due to the modeling errors, measurement errors and the approximations made in the derivations (cf. (4.2) and (4.3)). The initialization of $\boldsymbol{Q}$ is not straightforward and is constructed intuitively. To do so, different initial values of $\boldsymbol{Q}$ are tabulated fixing $\boldsymbol{P}(0|0) = 1000\boldsymbol{I}_5$ and $\boldsymbol{R}$ (cf. Figure 4.6 and Table 4.2, respectively) and checked how their initialization affects the Doppler frequency and range position accuracies. The true state to compute the RMSE (root mean square error) in Doppler and range is again the higher order polynomial fit to the measurements (as done for Figure 4.3(a) and Figure 4.5). The results are shown in Table 4.3 where the investigations are again performed for the same three data takes listed in Table 4.1.

From Figure 4.6 and Table 4.3 it is clear that the best accuracy is achieved with a high value of $\boldsymbol{P}(0|0)$ and low value of $\boldsymbol{Q}$.

In a concluding remark for the matrix initialization of the KF, it can be said that $\boldsymbol{R}$ should be estimated offline using either simulated or already available real experimental data. The matrix $\boldsymbol{P}(0|0)$ should be set higher and $\boldsymbol{Q}$ should be set smaller. From now on, for further investigations, $\boldsymbol{R} = \mathrm{diag}(350{,}5)$, $\boldsymbol{P}(0|0) = 1000I_{\mathrm{n}}$ and $\boldsymbol{Q} = 0.01\boldsymbol{I}_{\mathrm{n}}$ are set.

Table 4.3: Doppler frequency and range RMSE assessment for different initializations of $\boldsymbol{Q}$ at $\boldsymbol{P}(0|0) = 1000\boldsymbol{I}_5$ and $\boldsymbol{R} = \text{diag}(350,5)$. The numbers in bold show the best accuracy achieved with the given combination of $\boldsymbol{Q}$.

	Data Take I		Data Take II		Data Take III	
Q	Doppler [Hz]	Range [m]	Doppler [Hz]	Range [m]	Doppler [Hz]	Range [m]
$10\boldsymbol{I}_5$	11.42	0.80	**15.39**	1.45	13.60	0.68
$\boldsymbol{I}_5$	10.40	0.78	15.79	1.40	13.31	0.63
$0.1\boldsymbol{I}_5$	9.23	0.77	17.00	1.35	**12.95**	**0.62**
$0.01\boldsymbol{I}_5$	**9.13**	**0.71**	18.62	**1.17**	12.98	0.67

4.3.3 KF Consistency Check

In this section the consistency of the KF with the given initialization parameters is analyzed. The filter consistency check ensures that the initialized KF covariance matrices have acceptable level of performance and that the KF filter has estimated the target states correctly. With the given KF matrix initializations, the consistency of the KF can be checked by:

1. Normalized (state) estimation error squared (NEES) test [103]
2. Innovation magnitude bound test [104]
3. Normalized innovation squared (NIS) test [103]

The NEES test is possible only through simulations where the filter consistency is checked after several Monte Carlo runs. This is because in reality the true states of a target cannot be known and therefore, the state errors and the actual mean squared error cannot be measured.

The last two tests are applicable for the real data since they take into account the real-world measurements through the innovation (cf. (4.16)). In other words, the performance of the KF filter can be evaluated based on whether the measurements predicted by the KF agree with the received measurements [103].

When the KF has optimal performance then according to innovation magnitude bound test (second criteria), the magnitude of the innovation is bounded by $\pm 2\sqrt{\boldsymbol{S}(k)}$. Figure 4.7 shows the innovation sequence plots of the data take I-III (cf. Table 4.1) bounded by the magnitude $\pm\sqrt{\boldsymbol{S}(k)}$ and $\pm 2\sqrt{\boldsymbol{S}(k)}$. The plots indicate the unbiasedness of the innovation sequence over time as more than 95% of the values lie within the $\pm 2\sqrt{\boldsymbol{S}(k)}$ bounds. This simple test in most cases should be sufficient however, in practice, it is important to perform the NIS test for a more robust KF performance assessment.

The NIS ϵ_{NIS} at CPI k is expressed as [103]

$$\epsilon_{\text{NIS}}(k) = \boldsymbol{D}(k)^{\text{T}} \boldsymbol{S}(k)^{-1} \boldsymbol{D}(k). \tag{4.18}$$

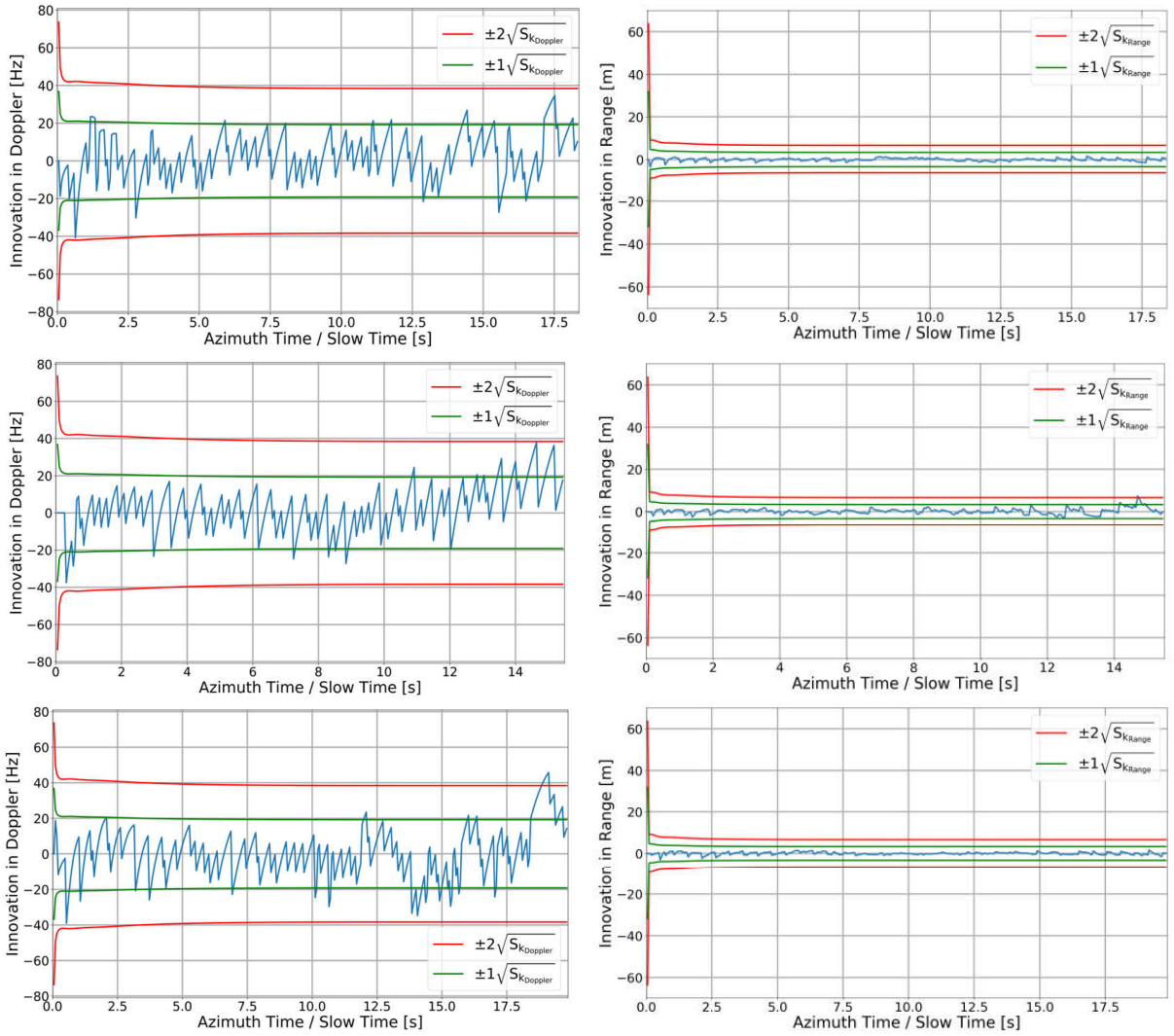

Figure 4.7: Innovation magnitude bound of target's Doppler frequency and range over azimuth time for data take I (top row), data take II (middle row) and data take III (bottom row).

Under the hypothesis H_0 that the filter assumptions are properly met then $\epsilon_{\text{NIS}}(k)$ is chi-square (χ^2) distributed with l DOF. For $l = 2$ (cf. (4.9)), the hypothesis is accepted if

$$\epsilon_{\text{NIS}}(k) \in [b_{\text{L}}, b_{\text{U}}]. \tag{4.19}$$

The interval $[b_{\text{L}}, b_{\text{U}}]$ is determined such that

$$P(\epsilon_{\text{NIS}}(k) \in [b_{\text{L}}, b_{\text{U}} | H_0]) = 1 - \alpha, \tag{4.20}$$

where b_{L} and b_{U} are the lower and upper bounds of the interval, respectively. For $\alpha = 0.05$ and two sided 95% confidence interval, b_{L} and b_{U} are 0.05 and 7.38, respectively. Figure 4.8 shows the NIS plot over azimuth time for data take I-III.

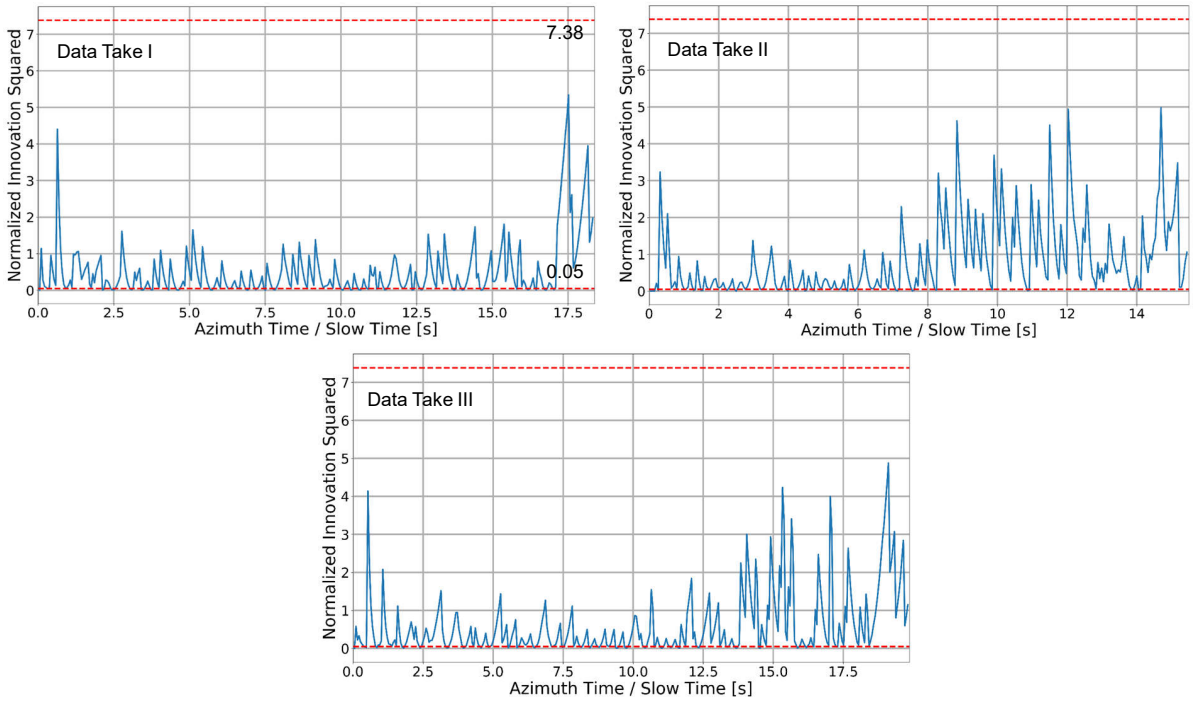

Figure 4.8: NIS plot computed over time for a real ship signal in data take I-III. The bounds are marked by the horizontal red dashed lines in the figure.

As shown in Figure 4.8 , the computed NIS is well within the given bounds (horizontal red dashed lines in the figure). Here only the upper bound is of interest because the lower bound is practically zero, i.e., $b_{\mathrm{L}} = 0.05$ and it is shown that the NIS is well below the upper bound [103]. That means for the real data with extended targets and the airborne acquisition geometry the proposed motion model and the selected initialization parameters can be used.

4.3.4 Motion Model Performance Assessment

In real scenarios it is expected that there will be missing measurements at certain azimuth times. This could be due to the lower backscatter received from the moving target or when the target is not illuminated by the antenna beam (cf. Figure 3.26(a)). In such situations the KF is able to give a predicted position (cf. (4.10)).

However, inaccurate predictions of the missed measurements may lead to a track loss. Therefore, "CV only" and (CV+CA) motion models of the KF are evaluated to assess their performance in the presence of missed measurements. In the "CV only"-based motion model, along with the Doppler, the range history is also modeled as CV by assuming it as piece-wise linear in adjacent CPIs. The (CV+CA) motion model was already presented in Section 4.2 where the target's Doppler frequency was modeled as CV and its range was modeled as CA.

For the investigations the gaps in the data were artificially introduced (cf. Figure 4.9). The gap duration was successively increased to a point after which the target track is lost. The performance achieved using the motion models are compared with the one where no

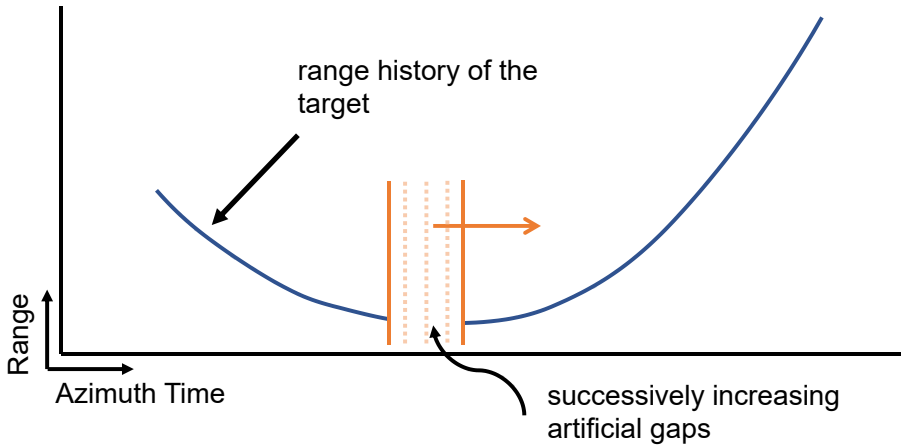

Figure 4.9: Illustration of the range history of a single moving target in range-time domain with an artificially introduced gap.

Table 4.4: Analysis of different methods in terms of time in seconds after which the target track and the position are lost. The position accuracy achieved using different methods are also shown. The numbers in bold show the best achieved accuracy. The results are from a real ship signal in X-band HH polarized F-SAR data.

Data Takes	Methods	Gap Time till Track is Lost [s]	Position Accuracy	
			Doppler RMSE [Hz]	Range RMSE [m]
Data Take I	No Motion Model	1.8	13.63	0.82
	CV Only	3.3	**9.04**	1.18
	CV+CA	**5.1**	9.13	**0.71**
Data Take II	No Motion Model	1.0	**17.67**	1.50
	CV Only	2.6	21.12	1.73
	CV+CA	**4.0**	18.62	**1.17**
Data Take III	No Motion Model	1.6	14.61	0.72
	CV Only	3.5	**9.52**	1.07
	CV+CA	**9.5**	12.98	**0.67**

motion model is considered. The results are shown in Table 4.4 again for the same three data takes (cf. Table 4.1). The position accuracy are also evaluated.

From Table 4.4 it can be said that, although, in terms of the position accuracy all methods perform similarly, the (CV+CA)-based target motion model can still be considered as a better model based on the gap duration till the track is lost (e.g., 9.5 s for data take III).

4.4 Chapter Summary

In this chapter a target motion model for tracking ships in the range-Doppler domain is proposed. Real ships in real RC airborne radar data were used for assessing the performance of the proposed motion model. The proposed motion model tracked the Doppler frequency and the slant range position of the target based on CV and CA, respectively. The motion model was incorporated within the structure of the KF for recursively predicting and updating the target positions over time. The KF requires the initialization of noise covariance matrices, a discussion on the plausible initialization of these matrices were also provided in this chapter. After setting the KF matrix initializations, the consistency of the KF was also checked based on the innovations. Filter consistency test results showed that the KF matrix initializations and the proposed motion model can be used for target state estimation purposes.

The robustness of the proposed (CV+CA)-based target motion model was also evaluated in terms of track duration where it was found that in comparison to other methods discussed in this chapter, the (CV+CA)-based motion model could maintain the target track for the longest time in the absence of target detections.

5 Ship Tracking using Single-Channel Range-Compressed Data

In this chapter a range-Doppler-based multi-target tracking (MTT) algorithm using single-channel RC radar data is proposed. The proposed tracking algorithm is suitable for dense multi-target scenarios. A powerful track management system is also developed which runs simultaneously within the tracker for updating the confirmed target tracks and for recognizing and terminating false or ghost targets. An additional challenge associated with MTT in the range-Doppler domain is the Doppler aliasing (or back-folding) effect. In this chapter the aliasing problem is briefly discussed with real experimental results. To validate the proposed range-Doppler-based MTT algorithm, results from both simulated and real linearly and circularly acquired experimental data from DLR's airborne radar sensor F-SAR are presented.

Parts of the methodology and the results presented in this chapter I have published in the peer-reviewed journal paper [63] and in the conference papers [105, 106].

5.1 Principle of the Algorithm

A complete MTT algorithm typically has two major parts. The first part contains the target motion and measurement model that aims to estimate the target kinematics over time. The second part of the MTT algorithm is data association where newly available measurements are assigned to already existing target tracks for reconstructing the trajectories of individual targets. The former is described in detail in Chapter 4 and the later is presented in this chapter.

Similar to the detection, MTT is also performed in the range-Doppler domain. Tracking in range-Doppler has the benefit that the target signals overlapping in time domain are in most cases separated in the Doppler domain, if they are for instance, not located in the same resolution cell or moving with different LOS velocities. For the latter case an example is shown in Figure 2.9 where different LOS velocities of the targets shift them to different Doppler frequencies.

The target tracks in range-Doppler domain are needed for:

- Mapping the detections accurately on the ground after computing additionally the DOA angle of the target. The ground tracks can later be compared with the AIS data for validation purposes (cf. Chapter 6), and

- Generating high resolution ISAR image sequences after successively extracting all the required ship data (cf. Figure 5.17(c)), which later on aid to target recognition and identification [107–109].

Therefore, tracking in range-Doppler is indispensable and a pre-requisite for the aforementioned applications.

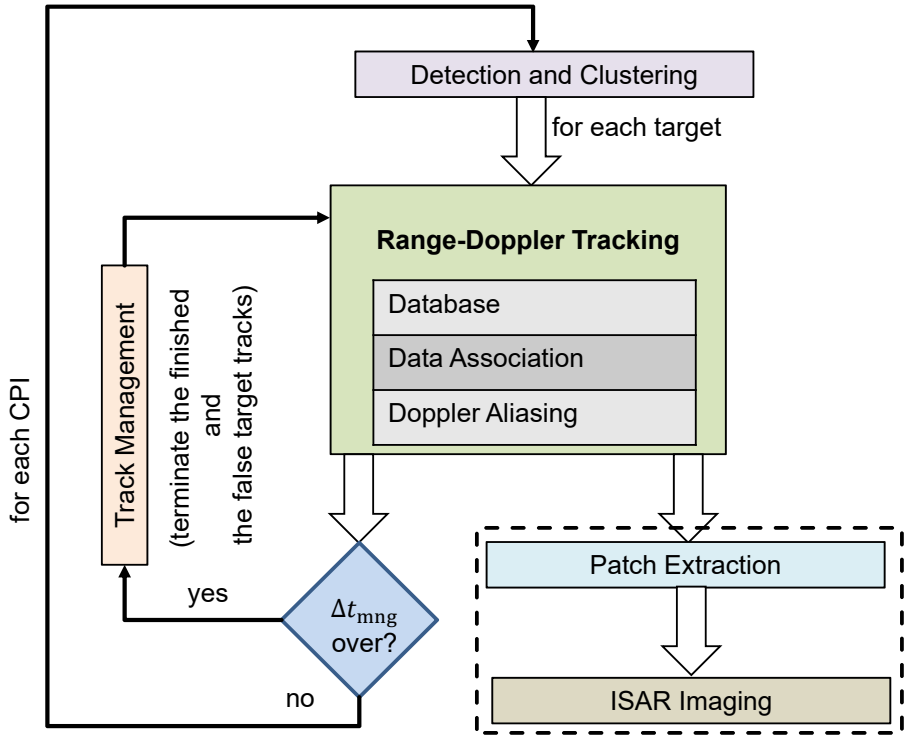

Figure 5.1: Simplified processing flowchart of the proposed MTT algorithm. The components of the tracker are shown within the range-Doppler tracking block. The dashed black rectangular block in the figure is important for ISAR imaging but not needed for tracking.

The simplified processing steps of the proposed multi-target tracker are shown in Figure 5.1. The MTT methodology can be summarized as:

1. Estimate the cluster center positions for each target (cf. Section 4.1.2).
2. Store the target position and its related motion parameters in a database (cf. Section 5.2).
3. Associate the targets to already existing tracks for MTT or generate new tracks (cf. Section 5.3).
4. Run track management after every Δt_{mng} seconds for updating the tracks (cf. Section 5.4.1).

5. Monitor also the Doppler frequency history of the target for taking into account the Doppler aliasing (cf. Section 5.4.2).

Details related to each processing block shown in Figure 5.1 are sequentially presented in the following sections.

5.2 SQLite Database Structure

A SQLite database structure was developed for storing the detection and clustering results and for doing MTT. SQLite is a self-contained, serverless and portable SQL (Structured Query Language) database engine with the disadvantage of supporting only a single writing process at a time. For writing several processes at a time, server-based databases such as MySQL and MariaDB are generally preferred [110]. The SQLite database tables can be extracted with low efforts if required in future.

The SQLite database has a table where each row of the table represents a detected target at each CPI. The column contains among others the target motion parameters. An example of a database table is shown in Figure 5.2. Additional details about the database table are given in Appendix A.

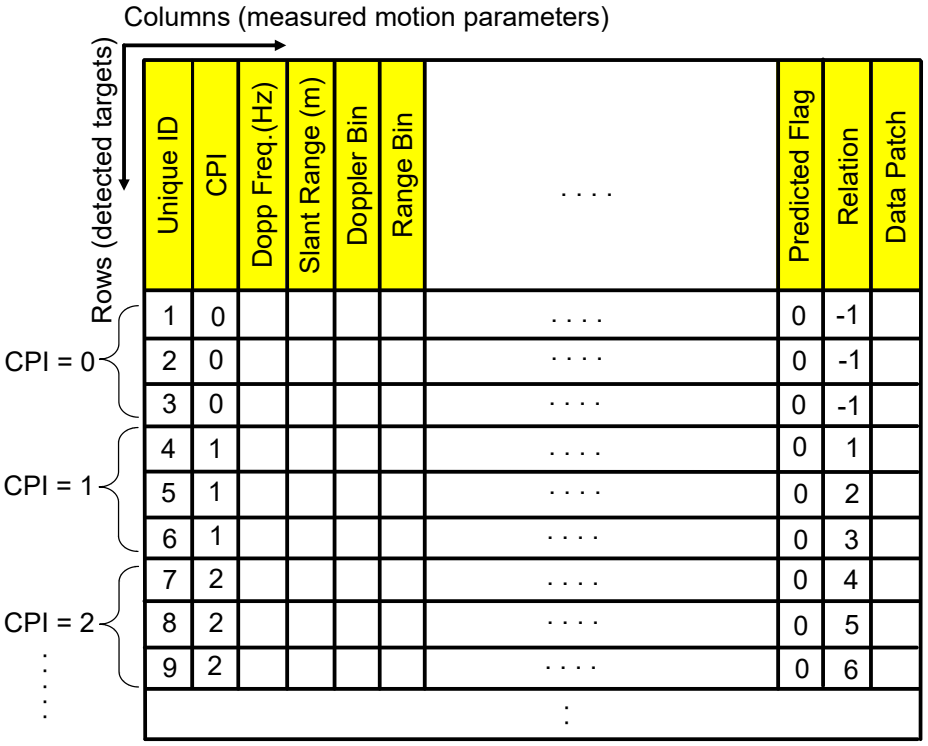

Figure 5.2: Simplified representation of a database table. The detected targets (along the rows) and their relevant motion parameters (along the columns) are shown in the table.

The table in Figure 5.2 shows that three exemplary targets were detected at CPI = 0. These targets are stored in the database and have their unique IDs (= unique row num-

bers) which increment automatically with subsequent detections in the following CPIs. The database is designed for storing and tracking an arbitrary number of targets, limited only by the available memory and the SQLite limitations. Other relevant parameters such as the positions and extents of the targets and the data patches belonging to the targets for ISAR imaging are also stored (dashed rectangular block in Figure 5.1). The table also has additional columns like a relation and a predicted flag (PF). Their importance and need are explained in later sections.

5.3 Relation Generation

For tracking multiple targets it is essential to establish a relation between the detected targets at a given CPI and the already existing tracks from the previous CPI. Figure 5.3 shows an example of the concept of relation generation using a database structure for tracking three consecutively detected targets.

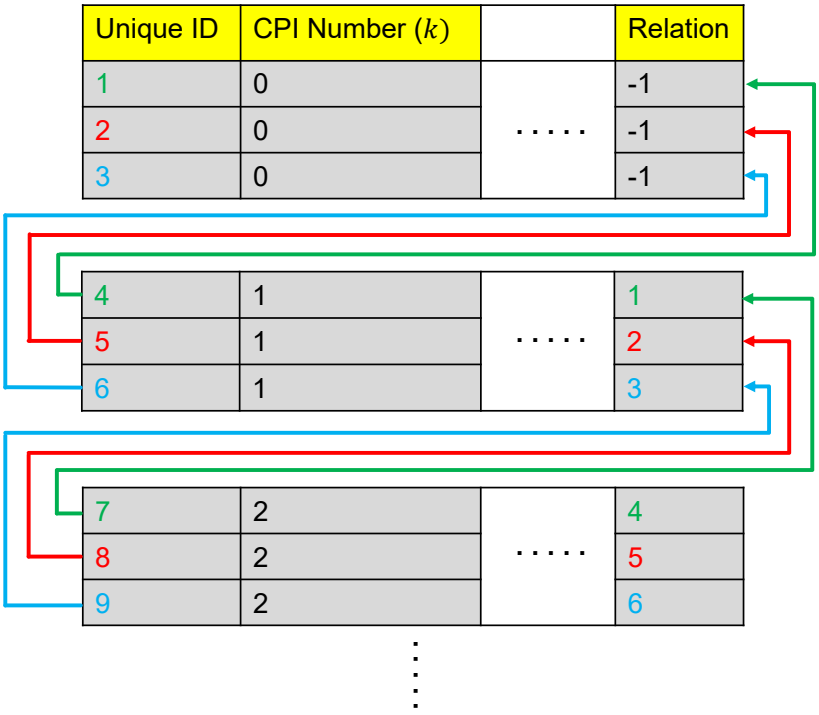

Figure 5.3: Principle of the relation generation using database. Arrows of the same color indicate the link between the unique IDs for one target detected at each CPI. In the relation field the unique ID of the previous detection belonging to the same track is listed.

In Figure 5.3 there are three detected targets at CPI=0. These targets are assigned to unique IDs. The unique IDs are the row numbers of the database table and for a newly added row it is incremented automatically.

If the same three targets are detected in the next CPI the unique IDs are again generated (i.e., new rows are added into the database). The relation columns of these

newly added rows are now updated with the unique IDs of the same targets from the previous CPI (see the relation columns at CPI = 1 and the Unique ID column at CPI = 0 in Figure 5.3). After the tracking is over a link between the unique rows belonging to the same target is established (arrows of the same color in Figure 5.3). For instance, in the figure it is shown that unique IDs 7-4-1 (green arrow) belong to the same target and likewise for the other two targets. A relation of -1 indicates that the target is detected for the first time and has no relation with any previously existing tracks.

5.3.1 Target-to-Track Association

In the previous section it was shown that unique row numbers belonging to the same target at different CPIs are linked to create the target tracks. Generating such links is possible only when the target detections at a current CPI are associated with the already established tracks from the previous CPI. In tracking literature this is known as data association. The concept of data association in the range-Doppler domain for a single target tracking is shown in Figure 5.4.

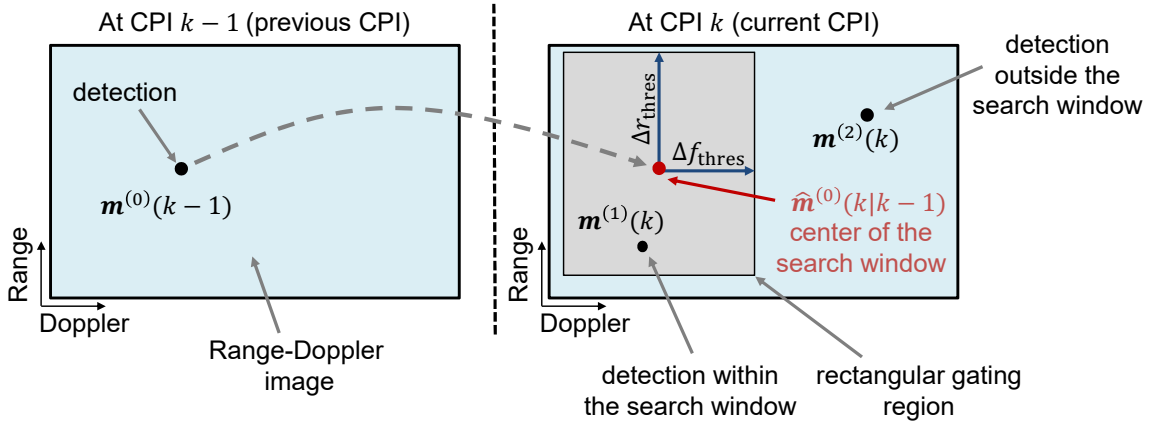

Figure 5.4: Illustration of the data association concept in the range-Doppler domain. The rectangular gate (gray color) in the current CPI is centered at the predicted measurement. Detections in the previous and current CPIs are marked in the figure as black dots.

In Figure 5.4 at CPI $k-1$ (previous CPI) only one measurement is found which is denoted as $\boldsymbol{m}^{(0)}(k-1)$. The track is initialized for this target and the motion parameters are stored into the database. At CPI k (current CPI) two measurements are observed ($\boldsymbol{m}^{(1)}(k)$ and $\boldsymbol{m}^{(2)}(k)$ in Figure 5.4). Data association is now performed as a two-step procedure. First, the position of the previously detected target is predicted at the current CPI. The position $\hat{\boldsymbol{m}}^{(0)}(k|k-1)$ (brown dot in the figure) is the KF-based predicted measurement of $\boldsymbol{m}^{(0)}(k-1)$ (cf. (4.16)). Second, a validation region centered around the predicted measurement (which is now an established track) is created. This is done in order to eliminate unlikely observation-to-track pairings. Detections falling within the gate of the track are considered for updating the track (cf. Figure 5.4 where $\boldsymbol{m}^{(1)}(k)$ lies in the gating region of $\hat{\boldsymbol{m}}^{(0)}(k|k-1)$). Detections lying outside the gate ($\boldsymbol{m}^{(2)}(k)$ in this

case) could either be a false target or a new target. The tracker will initiate a new track for such cases.

The gating concept illustrated in Figure 5.4 also works for MTT by creating the rectangular gate around individual target track. However, in MTT, when there is measurement uncertainty, i.e, when more than one measurement lie inside the gating region of a given track, measurement-to-track association is required. For this, a method is presented in Section 5.3.4.

5.3.2 Rectangular 1-Norm Gating

The rectangular gating shown in Figure 5.4 which is used for associating the radar-based measurement to an exiting track is mathematically expressed as

$$|m^{f_\mathrm{a}}(k) - \hat{m}^{f_\mathrm{a}}(k|k-1)| < \Delta f_\mathrm{thres} \tag{5.1}$$

$$|m^{r}(k) - \hat{m}^{r}(k|k-1)| < \Delta r_\mathrm{thres} \tag{5.2}$$

where $|m^{f_\mathrm{a}}(k) - \hat{m}^{f_\mathrm{a}}(k|k-1)|$ is the offset between the detected and predicted Doppler frequency and $|m^{r}(k) - \hat{m}^{r}(k|k-1)|$ is the offset between the detected and predicted range (cf. (4.16)). The terms Δf_thres and Δr_thres are the width (along Doppler) and the length (along range) of the rectangular region, respectively.

From Figure 5.4, (5.1) and (5.2), it is clear that the extents of the rectangular search window have to be first determined for associating detections to their corresponding target tracks. Before determining the extents of the rectangular gate, it is first necessary to investigate how the offsets shown in the left-hand-side of (5.1) and (5.2) vary in reality so that reasonable values of gate extents can be set. These offsets are obtained directly from one of the KF equations shown in (4.16). In the equation the disparity between the received measurement and the predicted measurement is clearly reflected. An example of these offsets (also known as innovations) estimated for a real moving ship in data take III (cf. Table 4.1) is shown over azimuth time in Figure 5.5.

From Figure 5.5 the maximum observed offsets in Doppler and range are approximately 40 Hz and 4 m, respectively. Moreover, these offsets also vary significantly over time. The factors that cause such variations were already explained in Section 4.3.2. For the relation generation the size of the rectangular window must be larger than these estimated offsets. A wise choice for the extents of the search window can be set three times the maximum offsets. This will prevent the track loss even if the maximum offsets are a bit larger than what is observed in Figure 5.5.

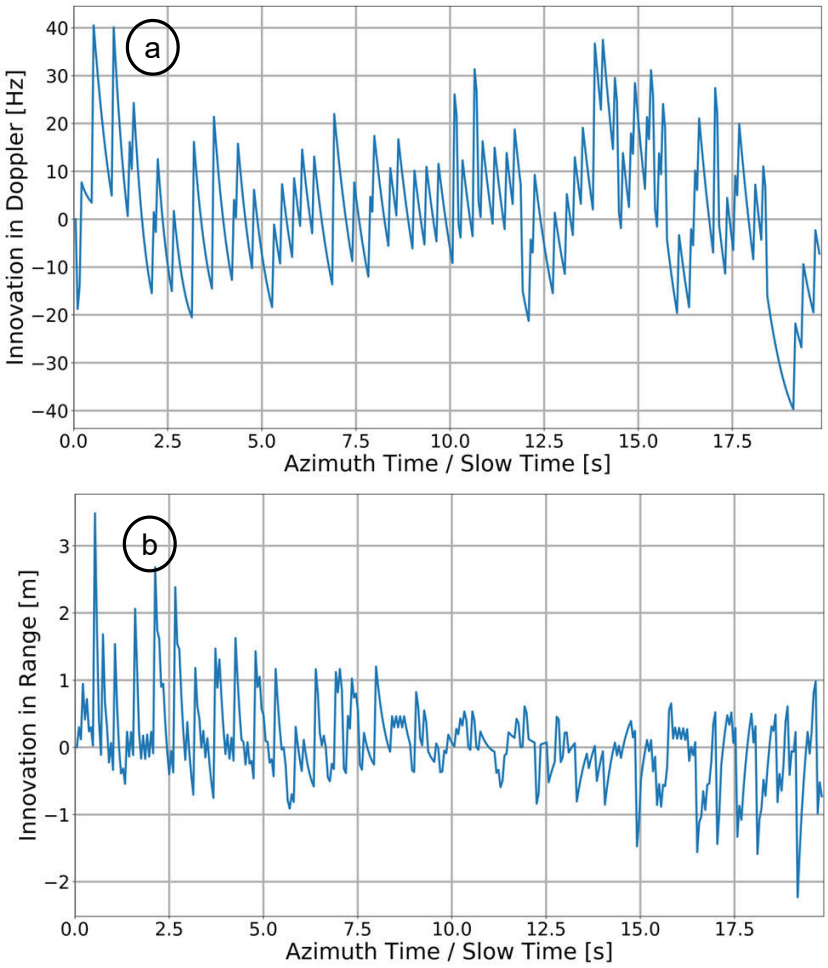

Figure 5.5: Residuals (or Innovations) computed using (4.16) for (a) Doppler frequency and (b) range positions of a real moving ship.

5.3.3 Measurement Uncertainty

There are situations, especially in dense scenarios with numerous ships anchoring or moving close together, when multiple measurements may fall within the gate of a single track causing measurement uncertainty. Two popular algorithms that are used for resolving such uncertainties and which are applied in the real-world problems are GNN (global nearest neighbor) [111] and JPDAF (joint probabilistic data association filter) [20].

Given a set of measurements and tracks, both GNN and JPDAF first compute the Mahalanobis distances [112] between the track and the measurements and compare them to a gating threshold to select the candidate measurements for each track. GNN then uses the Hungarian algorithm [113] for assigning the most likely measurements to the existing tracks [111]. JPDAF on the other hand, uses all the measurements within the validation region of the track and evaluates the measurement-to-track association probabilities and combine them to update the target state and covariance [114, 115]. For tracking an unknown number of targets, it is advisable to use a separate track management logic along with GNN and JPDAF [116]. The reasons for not using the state-of-the art methods like JPDAF in this thesis can be summarized as:

- JPDAF has been designed keeping in mind the dense multitarget scenarios where multiple targets are overlapping on the ground in the presence of heavily cluttered environment. In the multitarget tracking approach, which is proposed in this doctoral thesis, tracking is performed in the range-Doppler domain. In Doppler domain target overlapping is highly unlikely, as shown in Figure 2.9. Therefore, it is not really beneficial to use sophisticated and computation time intense tracking algorithms such as JPDAF in order to track targets in the range-Doppler domain where the targets are generally well-separated.
- With the increasing number of targets and measurement uncertainties, the computation time of JPDAF also increases. This happens because the JPDAF calculates the association probabilities between all available target tracks and all validated measurements in a single CPI. Afterwards, the target states and covariance for individual tracks are calculated taking into account these estimated probabilities which further increases the overall computation time.

5.3.4 Proposed Data Association Method

A rather simple but fast and efficient data association approach is presented in this section. The methodology is shown in Figure 5.6. To explain the method an example is shown in Figure 5.7.

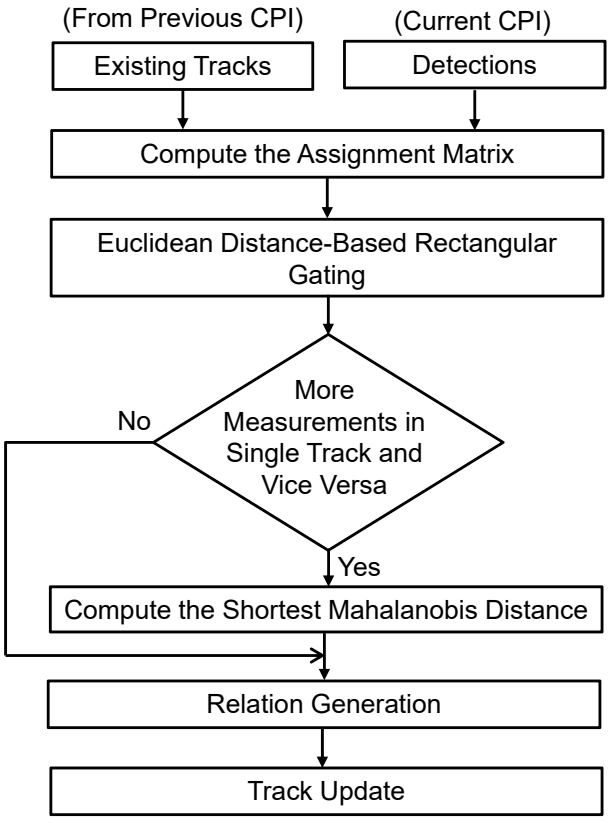

Figure 5.6: Data association methodology adopted in the range-Doppler domain when several detections belongs to a single track or vice versa.

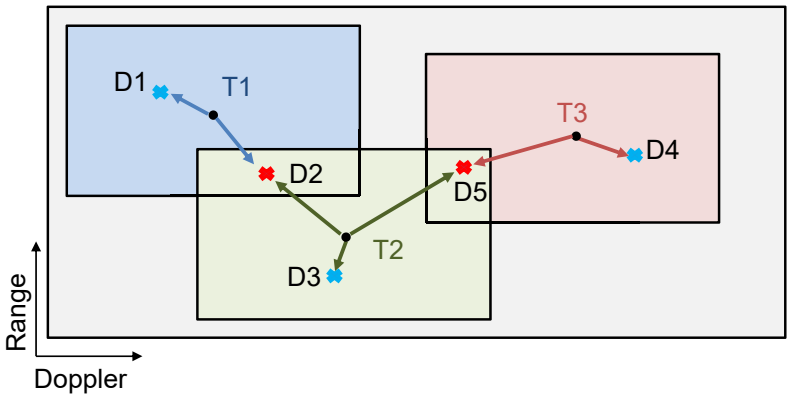

Figure 5.7: Case when more than one measurement falls within the rectangular gating region of an established track and vice versa. Arrows indicate the distances between the center of the rectangular gate and the measurements falling within the validation region of each track.

In Figure 5.7 at a given CPI, there are three established tracks (T1-T3) (predicted measurements from the previous CPI) and five detections (D1-D5). Detections D1 and D2 fall within T1, D2, D3 and D5 within T2, and D4 and D5 within T3.

As shown in Figure 5.6 to solve the measurement uncertainty an assignment matrix is initially computed by providing the number of tracks and detections. The elements of the assignment matrix are the Euclidean distance offsets between the existing tracks and the available detections. The assignment matrix is computed separately for Doppler and range because both are measured in different units. Based on the knowledge on Doppler and range bin sizes a rectangular gating region around each track for selecting potential target-originated measurements is created (cf. Figure 5.4, (5.1) and (5.2)).

After applying the gating if there are more than one candidate measurement of a confirmed track (cf. Figure 5.7 where there are three detections within the validation region of track T2), the Mahalanobis distances only between the track and its validated measurements are then computed (cf. Figure 5.8(b)). The Mahalanobis distance is used because the dimensions are not equally weighted. To estimate the Mahalanobis distance covariance matrix is required which in this case is the covariance of the innovation vector $\boldsymbol{D}(k)$ (cf. $\boldsymbol{S}(k)$ in (4.17)).

Assume that in a CPI there are N_{vm} number of validated measurements lying within the rectangular validation region of a particular track. The Mahalanobis distances $\{d_{\text{Mi}}\}_{n=1}^{N_{\text{vm}}}$ between the track and its validated measurements is calculated. The measurement corresponding to the minimum Mahalanobis distance is considered for the track update. For a given track the minimum Mahalanobis distance d_{min} can be mathematically expressed as

$$d_{\text{min}} = \min(\{d_{\text{Mi}}\}_{n=1}^{N_{\text{vm}}}), \tag{5.3}$$

where d_{M} is the Mahalanobis distance which is written as

$$\{d_{\mathrm{Mi}}\}_{n=1}^{N_{\mathrm{vm}}} = (\{\boldsymbol{D}(k)\}_{n=1}^{N_{\mathrm{vm}}})^T \boldsymbol{S}(k)^{-1} \{\boldsymbol{D}(k)\}_{n=1}^{N_{\mathrm{vm}}}, \tag{5.4}$$

where the terms $\boldsymbol{D}(k)$ and $\boldsymbol{S}(k)$ are shown in (4.16) and (4.17), respectively. An example to resolve the measurement uncertainty is shown in Figure 5.8 which is specifically solved for the situation illustrated in Figure 5.7.

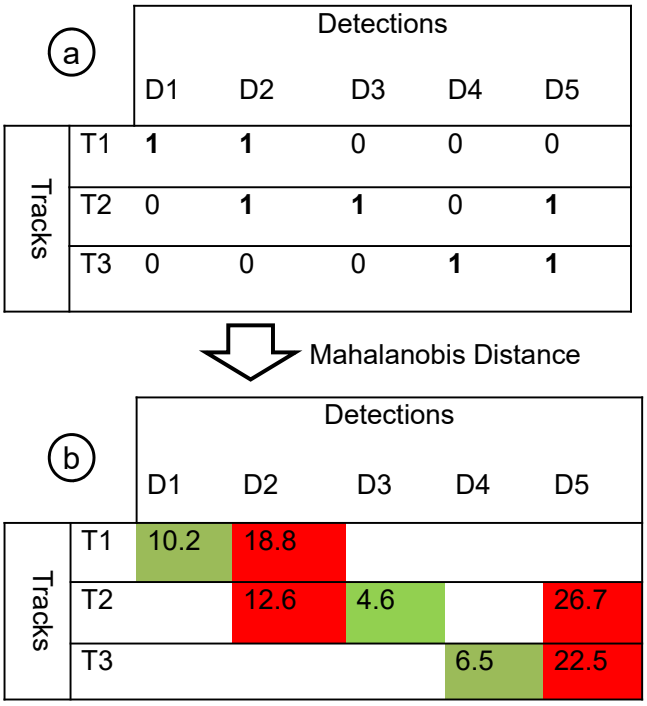

Figure 5.8: Illustration of the measurement uncertainty situation corresponding to Figure 5.7. (a) Binary matrix computed after applying rectangular gating. Bold values in the matrix show that more than one detection is in the gating region of each track (see also Figure 5.7). (b) Mahalanobis distances measured only between the track and its validated measurements. Detections assigned to their respective tracks (shortest Mahalanobis distance) are highlighted in green and the unassigned detections are highlighted in red.

As shown in Figure 5.8(b), after using (5.3), the detections D1, D3 and D4 are assigned to tracks T1, T2 and T3, respectively. The unassociated detections D2 and D5 initiate their own new tracks. This method of data association works well for all the investigated airborne radar data.

5.4 Track Handling

The approaches discussed so far in this chapter are mandatory for doing multitarget tracking. However, during tracking, several false targets either from the sea clutter or from the true target itself might appear in the scene which needs to be handled in order

to control or reduce the number of false tracks and maintain the continuity of true target tracks. This section addresses these problems in detail using both simulated and real experimental radar data with real targets.

5.4.1 Track Management

Every unassigned detection initiates a tentative track. If the detection belongs to a real target then the target is expected to be detected in several subsequent CPIs. Such a track then becomes a confirmed track. Once the target moves out of the antenna beam it is no longer detected and therefore, should be terminated. Also, if there exist some false targets (or clutter), they should also be terminated as they are not originated from real targets. To do this, a track management scheme is employed for updating the confirmed tracks and also for terminating the finished tracks and false targets [117].

The concept of the track management is illustrated in Figure 5.9. Track management runs periodically within the tracker. For the F-SAR radar data, it is run after, e.g., every 2 s (can be defined by the user) which corresponds to approximately 40 CPIs as per the current F-SAR system configuration (cf. Table B.1 in page 150).

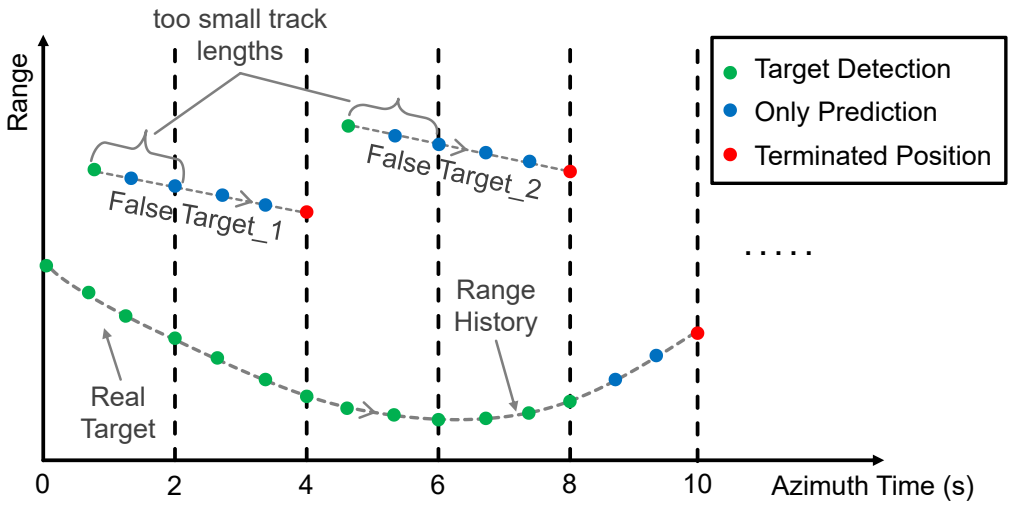

Figure 5.9: Schematic representation of track management when real and false targets are present in the scene. Green dots are target detections and blue dots are "only predictions". The predictions are given by the KF. Terminated target positions are marked by the red dots.

As an example, in Figure 5.9, there are three targets. One of them is a real target and the others are false targets. Each target initiates its own track in its very first detection (given by the green dots). A value of "zero" is then assigned in the predicted flag (PF) column (cf. Figure 5.2) of each target which implies that these are detected targets. In the next time step, only the real target is detected and the rest are not detected. In the absence of the detection, the target position is predicted by the KF (given by the blue

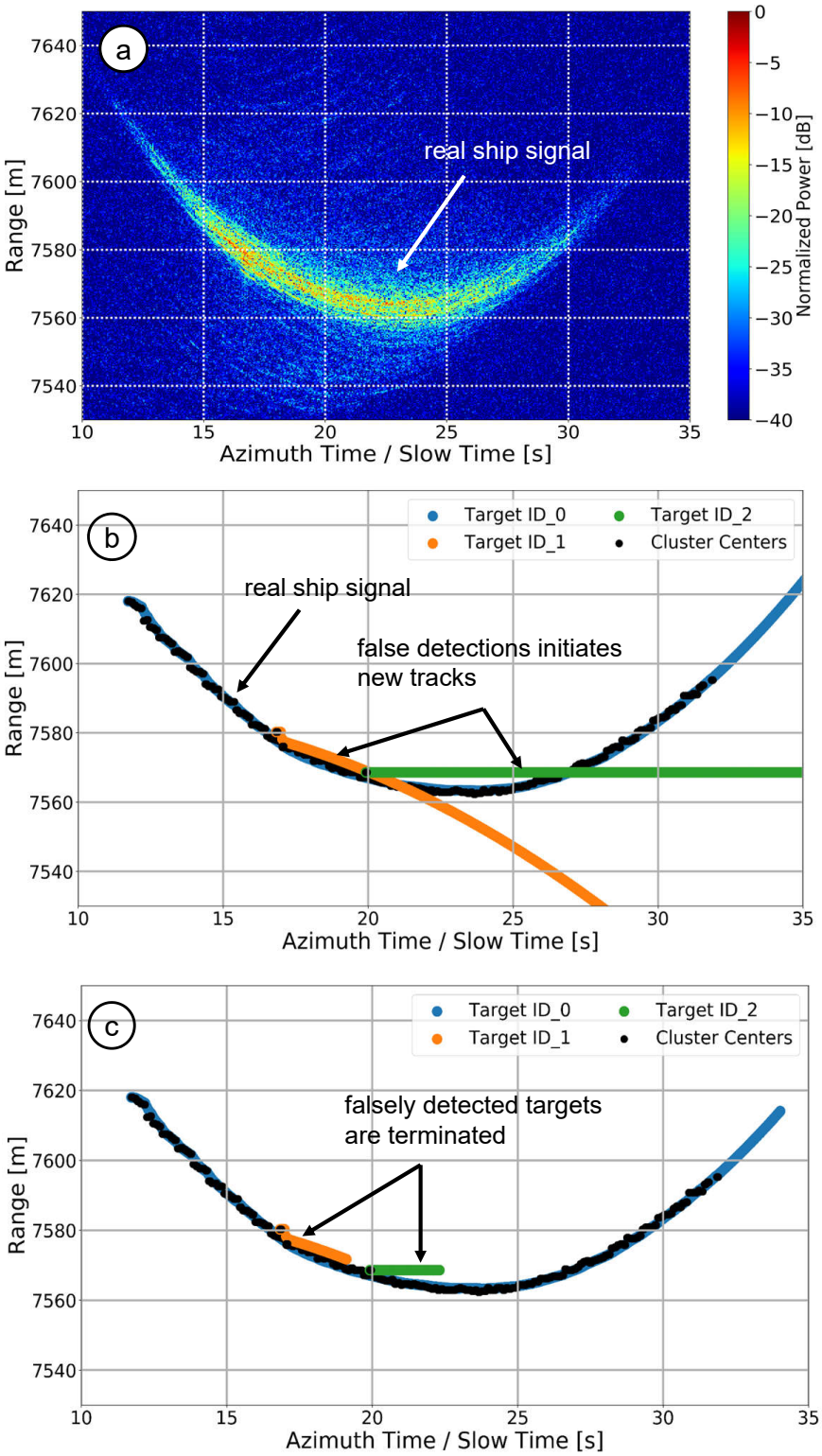

Figure 5.10: (a) Real single moving ship in X-band F-SAR radar data. Tracking results (b) without and (c) with track management. Target ID_0 is the trajectory of the real ship. The real ship and the false targets are marked in the figure. For visualization purposes, the tracks are shown in time domain rather than in range-Doppler where the detection and tracking were actually carried out.

dots). For the predicted measurement a value of "one" is now assigned in its PF column. As the tracking continues, at CPI = 40 (i.e., nearly after 2 s), the individual target tracks

are extracted and their track lengths are determined. As shown in the figure each target should at least be tracked for 2 s. This is because the observation time of less than 2 s is too small to terminate the targets (see false targets in Figure 5.9). For the tracks that are equal to 2 s, their prediction percentage (PP) are estimated using

$$\mathrm{PP}(\%) = \frac{N_{\mathrm{pred}} \times 100}{N_{\mathrm{L}}}, \tag{5.5}$$

where for each extracted track, N_{pred} is the total number of CPIs in which the target is only predicted and N_{L} is the total extracted track length, i.e., 40 CPIs (= 2 s) in the shown example. The PP threshold is set to 70% which means that the targets that are "only predicted" for more than 70% of the time without having their corresponding detections are terminated. In the figure the real target is also terminated after 10 s (it was last observed at 8 s).

An example of tracking a single real ship target in data take III (cf. Table 4.1) in the presence of false targets and with and without using track management is shown in Figure 5.10. As shown in the figure Target ID_0 belongs to a real ship target, whereas Target ID_1 and Target ID_2 are the false targets, which are also termed as "ghost targets". With track management it was possible to terminate such target tracks after a short time.

5.4.2 Doppler Aliasing

Another major challenge while tracking targets in the range-Doppler domain is to handle the Doppler aliasing. It is a special condition that occurs mainly when the Doppler shift of the target is larger than the PRF limit of the radar system [118–120]. Larger Doppler shifts of the target are the consequences of either squinted radar acquisition geometry or its high radial velocity (cf. (2.14)). The maximum unambiguous radial velocity $v_{\mathrm{r,max}}$ of the target in the non-squinted case depends on the PRF and can be written as

$$v_{\mathrm{r,max}} = \frac{\lambda \cdot \mathrm{PRF}}{2}. \tag{5.6}$$

When the target's radial velocity is larger than $v_{\mathrm{r,max}}$, the target appears back-folded (or aliased) in Doppler domain.

To illustrate the aliasing effect an exemplary range history of a single moving target in the range-Doppler plane is shown in Figure 5.11. The target track has already been initialized (cf. CPI k_0 in Figure 5.11) and the detections are tracked in subsequent CPIs. At CPI = k_{als}, the KF predicts the Doppler frequency that is smaller than -PRF/2. The target detection to be used to assign to this track is found approximately one PRF apart and nearly at the same range (aliased detection). This is because the target's Doppler frequency shifts that are smaller than -PRF/2 are back-folded and detected from PRF/2 onward. As a result, the tracker initiates a new track for the aliased detection (cf. orange

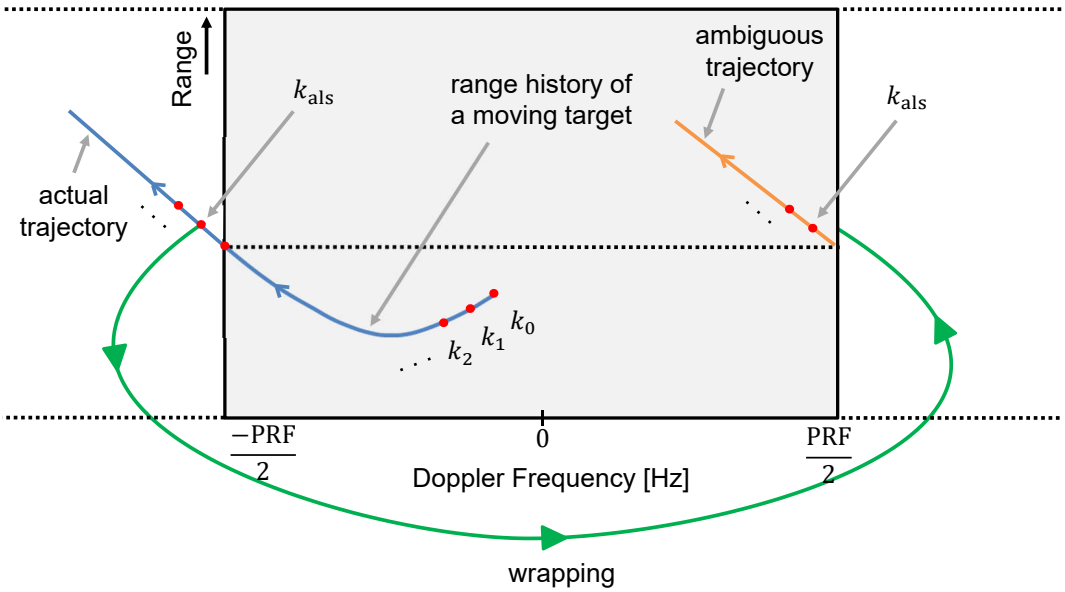

Figure 5.11: Illustration of the Doppler aliasing effect of a single target. In the figure the actual and the ambiguous range histories belonging to the same target are shown in blue and orange colors, respectively. Red dots indicate the CPIs.

curve in Figure 5.11). In reality however, there is only one target in the scene (complete blue curve in Figure 5.11).

To further understand the aliasing problem, a real moving ship signal in real X-band F-SAR radar data is shown in Figure 5.12. The target is moving towards -PRF/2. For demonstration purposes, the data are sub-sampled to a PRF of approximately 800 Hz.

In Figure 5.12(a), the center position of the real ship is at around -180 Hz. After tracking the ship for some CPIs, the same ship appears simultaneously at both ends of the PRF limits (cf. Figure 5.12(b)). This is due to the ship motion which causes a smear along Doppler and the extended nature of the ship in high resolution data. Depending on the ship size, the situation shown in Figure 5.12(b) can occur in multiple consecutive CPIs. Finally, in Figure 5.12(c) the ship is completely aliased and appears roughly at around 250 Hz and continues to move further. The goal is to recognize the back-folding occurring in Doppler in order to extract the unambiguous target range and Doppler history without wrapping effects.

For resolving the Doppler aliasing the Doppler frequency of the aliased detection must be updated during tracking or track management. If the target is moving towards -PRF/2 and the aliased (or the backfolded) detection occurred in the right as shown in Figure 5.11 and Figure 5.12(b)(c), then from the Doppler frequency of the aliased detection one PRF interval has to be subtracted. If the target is moving towards PRF/2, which practically does not occur if the aircraft velocity is much higher than the target velocity, one PRF interval has to be added. By doing this a new track initiation from the aliased target can be avoided and a single unambiguous target track in range-Doppler can be extracted.

Figure 5.13 shows the real single ship trajectory reconstruction before and after solving the aliasing problem. The PRF used in this case is approximately 1.2 kHz. In Figure 5.13(a) after tracking the ship for nearly 1 s it is found aliased. That is why in Figure

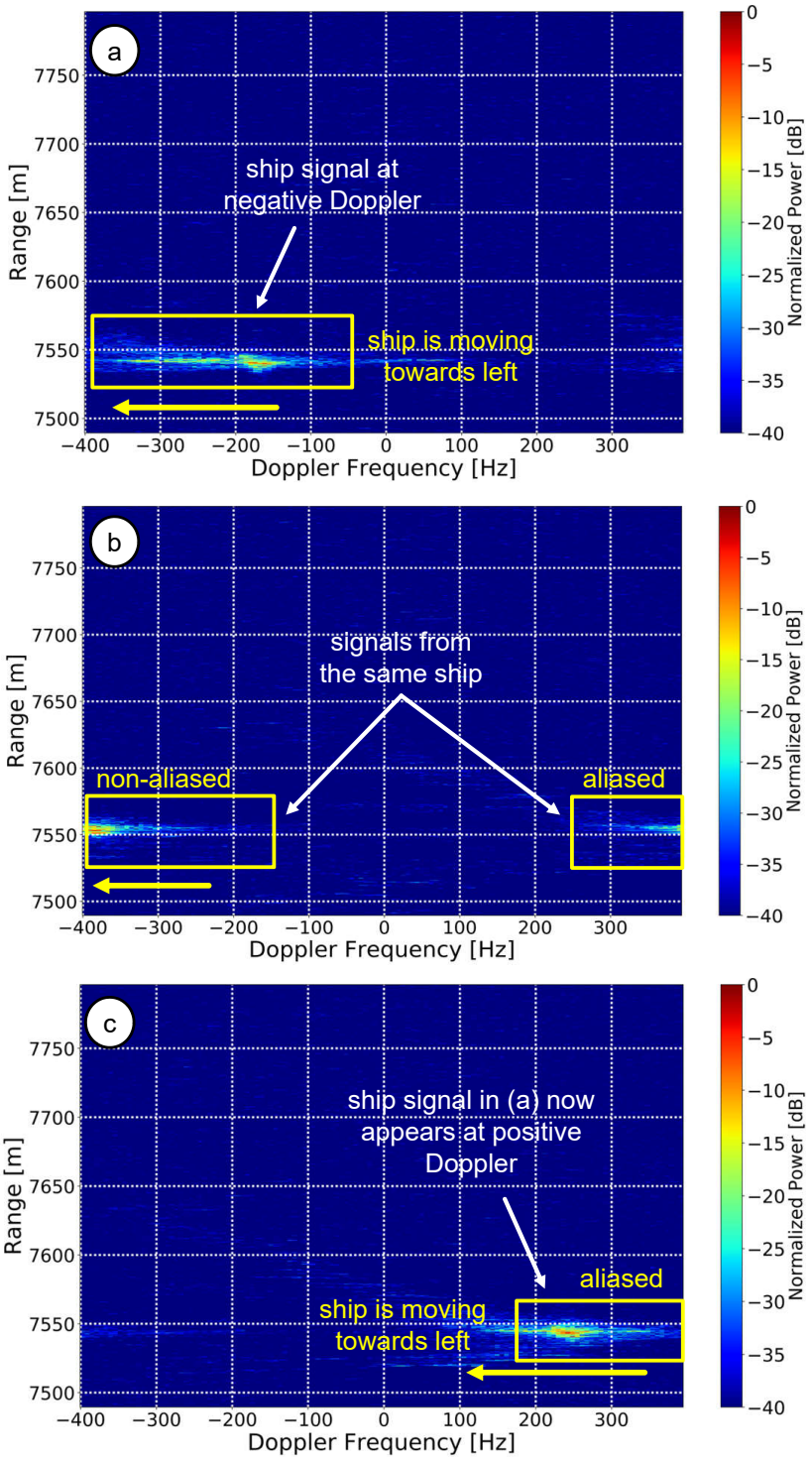

Figure 5.12: Range-Doppler images of a single real moving ship observed at different CPIs. (a) Ship is originally moving towards -PRF/2. (b) Ship now appears simultaneously at both ends of the PRF bandwidth (indicated by the arrow). (c) Ship shown in (a) now appears at positive Doppler.

5.13(a) there are two target tracks belonging to the same target. Target ID_0 is terminated after certain time because of track management (cf. Section 5.4.1) and Target ID_1 gets initialized at the point of aliasing. However, after the aliasing correction only one target appears during the entire illumination time (cf. Target ID_0 in Figure 5.13(b)).

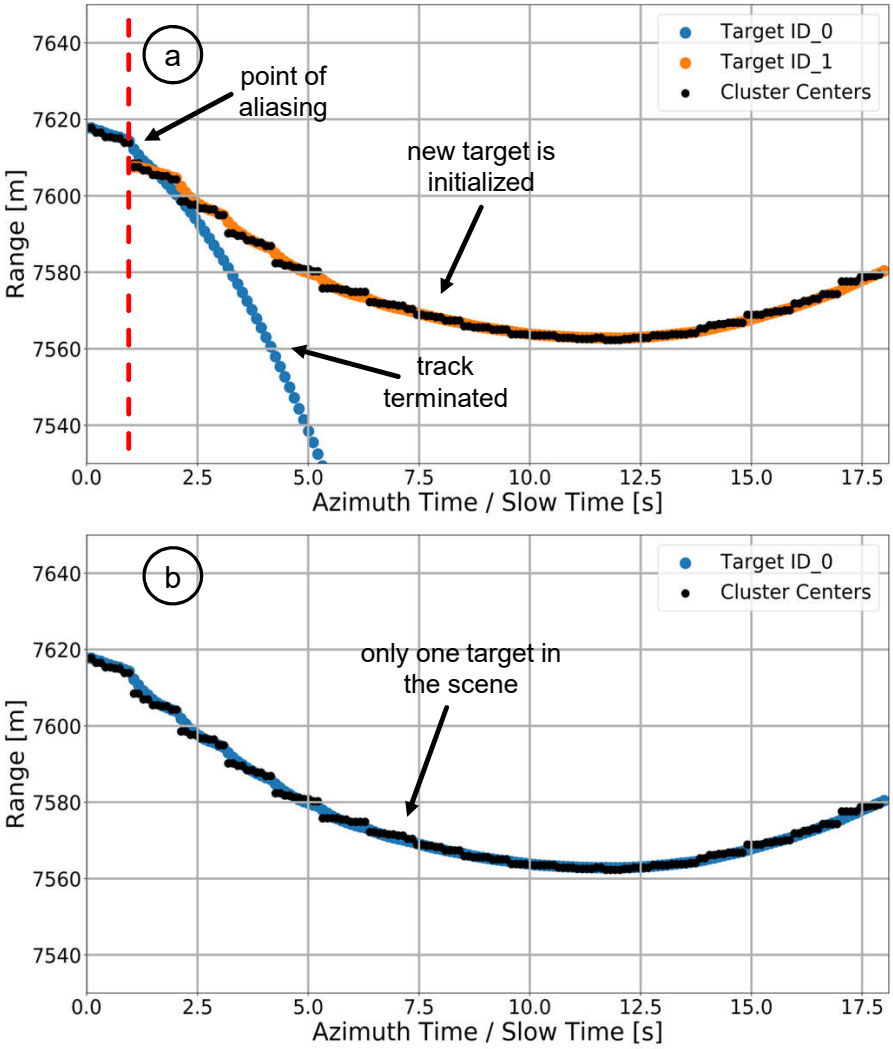

Figure 5.13: Real ship track (a) before and (b) after the aliasing correction. The corresponding real ship signal was already shown in Figure 5.10(a). The point of aliasing is marked in the figure. The tracking is performed in the range-Doppler domain, for visualization purposes the target tracks are projected back to time domain.

5.4.3 Simulation Results

In the previous sections the effects of false targets and Doppler aliasing were shown using a single target and the results after resolving these effects are shown in Figures 5.10 and 5.13, respectively. In this section these effects are shown using three simulated moving targets. The targets have overlapping range histories in time domain (cf. Figure 5.14(b)) and the aforementioned effects together with missing target detections are artificially included in the simulation. Simulated radar data acquisition and moving target parameters are given in Table 5.1.

The tracking results of the three simulated moving targets are shown in Figure 5.14. Tracking is implemented in the range-Doppler domain, only for visualization purposes, the target tracks are shown in time domain.

In Figure 5.14(b), the gaps are artificially introduced for TargetID_0 (blue) and Target ID_2 (green) which are filled by the KF-based predictions (cf. (4.10)). Moreover,

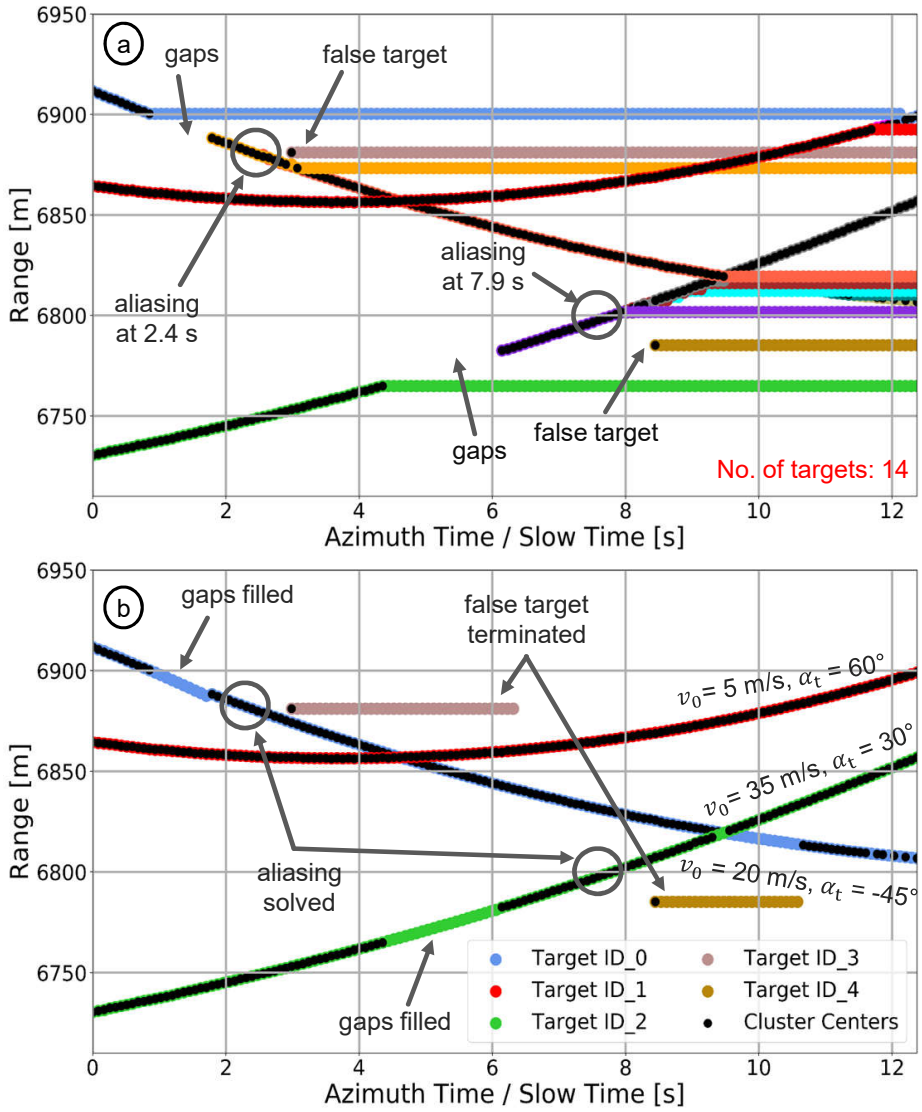

Figure 5.14: Simulated tracked range histories of three targets (a) without and (b) with considering the motion model, track management and Doppler aliasing. Artificially introduced gaps, false detections and aliasing points are marked in the figure.

Table 5.1: Moving Target Simulation Parameters

Simulation Parameters,	Assumed Values
Platform velocity [m/s]	91
Platform altitude above ground [m]	5000
Wavelength [m]	0.0306
Pulse repetition frequency [Hz]	1500
Chirp bandwidth [MHz]	100
Target absolute ground velocities [m/s]	5, 20, 35 (cf. Figure 5.14)
Target moving directions w.r.t. azimuth [°]	60, -45, 30 (cf. Figure 5.14)
Scene duration [s]	12.5
TX/RX antenna length [m]	0.3

they are also found aliased at 2.4 s and 7.9 s, respectively, which in the end resulted in several ambiguous targets as shown in Figure 5.14(a). The reason is that the PRF is not sufficiently high (cf. Table 5.1 where the PRF is 1.5 KHz) to accommodate the larger Doppler shifts caused due to their higher ground velocities (20 m/s and 35 m/s for TargetID_0 and TargetID_2, respectively). In addition, without using track management, the artificially added false target tracks are also never terminated. However, from Figure 5.14(b) it is clear that after using a Kalman filter with (CV+CA)-based target motion model as discussed in Section 4.2, track management (running here approximately after every 2 s) and recognizing and correcting the Doppler back-folding (cf. Section 5.4.2), the total number of tracked target tracks is reduced from 14 to 3 (plus 2 artificially introduced false targets which are terminated after 2 to 4 s), which can be considered as very good.

5.5 Data Patch Extraction

One of the primary outcomes of the MTT algorithm is the ship data patches in range-time domain (cf. dashed rectangular block in Figure 5.1). The extracted data patches are used for generating high resolution ISAR image sequences of the ships which can later be utilized for ship recognition and identification purposes.

For explaining the data patch extraction procedure, consider Figure 4.2(b). In the figure it is shown that in a single CPI in range-Doppler, a clustered ship target has a centroid position and a bounding box. The bounding box contains the range and Doppler extents of the ship cluster with some guard zones. For patch extraction in time domain and, hence, for ISAR imaging, the ship's range bins obtained from the bounding box are used. An example is illustrated in Figure 5.15.

In Figure 5.15 top, there is only one ship present in the radar data. Furthermore, the ship occupies a certain number of azimuth and range samples in the data. For ISAR imaging either of the two variants of the ship data patches, as shown in Figure 5.15 bottom are needed. Variant 1 in the figure contains the ship data patches which are directly retrieved from the tracker, whereas for obtaining variant 2, an additional rough range cell migration correction is performed on variant 1 as a preliminary step for ISAR imaging. For this rough range cell migration correction, again the known target track, i.e., range over azimuth time, can be used.

An example of ship data patch extraction on real RC airborne radar data containing a real ship signal is shown in Figure 5.16. Details related to the acquired radar data is discussed in Section B.1.1 (cf. page 148) and the radar system and acquisition geometry parameters are given in Table B.1 (cf. page 150).

Figure 5.16 top shows real airborne radar data acquired over a large area on the ground ($\approx 65\,\mathrm{km}^2$). After tracking a very small part of the acquired radar data, as shown in Figure 5.16 bottom is extracted. Note that the non-uniform ship data patches in the figure are due to cluster size variations caused by signal amplitude fluctuations over time.

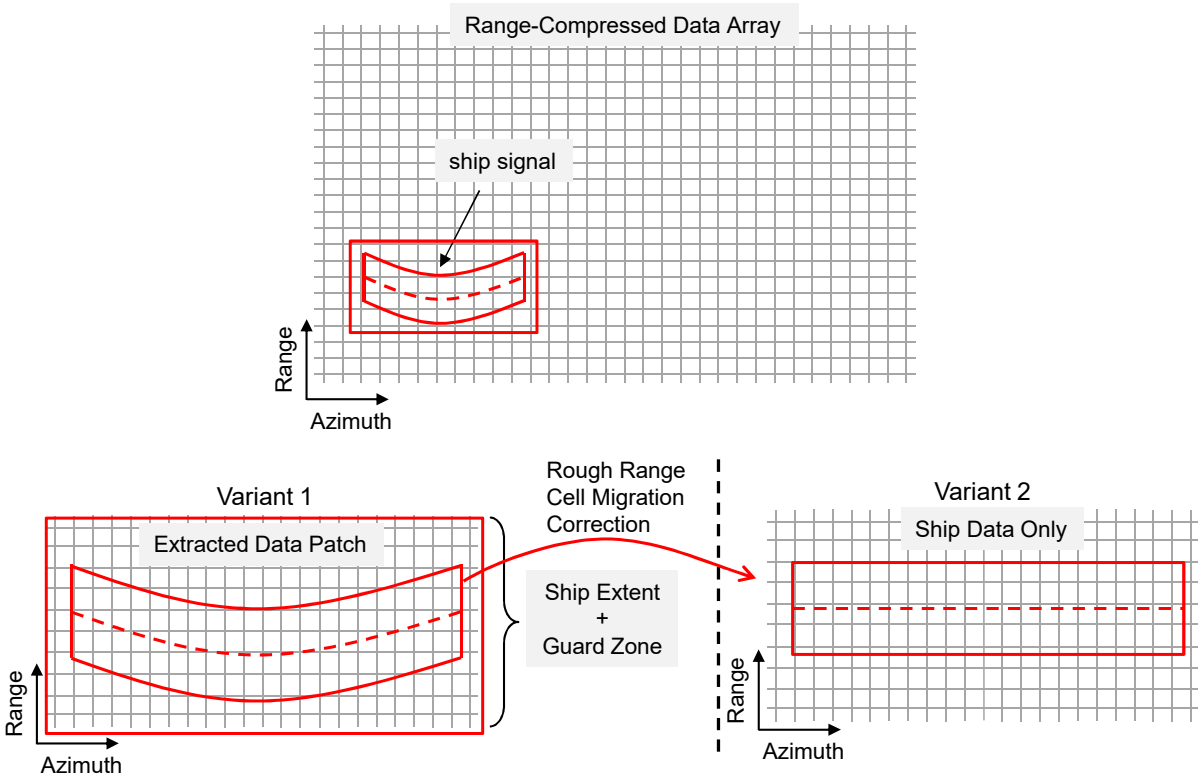

Figure 5.15: Illustration showing the ship data patch extraction for the potential future onboard air-based maritime surveillance. Top: Acquired RC airborne radar data in the range-time domain. A single ship signal present in the data is marked in the figure. Bottom left: Extracted ship data patch with some guard zones after performing detection and tracking onboard the aircraft. Bottom right: Ship data patch after a rough range cell migration correction. Either of the two variants in the figure can be transferred to the ground for further processing.

5.5.1 Data Reduction

The volume of the acquired airborne radar data is generally very high, especially if the radar data are acquired with very high resolution over large swaths and long observation times. Transferring the entire raw or RC radar data to ground is a very time-consuming process. The data transfer could even take hours, depending upon numerous factors such as the scene size, system parameters, data resolution, number of receiving channels and mainly the available transmission bandwidth. Therefore, in the future, almost all processing related to air-based ship surveillance is suggested to be carried out onboard the aircraft. Only the data patches or the ISAR image sequences (if ISAR imaging is also performed onboard) of individual ships shall be transferred to the ground. By doing this, large amount of data reduction is possible.

As an example, consider a scene size of 30 km^2 (3 km in ground range and 10 km in azimuth) of the ocean surface. Already discussed in Section 3.5.4, for 30 km^2 of ocean area there are approximately 260×10^3 azimuth and 6×10^3 number of range samples. Furthermore, assume that there is only one ship in the data. The ship is 100 m long and it is moving perpendicular w.r.t the aircraft motion and it is illuminated by the radar antenna beam for nearly 10 s. The number of azimuth and range samples for this ship

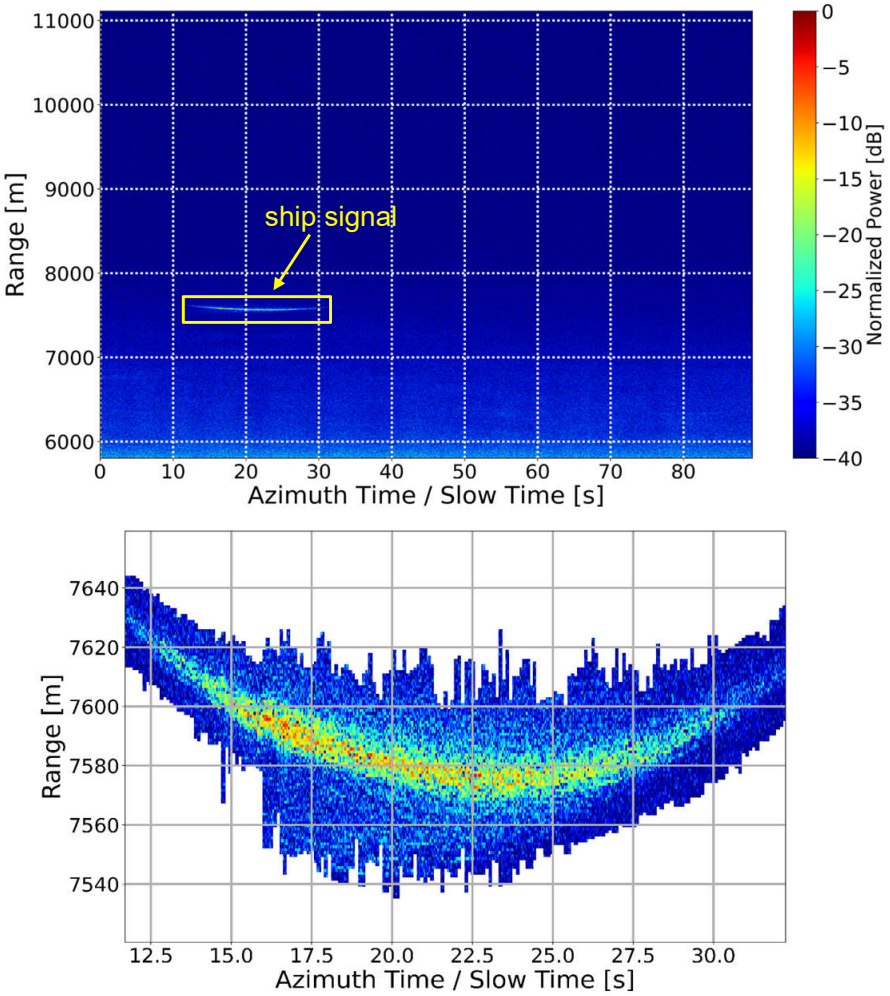

Figure 5.16: Top: Real X-band VV polarized F-SAR RC airborne radar data. The data were acquired using a linear flight track. A real single ship signal contained in the acquired radar data is marked in the figure. Bottom: Extracted ship data patch in the azimuth time domain after using the tracking information.

is approximately calculated as 25×10^3 and 200, respectively. Considering that there are 1 to 10 ships of same length in the surveillance area then only 0.3% to 3% of the total radar data needs to be transferred to the ground for further processing, respectively. This could not only save a lot of time on data downlink but also enable an efficient ship surveillance.

5.5.2 ISAR Imaging

ISAR is a radar imaging technique which is used for generating two- or even three-dimensional images of non-cooperative moving targets [108,121]. For the proposed airborne-based maritime surveillance the data patches of individual ships along azimuth (cf. Figure 5.15 bottom) are fed to the ISAR processor for generating their focused image sequences [49, 122].

A typical ISAR imaging algorithm is comprised of motion compensation step followed by Fourier transform along azimuth for getting a focused range-Doppler image of the ship.

Motion compensation is achieved by range realignment [123] and phase compensation [124]. The former corrects the misaligned range profiles of the detected ships and the later compensates the phase errors that arises due to target motion. After doing these operations and afterwards an additional cross-range scaling, a focused ISAR image of the ship in ground range/cross-range can be obtained (cf. Figure 5.19) [108] .

5.6 Experimental Results with Real Data

In this section tracking and some preliminary ISAR results of a real ship using real RC airborne radar data are provided. The radar data were acquired simultaneously in X- and L-band using F-SAR sensor. The data contained a real controlled German police ship which was observed for more than 400 s using circular acquisition geometry. Details of the flight experiments are given in Section B.1.1 (cf. page 148) and the system and acquisition geometry parameters of the acquired airborne radar data are listed in Table B.1 (cf. page 150).

5.6.1 Tracking Results

Figure 5.17 shows the tracking results of a real moving ship in circularly acquired X-band HH polarized F-SAR airborne radar data. Additional information related to the tracked targets in Figure 5.17(b) is listed in Table 5.2.

In the circular radar data shown in Figure 5.17(a), the detected and clustered real ship signal (cf. Section 4.1.2) is tracked using the (CV+CA) motion model-based KF (cf. Section 4.2) and the data association method presented in Section 5.3.4. From detection to tracking, all the algorithms are implemented in the range-Doppler domain.

As shown in Figure 5.17(b) there are in total nine target tracks. It is also observed that if the gaps are significantly larger (in the order of several minutes) multiple new target tracks from a single target are created (cf. Figure 5.17(b) and Table 5.2 where a single police ship has five different target tracks).

In addition, some false targets or clutter are also detected, but they are very well handled by the track management system (cf. Section 5.4.1). Since there were larger gaps in the data, the tracks were therefore checked by the track management after every 4 s (cf. Table 5.2 where the false targets are tracked for more than 4 s).

Using the tracked range information of the ship, the data belonging to the ship signal are also successively extracted in time domain and are shown in Figure 5.17(c). The extracted ship signals are used for generating the ISAR image sequences.

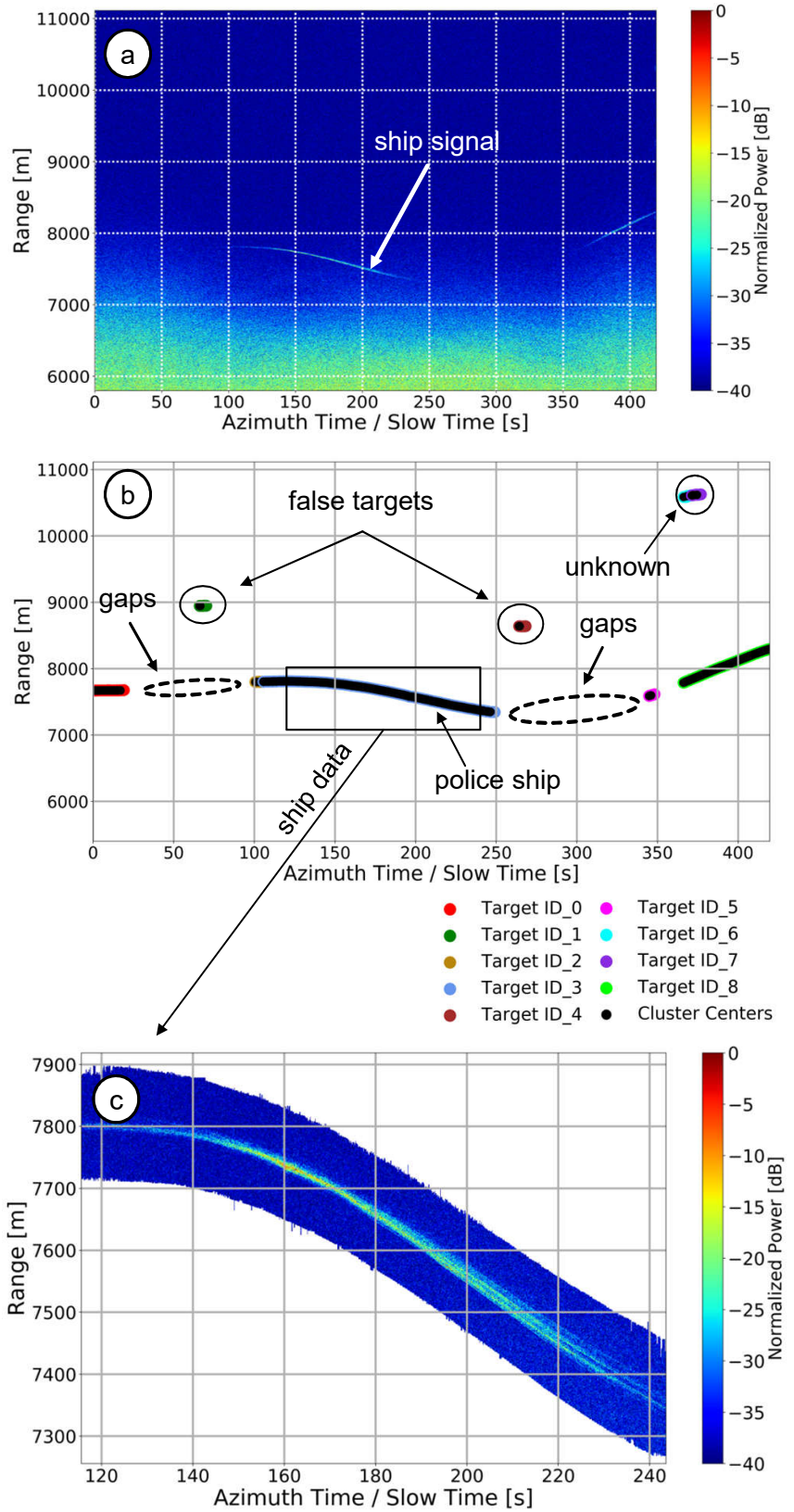

Figure 5.17: (a) Circularly acquired real single-channel HH pol RC X-band radar data. (b) Tracking results are shown in time domain after applying the detection and tracking algorithms in the range-Doppler domain. The police ship, false and unknown targets and gaps are marked in the figure. (c) Zoomed-in detail of the successively extracted ship data patch in time domain for ISAR imaging.

Table 5.2: Track duration of each tracked target from the tracking results shown in Figure 5.17(b).

Tracked Targets	Track Duration [s]	Remarks
Target ID_0	19.16	police ship
Target ID_1	4.26	false target
Target ID_2	4.89	police ship
Target ID_3	143.7	police ship
Target ID_4	4.26	false target
Target ID_5	3.51	police ship
Target ID_6	4.47	unknown
Target ID_7	5.75	unknown
Target ID_8	53.6	police ship

5.6.2 State-of-the-Art Tracker Performance Metrics

To evaluate the tracker performances there exist several state-of-the-art metrics like optimal sub-pattern assignment (OSPA) [125] or generalized OSPA (GOSPA) [126]. However, these metrics are primarily used for coastal radars or ship-borne radars with rotating antennas with narrow pencil-shaped azimuth beams [20, 127]. In order to evaluate such metrics, information like the true ground position of the target and the time duration of its true trajectory in the region of interest must be known. These metrics in our airborne radar scenario cannot be used because of two main reasons:

- Due to the use of only a single receiving channel, there is no angle information of the target. As a result, the tracks cannot be projected on the ground and therefore, its position on the ground cannot be calculated.
- As shown in Figure 1.1, due to the antenna pattern weighting, wider antenna beam and the non-ideal platform motion, it is also impossible to know exactly when the target will enter and exit the beam. Therefore, true time on target cannot be determined.

Considering the aforementioned reasons, it can be said that the popular metrics which have been used for evaluating the multitarget tracking performance for marine radar datasets are not suitable for the airborne radar data which are investigated in this thesis.

5.6.3 Range Accuracy in Circular Data

In this section the range position accuracy results of the controlled police ship using both X- and L-band real single-channel airborne radar data acquired simultaneously during the circular flight track are presented. The X- and L-band circular radar data with the police ship were already shown in Figure 5.17(a) and Figure 3.27(a), respectively.

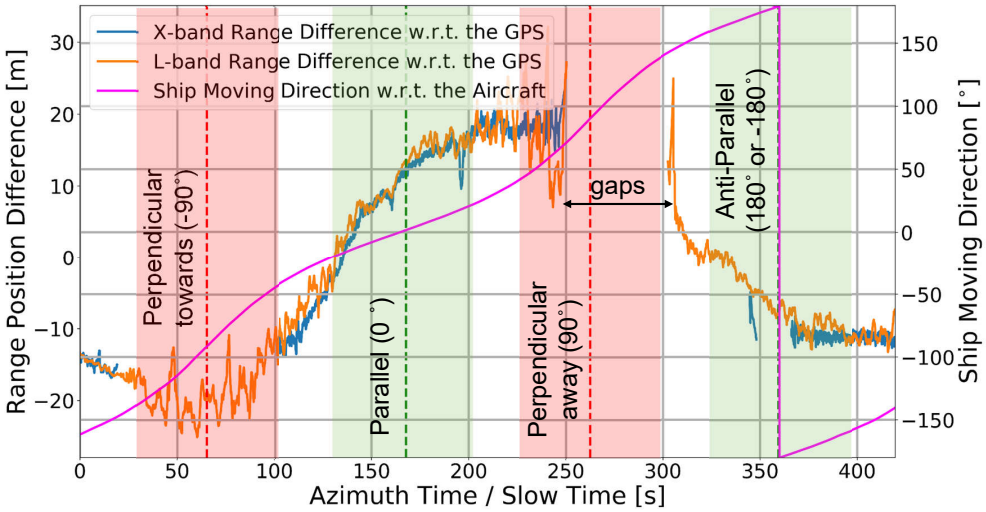

Figure 5.18: Range position differences computed over azimuth time for the controlled police ship with dimensions 66 m × 11 m in both X- and L-band real airborne radar data acquired simultaneously during the circular flight track. Gaps marked in the figure, e.g., between 250-305 s, occur when the target is not illuminated by the radar antenna beams. In the figure, red and green vertical dashed lines with colored guard zones correspond to the time instants when the ship moving direction was perpendicular (either towards or away) and parallel or anti-parallel with respect to the aircraft flight direction, respectively.

For the accuracy assessment, the measured range position of the ship is compared with its reference range position. The measured range position is derived from the center of gravity of the ship cluster (cf. Section 4.1.2) and since it is a single position for the ship, it is biased by the ship size (cf. Table 4.1 where the ship's length and beam are 66 m and 11 m, respectively).

The reference range position of the ship is calculated by using the GPS (Global Positioning System) position of the ship and the position of the aircraft at the same azimuth time. Note here that the position of the GPS antenna on the ship is not known. Therefore, the reference range position of the ship is also biased by the ship size.

After having the measured and the reference range positions of the ship at each azimuth time, the range position differences are computed and the results are shown in Figure 5.18.

From Figure 5.18 it can be seen that there are significant gaps in the computed range position differences in X-band circular data compared to the L-band data. This is because the 3 dB azimuth beamwidth of the X-band antenna is smaller than that of the L-band antenna (cf. Table B.1 in page 150). Moreover, during a circular flight, the cross-wind significantly change the yaw angle of the aircraft and the target is not always illuminated by the narrower antenna beam of the X-band radar.

Furthermore, it is also observed that the range position differences vary significantly during the total illumination time. Signal amplitude fluctuations and its constantly changing moving direction with respect to the aircraft (magenta curve in Figure 5.18) are

responsible for changing the measured and true range positions of the ship because of the bias caused by the ship size.

The minimum and the maximum range position differences for the X- and L-band circular radar data are (0.002 m, 23.25 m) and (0.005 m and 32.22 m), respectively. For both the frequency bands, the observed maximum range position differences are within 66 m, which is the length of the ship.

Finally, the RMSEs of the tracked ship range history in X- and L-band radars are calculated and they are found to be 13.18 m and 13.75 m, respectively. For the ship that has a length of 66 m and a beam of 11 m, the calculated RMSE can be considered as very good.

5.6.4 Preliminary ISAR Imaging Results

One primary advantage of circular flights is that, due to the very long observation time, dozens or even hundreds of ISAR images of the ships can be obtained under different aspect angles and used later for ship classification and recognition purposes. In Figure 5.19 a small cut of such an ISAR image sequence is shown.

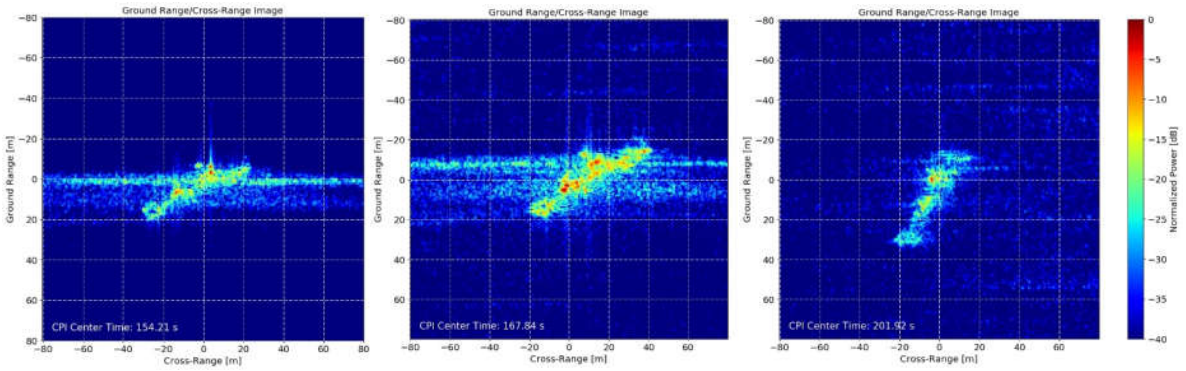

Figure 5.19: Some ISAR images obtained from the extracted RC ship data shown in Figure 5.17(c). The data were extracted after using the tracking information. The images correspond to different azimuth times and the coherent integration time for each image is 1.7 s [49].

In the figure the ISAR images were generated from the extracted data patch shown in Figure 5.17(c) by applying the ISAR processor discussed in [49]. A coherent integration time of 1.7 s was used for each ISAR image. The achievable azimuth (or cross-range) resolution is a function of the radar system wavelength, the coherent integration time and the target motion itself [108].

5.7 Chapter Summary

This chapter proposed a novel range-Doppler-based MTT algorithm using single-channel RC airborne radar data. The algorithm is applicable for linear and circular flight tracks, as shown in this chapter. However, there exists also no restriction for arbitrary flight tracks if the data are processed using small CPIs. The proposed MTT algorithm is also expected to have real-time capability after an efficient implementation of the algorithm in a parallelized way using multicore or multiprocessing computers. The proposed tracker is comprised of the following components:

1. a simple but efficient data association block to do MTT and also to resolve detection uncertainties;
2. a powerful track management system running simultaneously within the tracker for updating the confirmed tracks and for terminating the false and already finished tracks;
3. a Doppler aliasing block for extracting the true target range history and, hence, the unambiguous Doppler history by identifying and considering the Doppler back-folding.

The tracker also extracts simultaneously the ship data patches in time domain that can later be used for ISAR image generation and recognition purposes. The complete tracking module including the track management is designed using an SQLite database as the core. The proposed tracking methodology was validated by using both simulated and real experimental airborne radar data.

It is pointed out here that the proposed MTT algorithm can be integrated into multichannel radar systems where with the help of an additional estimated direction-of-arrival (DOA) angle, the tracked Doppler and range history of the target can directly be projected to the ground. Details related to multichannel radar data processing and geocoding techniques are presented in Chapter 6.

6 Multichannel Data Processing and Geocoding

This chapter presents methods for geocoding the extended targets using multichannel RC airborne radar data. With multiple receiving antennas that are arranged in the along-track direction of the aircraft, the radar-based detections from the targets can directly be projected to the ground after computing their DOA angles. Most state-of-the-art DOA angle estimation methods assume one detection per target. These methods cannot be applied one-to-one on extended targets like ships, because individual ships in high resolution data are generally composed of several distinct radar detections. In this chapter different methods for estimating the DOA angle for extended targets are formulated and discussed. The performance of the proposed methods is assessed by using simultaneously acquired AIS data of real ships. Experimental radar data from the DLR's multichannel airborne DBFSAR system are used for validating the proposed methods in real maritime scenarios.

Parts of the results and discussions provided in this chapter I have published in the peer-reviewed journal paper [128]. I have also co-authored the journal papers [36,61] where I have contributed in the development of the algorithms, and the geocoding results shown in these papers are based on the methodology proposed in this chapter.

6.1 Introduction

In the previous chapters of this doctoral thesis the focus was on a single receiving channel which was solely used for detecting and tracking targets in the range-Doppler domain. However, single-channel systems have some limitations, for instance, with single-channel systems it is not possible to do efficient clutter suppression in order to detect slowly moving targets with low RCS that are embedded inside the clutter bandwidth. Furthermore, such systems are also incapable of projecting the radar-based target detections to the ground due to lack of angle information of the target. To overcome these limitations of single-channel systems, multichannel systems are used.

In a multichannel radar system when multiple receiving antennas are arranged in the azimuth direction of the aircraft and if they are separated with a certain along-track baseline, the signals received by these antennas can be combined after applying, e.g, STAP-based clutter suppression techniques [129] for suppressing the ocean clutter. By doing this, the detectability of low observable slowly moving targets which are present inside the clutter Doppler spectrum can be enhanced. For suppressing the clutter and to improve the target's detectability, at least two receive (RX) channels separated with a certain baseline in azimuth are necessary. Clutter suppression techniques are briefly discussed but not investigated in detail in this chapter.

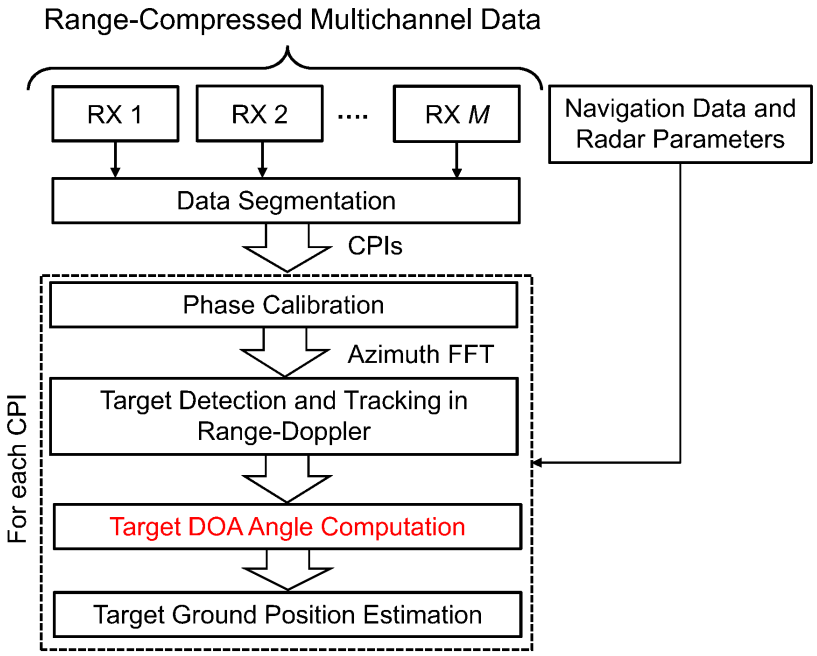

Figure 6.1: Simplified flowchart for estimating the target ground position using multichannel airborne radar data. The DOA angle estimation block (shown in red) is the focus of this chapter.

With an additional third receiving antenna, along with clutter suppression, it is also possible to robustly estimate the motion parameters of the targets on the ground [33], especially the target position on the ground after computing additionally the DOA angle of the detected targets. The focus of this chapter is on the DOA angle estimation methods using multiple receiving channels.

Before estimating the target's DOA angle and its ground position the phases of the received signals are first calibrated [130–132]. Phase calibration is indispensable because in real-world, nonlinear aircraft motion caused by the atmospheric turbulence causes unwanted phases differences among different RX channels of a multichannel system. Incorrect phases can significantly degrade the accuracy of the target's DOA angle which then impacts the target's position accuracy on the ground. Therefore, in multichannel data processing phase calibration is necessary in order to obtain accurate DOA angles and, hence, accurate positions of the targets on the ground.

A simplified multichannel airborne radar data processing flowchart for DOA angle estimation and target geolocation is shown in Figure 6.1.

The algorithm operates on multichannel RC airborne radar data (receive channels RX 1, RX 2.... RX M in the figure are the multiple receiving channels). The multichannel data are initially partitioned into smaller CPIs along the azimuth direction. The length of the CPI is system parameter dependent (cf. Section 2.7). The CPIs are then calibrated for correcting the phase offsets among the receiving channels [61]. After calibration individual CPIs are then transformed into the range-Doppler domain via azimuth FFT (cf. Section 2.6).

Target detection is carried out in the range-Doppler domain, where after detection, its slant range and Doppler frequency position are measured and tracked over time. Details related to the detection and tracking algorithms are presented in Chapter 3 and Chapter 5, respectively.

Once a target is detected its DOA angle is estimated via a beamforming operation [133]. With the estimated DOA angle, the measured slant range, the known terrain elevation, and the known geographical aircraft position and the attitude angles, the target position on the ground can directly be computed. Successive target detection and mapping on the ground creates the target track that can further be fused with the simultaneously acquired AIS data for validation purposes [63]. Note that an additional tracking can also be applied on the geographical positions as the second tracking step, with the main goal of improving the accuracy of the computed geographical positions. Ground track refinement methods are the future outlook of this doctoral thesis.

In the next sections multichannel radar data processing steps with the final goal of calculating the geographical positions of the targets are presented.

6.2 Target Detection using Multichannel Data

Most state-of-the-art methods for target detection using multichannel data generally use single-channel data structure [33]. In this sense, the detection framework shown in Figure 3.1 which operates on single-channel radar data, can be used for target detection using multichannel data after transforming the multichannel data to single-channel data. The multichannel radar data can be reduced to single-channel data in three different ways, as shown in Figure 6.2.

In the figure it can be seen that the single-channel radar data in the presence of multiple receiving channels can either be the data acquired using one of the receiving channels (mode 1), the sum-channel data (mode 2) or the clutter-suppressed data (mode 3). In this thesis target detection is carried out using one of the receiving channels, as shown by the mode 1 in the top left of Figure 6.2. From computation-time perspective, target detection using this mode is the fastest with the disadvantage of degraded detection capability of slow moving targets with low RCS.

For improving the detectability of such targets, the sum-channel or the clutter-suppressed radar data can be used. In the sum-channel data, due to the coherent addition of the number of receiving channels, the target SNR and, hence, the target detectability can be increased. The sum-channel data $Z_{\text{sum}}(r, f_{\text{a}})$ in Doppler domain can be expressed as

$$Z_{\text{sum}}(r, f_{\text{a}}) = |\boldsymbol{d}^{\text{H}}(u)\boldsymbol{Z}(r, f_{\text{a}})|, \tag{6.1}$$

where $(\cdot)^{\text{H}}$ is the Hermitian operator (conjugate transpose), $\boldsymbol{d}(u)$ is the beamforming vector (cf. (2.27)) and $\boldsymbol{Z}(r, f_{\text{a}})$ denotes the complex multichannel data in the range-Doppler domain. Note that the sum-channel data only improves the target SNR but does

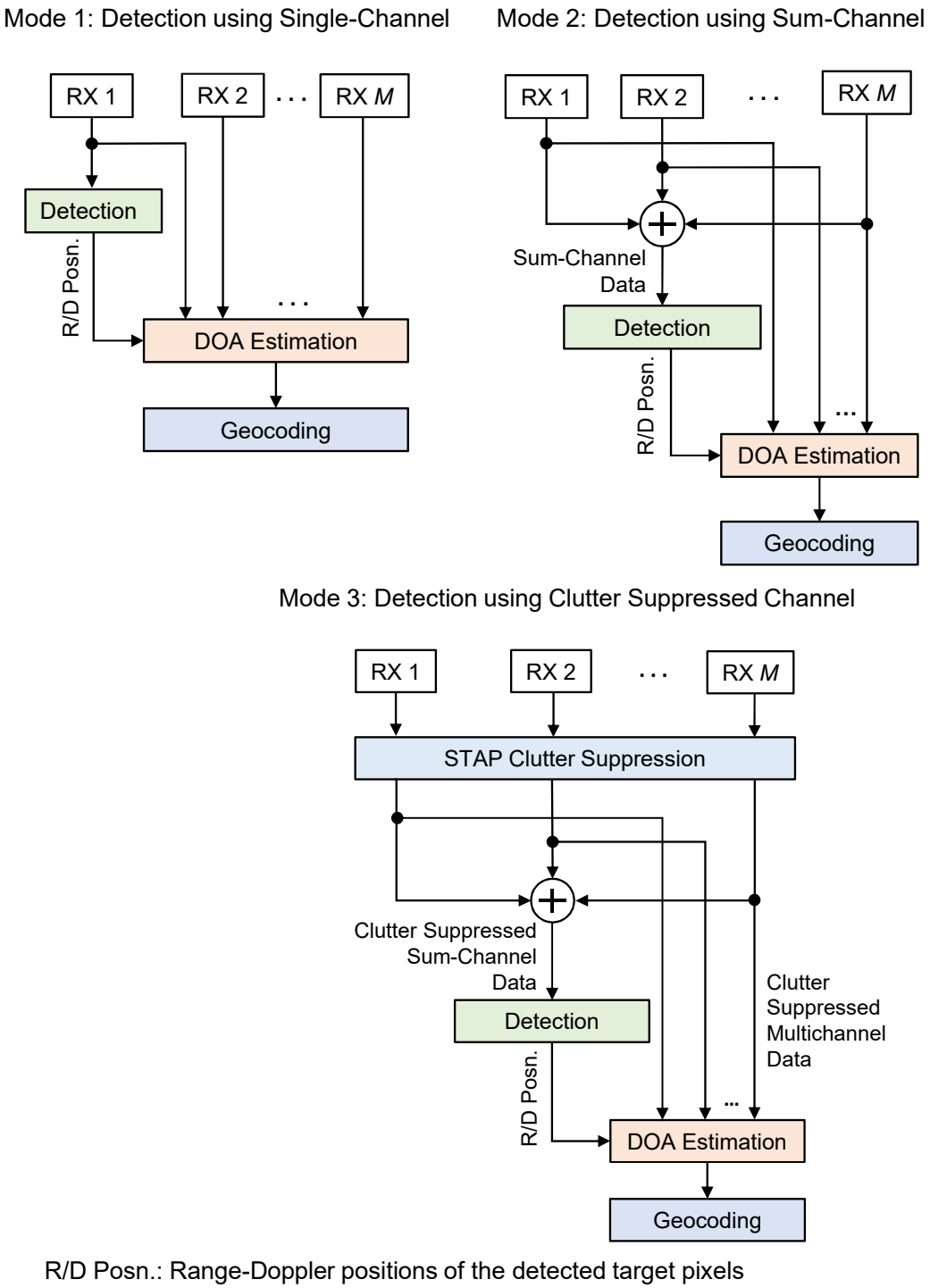

Figure 6.2: Target detection strategy using multiple receiving channels. The multichannel radar data are transformed into three different single-channel radar data types. The detection, DOA estimation and geocoding algorithms are same for all the modes. In this case, RX 1, RX 2,.. RX M are the multichannel range-compressed data of a CPI in range-Doppler domain.

not guarantee the detectability of low RCS targets that are embedded within the clutter band. This is because by adding channels coherently, along with the target power the clutter power is also coherently added. For such situations, clutter suppression becomes necessary.

STAP is a very prominent multichannel clutter suppression technique. It not only suppresses the clutter but also enhances the target signal energy. The STAP-based clutter suppressed data $Z_{\mathrm{cs}}(r, f_{\mathrm{a}})$ can be written as

$$Z_{\mathrm{cs}}(r, f_{\mathrm{a}}) = |\boldsymbol{d}^{\mathrm{H}}(u)\hat{\boldsymbol{R}}_{\mathbf{W}}^{-1}(f_{\mathrm{a}})\boldsymbol{Z}(r, f_{\mathrm{a}})|, \tag{6.2}$$

where $\hat{\boldsymbol{R}}_{\mathbf{W}}(f_{\mathrm{a}})$ is the clutter covariance matrix (CCM). For achieving a good clutter suppression capability, the CCM is generally estimated from the real data. For taking into account the statistical variability of the data over space and time, the estimated CCM needs to be frequently updated. When the CCM is estimated from the real data, it is called "empirical CCM" which can be computed as [62, 134]

$$\hat{\boldsymbol{R}}_{\mathbf{W}} = \frac{1}{\mathrm{n_r}} \sum_{k=1}^{\mathrm{n_r}} \boldsymbol{Z}_{\mathrm{k}} \boldsymbol{Z}_{\mathrm{k}}^{\mathrm{H}} \tag{6.3}$$

where $\mathrm{n_r}$ is the total number of range bins.

The performance of sum-channel data and STAP-based clutter suppressed data for target detection is not investigated in this doctoral thesis. However, the beamforming vector $\boldsymbol{d}(u)$ in (6.1) is used for estimating the DOA angle of the detected target, and in case of strong clutter contribution, the covariance matrix $\hat{\boldsymbol{R}}_{\mathbf{W}}(f_{\mathrm{a}})$ in (6.2) can be used for clutter suppression purposes.

6.3 State-of-the-art DOA Angle Estimation for Point-Like Targets

After detecting the targets in the range-Doppler domain, the DOA angle is estimated for projecting the radar-based target detections to the ground via a geocoding operation. A point-like target is assumed for estimating the DOA angle. The multichannel acquisition geometry for this task with the target of interest is shown in Figure 6.3 (cf. also Figure 2.6). In the figure an antenna array that consists of M number of receiving channels is shown. The multiple receiving channels are arranged in the along-track (or azimuth) direction of the aircraft. The multichannel signal model for this acquisition geometry was already given in (2.27).

Referring to (2.27), the beamforming vector $\boldsymbol{d}$ shown in the equation is used for estimating the directional cosine and, hence, the DOA angle of the target. This is done through a maximum likelihood estimator which is expressed as [135]

$$\hat{u} = \underset{u}{\mathrm{argmax}} |\boldsymbol{d}^{\mathrm{H}}(u)\hat{\boldsymbol{R}}_{\mathbf{W}}^{-1}(f_{\mathrm{a}})\boldsymbol{Z}_{\mathrm{t}}(r, f_{\mathrm{a}})|^2, \tag{6.4}$$

where $\hat{u}$ is the estimated directional cosine and $\boldsymbol{Z}_{\mathrm{t}}(r, f_{\mathrm{a}})$ denotes the target's multichannel data vector at slant range r and Doppler frequency f_{a}, which is obtained after detecting the target in the range-Doppler domain.

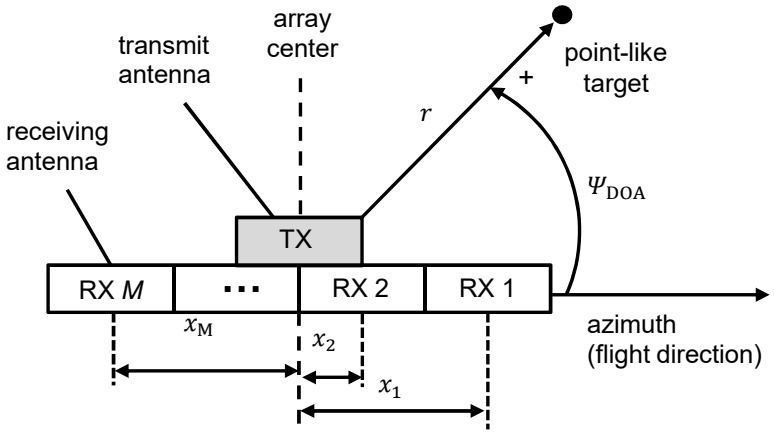

Figure 6.3: Simplified multichannel data acquisition geometry with M receiving channels and the target of interest. The target range r and its corresponding DOA angle ψ_{DOA} are shown in the figure. The terms $x_1, x_2, ...x_{\mathrm{M}}$ are the antenna center positions in azimuth direction with respect to the array origin.

When the targets are expected to have high SCNR, they can be detected without performing any clutter suppression. Therefore, the term $\hat{\boldsymbol{R}}_{\mathbf{W}}(f_{\mathrm{a}})$ shown in (6.4) can be omitted and the directional cosine of the target can be rewritten as

$$\hat{u} = \underset{u}{\operatorname{argmax}} |\boldsymbol{d}^{\mathrm{H}}(u)\boldsymbol{Z}_{\mathrm{t}}(r, f_{\mathrm{a}})|^2. \tag{6.5}$$

This simpler equation is used later on for avoiding any biases on the performance assessment caused by clutter suppression. The DOA angle of the target with respect to the antenna array axis is then computed as

$$\hat{\psi}_{\mathrm{DOA,ar}} = \cos^{-1}(\hat{u}). \tag{6.6}$$

The directional cosine u with respect to the antenna array can also be expressed as a function of Doppler frequency f_{a} and the LOS velocity v_{r0} of the target as [60]

$$u(f_{\mathrm{a}}, v_{\mathrm{r0}}) = \cos(\psi_{\mathrm{DOA}}) = \frac{\lambda f_{\mathrm{a}}}{2v_{\mathrm{p}}} + \frac{v_{\mathrm{r0}}}{v_{\mathrm{p}}}. \tag{6.7}$$

Rearranging (6.7), the LOS velocity of the target can be calculated as

$$v_{\mathrm{r0}} = v_{\mathrm{p}} \cdot u - \frac{\lambda}{2} \cdot f_{\mathrm{a}}. \tag{6.8}$$

After estimating the target's Doppler frequency and directional cosine unambiguously, the above equation can directly be used for computing the target's LOS velocity.

6.4 DOA Angle Estimation Methods for Extended Targets

6.4.1 Problem Statement

For estimating the DOA angle the targets in classical moving target indication (MTI) algorithms are assumed as point-like targets, as shown in Section 6.3. This assumption is certainly valid for smaller targets (e.g., road vehicles) in low resolution data where each target of interest is within a single radar resolution cell [48]. However, in high resolution data, targets like ships usually appear as extended targets occupying more than a single resolution cell and, as a result, state-of-the-art DOA angle estimation methods which are designed for point-like targets,cannot be applied directly to extended targets.

An example is shown in Figure 6.4, where the ship HAM 316 (cf. Table B.3 in page 152 for specifications) has more than 4000 radar-based detections in a single CPI.

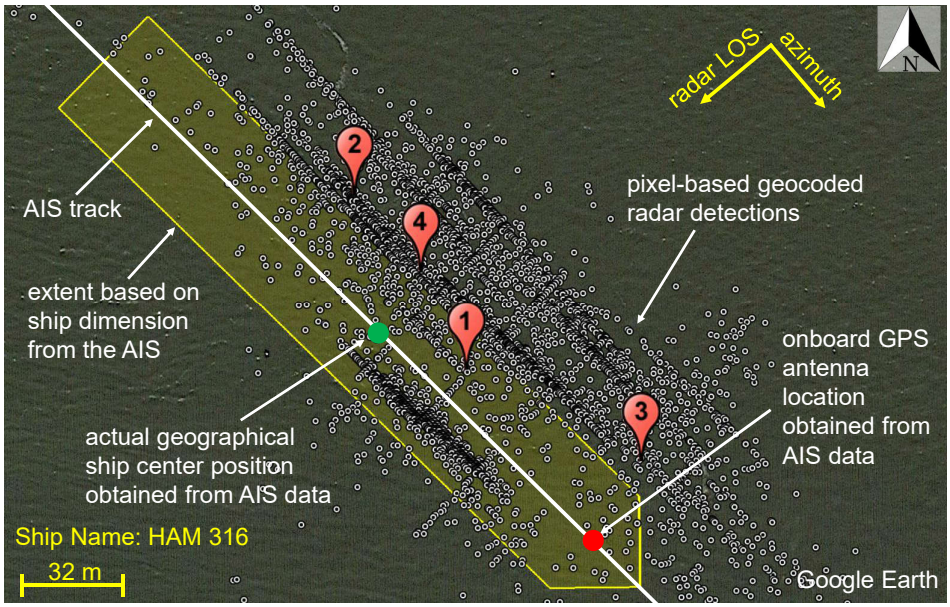

Figure 6.4: Geocoded radar-based detections obtained from a real ship at a specific time instant using real multichannel airborne radar data. Due to the side-looking acquisition geometry of the radar and the ship height, the detections are slightly displaced towards the radar in its LOS direction. Positions 1, 2, 3 and 4 in the figure are based on the methods proposed in Section 6.4.2.

It can be seen from the figure that the pixel-based detections obtained from the ship are spatially distributed. This is because each detection is mapped on the ground according to a specific DOA angle. The goal is to determine a single DOA angle, so that a single position of the extended target on the ground can be determined. By doing this, the target tracking becomes easier. In the next section four different methods for estimating a single representative DOA angle of an extended target are presented. All point-like target detections of the extended target are combined in different ways, firstly for being able to provide an object-based position estimation at all and, secondly, for

improving the geocoding accuracy. The goal is to have a single representative position for each extended target which, e.g., can be used later on for tracking purposes as described in [52] and [36].

6.4.2 Proposed Methods

For an extended target, after detecting and clustering its several pixel-based detections in a single CPI, the complex pixels belonging to the target are arranged as $\boldsymbol{Z}_{\mathrm{t,set}} = \{\boldsymbol{Z}_{\mathrm{t}}(r_1, f_{\mathrm{a1}}), \boldsymbol{Z}_{\mathrm{t}}(r_2, f_{\mathrm{a2}})....., \boldsymbol{Z}_{\mathrm{t}}(r_{\mathrm{N}}, f_{\mathrm{aN}})\}$, where N is the number of target-originated pixels in a cluster (cf. Figure 6.4 where N>4000).

With the given set of complex target pixels $\boldsymbol{Z}_{\mathrm{t,set}}$, the DOA angle of an extended target is computed based on: 1) the average complex amplitude (ACA); 2) the maximum of the absolute amplitude (MAA); 3) the complex amplitude at the nearest neighbor to the center of gravity (NNCG) of the cluster and 4) the mean DOA angle of the target pixels. For the first three methods, their respective complex signals that are used to estimate a single DOA angle for an extended target are expressed as

$$\boldsymbol{Z}_{\mathrm{t,ACA}}(r, f_{\mathrm{a}}) = \frac{1}{N}\sum_{n=1}^{N} \boldsymbol{Z}_{\mathrm{t}}(r_{\mathrm{n}}, f_{\mathrm{an}}), \tag{6.9}$$

$$\boldsymbol{Z}_{\mathrm{t,MAA}}(r, f_{\mathrm{a}}) = \max|\{\boldsymbol{Z}_{\mathrm{t}}(r_{\mathrm{n}}, f_{\mathrm{an}})\}_{n=1}^{N}|, \tag{6.10}$$

$$\boldsymbol{Z}_{\mathrm{t,NNCG}}(r, f_{\mathrm{a}}) = \boldsymbol{Z}_{\mathrm{t}}(r_{\mathrm{NNCG}}, f_{\mathrm{NNCG}}), \tag{6.11}$$

where r_{NNCG} and f_{NNCG} are the range and Doppler positions of the NNCG pixel. By inserting independently the left-hand-side variables of the equations (6.9)-(6.11) in (6.5), the directional cosine is obtained, and finally, the DOA angle of the target can be computed using (6.6).

For the fourth method, the DOA angle of the extended target is estimated as

$$\bar{\psi}_{\mathrm{DOA}} = \frac{1}{N}\sum_{n=1}^{N} \hat{\psi}_{\mathrm{DOA_n}}, \tag{6.12}$$

where $\bar{\psi}_{\mathrm{DOA}}$ is the mean DOA angle of the target and $\hat{\psi}_{\mathrm{DOA_n}}$ is the DOA angle of the n^{th} target pixel, which is computed using (6.6).

Although not investigated in this chapter the mean DOA method shown in (6.12) is generally not robust against 2π phase wrappings. For instance, phase transitions from 2π to 0 would lead to wrong mean DOA angle estimates. To avoid this, some additional efforts are needed.

One approach would be to first normalize the complex amplitude of the target pixel so that a unity vector, and hence, only the signal phase is obtained. The normalized complex amplitude $\boldsymbol{Z}_{\mathrm{t,norm}}(r, f_{\mathrm{a}})$ can be computed as

$$\boldsymbol{Z}_{\mathrm{t,norm}}(r, f_{\mathrm{a}}) = \frac{1}{|\boldsymbol{Z}_{\mathrm{t}}|}\boldsymbol{Z}_{\mathrm{t}}(r, f_{\mathrm{a}}), \quad \forall \boldsymbol{Z}_{\mathrm{t}}(r, f_{\mathrm{a}}) \in \boldsymbol{Z}_{\mathrm{t,set}} \tag{6.13}$$

After normalizing all target-originated complex pixel amplitudes to a value of 1, the DOA angle estimation method based on ACA (cf. (6.9)) can be applied afterwards on all unit vector complex amplitudes. By doing this, it can be expected that the biased caused by the phase wrapping in mean DOA method is eliminated. This method is briefly discussed in this section but its performance is not evaluated. In this chapter more emphasis has been given on the four methods which are described using equations (6.9)-(6.12).

As an example, these four methods are used for estimating the geographical position of the ship HAM 316 at a specific time instant. The geocoding results are shown in Figure 6.4. It can be seen from the figure that the estimated ground positions of the ship are different because for each method, the computed DOA angle is different. In Section 6.7.6 the accuracy of the estimated target ground positions achieved by these methods is evaluated and discussed in detail.

6.5 Target Geolocation

After estimating the DOA angle of a target its position on the ground is computed based on the acquisition geometry shown in Figure 6.5. In the figure the coordinate system (x, y, z) whose x-axis is parallel to the aircraft's azimuth direction and the global coordinate system $(x_{\mathrm{UTM}}, y_{\mathrm{UTM}}, z_{\mathrm{UTM}})$, referred to as ENU (east, north, up) or UTM (Universal Transverse Mercator) coordinates are shown. Note that the z-axis in the figure is parallel to z_{UTM}.

The distances Δx_{r} and Δy_{r} which are measured between the platform and the target on the ground in (x, y, z) coordinate system are computed as

$$\Delta x_{\mathrm{r}} = r_{\mathrm{t}} \cos(\hat{\psi}_{\mathrm{DOA,az}}), \tag{6.14}$$

$$\Delta y_{\mathrm{r}} = \sqrt{(r_{\mathrm{t}} \sin(\hat{\psi}_{\mathrm{DOA,az}}))^2 - h_{\mathrm{t}}^2}, \tag{6.15}$$

respectively, where r_{t} is the target's slant range, $\hat{\psi}_{\mathrm{DOA,az}}$ is the DOA angle estimated with respect to the aircraft's azimuth direction and $h_{\mathrm{t}} = z_{\mathrm{p}} - z_{\mathrm{t}}$.

Finally, the target position vector $\boldsymbol{x}_{\mathrm{t,UTM}}$ in UTM coordinates can be calculated as

$$\boldsymbol{x}_{\mathrm{t,UTM}} = \boldsymbol{x}_{\mathrm{p,UTM}} + \Delta x_{\mathrm{r}}\, \boldsymbol{e}_{\mathrm{x}} + \Delta y_{\mathrm{r}}\, \boldsymbol{e}_{\mathrm{y}} - h_{\mathrm{t}}\, \boldsymbol{e}_{\mathrm{z}}, \tag{6.16}$$

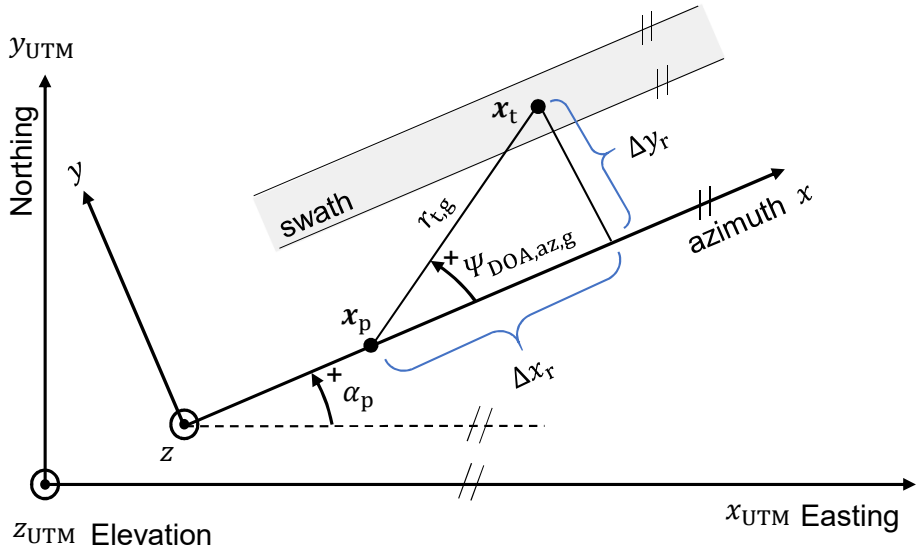

Figure 6.5: Simplified top-view acquisition geometry for estimating the target position on the ground. In the figure $\boldsymbol{x}_\text{p}$ and $\boldsymbol{x}_\text{t}$ are the platform and the target position vectors, respectively. The terms $\psi_{\text{DOA,az,g}}$ and $r_{\text{t,g}}$ are the ground projections of $\psi_{\text{DOA,az}}$ and r_t, respectively.

where $\boldsymbol{x}_{\text{p,UTM}}$ is the platform position vector in UTM coordinates. The vectors shown in (6.16) are written as [61]

$$\boldsymbol{e}_\text{x} = [\cos(\alpha_\text{p}), \sin(\alpha_\text{p}), 0]^\text{T}, \tag{6.17}$$

$$\boldsymbol{e}_\text{y} = [A\,\sin(\alpha_\text{p}), -A\,\cos(\alpha_\text{p}), 0]^\text{T}, \tag{6.18}$$

$$\boldsymbol{e}_\text{z} = [0, 0, 1]^\text{T}, \tag{6.19}$$

where α_p is the aircraft's course angle measured with respect to the UTM Easting (x-axis). The term A in (6.18) is equal to 1 for a right-looking antenna and -1 for a left-looking antenna.

6.6 Multichannel Data Calibration

Data calibration is a crucial step in multichannel radar data processing for obtaining accurate DOA angle and, hence, accurate position of the ground moving targets. To explain the need for calibration, Figure 6.6 is shown.

In Figure 6.6 two DOA angles can be seen. One DOA angle is measured with respect to the antenna array ($\psi_{\text{DOA,ar}}$), as shown by the red axis in the figure and the other DOA angle is measured with respect to the flight direction ($\psi_{\text{DOA,az}}$), as shown by the blue axis. For estimating accurately the ground position of the target using multichannel

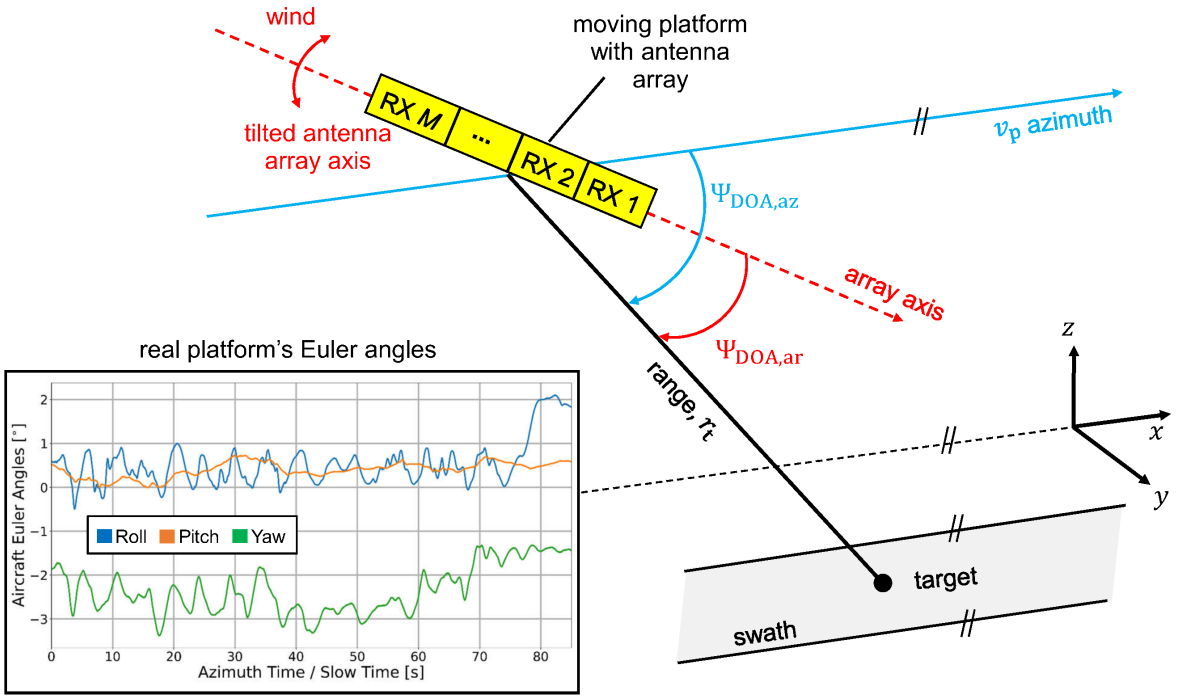

Figure 6.6: Simplified multichannel antenna array with tilted acquisition geometry due to aircraft's Euler angle variations. In the figure DOA angles measured with respect to the antenna array and the aircraft's azimuth axis are shown. The acquisition geometry is shown in the (x, y, z) coordinate system (cf. Figure 6.5) [61].

data, $\psi_{\mathrm{DOA,az}}$ is used (cf. Figure 6.5, (6.14) and (6.15)). However, conventional DOA angle estimation algorithms estimate $\psi_{\mathrm{DOA,ar}}$ (cf. (6.6)). In order to use $\psi_{\mathrm{DOA,ar}}$ for computing the target's ground position the antenna array must be perfectly aligned with the aircraft's azimuth direction so that after alignment, $\psi_{\mathrm{DOA,az}} = \psi_{\mathrm{DOA,ar}}$ (cf. Figure 2.6).

However, in practice, atmospheric turbulence causes variations in the aircraft's Euler angles (cf. Figure 6.6). These variations tilt the antenna array with respect to the aircraft's azimuth direction (cf. red axis in Figure 6.6). Such tilts introduce unwanted phase differences among multiple receiving channels and as a result, $\psi_{\mathrm{DOA,az}} \neq \psi_{\mathrm{DOA,ar}}$. These undesired phase differences among multiple RX channels need to be compensated so that the DOA angle and, hence, the target ground position can be accurately estimated. By calibrating the phases this will give the same results which will be obtained if the antenna array would be perfectly aligned with the aircraft's azimuth direction. In other words, it can be said that after phase calibration, $\psi_{\mathrm{DOA,az}} = \psi_{\mathrm{DOA,ar}}$.

In this thesis the algorithm proposed in [61] is used for calibrating the phases of the multichannel radar data. The proposed phase calibration algorithm has real-time capability and it is also robust against strong aircraft Euler angle variations. It compensates the undesired phase differences via first-order motion compensation techniques. For this, it uses the precise geographical positions of all bistatic phase centers of the receiving antennas as well as the terrain's elevation from a digital elevation model (DEM).

To examine the robustness of the phase correction algorithm, Figure 6.7 shows the ATI (along-track interferometry) phase offsets between channel 1 and channel 2 of real

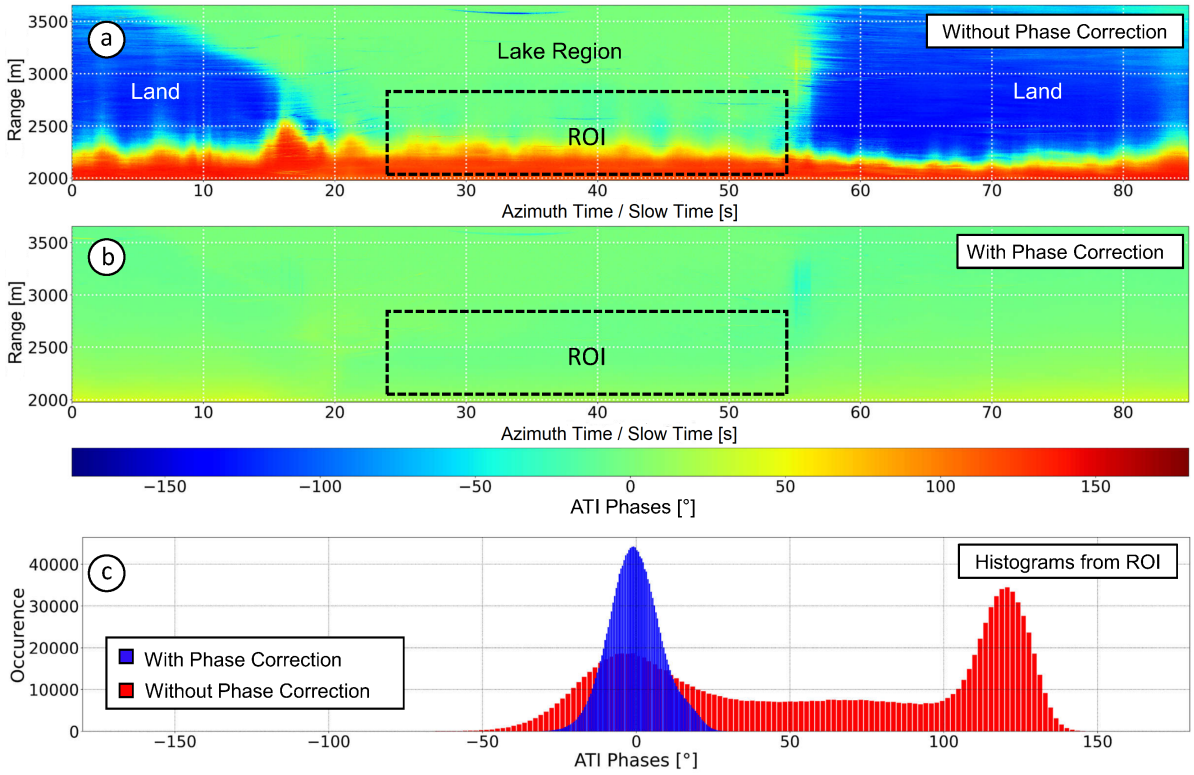

Figure 6.7: ATI phase offsets calculated between channel 1 and channel 2 of multichannel radar data set IV (cf. Figure 6.9 top)(a) before and (b) after applying the phase correction algorithm proposed in [61]. (c) Histogram plots of the ATI phases for the ROI shown in (a) and (b).

multichannel radar data (cf. data set IV in Figure 6.9 top) before and after phase correction. The ATI phase offsets are estimated by multiplying the complex signal received by the first antenna element in the aircraft's azimuth direction with the complex conjugate of the co-registered signal of the second antenna.

In Figure 6.7(a) it can be seen that without applying the phase correction, the computed ATI phase offsets vary along range and azimuth due to the Euler angle variations caused by the atmospheric turbulence. However, after phase correction, the obtained ATI phases are well compensated and are nearly equal to zero (cf. Figure 6.7(b)). This is confirmed by the histogram plot shown in Figure 6.7(c) where the ATI phase offsets for the selected ROI are centered at zero degrees for the phase calibrated data.

6.7 Experimental Results and Discussion

After discussing important multichannel data processing steps and proposing different DOA angle estimation methods for extended targets, the performance of the proposed methods are evaluated in this section. Real ships present in real multichannel airborne radar data are used for the evaluation purposes. The multichannel radar data were acquired using DLR's DBFSAR airborne radar system in real maritime scenarios. This section first provides some details of the multichannel flight campaigns that were conducted using DBFSAR senor followed by the experimental results and discussions.

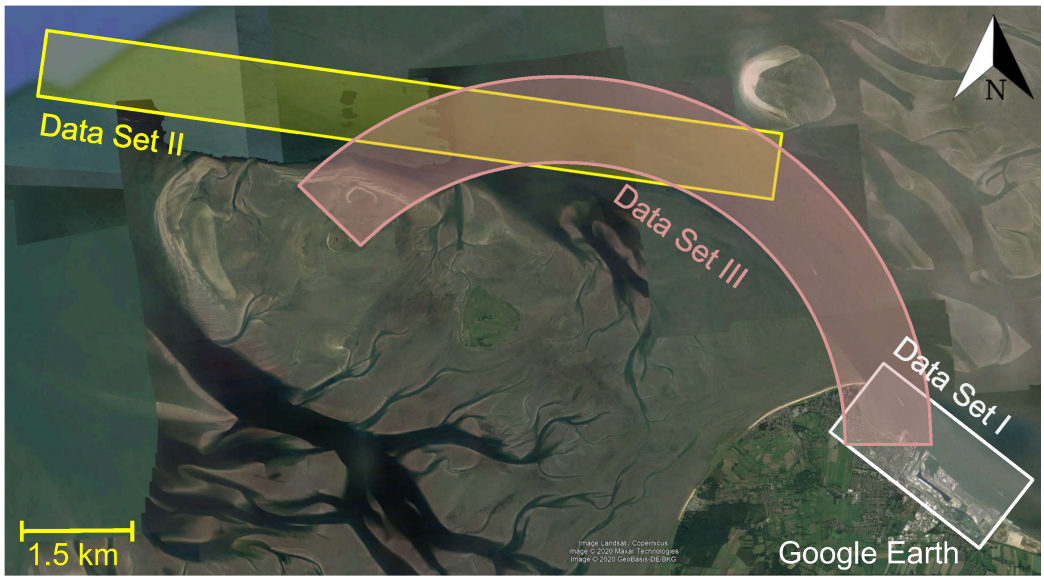

Figure 6.8: Google Earth image showing the test site in North Sea near Cuxhaven, Germany. The data sets marked in the figure are described in Table B.2 (cf. page 151).

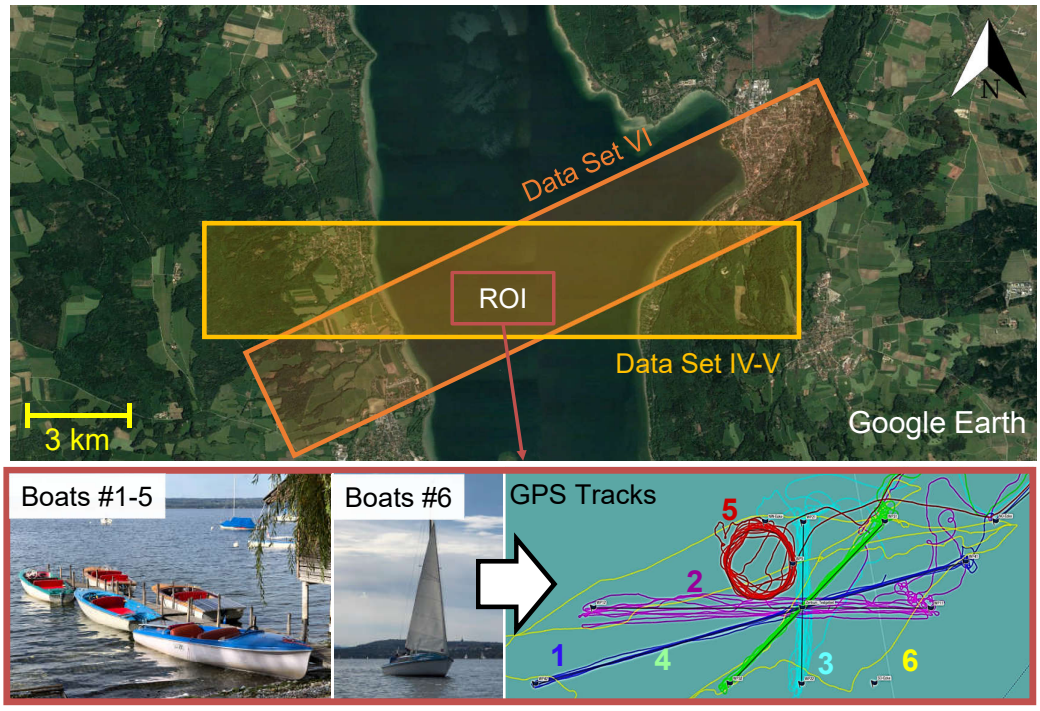

Figure 6.9: Top: Google Earth image of the Ammersee test site. The data sets marked in the figure are described in Table B.4 (cf. page 153). Bottom: Optical ground image of five small controlled electrical boats and one sailing boat with their corresponding GPS tracks [61].

6.7.1 Multichannel Flight Campaigns

Two multichannel flight campaigns using the DBFSAR airborne radar sensor were carried out in the frame of this doctoral thesis. The first flight campaign was conducted in 2019 in the North Sea near town Cuxhaven in Germany where several ships of opportunity were observed. Figure 6.8 shows the Google Earth image of the North Sea test site where several

multichannel radar data were acquired. In the figure data sets I and II were acquired during a linear flight track (in stripmap mode) and the data set III were acquired during a circular flight track to observe a semi-annulus region. The acquisition geometry and the system parameters of the acquired radar data are listed in Table B.2 (cf. page 151).

The second flight campaign was conducted in 2020 over the Lake Ammersee in southern Germany. Figure 6.9 top shows the the Google Earth view of the Ammersee test site. For the investigations three radar data sets from this campaign were considered. In the figure data set IV and V were acquired in the same azimuth direction. The radar data acquisition and geometry parameters for these data sets are listed in Table B.4 (cf. page 153).

The goal of the Ammersee flight campaign was to detect, track and geolocate slowly moving small boats. For this reason, five electrical boats (size $\approx$ 3.5 m x 1.5 m) and a sailboat (size $\approx$ 5.0 m x 2.0 m) were considered in this experiment. It can be seen in the bottom right of Figure 6.9 that the boats #1-4 moved in linear tracks whereas, boat #5 moved in circles and boat #6 moved freely within the given ROI.

6.7.2 Ground Truth Data

Ground truth data are needed for assessing the performance of the proposed DOA angle estimation methods and for evaluating the position accuracy achieved by these methods. For the North Sea campaign the received AIS positions from the ships (cf. Figure B.5) and for the Ammersee campaign the GPS positions of the boats (cf. Figure 6.9, bottom), obtained from handheld GPS tracking devices, are used as the ground truth.

Reference Ship Position

The GPS antenna of the AIS transceiver is used for determining the ship's "true" position on the ocean surface and for evaluating the ground position accuracy. However, the GPS antenna may be mounted at different positions on different ships. For instance, in Figure 6.4, the GPS antenna is located in the front of the ship, as shown by the red circle in the figure. Because of such inconsistency in the GPS antenna or the AIS positions, it is not advisable to use them directly for evaluating the position accuracy on the ground. Moreover, in Figure 6.4 it also can be observed, that the position estimates labeled with the red pins 1, 2, 3 and 4 are never located at the edges of the clustered pixel-based detections (white dots in Figure 6.4), but are located closer to the cluster center.

To address this issue and to make the evaluation fair and consistent, the actual geographical ship center position is computed for each ship and it is used as the reference position for accuracy assessment purposes. This ship center position is derived from the AIS data by taking into account the known ship dimensions (yellow border in Figure 6.4) and the known location of onboard GPS antenna (red dot in Figure 6.4). An example is already shown in Figure 6.4 where the green circle in the figure is the ship center position obtained from the AIS data. Note that this operation is required for the ships that are present in the North Sea data sets due to their large size, and it is not necessary for the

boats in the Ammersee campaign since the boats in the data are very small (less than 5 m).

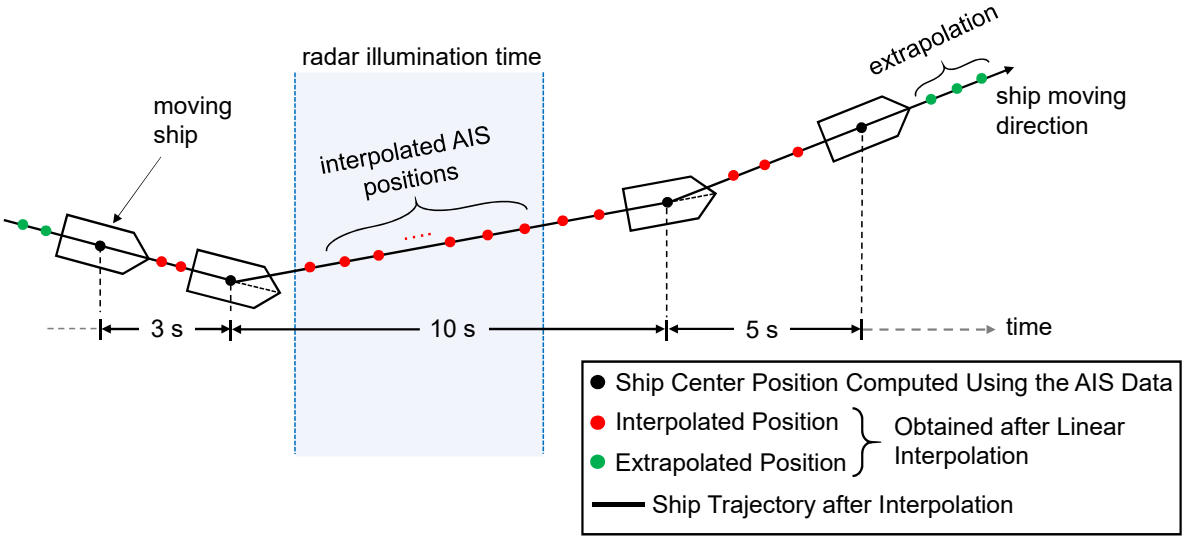

Figure 6.10: Exemplary illustration showing the interpolated AIS-based ship center positions which are obtained after linear interpolation. The figure also shows the time during which the airborne radar illuminates the ship. Ship center position computed from the AIS, interpolated and extrapolated (where the ship position is predicted after some time) positions in the figure are indicated by the black, red and green dots, respectively.

After computing the ship center positions, they are interpolated. Interpolation is necessary because the AIS-based ship position messages are obtained irregularly and their reporting interval can vary between two seconds and three minutes depending on the vessel's speed and/or course angle changes [136]. Besides, the time corresponding to the ship's center position do not usually match with the CPI center time of the radar acquisition.

To explain this, a simple example is shown in Figure 6.10. In the figure, irregularly received ship center positions from the AIS and the time when the airborne radar illuminates the ship (blue shaded region) can be seen. During the illumination the radar computes the geographical positions of the ship for different time instants. However, there are no corresponding AIS-based ship center positions available at the time of illumination. To fill the gaps in ship center positions, linear interpolation is performed with an assumption that between two ship center positions, the ship is moving with a constant velocity (cf. ship trajectory after interpolation in Figure 6.10). After interpolating the ship center positions it can be expected the true and the measured positions are both time-aligned and the position accuracy can be evaluated over time or over several successive CPIs (cf. Figure 6.13 center). Note that for future applications high precision is required. Therefore, instead of linear interpolation, a quadratic function or even higher order polynomial functions shall be used.

Reference DOA angle

The reference DOA angle is computed for validating the proposed DOA angle estimation methods. For computing the reference DOA angle, the reference range is first obtained.

If $(x_\mathrm{t}, y_\mathrm{t}, z_\mathrm{t})$ is the target position (reference ship center position) and $(x_\mathrm{p}, y_\mathrm{p}, z_\mathrm{p})$ is the aircraft position in (x, y, z) coordinate system (cf. Figure 6.5), the reference range $r_{\mathrm{t,ref}}$ is calculated as

$$r_{\mathrm{t,ref}} = \sqrt{(x_\mathrm{t} - x_\mathrm{p})^2 + (y_\mathrm{t} - y_\mathrm{p})^2 + (z_\mathrm{t} - z_\mathrm{p})^2}. \tag{6.20}$$

The reference DOA angle $\psi_{\mathrm{DOA,ref}}$ is then computed using the following expression

$$\psi_{\mathrm{DOA,ref}} = \cos^{-1}\left(\frac{x_\mathrm{t} - x_\mathrm{p}}{r_{\mathrm{t,ref}}}\right). \tag{6.21}$$

6.7.3 Phase Calibration Results

Before evaluating the accuracy of the proposed DOA angle estimation methods, the performance of phase calibration is first evaluated. For this, geocoding results of real targets in real multichannel data obtained before and after phase calibration are presented in this section. The results are shown in Figure 6.11. They are generated for the controlled boats which were present in the multichannel data set IV of the Ammersee campaign (cf. Figure 6.9 top). The ACA-based DOA angle estimation method shown in (6.9) and the geocoding method discussed in Section 6.5 are used for mapping the detections to the ground.

From Figure 6.11 top it can be seen that without applying phase correction the radar-based geocoded detections from the boats are significantly displaced from their corresponding actual GPS tracks, giving an average position error of approximately 200 m. However, after correcting the phases, the geocoded detections from the boats are found closer to their corresponding GPS tracks and the position error significantly reduced to less than 20 m. More discussions on the ground position accuracy achieved with and without phase calibration for all the boats in the multichannel data sets are provided in [61].

It is mentioned here that all plots, accuracy assessment tables and final geocoding results which will be shown in the next sections are obtained after phase calibration. This is because only after phase calibration the accuracy of the obtained estimates can be evaluated and compared with the ground truth data.

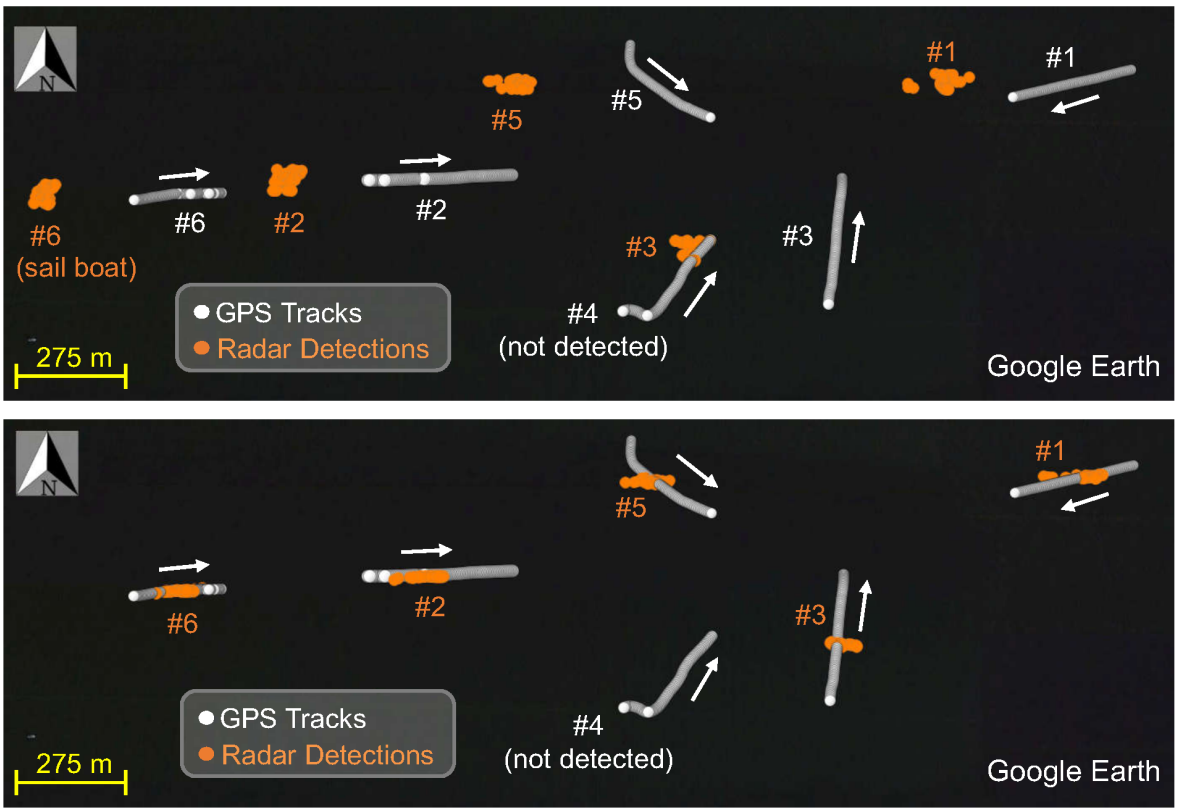

Figure 6.11: Geocoded radar detections (orange) and GPS tracks (white) of the moving boats in multichannel data set IV (cf. Figure 6.9 top): without (top) and with phase correction (bottom). The boats are shown in Figure 6.9 bottom. Boat #4 is not detected in the data due to its low SCNR. Arrows in the figure indicate the moving directions of the boats [61].

6.7.4 DOA Angle Distribution

Figure 6.12 provides a visual representation of the measured DOA angle distribution by plotting the PDF of the DOA angles for ship HAM 316 (cf. Figure 6.4 and data set I in Table B.3) obtained from a single CPI, together with the DOA angles computed using the methods proposed in Section 6.4.2.

From the figure it can be seen that the DOA angles seemingly follow a Gaussian distribution. In addition, the DOA angles estimated using the four methods, the DOA angle estimated from the AIS position and the reference DOA angle estimated from the ship center position are all within the $\pm 3\sigma_{\mathrm{DOA}}$ limit of the distribution.

In the next sections the performance of the proposed DOA angle estimation methods are evaluated. For the assessment of the proposed methods, the target's DOA angle difference, the azimuth position difference and the RMSE of the target absolute position on the ground are used as the performance metrics.

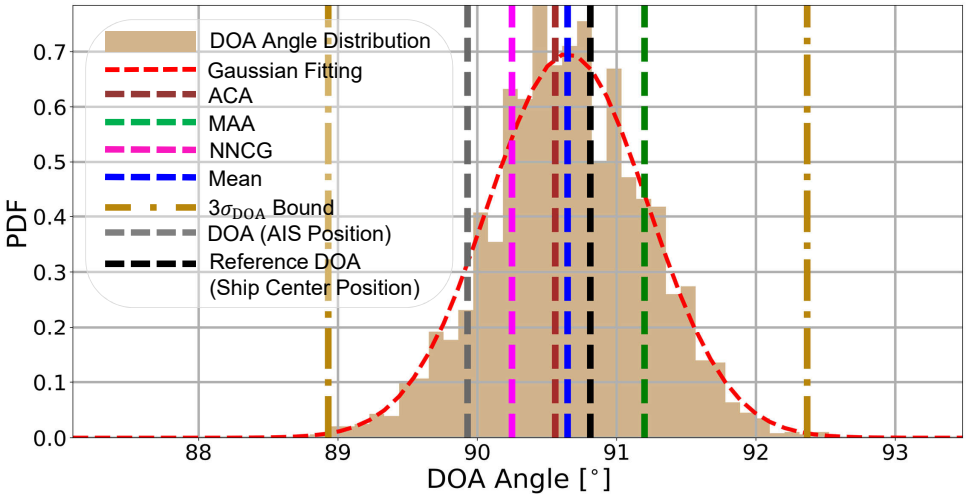

Figure 6.12: Normalized histogram of the estimated DOA angles available from ship HAM 316 (cf. Figure 6.4) in a single CPI. In the figure, the DOA angles estimated using the four proposed methods, the DOA angles based on the AIS position and the ship center position are shown.

6.7.5 DOA Angle and Azimuth Position Difference

The DOA angle difference $\Delta\psi_{\mathrm{DOA}}$ is computed between the estimated and the reference DOA angles of the target. The DOA angle difference is further used for computing the target's azimuth position difference Δx_{az} which is expressed as [60]

$$\Delta x_{\mathrm{az}} = r_{\mathrm{t}} \cdot \sin(\Delta\psi_{\mathrm{DOA}}), \tag{6.22}$$

where the term r_{t} is the target's slant range which in case of an extended target is obtained based on the method discussed in Section 4.1.2.

Figure 6.13 top and center show $\Delta\psi_{\mathrm{DOA}}$ and Δx_{az} estimates for the proposed methods over several successive CPIs for the ship AURORA, respectively. The ship is detected in data set III (cf. Figure 6.9) and its AIS-based specification are given in Table B.3 (cf. page 152).

For Figure 6.13 top the average DOA angle differences obtained using the ACA, MAA, NNCG and the mean DOA methods are 0.12°, 0.28°, 1.03° and 0.18°, respectively. Their corresponding average azimuth position differences are calculated as 7.06 m, 16.22 m, 59.73 m and 10.77 m, respectively.

For the methods based on MAA and NNCG, the DOA angle and the azimuth position differences are the highest. This is because the DOA angles calculated for these methods are based on the phase derived from a single pixel. Such a phase value is susceptible to a high additive phase noise component that can bias the estimated DOA angle and, hence, the ground position accuracy of the extended target, especially under low SCNR conditions which may occur due to small aspect angle change.

On the other hand, for the method based on ACA, the DOA angle is estimated after averaging the complex amplitude pixels of the target. By averaging it is expected that

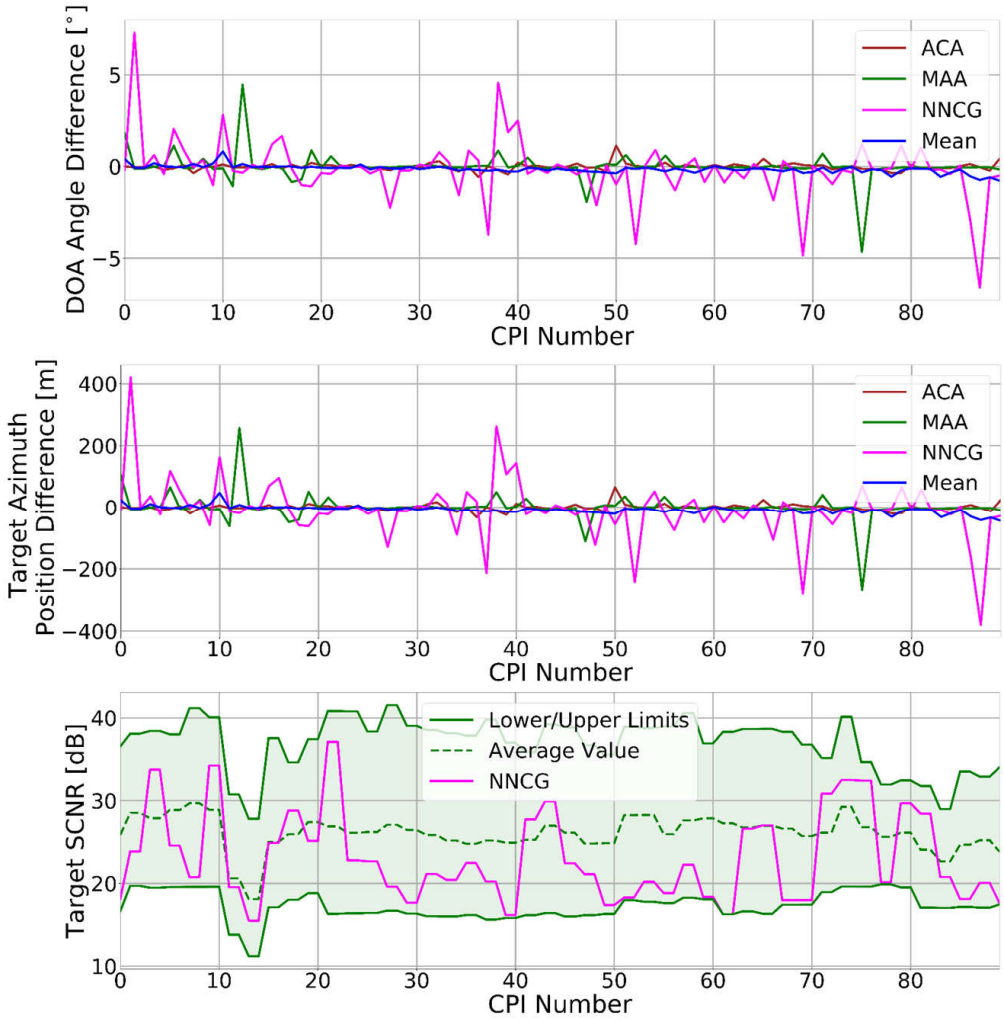

Figure 6.13: Ship AURORA: DOA angle difference (top), its corresponding azimuth position difference (center) and its SCNR band (bottom) over several successive CPIs.

the phase fluctuations among the detected target pixels is significantly reduced and thus, the estimated DOA angle is improved as shown by the brown curve in Figure 6.13 top. For the method based on the mean DOA angle, it can be seen that, like the ACA-based method, the estimated DOA angles and the azimuth position differences also show low fluctuations.

However, it is pointed out here that if individual CPIs contain thousands of detected target pixels, as shown in Figure 6.4, the ACA-based method can be up to thousand times faster than the mean DOA angle method. To show this, the average processing time needed for computing the DOA angles using all proposed methods are calculated and the results are shown in Table 6.1. Ship HAM 316 shown in Figure 6.4 was chosen for calculating the processing times needed by each method. Each method is executed hundred times and an average processing time is then obtained. The processing server used for this purpose is a 32-core 2.10 GHz Intel(R) Xeon(R) Gold 6130 CPU, which has several running tasks and is simultaneously used by other users (cf. Section 3.5.4).

In Table 6.1 it can be seen that in comparison to the ACA-based method, the mean DOA method is nearly four thousand times slower. This is because for the latter method,

Table 6.1: Average processing time of the proposed DOA estimation methods needed for determining the geographical positions of the ship HAM 316 shown in Figure 6.4 in a single CPI.

Estimation Methods	Processing time [s]
ACA	6.5e-03
MAA	5.07e-03
NNCG	5.46e-03
Mean DOA	21.22

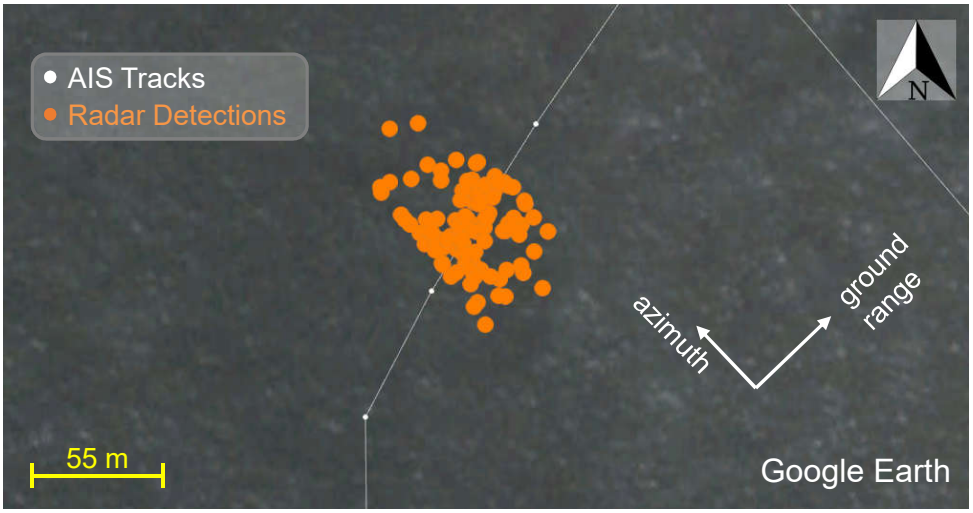

Figure 6.14: Google Earth visualization of ship AURORA. The AIS tracks (white) and radar-based geocoded detections (orange) of the ship for all CPIs are shown in the figure.

the beamforming and, hence, the DOA angle is estimated for each detected target pixel (cf. (6.5)) and for the ACA-based method, beamforming is performed only once, i.e., on the average complex target amplitude only. Therefore, the method based on ACA is more suitable for real-time applications.

The ACA-based method is used for geocoding the ship AURORA and its Google Earth representation is shown in Figure 6.14. In the figure the geocoded detections from the ship are shown for all CPIs (cf. Figure 6.13 where the ship has been detected and tracked in over 80 CPIs).

6.7.6 Ground Position Estimation Accuracy

This section is divided into two parts. In the first part the performance of the proposed DOA angle estimation methods using all ships present in 2019 North Sea multichannel radar data sets are evaluated. Based on the geocoding results, an appropriate DOA angle estimation method is then selected. In the second part the selected DOA angle estimation method from the first part is used for evaluating the ground position estimation accuracy of the boats in the Ammersee data sets followed by their Google Earth visualizations.

Table 6.2: RMSE assessment of the absolute ground positions of all the ships in the North Sea multichannel data sets using the proposed DOA angle estimation methods. The AIS-based specifications of the ships are given in Table B.5 (cf. page 151). The numbers in bold show the best accuracy achieved with the proposed methods. Tracking time and the target average SCNR values are some additional information of the ships obtained after tracking (cf. Chapter 5).

	Absolute Ground Position Error [m]				Tracked Time [s]	Target Average SCNR [dB]
	ACA	MAA	NNCG	Mean		
Ship Name			Data Set I			
LANGELAND	27.27	62.17	110.47	**12.22**	4.31	28.76
LONGDUIN	34.83	35.91	59.79	**11.82**	2.85	19.32
HAM 316	37.44	51.34	159.92	**27.55**	4.25	27.71
			Data Set II			
CHARISMA	15.98	41.71	89.76	**12.32**	4.72	23.45
HOFFNUNG CUX10	**11.91**	48.33	80.79	14.44	4.85	22.16
SAPHIR	9.21	38.82	98.08	**6.67**	5.49	29.11
GEO GRAPH	17.39	32.31	69.29	**13.43**	4.13	25.18
UTHOERN	11.39	24.67	86.42	**6.05**	4.13	27.43
WANGEROOGE	14.22	52.21	52.86	**11.86**	3.96	25.35
FAIR LADY	30.03	66.38	129.65	**28.13**	6.62	32.35
MT BLUE STAR	111.54	**98.63**	166.17	100.93	4.68	28.64
VEGA GRANAT	69.02	58.18	135.95	**37.05**	4.17	31.03
			Data Set III			
GEO GRAPH	14.66	64.31	126.49	**12.18**	4.04	28.55
TINA CUX-5	**17.35**	50.99	144.35	19.65	4.72	25.64
AURORA	**13.52**	45.06	110.19	17.33	4.04	26.07
PILOTVESSEL HANSE	**23.08**	106.84	109.24	42.97	3.45	31.93
RMS RATINGEN	**32.82**	53.03	140.59	33.25	3.49	33.25
LONGDUIN	48.93	54.05	188.77	**26.03**	3.79	30.11
Average	30.03	54.72	114.38	**24.14**		

The ground position accuracy results for all the ships in North Sea data sets obtained using the DOA estimation methods proposed in Section 6.4.2 are shown in Table 6.2. The methods based on the mean DOA angle and the ACA are the best ones, achieving an overall position accuracy of 24 m and 30 m, respectively. Among these two methods, the ACA-based method is preferred because it is by a factor of thousand times computationally more efficient than the mean DOA angle method (cf. Table 6.1), making it a suitable choice for future real time applications where low processing time is important.

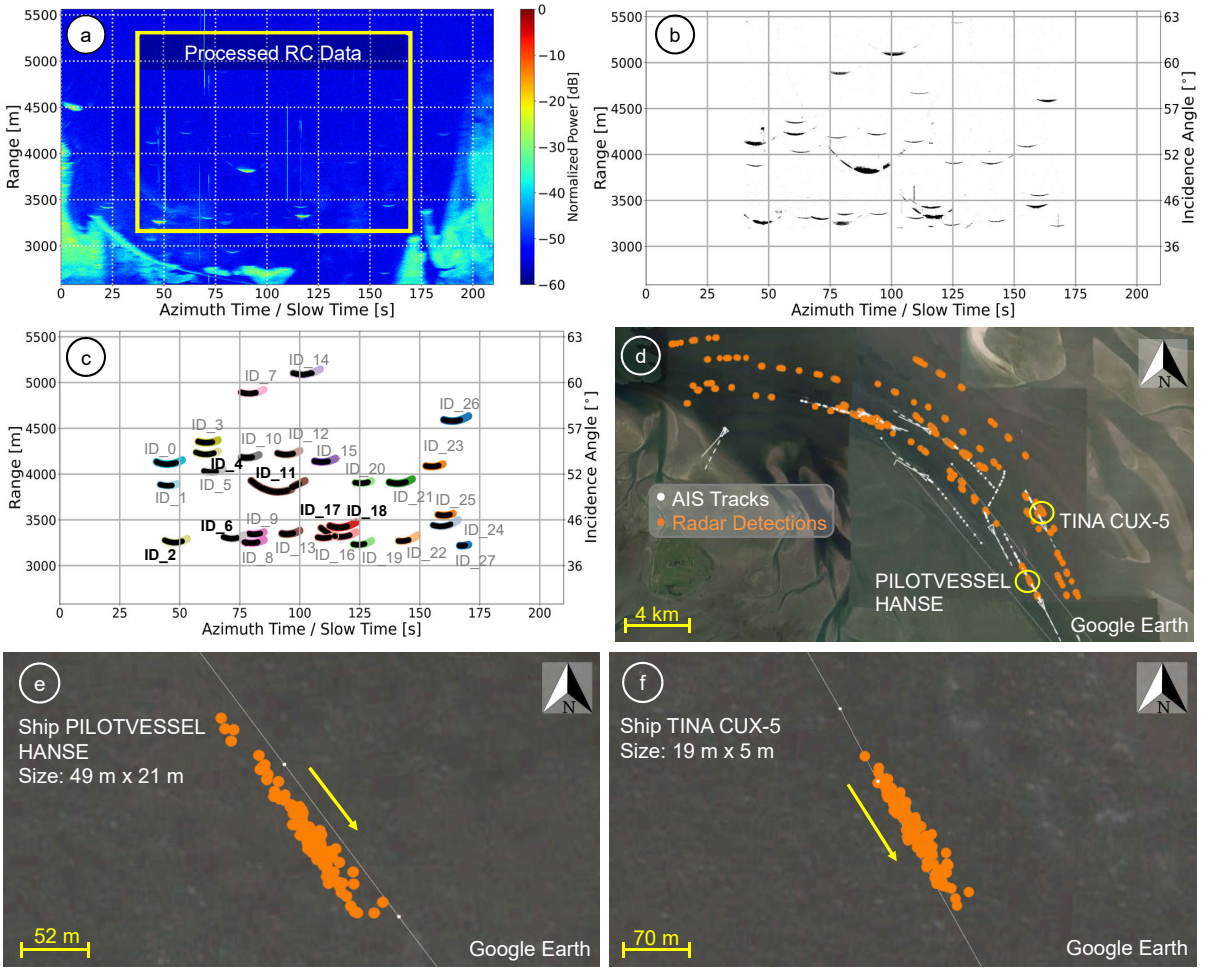

Figure 6.15: Geocoding results for multichannel radar data set III. (a) Real RC X-band VV polarized airborne radar data. The data were acquired during a circular flight track to observe a semi-annulus region. RC data containing only the ocean is shown within the yellow box in the figure. (b) Binary target detection map of the processed RC data shown in (a). (c) Ship tracking results. Tracked ships with their individual IDs are marked in the figure. Targets with ID_2, ID_4, ID_6, ID_11, ID_17 and ID _18 corresponds to ships PILOTVESSEL HANSE, TINA CUX-5, AURORA, LONGDUIN, RMS RATINGEN and GEO GRAPH, respectively (cf. Data set III in Table 6.2). (d) Google Earth visualization of the geocoded radar-based detections of all the tracked ships in the data. Detailed view of the mapped detections from (e) Ship PILOTVESSEL HANSE and (f) Ship TINA CUX-5. Ship dimensions are shown in the figure. The arrows indicate the ships' moving direction.

The ACA-based method is used for geocoding the radar-based detections of all the ships in North Sea data sets. Figure 6.15 shows the geocoding results of the multichannel data set III (semi-circular flight in Figure 6.8). Along with the geocoding results, its corresponding detection and tracking results are also provided. For the multichannel data sets I and II, their final geocoding results are shown in Figures C.1 (page 155) and C.2 (page 156), respectively.

The ACA-based DOA angle estimation method is also used for calculating the absolute ground position errors of the detected boats in the Ammersee data sets IV-VI (cf. Figure 6.9). The results are shown in Table 6.3. From the table it can be seen that the position errors of the boats are better than 20 m, which can be considered very good, given the

Table 6.3: Absolute ground position errors of the detected boats in multichannel data sets IV-VI. Boats #1-5 are the electric boats and Boat #6 is the sailboat (cf. Figure 6.9 bottom) [61].

Boat (#)	Absolute Ground Position Error [m]	Tracking Time [s]	Target Average SCNR [dB]	Ship Moving Direction w.r.t the Aircraft [°]
Data Set IV				
1	17.21	3.83	17.40	12
2	16.62	3.06	16.43	180
3	10.42	1.96	15.96	262
5	10.21	3.53	15.29	141
6	9.72	3.62	18.63	177
Data Set V				
1	9.67	2.34	19.27	195
2	15.84	3.45	17.95	176
4	10.19	2.55	16.83	227
5	14.33	2.46	14.27	-47
6	10.31	3.74	19.11	40
Data Set VI				
1	19.16	3.28	17.12	175
2	10.21	3.36	15.71	-23
3	7.63	0.68	13.71	239
4	10.39	3.48	19.44	186
5	13.38	3.23	14.15	-72
6	9.31	2.04	22.61	-13

SCNR of the moving boats and the strongly changing aircraft Euler angles of the acquired radar data (cf. Figure 6.6 left).

Note that in data set IV and V in Table 6.3, Boat #4 and Boat #3 were not detected, respectively. This is because the boats have low reflectivity due to their dimensions and structure. Moreover, since the boats were also moving very slow, they were embedded inside the clutter region, making them harder to detect. One way to enhance the detectability of these boats is to use either sum-channel data or STAP-based clutter-suppressed data (cf. mode 2 and mode 3 in Figure 6.2). However, these investigations are out of the scope of the present doctoral thesis.

Finally, Figure 6.16 shows the geocoding results obtained for data set VI using the ACA method. Similar to Figure 6.15, its corresponding detection and tracking results are also provided. For multichannel data sets IV and V, their final geocoding results are shown in Figures C.3 and C.4 in pages 157 and 158, respectively.

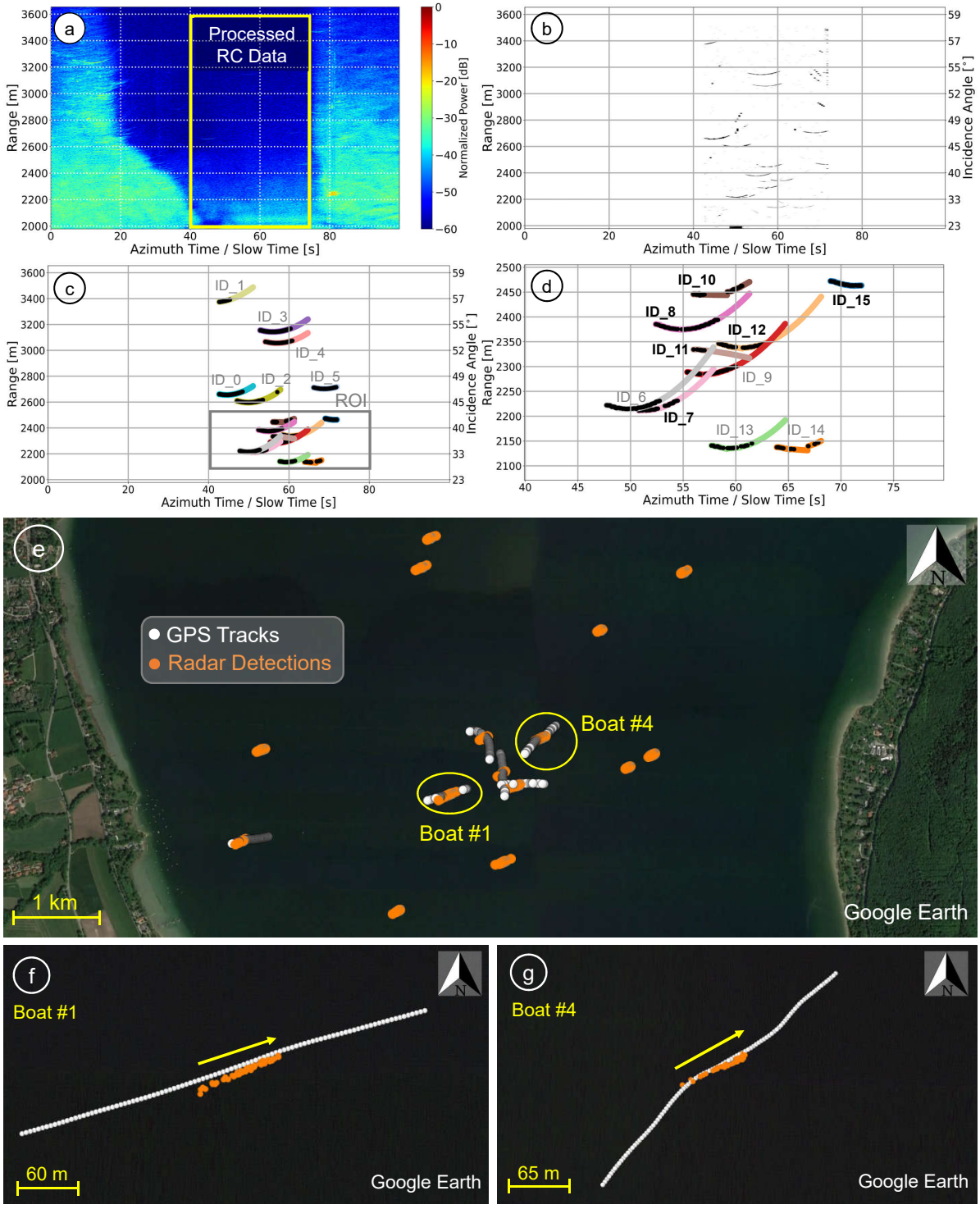

Figure 6.16: Geocoding results for multichannel radar data set VI. (a) Real RC X-band VV polarized airborne radar data. Data containing the radar backscatter from the lake region is shown within the yellow box in the figure. (b) Binary target detection map of the processed RC data shown in (a). (c) Tracking results. Tracked targets with their individual IDs are marked in the figure. (d) Zoom in detail of the ROI shown in (c). The ROI contains the controlled boats used for the experiments. All boats are detected in this data set. Targets with ID_7, ID_8, ID_10, ID_11, ID_12, and ID_15 corresponds to Boat numbers 2, 4, 5, 3, 1 and 6, respectively (cf. Data set VI in Table 6.3). (e) Google Earth visualization of the geocoded radar-based detections of all the tracked targets in the data. Detailed view of the mapped detections from (f) Boat #1 and (g) Boat #4. Arrows indicate the boats' moving direction.

6.7.7 Line-of-Sight Velocity and Moving Direction Estimation

Although not investigated in this chapter the velocity and the moving direction of the target can be estimated using the ground track information shown in Figure 6.17. In the figure the target is assumed to move along a straight line with a certain velocity v_0 and moving direction α_t. For simplicity, the target acceleration is ignored in the estimation and the target is assumed to move with a constant velocity.

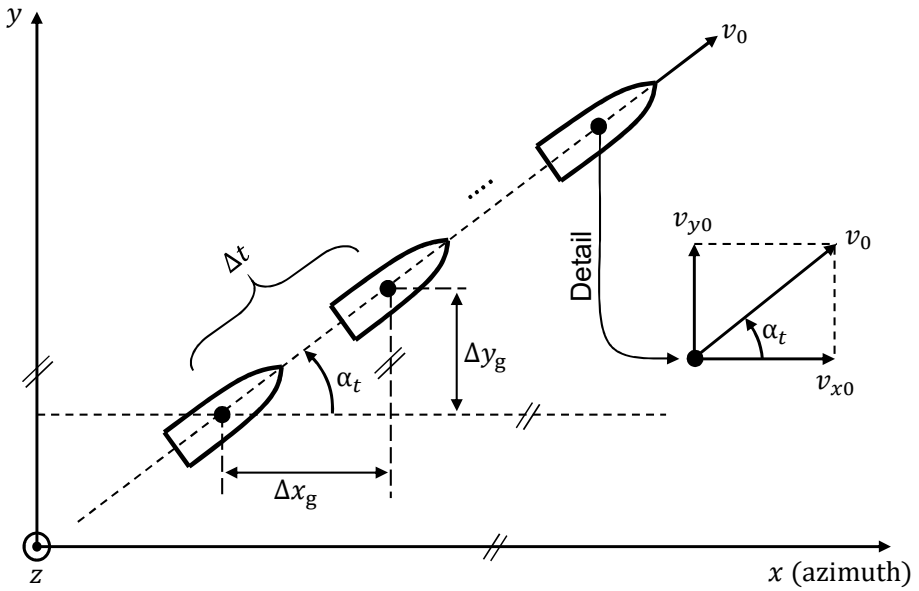

Figure 6.17: Target moving along a straight line in Cartesian coordinates. In the figure target's absolute ground velocity and moving direction are shown.

Assuming that the target has moved distances Δx_g in along-track and Δy_g in across-track direction in time Δt, then the target's along-track velocity $\hat{v}_\mathrm{x0}$ and the ground range velocity $\hat{v}_\mathrm{y0}$ can be estimated as

$$\hat{v}_\mathrm{x0} = \frac{\Delta x_\mathrm{g}}{\Delta t}, \tag{6.23}$$

$$\hat{v}_\mathrm{y0} = \frac{\Delta y_\mathrm{g}}{\Delta t}, \tag{6.24}$$

respectively. The absolute ground velocity of the target is then computed as

$$\hat{v}_0 = \sqrt{\hat{v}_\mathrm{x0}^2 + \hat{v}_\mathrm{y0}^2}. \tag{6.25}$$

The target's moving direction with respect to the along-track direction can be obtained by using

$$\hat{\alpha}_{\mathrm{t}} = \arctan\left(\frac{\hat{v}_{\mathrm{y0}}}{\hat{v}_{\mathrm{x0}}}\right). \tag{6.26}$$

For estimating the target motion parameters using (6.25) and (6.26), large tracking times are required so that the targets are able to travel at least their size during the total observation time. However, not all ships, especially larger ones with short tracking times, manage to travel their own lengths in total illumination time. For these vessels the LOS velocity computed from (6.8) and the estimated Doppler slope obtained as a byproduct of the ISAR imaging algorithm can be used for a rough velocity and moving direction estimation [33,137]. The investigation of these promising approaches are left for the future (cf. #3 in Section 7.2).

6.8 Chapter Summary

In this chapter a comprehensive multichannel radar data processing and geocoding techniques for projecting extended targets on the ground were presented. Targets were mapped to the ground after estimating their DOA angles via a geocoding operation. Different DOA angle estimation methods for extended targets were proposed and discussed in this chapter. The accuracy of the proposed methods were evaluated using real X-band VV polarized multichannel radar data sets acquired with the DLR's DBFSAR system, in which ships and boats with different dimensions and moving directions were contained. Based on the experimental results, it is recommended using the average complex amplitude method for estimating the DOA angles of extended targets. This method allows not only for achieving an acceptable position accuracy, but it is also computationally efficient and has real-time processing capability.

It is pointed out here that in two of the investigated multichannel radar data, two slowly moving boats (one in each data) were not detected because of very strong clutter power contribution. In the future clutter suppression techniques based either on STAP or displaced phase center antenna (DPCA) [138] are envisaged to improve the target detection capability. Furthermore, in this doctoral thesis, due to lack of appropriate multichannel radar data, target motion parameters such as absolute velocity on the ground and moving direction were not estimated. Therefore, more flight experiments shall be planned in the future, especially circular flights with long observation times like the one shown in Figure B.1 bottom (cf. page 147) which unfortunately, was carried out without having multiple RX channels. In future campaigns, similar flight tracks will be considered but with the multichannel DBFSAR system.

7 Discussion and Outlook

This section summarizes the results obtained in this doctoral thesis and provides an outlook for the future research and development on airborne radar-based maritime moving target monitoring using these results.

7.1 Discussion

In this thesis a maritime surveillance processing chain using airborne radar sensors was presented. The thesis contributed to the development of novel algorithms for target detection, tracking and geocoding modules of the processing chain. As input range-compressed (RC) airborne radar data were used for developing the algorithms. For target detection and tracking, single-channel RC radar data whereas for geocoding, multichannel RC radar data were used. The reasons for preferring RC data over fully focused SAR images were justified in Chapter 2.

Target detection was carried out in the range-Doppler domain of the RC data. The benefits of detecting targets in the range-Doppler domain were explained in Section 2.6. Targets were detected after computing a threshold using CFAR-based sea clutter models. For a valid and bias-free detection threshold computation, "target-free" ocean training data is necessary. Therefore, an automatic training data extraction procedure was developed in Chapter 3. It has a novel target pre-detection module which cancels the outliers in the form of bright target peaks and high clutter peaks in time domain, followed by normalization over Doppler with remaining samples and finally, detection threshold computation using a suitable sea clutter model.

Considering the strong sea spikes, present mainly in the near and mid range ($15° - 30°$ incidence angle), and the low CNR (clutter-to-noise ratio) in the far range ($> 50°$ incidence angle) of the airborne radar data, it was found that the conventional K-distribution model is not a good choice. Therefore, several stochastic sea clutter models were investigated in the chapter and two different models for CFAR detection were recommended: the K-Rayleigh distribution in near and mid ranges and the 3MD model in far range. In these models, the threshold amplitude errors and the false alarm rate errors were found to be at the minimum level, which significantly improved the target detection capability at the cost of increased computation time.

After detection, individual ships were tracked in the range-Doppler domain using a motion model proposed in Chapter 4. Since ships are extended targets in high resolution data, the center of gravity of the ship clusters were tracked by the motion model. The motion model was incorporated in the framework of the Kalman filter for a more robust and efficient target state estimation. The proposed motion model together with the Kalman

filter provide not only an accurate target motion modeling but it also has the ability to close the gaps in the target trajectory caused due to several missed target detections.

Furthermore, in a multi-target tracking (MTT) scenario, along with the target motion model and the Kalman filter, a data association method was proposed in Chapter 5 for associating the detections at the current time step with already existing tracks for reconstructing the trajectory of individual targets. During tracking, several false or ghost target tracks were automatically recognized and terminated by the track management algorithm, which was integrated within the tracker. In addition, the tracker was also able to detect and correct the Doppler aliasing for obtaining target range and Doppler history without any wrapping effects. The entire MTT framework was developed using a SQLite database structure. The database can store all the tracked targets with their relevant motion-related parameters which can easily be extracted with low efforts, if required in future. The target tracks in range-Doppler were then utilized for two main applications; first, for extracting simultaneously the ship data patches in time domain which can be used for generating the high resolution inverse SAR (ISAR) image sequences of the target and second, for projecting the target tracks to ground after computing additionally the DOA angle using the multichannel radar system.

In Chapter 6 different DOA angle estimation methods for geocoding the extended targets using multichannel radar data were proposed. Based on the experimental results which contained real ships and small boats with different dimensions and moving directions, it was recommended to use the method based on the average complex amplitude. This method was found not only computationally more efficient, but also gave a position accuracy of less than 30 m, which is very good for radar-based ship monitoring using an airborne radar sensor.

In this thesis, all the aforementioned algorithms are complete and fully functional. The overall performance of these algorithms have high potential for airborne radar-based moving target monitoring, especially when taking into account that the algorithms are applicable for simple to complex real maritime scenarios and to strongly changing aircraft attitude angles.

7.2 Future Work and Outlook

The ongoing research activities presented in this section will incorporate the results and findings of this doctoral thesis to further strengthen the ship surveillance capability of airborne radars.

1. **Optimization of the detection algorithm:** The detection algorithm presented in Chapter 3 showed very good detection performance at the cost of high computation time (cf. Table 3.6). In future a multiprocessing approach where multiple cores will be used for implementing the algorithm in a parallelized manner, taking also into account graphical processing units (GPUs) is recommended for reducing the computation time.

2. **Clutter suppression using multichannel data:** In the case of high sea states where the radar backscatter received from the sea clutter is very strong, the detectability of slow moving targets with low RCS significantly decreases. In order to improve the target detection capability various clutter suppression techniques based on, e.g., DPCA or STAP shall be investigated. By suppressing the clutter and increasing the target SCNR, these techniques will enable the detectability of the targets with low RCS embedded within the clutter Doppler spectrum. For this, additional flight campaigns over locations with different sea states are needed.

3. **Ship motion parameter estimation:** Methods for estimating relevant ship motion parameters such as its absolute ground velocity and moving direction shall be investigated. For instance, the DOA equation shown in (6.7) and the focusing parameters obtained from the ISAR imaging may be used for estimating the LOS velocity and the moving direction, respectively. In addition, for ships that have traveled more than their size during the entire observation time, their motion parameters can also be estimated using (6.25) and (6.26). Note that to improve the accuracy of the estimated motion parameters, an additional tracking of the computed geocoded positions might be needed. Such a tracking may refine the ground position of the target, thereby improving not only the accuracy of the target's position on the ground but also the accuracy of the estimated motion parameters.

4. **Ship size estimation:** Ship dimensions are one of the salient features for ship discrimination and classification. High resolution radar data (i.e., ISAR images) have an advantage that ships usually appear as extended targets occupying more than a single radar resolution cell. Such data can be exploited for ship size estimation. In the future various methods, for instance, polygon fitting or deep learning-based methods [139, 140] shall be investigated for estimating the ship size and also its orientation over several successive CPIs.

5. **More flight experiments:** More radar data sets are needed to further enhance the robustness of the algorithms developed in the frame of this thesis. Therefore, more flight experiments shall be planned in the future acquiring multichannel radar data along circular or even arbitrary flight tracks with longer observation times. These data sets shall be acquired at different sea states and shall contain different types of boats moving at different speeds and moving directions.

Bibliography

[1] Statista Research Department, "Number of ships in the world merchant fleet as of January 1, 2021, by type," https://www.statista.com/statistics/264024/number-of-merchant-ships-worldwide-by-type/, 2021, [Online; accessed 18-March-2022].

[2] The Maritime Excecutive, "IMB: Gulf of Guinea attacks drive increase in global piracy numbers," https://www.maritime-executive.com/article/imb-gulf-of-guinea-attacks-drive-increase-in-global-piracy-numbers, 2021, [Online; accessed 18-Jan-2021].

[3] Infomigrants, "2021: Migrants continue to cross channel in hope of reaching UK," https://www.infomigrants.net/en/post/29579/2021-migrants-continue-to-cross-channel-in-hope-of-reaching-uk, 2021, [Online; accessed 18-Jan-2021].

[4] WSPA, "Illegal fishing nets kill sea turtles in waters off South Texas near maritime boundary line," https://www.wspa.com/news/illegal-fishing-nets-kill-sea-turtles-in-waters-off-south-texas-near-maritime-boundary-line/, 2021, [Online; accessed 18-Jan-2021].

[5] J. Kraska and R. Pedrozo, *International Maritime Security Law*. Martinus Nijhoff Publishers, 2013.

[6] F. Vreÿ, "Turning the tide: Revisiting African maritime security," *Scientia Militaria: South African Journal of Military Studies*, vol. 41, no. 2, pp. 1–23, 2013.

[7] N. Klein, *Maritime Security and the Law of the Sea*. Oxford University Press, 2011.

[8] H. M. Helal and O. I. Hassan, "Maritime surveillance: An integral part of maritime security," *Border Security and Safety*, pp. 184–195, 2017.

[9] International Maritime Organization, "Vessel traffic services," https://www.imo.org/en/OurWork/Safety/Pages/VesselTrafficServices.aspx, [Online; accessed 14-Jan-2021].

[10] ——, "Long-range identification and tracking (LRIT)," https://www.imo.org/en/OurWork/Safety/Pages/LRIT.aspx, [Online; accessed 14-Jan-2021].

[11] European Commission, "Vessel monitoring system (VMS)," https://ec.europa.eu/fisheries/cfp/control/technologies/vms_en, [Online; accessed 14-Jan-2021].

[12] International Maritime Organization, "AIS transponders," https://www.imo.org/en/OurWork/Safety/Pages/AIS.aspx, [Online; accessed 14-Jan-2021].

[13] A. G. Bole, A. D. Wall, and A. Norris, *Radar and ARPA Manual: Radar, AIS and Target Tracking for Marine Radar Users*. Butterworth-Heinemann, 2013.

[14] W. Wei, P. Yingning, Q. Taifan, and L. Yongtan, "HF OTHR target detection and estimation subsystem," *IEEE Aerospace and Electronic Systems Magazine*, vol. 14, no. 4, pp. 39–45, 1999.

[15] Y. Cheng, "Satellite-based AIS and its comparison with LRIT," *TransNav: International Journal on Marine Navigation and Safety of Sea Transportation*, vol. 8, no. 2, pp. 183–187, 2014.

[16] E. Meger, "Limitations of satellite AIS: Time machine wanted!" https://www.cloudeo.group/sites/default/files/product_images/06_Limitations_of_Satellite_AIS.pdf, [Online; accessed 14-Jan-2021].

[17] J. N. Briggs, *Target Detection by Marine Radar*. Institution of Engineering and Technology, 2004.

[18] K. Granström, A. Natale, P. Braca, G. Ludeno, and F. Serafino, "PHD extended target tracking using an incoherent X-band radar: Preliminary real-world experimental results," in *17th International Conference on Information Fusion*. Salamanca, Spain: IEEE, 2014, pp. 1–8.

[19] G. Vivone, P. Braca, K. Granström, A. Natale, and J. Chanussot, "Converted measurements random matrix approach to extended target tracking using X-band marine radar data," in *18th International Conference on Information Fusion*. Washington, DC, USA: IEEE, 2015, pp. 976–983.

[20] G. Vivone and P. Braca, "Joint probabilistic data association tracker for extended target tracking applied to X-band marine radar data," *IEEE Journal of Oceanic Engineering*, vol. 41, no. 4, pp. 1007–1019, 2016.

[21] G. Siegert, J. Hoth, P. Banyś, and F. Heymann, "Generic framework for vessel detection and tracking based on distributed marine radar image data," *CEAS Space Journal*, vol. 11, no. 1, pp. 65–79, 2019.

[22] J. S. Fowdur, M. Baum, and F. Heymann, "Tracking targets with known spatial extent using experimental marine radar data," in *22th International Conference on Information Fusion*. Ottawa, ON, Canada: IEEE, 2019, pp. 1–8.

[23] Furuno, "Operator's guide to marine radar," https://www.hwhelectronics.com/pdf/furuno-radar-guide-min.pdf, [Online; accessed 14-Jan-2021].

[24] D. S. Ilcev, "Introduction to coastal HF maritime surveillance radars," *Polish Maritime Research*, vol. 26, no. 3, pp. 153–162, 2019.

[25] B.-Y. Liu, "HF Over-the-horizon radar system performance analysis," Naval Postgraduate School Monterey, California, techreport ADA474069, 2007.

[26] T. Ponsford and J. Wang, "A review of high frequency surface wave radar for detection and tracking of ships," *Turkish Journal of Electrical Engineering and Computer Sciences*, vol. 18, no. 3, pp. 409–428, 2010.

[27] P. Braca, R. Grasso, M. Vespe, S. Maresca, and J. Horstmann, "Application of the JPDA-UKF to HFSW radars for maritime situational awareness," in *15th International Conference on Information Fusion*. Singapor: IEEE, 2012, pp. 2585–2592.

[28] P. Braca, S. Maresca, R. Grasso, K. Bryan, and J. Horstmann, "Maritime surveillance with multiple over-the-horizon HFSW radars: An overview of recent experimentation," *IEEE Aerospace and Electronic Systems Magazine*, vol. 30, no. 12, pp. 4–18, 2015.

[29] C. A. Balanis, *Antenna theory: Analysis and Design*. John wiley & sons, 2016.

[30] M. I. Skolnik, *Introduction to Radar Systems.* McGraw Hill, 1980.

[31] I. G. Cumming and F. H. Wong, *Digital Processing of Synthetic Aperture Radar Data.* Artech House Publishers, 2005.

[32] A. Moreira, P. Prats-Iraola, M. Younis, G. Krieger, I. Hajnsek, and K. P. Papathanassiou, "A tutorial on synthetic aperture radar," *IEEE Geoscience and Remote Sensing Magazine*, vol. 1, no. 1, pp. 6–43, 2013.

[33] S. V. Baumgartner and G. Krieger, "Chapter 18 - Multi-channel SAR for ground moving target indication," in *Academic Press Library in Signal Processing: Volume 2.* Elsevier, 2014, vol. 2, pp. 911–986.

[34] S. V. Baumgartner, "Traffic monitoring with air-and spaceborne synthetic aperture radar," phdthesis, Fakultät für Elektrotechnik und Informationstechnik, Karlsruhe Institute of Technology, 2014.

[35] Andreas Reigber, Ralf Horn, Anton Nottensteiner, Pau Prats, Rolf Scheiber, Karl-Heinz Bethke and Stefan Baumgartner, "Current status of DLR's new F-SAR sensor," in *8th European Conference on Synthetic Aperture Radar.* Aachen, Germany: VDE, 2010, pp. 1–4.

[36] Andreas Reigber, Eric Schreiber, Kurt Trappschuh, Sebastian Pasch, Gerhard Müller, Daniel Kirchner, Daniel Gesswein, Stefan Schewe, Anton Nottensteiner, Markus Limbach, Alicja Schreiber, Tobias Rommel, Ralf Horn, Marc Jäger, Rolf Scheiber, Stefan V. Baumgartner, Sushil Kumar Joshi, Andre Barros Cardoso da Silva and Alberto Moreira, "The high-resolution digital-beamforming airborne SAR system DBFSAR," *Remote Sensing*, vol. 12, no. 11, p. 1710, 2020.

[37] J. H. Ender and A. R. Brenner, "PAMIR–A wideband phased array SAR/MTI system," *IEE Proceedings-Radar, Sonar and Navigation*, vol. 150, no. 3, pp. 165–172, 2003.

[38] V. Gracheva and D. Cerutti-Maori, "First results of maritime MTI with PAMIR multichannel data," in *International Conference on Radar.* Adelaide, SA, Australia: IEEE, 2013, pp. 458–463.

[39] N. Stacy and M. Burgess, "Ingara: The Australian airborne imaging radar system," in *International Geoscience and Remote Sensing Symposium*, vol. 4. Pasadena, CA, USA: IEEE, 1994, pp. 2240–2242.

[40] D. J. Crisp, N. J. Stacy, D. Hudson, P. B. Pincus, and A. S. Goh, "Polarimetric analysis of maritime SAR data collected with the DSTO Ingara X-band radar," in *International Geoscience and Remote Sensing Symposium.* Barcelona, Spain: IEEE, 2007, pp. 3870–3873.

[41] R. Werninghaus and S. Buckreuss, "The TerraSAR-X mission and system design," *IEEE Transactions on Geoscience and Remote Sensing*, vol. 48, no. 2, pp. 606–614, 2009.

[42] G. Krieger, A. Moreira, H. Fiedler, I. Hajnsek, M. Werner, M. Younis, and M. Zink, "TanDEM-X: A satellite formation for high-resolution SAR interferometry," *IEEE Transactions on Geoscience and Remote Sensing*, vol. 45, no. 11, pp. 3317–3341, 2007.

[43] S. V. Baumgartner and G. Krieger, "Dual-platform large along-track baseline GMTI," *IEEE Transactions on Geoscience and Remote Sensing*, vol. 54, no. 3, pp. 1554–1574, 2015.

[44] D. J. Crisp, "A ship detection system for RADARSAT-2 dual-pol multi-look imagery implemented in the ADSS," in *International Conference on Radar*. Adelaide, SA, Australia: IEEE, 2013, pp. 318–323.

[45] P. W. Vachon, C. Kabatoff, and R. Quinn, "Operational ship detection in Canada using RADARSAT," in *International Geoscience and Remote Sensing Symposium*. Quebec City, QC, Canada: IEEE, 2014, pp. 998–1001.

[46] F. Covello, F. Battazza, A. Coletta, E. Lopinto, C. Fiorentino, L. Pietranera, G. Valentini, and S. Zoffoli, "COSMO-SkyMed an existing opportunity for observing the Earth," *Journal of Geodynamics*, vol. 49, no. 3, pp. 171–180, 2010.

[47] D. Pastina, F. Fico, and P. Lombardo, "Detection of ship targets in COSMO-SkyMed SAR images," in *RadarCon (RADAR)*. Kansas City, MO, USA: IEEE, 2011, pp. 928–933.

[48] M. Mertens and R. Kohlleppel, "Ground target tracking with experimental data of the PAMIR system," in *17th International Conference on Information Fusion*. Salamanca, Spain: IEEE, 2014, pp. 1–8.

[49] S. V. Baumgartner, "Linear and circular ISAR imaging of ships using DLR's airborne sensor F-SAR," in *International Conference on Radar Systems*. Belfast, UK: IET, 2017, pp. 1–5.

[50] S. Brusch, S. Lehner, T. Fritz, M. Soccorsi, A. Soloviev, and B. van Schie, "Ship surveillance with TerraSAR-X," *IEEE Transactions on Geoscience and Remote Sensing*, vol. 49, no. 3, pp. 1092–1103, 2011.

[51] C. Livingstone, M. Dragosevic, and S. Chu, "Ship detection and measurement of ship motion by multi-aperture synthetic aperture radar," Defence Research and Development Canada, techreport DRDC-RDDC-2014-R17, 2014.

[52] S. V. Baumgartner and S. K. Joshi, "Promising techniques for future maritime surveillance demonstrated with DLR's airborne radar sensors F-SAR and DBFSAR," in *ESA Advanced RF Sensorsand Remote Sensing Instruments*. Noordwijk, The Netherlands: European Space Agency, Nov. 2019, pp. 1–6.

[53] R. E. Kalman *et al.*, "A new approach to linear filtering and prediction problems," *Journal of basic Engineering*, vol. 82, no. 1, pp. 35–45, 1960.

[54] M. Owens, *The Definitive Guide to SQLite*. Apress, 2006.

[55] S. V. Baumgartner, R. Scheiber, F. Bordoni, G. Krieger, and M. Peichl, "HAPS: Potentials, applications and requirements for radar remote sensing," in *HAPS4ESA - Towards an ESA Stratospheric High Altitude Pseudo-Satellites (HAPS) programme for Earth Observation, Telecommunications and Navigation*. Noordwijkerhout, The Netherlands: European Space Agency, 2017.

[56] J. C. Curlander and R. N. McDonough, *Synthetic Aperture Radar: Systems and Signal Processing*. Wiley, New York, 1991.

[57] C. A. Wiley, "Synthetic aperture radars," *IEEE Transactions on Aerospace and Electronic Systems*, no. 3, pp. 440–443, 1985.

[58] S. V. Baumgartner and G. Krieger, "Fast GMTI algorithm for traffic monitoring based on a priori knowledge," *IEEE Transactions on Geoscience and Remote Sensing*, vol. 50, no. 11, pp. 4626–4641, 2012.

[59] A. W. Doerry, "Ship dynamics for maritime ISAR imaging," Sandia National Laboratories, techreport SAND2008-1020, 2008.

[60] J. H. Ender, C. H. Gierull, and D. Cerutti-Maori, "Improved space-based moving target indication via alternate transmission and receiver switching," *IEEE Transactions on Geoscience and Remote Sensing*, vol. 46, no. 12, pp. 3960–3974, 2008.

[61] A. Barros Cardoso da Silva, S. K. Joshi, S. V. Baumgartner, F. Q. de Almeida, and G. Krieger, "Phase correction for accurate DOA angle and position estimation of ground moving targets using multi-channel airborne radar," *IEEE Geoscience and Remote Sensing Letters*, vol. 19, pp. 1–5, 2022.

[62] W. L. Melvin, "A STAP overview," *IEEE Aerospace and Electronic Systems Magazine*, vol. 19, no. 1, pp. 19–35, 2004.

[63] S. K. Joshi, S. V. Baumgartner, and G. Krieger, "Tracking and track management of extended targets in range-Doppler using range-compressed airborne radar data," *IEEE Transactions on Geoscience and Remote Sensing*, vol. 60, pp. 1–20, 2022.

[64] A. Barros Cardoso da Silva, "A priori knowledge-based post-Doppler STAP for traffic monitoring with airborne radar," phdthesis, Fakultät für Elektrotechnik und Informationstechnik, Karlsruhe Institute of Technology, 2019.

[65] S. K. Joshi, S. V. Baumgartner, A. Barros Cardoso da Silva, and G. Krieger, "Range-Doppler based CFAR ship detection with automatic training data selection," *Remote Sensing*, vol. 11, no. 11, pp. 1270–1305, 2019.

[66] S. K. Joshi and S. V. Baumgartner, "Sea clutter model comparison for ship detection using single channel airborne raw SAR data," in *12th European Conference on Synthetic Aperture Radar*. Aachen, Germany: VDE, 2018, pp. 1–5.

[67] ——, "Automatic CFAR ship detection in single-channel range-compressed airborne radar data," in *20th International Radar Symposium*. Ulm, Germany: IEEE, 2019, pp. 1–8.

[68] ——, "Training data selection strategy for CFAR ship detection in range-compressed radar data," in *International Radar Conference*. Toulon, France: IEEE, 2019, pp. 1–5.

[69] ——, "Ship detection using linear and circular range-compressed airborne radar data," in *13th European Conference on Synthetic Aperture Radar*. Online: VDE, 2021.

[70] S. D. Himonas and M. Barkat, "Automatic censored CFAR detection for nonhomogeneous environments," *IEEE Transactions on Aerospace and Electronic systems*, vol. 28, no. 1, pp. 286–304, 1992.

[71] H. Rohling, "Radar CFAR thresholding in clutter and multiple target situations," *IEEE Transactions on Aerospace and Electronic Systems*, vol. AES-19, no. 4, pp. 608–621, 1983.

[72] M. El Mashade, "Monopulse detection analysis of the trimmed mean CFAR processor in nonhomogeneous situations," *IEE Proceedings-Radar, Sonar and Navigation*, vol. 143, no. 2, pp. 87–94, 1996.

[73] J. T. Rickard and G. M. Dillard, "Adaptive detection algorithms for multiple-target situations," *IEEE Transactions on Aerospace and Electronic Systems*, vol. AES-13, no. 4, pp. 338–343, 1977.

[74] Y. Cui, G. Zhou, J. Yang, and Y. Yamaguchi, "On the iterative censoring for target detection in SAR images," *IEEE Geoscience and Remote Sensing Letters*, vol. 8, no. 4, pp. 641–645, 2011.

[75] D. Tao, S. N. Anfinsen, and C. Brekke, "Robust CFAR detector based on truncated statistics in multiple-target situations," *IEEE Transactions on Geoscience and Remote Sensing*, vol. 54, no. 1, pp. 117–134, 2015.

[76] C. Leys, C. Ley, O. Klein, P. Bernard, and L. Licata, "Detecting outliers: Do not use standard deviation around the mean, use absolute deviation around the median," *Journal of Experimental Social Psychology*, vol. 49, no. 4, pp. 764–766, 2013.

[77] R. W. Schafer, "What is a Savitzky-Golay filter?" *IEEE Signal Processing Magazine*, vol. 28, no. 4, pp. 111–117, 2011.

[78] R. Bamler, "Doppler frequency estimation and the Cramer-Rao bound," *IEEE Transactions on Geoscience and Remote Sensing*, vol. 29, no. 3, pp. 385–390, 1991.

[79] S. Watts and L. Rosenberg, "A comparison of coherent and non-coherent radar detection performance in radar sea clutter," in *International Conference on Radar Systems*. Belfast, UK: IET, 2017, pp. 1–6.

[80] L. Rosenberg and S. Watts, "Model based coherent detection in medium grazing angle sea-clutter," in *IEEE Radar Conference (RadarConf)*. Philadelphia, PA, USA: IEEE, 2016, pp. 1–6.

[81] A. Barros Cardoso da Silva and S. V. Baumgartner, "Training data selection and update for airborne post-Doppler space-time adaptive processing," in *12th European Conference on Synthetic Aperture Radar*. Aachen, Germany: VDE, 2018, pp. 1285–1290.

[82] D. J. Crisp, L. Rosenberg, N. J. Stacy, and Y. Dong, "Modelling X-band sea clutter with the K-distribution: Shape parameter variation," in *International Radar Conference "Surveillance for a Safer World"*. Bordeaux, France: IEEE, 2009, pp. 1–6.

[83] A. B. C. da Silva, S. V. Baumgartner, and G. Krieger, "Training data selection and update strategies for airborne post-Doppler STAP," *IEEE Transactions on Geoscience and Remote Sensing*, vol. 57, no. 8, pp. 5626–5641, 2019.

[84] K. D. Ward, S. Watts, and R. J. Tough, *Sea clutter: Scattering, the K distribution and radar performance*. IET, 2006, vol. 20.

[85] C. H. Gierull and I. C. Sikaneta, "Improved SAR vessel detection based on discrete texture," in *11th European Conference on Synthetic Aperture Radar*. Hamburg, Germany: VDE, 2016, pp. 523–526.

[86] K. Ward, "Compound representation of high resolution sea clutter," *Electronics letters*, vol. 17, no. 16, pp. 561–563, 1981.

[87] E. Jakeman, "On the statistics of K-distributed noise," *Journal of Physics A: Mathematical and General*, vol. 13, no. 1, pp. 31–48, 1980.

[88] P. Lombardo and C. Oliver, "Estimation of texture parameters in K-distributed clutter," *IEE Proceedings-Radar, Sonar and Navigation*, vol. 141, no. 4, pp. 196–204, 1994.

[89] H. Greidanus, "Applicability of the K distribution to RADARSAT maritime imagery," in *International Geoscience and Remote Sensing Symposium*, vol. 7. Anchorage, AK, USA: IEEE, 2004, pp. 4715–4718.

[90] D. Blacknell and R. Tough, "Parameter estimation for the K-distribution based on [z log (z)]," *IEE Proceedings-Radar, Sonar and Navigation*, vol. 148, no. 6, pp. 309–312, 2001.

[91] J. J. Moré, "The Levenberg-Marquardt algorithm: implementation and theory," in *Numerical analysis*. Springer, 1978, pp. 105–116.

[92] N. J. Redding, "Estimating the parameters of the K distribution in the intensity domain," Electronics Research Lab Salisbury (Australia), techreport ADA368069, 1999.

[93] M. D. Henschel, M. T. Rey, J. Campbell, and D. Petrovic, "Comparison of probability statistics for automated ship detection in SAR imagery," in *International Conference on Applications of Photonic Technology III: Closing the Gap between Theory, Development, and Applications*, vol. 3491, International Society for Optics and Photonics. Ottawa, Canada: SPIE, 1998, pp. 986–991.

[94] C. H. Gierull and I. Sikaneta, "A compound-plus-noise model for improved vessel detection in non-Gaussian SAR imagery," *IEEE Transactions on Geoscience and Remote Sensing*, vol. 56, no. 3, pp. 1444–1453, 2018.

[95] S. Bocquet, L. Rosenberg, and C. H. Gierull, "Parameter estimation for a compound radar clutter model with trimodal discrete texture," *IEEE Transactions on Geoscience and Remote Sensing*, vol. 58, no. 10, pp. 7062–7073, 2020.

[96] L. Rosenberg, S. Watts, and S. Bocquet, "Application of the K+Rayleigh distribution to high grazing angle sea-clutter," in *International Radar Conference*. Lille, France: IEEE, 2014, pp. 1–6.

[97] D. A. Abraham and A. P. Lyons, "Reliable methods for estimating the K-distribution shape parameter," *IEEE Journal of Oceanic Engineering*, vol. 35, no. 2, pp. 288–302, 2010.

[98] C. H. Gierull, "Numerical recipes to determine the performance of multi-channel GMTI radars," Defence Research and Development Canada, Ottawa, Canada, techreport TM 2011-230, 2011.

[99] B. Tings, C. Bentes, D. Velotto, and S. Voinov, "Modelling ship detectability depending on TerraSAR-X-derived metocean parameters," *CEAS Space Journal*, vol. 11, no. 1, pp. 81–94, 2019.

[100] M. Martorella, D. Pastina, F. Berizzi, and P. Lombardo, "Spaceborne radar imaging of maritime moving targets with the Cosmo-SkyMed SAR system," *IEEE Journal of Selected Topics in Applied Earth Observations and Remote Sensing*, vol. 7, no. 7, pp. 2797–2810, 2014.

[101] D. Cerutti-Maori, I. Sikaneta, and C. H. Gierull, "Optimum SAR/GMTI processing and its application to the radar satellite RADARSAT-2 for traffic monitoring," *IEEE Transactions on Geoscience and Remote Sensing*, vol. 50, no. 10, pp. 3868–3881, 2012.

[102] M. Ester, H.-P. Kriegel, J. Sander, X. Xu *et al.*, "A density-based algorithm for discovering clusters in large spatial databases with noise," in *International Conference on Knowledge Discovery and Information Retrieval*, vol. 96, no. 34. Portland, Oregon: AAAI Press, 1996, pp. 226–231.

[103] Y. Bar-Shalom, X. R. Li, and T. Kirubarajan, *Estimation with Applications to Tracking and Navigation: Theory Algorithms and Software.* John Wiley & Sons, 2004.

[104] I. Reid and H. Term, "Estimation II: 1 Discrete-time Kalman filter," *University of Oxford, Lecture Notes*, 2001.

[105] S. K. Joshi and S. V. Baumgartner, "Ship tracking in high-resolution range-compressed airborne radar data acquired during linear and circular flight tracks," in *Radar Conference (RadarConf20).* Florence, Italy: IEEE, 2020, pp. 1–6.

[106] ——, "Range-Doppler tracking of ships using single-channel airborne radar data," in *13th European Conference on Synthetic Aperture Radar.* Online: VDE, 2021, pp. 1–6.

[107] M. M. Menon, E. R. Boudreau, and P. J. Kolodzy, "An automatic ship classification system for ISAR imagery," *The Lincoln Laboratory Journal*, vol. 6, no. 2, pp. 289–308, 1993.

[108] V. C. Chen and M. Martorella, *Inverse Synthetic Aperture Radar Imaging: Principles, Algorithms and Applications.* Institution of Engineering and Technology, 2014.

[109] M. Leclerc, R. Tharmarasa, M. C. Florea, A.-C. Boury-Brisset, T. Kirubarajan, and N. Duclos-Hindié, "Ship classification using deep learning techniques for maritime target tracking," in *21st International Conference on Information Fusion (FUSION).* Cambridge, UK: IEEE, 2018, pp. 737–744.

[110] R. J. Dyer, *Learning MySQL and MariaDB: Heading in the right direction with MySQL and MariaDB.* O'Reilly Media, Inc., 2015.

[111] P. Konstantinova, A. Udvarev, and T. Semerdjiev, "A study of a target tracking algorithm using global nearest neighbor approach," in *International Conference on Computer Systems and Technologies (CompSysTech'03).* Rousse, Bulgaria: Association for Computing Machinery, 2003, pp. 290–295.

[112] R. De Maesschalck, D. Jouan-Rimbaud, and D. L. Massart, "The Mahalanobis distance," *Chemometrics and intelligent laboratory systems*, vol. 50, no. 1, pp. 1–18, 2000.

[113] H. W. Kuhn, "The Hungarian method for the assignment problem. In 50 Years of Integer Programming 1958-2008," *Springer*, vol. 6, pp. 29–47, 2010.

[114] Y. Bar-Shalom, F. Daum, and J. Huang, "The probabilistic data association filter," *IEEE Control Systems Magazine*, vol. 29, no. 6, pp. 82–100, 2009.

[115] B.-n. Vo, M. Mallick, Y. Bar-shalom, S. Coraluppi, R. Osborne III, R. Mahler, and B.-t. Vo, "Multitarget tracking," *Wiley Encyclopedia of Electrical and Electronics Engineering*, pp. 1–15, 1999.

[116] F. Meyer, P. Braca, P. Willett, and F. Hlawatsch, "A scalable algorithm for tracking an unknown number of targets using multiple sensors," *IEEE Transactions on Signal Processing*, vol. 65, no. 13, pp. 3478–3493, 2017.

[117] E. Hyun and J.-H. Lee, "Multi-target tracking scheme using a track management table for automotive radar systems," in *17th International Radar Symposium*. Krakow, Poland: IEEE, 2016, pp. 1–5.

[118] N. Gebert, G. Krieger, and A. Moreira, "Digital beamforming for HRWS-SAR imaging: system design, performance and optimization strategies," in *International Symposium on Geoscience and Remote Sensing*. Denver, CO, USA: IEEE, 2006, pp. 1836–1839.

[119] J. E. Luminati, T. B. Hale, M. A. Temple, M. J. Havrilla, and M. E. Oxley, "Doppler aliasing reduction in SAR imagery using stepped-frequency waveforms," *IEEE Transactions on Aerospace and Electronic Systems*, vol. 43, no. 1, pp. 163–175, 2007.

[120] S. V. Baumgartner and G. Krieger, "Simultaneous high-resolution wide-swath SAR imaging and ground moving target indication: Processing approaches and system concepts," *IEEE Journal of Selected Topics in Applied Earth Observations and Remote Sensing*, vol. 8, no. 11, pp. 5015–5029, 2015.

[121] M. Martorella, F. Salvetti, D. Staglianò, and E. Giusti, "Three-dimensional ISAR imaging: A review," *The Journal of Engineering*, vol. 2019, no. 20, pp. 6823–6828, 2019.

[122] S. V. Baumgartner, "Circular and polarimetric ISAR imaging of ships using airborne SAR sensors," in *12th European Conference on Synthetic Aperture Radar*. Aachen, Germany: VDE, 2018, pp. 116–121.

[123] J. M. Muñoz-Ferreras and F. Pérez-Martínez, "Subinteger range-bin alignment method for ISAR imaging of noncooperative targets," *EURASIP Journal on Advances in Signal Processing*, vol. 2010, pp. 1–16, 2010.

[124] H. L. Chan and T. S. Yeo, "Noniterative quality phase-gradient autofocus (QPGA) algorithm for spotlight SAR imagery," *IEEE Transactions on Geoscience and Remote Sensing*, vol. 36, no. 5, pp. 1531–1539, 1998.

[125] D. Schuhmacher, B.-T. Vo, and B.-N. Vo, "A consistent metric for performance evaluation of multi-object filters," *IEEE Transactions on Signal Processing*, vol. 56, no. 8, pp. 3447–3457, 2008.

[126] A. S. Rahmathullah, Á. F. García-Fernández, and L. Svensson, "Generalized optimal sub-pattern assignment metric," in *20th International Conference on Information Fusion (Fusion)*. Xi'an, China: IEEE, 2017, pp. 1–8.

[127] J. S. Fowdur, M. Baum, and F. Heymann, "A marine radar dataset for multiple extended target tracking," in *1st Maritime Situational Awareness Workshop (MSAW)*. Lerici, Italy: CMRE, 2019, pp. 1–7.

[128] S. K. Joshi, S. V. Baumgartner, A. Barros Cardoso da Silva, and G. Krieger, "Direction-of-arrival angle and position estimation for extended targets using multichannel airborne radar data," *IEEE Geoscience and Remote Sensing Letters*, vol. 19, pp. 1–5, 2022.

[129] J. Ward, "Space-time adaptive processing for airborne radar," in *International Conference on Acoustics, Speech, and Signal Processing*. Detroit, MI, USA: IEEE, 1995, pp. 2809–2812.

[130] C. H. Gierull, *Digital channel balancing of along-track interferometric SAR data*. Defence R & D Canada-Ottawa, 2003.

[131] L. Yang, T. Wang, and Z. Bao, "Ground moving target indication using an InSAR system with a hybrid baseline," *IEEE Geoscience and Remote Sensing Letters*, vol. 5, no. 3, pp. 373–377, 2008.

[132] A. B. C. da Silva, S. V. Baumgartner, F. Q. de Almeida, and G. Krieger, "In-flight multichannel calibration for along-track interferometric airborne radar," *IEEE Transactions on Geoscience and Remote Sensing*, vol. 59, no. 4, pp. 3104 – 3121, 2020.

[133] L. C. Godara, "Application of antenna arrays to mobile communications. II. beamforming and direction-of-arrival considerations," *Proceedings of the IEEE*, vol. 85, no. 8, pp. 1195–1245, 1997.

[134] F. C. Robey, D. R. Fuhrmann, E. J. Kelly, and R. Nitzberg, "A CFAR adaptive matched filter detector," *IEEE Transactions on Aerospace and Electronic Systems*, vol. 28, no. 1, pp. 208–216, 1992.

[135] D. Cerutti-Maori, J. Klare, A. R. Brenner, and J. H. Ender, "Wide-area traffic monitoring with the SAR/GMTI system PAMIR," *IEEE Transactions on Geoscience and Remote Sensing*, vol. 46, no. 10, pp. 3019–3030, 2008.

[136] K. D. Schwehr and P. A. McGillivary, "Marine ship automatic identification system (AIS) for enhanced coastal security capabilities: An oil spill tracking application," in *OCEANS*. Vancouver, BC, Canada: IEEE, 2007, pp. 1–9.

[137] C. Noviello, G. Fornaro, P. Braca, and M. Martorella, "Fast and accurate ISAR focusing based on a Doppler parameter estimation algorithm," *IEEE Geoscience and Remote Sensing Letters*, vol. 14, no. 3, pp. 349–353, 2017.

[138] L. Lightstone, D. Faubert, and G. Rempel, "Multiple phase centre DPCA for airborne radar," in *National Radar Conference*. Los Angeles, CA, USA: IEEE, 1991, pp. 36–40.

[139] M. Stasolla and H. Greidanus, "The exploitation of Sentinel-1 images for vessel size estimation," *Remote Sensing Letters*, vol. 7, no. 12, pp. 1219–1228, 2016.

[140] Y. Ren, X. Li, and H. Xu, "A deep learning model to extract ship size from Sentinel-1 SAR images," *IEEE Transactions on Geoscience and Remote Sensing*, vol. 60, pp. 1–14, 2021.

[141] S. V. Baumgartner and S. K. Joshi, "Onboard processing concept for maritime surveillance demonstrated with DLR's airborne radar sensors F-SAR and DBFSAR," in *13th European Conference on Synthetic Aperture Radar*. Online: VDE, 2021, pp. 1–6.

A SQLite Database Specifications

This appendix provides information related to the target motion parameters stored in the columns of each row of the SQLite database table. The SQLite database was used for multi-target tracking which is described in detail in Chapter 5 (cf. page 79). Table A.1 shows 22 different parameters of each detected target which is stored in a single row in the SQLite database table.

Table A.1: Target motion parameters stored in each row (or for each detected target at each CPI) of the SQLite database table.

Column	Parameters	Unit	Datatype	Example	Explanation
0	target azimuth bin	bin	integer	25600	azimuth bin w.r.t. the origin of the entire radar data array
1	target range bin	bin	integer	7401	range bin of the cluster centroid w.r.t. the origin of the entire radar data array
2	GPS seconds of week	s	float	315122	GPS time in seconds starting on Sundays at 00:00 a.m.
3	target Doppler bin	bin	integer	99	Doppler bin of the cluster centroid
4	target Doppler frequency	Hz	float	657.31	Kalman Filter corrected Doppler frequency of the cluster centroid
5	target cluster lower Doppler bin	bin	integer	97	lower Doppler bin of target cluster bounding box
6	target cluster lower range bin	bin	integer	7391	near range bin (w.r.t. the origin of the entire data array) of target cluster bounding box
7	cluster width in Hz	Hz	float	130.78	width of cluster bounding box
8	cluster height in m	m	float	9.89	height of cluster bounding box
9	cluster width in bins	bin	integer	7	cluster width in Doppler bins
10	cluster height in bins	bin	integer	33	cluster height in range bins
11	target pixels	none	integer	51	total number of radar-based target detections in a cluster
12	predicted flag	none	integer	0	0 means target was “detected“ at a given instant of time and 1 means it was “predicted“
13	relation	none	integer	-1	contain unique ID of target from previous CPI or it is -1 if target is detected first time

continued on next page

Table A.1 – continued from previous page

Column	Parameters	Unit	Datatype	Example	Explanation
14	target slant range	m	float	7618.02	Kalman Filter corrected slant range of the cluster centroid
15	target SCNR	dB	float	25.12	estimated signal-to-clutter-plus-noise ratio
16	DOA angle	deg	float	90.45	direction-of-arrival angle of the detected target
17	LOS velocity	m/s	float	2.32	line-of-sight velocity of the target
18	target latitude	deg	float	53.452	latitude of the detected target in WGS84 datum
19	target longitude	deg	float	8.895	longitude of the detected target in WGS84 datum
20	target data patch in time domain	none	text	none	filename of the extracted patch in range-time domain
21	target data patch in Doppler domain	none	text	none	filename of the extracted patch in range-Doppler domain

B Experimental Setup and Radar Datasets

This appendix provides details about the single- and multichannel channel flight campaigns conducted using DLR's F-SAR and DBFSAR airborne radar systems, respectively.

B.1 Single-channel F-SAR Campaign

The airborne radar sytem F-SAR (*Flugzeug*-SAR) [35] is developed and operated by the DLR's Microwaves and Radar Institute. The F-SAR system is capable of acquiring fully polarimetric radar data simultaneously at different frequencies namely, X-, C-, S-, L- and P-band.

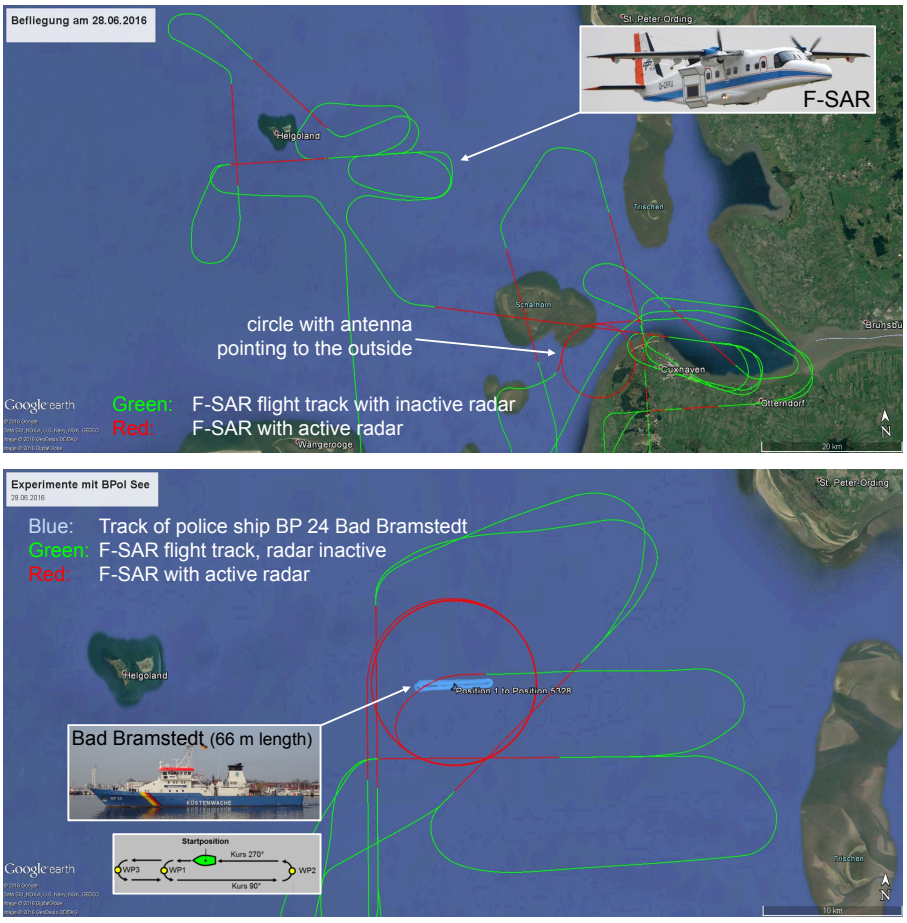

Figure B.1: Flight tracks flown during the two-day North Sea F-SAR campaign in the year 2016 (top: day 1; bottom: day 2) [122].

B.1.1 2016 North Sea Flight Campaign

A two-day F-SAR flight campaign was conducted in June 2016 in the North Sea [49]. All single-channel radar data, in total more than 1 terabytes (TB), were acquired fully polarimetric and simultaneously in X- and L-band. Additionally, the AIS data transmitted by the ships were also available for ground truth purposes. At the first day of the campaign, the island Helgoland and the town Cuxhaven, including the coastal areas and ships of opportunity were observed, mainly during linear flight tracks but also during a circular track with the radar antenna pointing not to the circle center but to the opposite direction (cf. red circle in Figure B.1, top). At the second day, a dedicated experiment with a controlled ship operated by the German federal police was carried out. The ship moved with velocities of 0 to 20 kn (knots) between three different waypoints. The circular flight tracks, this time with the antenna pointing to the circle center, were flown with a radius of 5600 m resulting in a total ship observation time of approximately 400 seconds (= 6.7 minutes) per circle (cf. red circle in Figure B.1, bottom) [49].

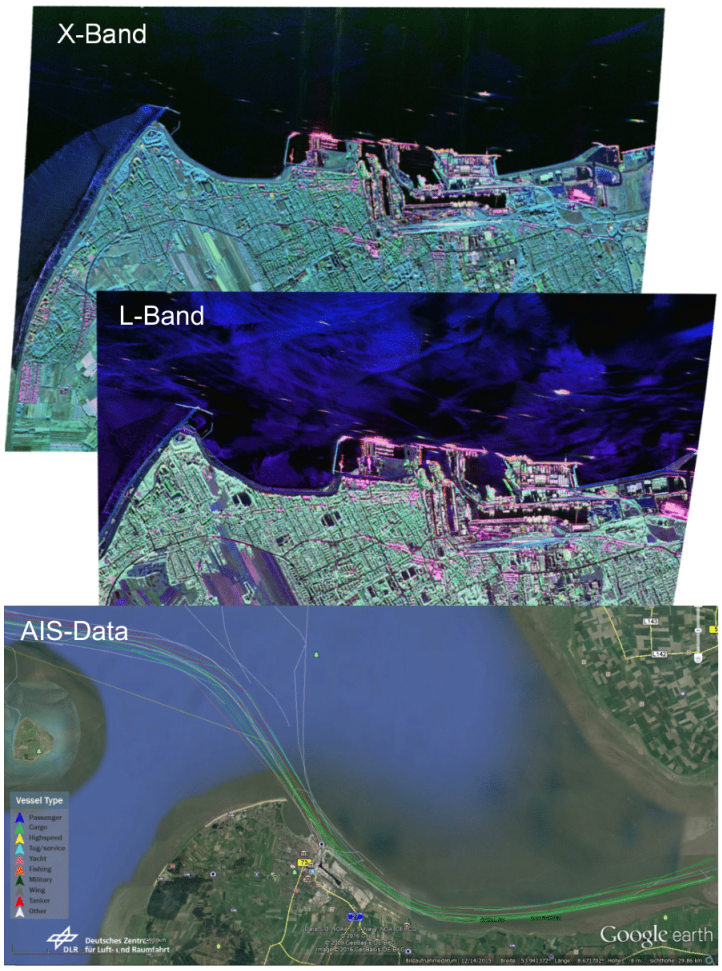

Figure B.2: Simultaneously acquired fully polarimetric X- and L-band radar data and the AIS data available from 2016 F-SAR flight campaign conducted in the region around Cuxhaven in Germany [122].

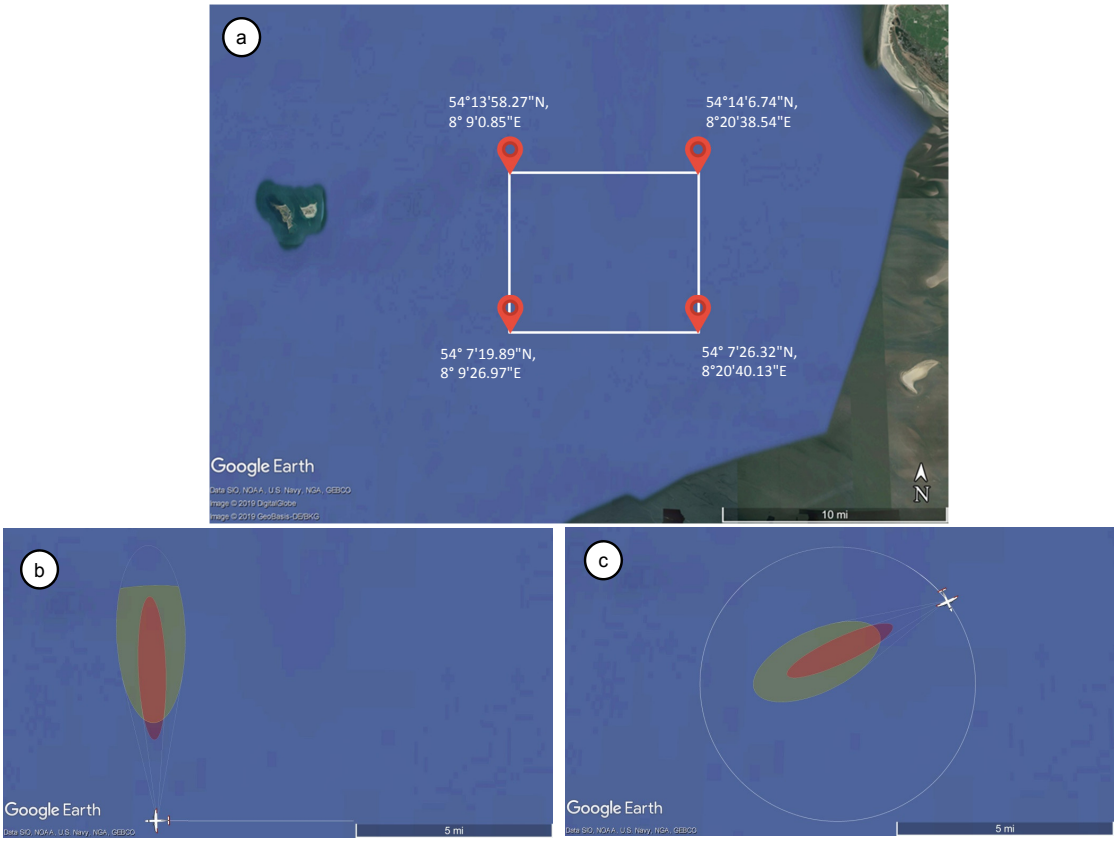

Figure B.3: (a) Google Earth image showing a part of the test site in North Sea. The region within the white box marks the area where the data were acquired during (b) a linear and (c) a circular F-SAR flight track. The red and yellow ellipses in (b) and (c) are the 3 dB antenna footprints of the X- and L-band antenna, respectively.

A small part of the acquired fully polarimetric radar data as well as the available AIS data are shown in Figure B.2. Corresponding Google Earth image of the scene where the flight experiments were conducted is shown in Figure B.3. In Table B.1 the X- and L-band system and acquisition geometry parameters used during the experiments are provided.

B.2 Multichannel DBFSAR Campaigns

The DBFSAR (digital beamforming SAR) system [36] is an advanced new airborne radar system also developed by the DLR's Microwaves and Radar Institute. The DBFSAR antenna configuration for MTI applications is shown in Figure B.4. In the figure two single-pol X-band transmit antennas, six independent single-pol receive antennas and a dual-pol imaging antenna can be seen. The short transmit antenna TX1 allows for a longer observation and tracking time due to its wide azimuth antenna beam. The long transmit antenna TX2 is used for limiting the clutter bandwidth and, thus, for decreasing the minimum detectable velocity of the target (cf. (3.1)).

The aircraft is additionally equipped with a LTE (long term evolution) router for transferring the data onto ground and a dual-channel AIS receiver for anomaly detection

Table B.1: Important F-SAR system and acquisition geometry parameters.

Parameters	Typical Values
Average platform velocity [m/s]	83.55
Average platform altitude over ground [m]	5637
Polarization	HH, HV, VH and VV
Chirp bandwidth for X- and L-band [MHz]	384, 150
Range resolution for X- and L-band [m]	0.39, 1.0
Incidence angle range [°]	15-60
Radar wavelength for X- and L-band [m]	0.0306, 0.226
Pulse repetition frequency [Hz]	2403.85
3 dB antenna azimuth beamwidth for X- and L-band [°]	8, 18
Azimuth antenna length for X- and L-band [m]	0.3 m (TX), 0.2 m (RX) (X-band) 0.3 m (TX), 0.3 m (RX) (L-band)
Geographical coordinates	Shown in Figure B.3a

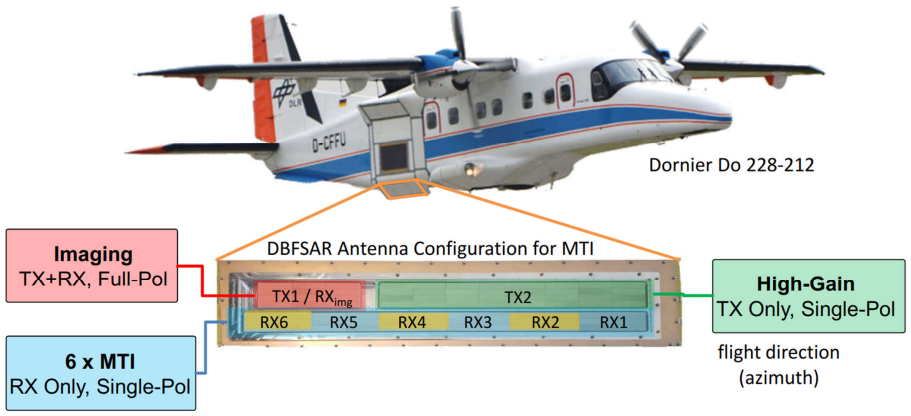

Figure B.4: Multichannel DBFSAR antenna configuration for MTI applications [141].

and for validation purposes. In the next two sections some details of the real experimental multichannel flight campaigns conducted using the DBFSAR system are provided.

B.2.1 2019 North Sea Flight Campaign

In November 2019 a multichannel flight campaign using DBFSAR was carried out in the North Sea near Cuxhaven, Germany. The aircraft was flying at an altitude of approximately 2400 m above ground. The AIS receiver onboard the aircraft received the AIS signals from ships with distances up to 200 km away from the aircraft, as shown in Figure B.5. Radar data and acquisition geometry parameters are given in Table B.2 and the AIS-based specifications of the ships which were observed in the acquired radar data are given in Table B.3.

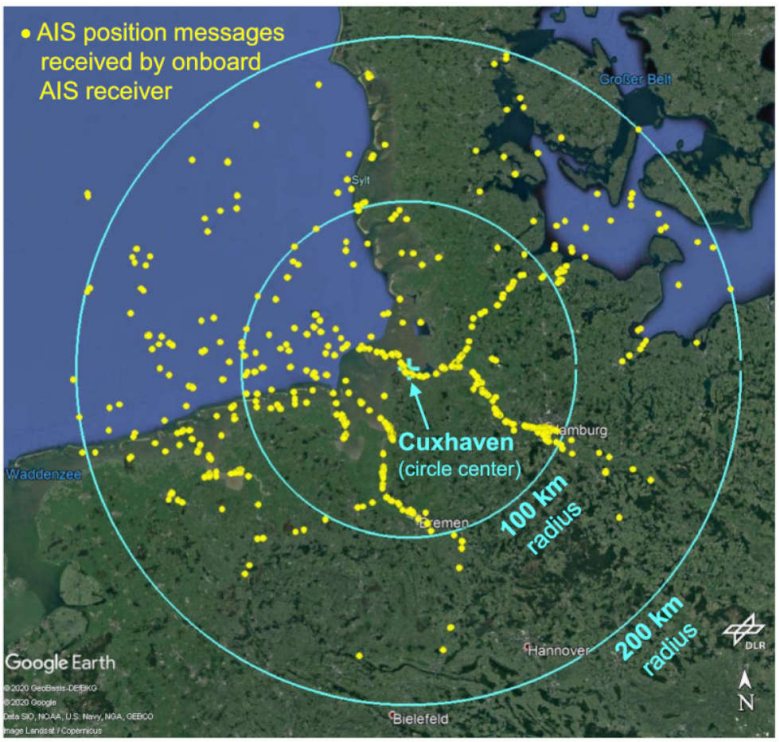

Figure B.5: Received AIS messages during a flight campaign conducted in the North Sea. Yellow dots in the figure are the received ship AIS position messages [36].

Table B.2: Radar system and acquisition geometry parameters of the real X-band multichannel DBFSAR airborne radar data for the 2019 North Sea campaign. Data set I-III in the table are shown in Figure 6.8 top (cf. page 117).

Parameters	Values		
	Data Set I	Data Set II	Data Set III
Average platform velocity [m/s]	90.9	90.5	84.9
Average platform altitude over ground [m]	2469.7	2465.3	2468.6
Aircraft course angle [°]	135	282	235-358
Maximum squint angle [°]		2	
Number of TX/RX channels		1/6	
Physical antenna separation [m]		0.2	
Polarization		VV	
Chirp bandwidth [MHz]		500	
Range resolution [m]		0.3	
Incidence angle range [°]	19.5-59.7	18.8-59.6	19.3-64
Radar wavelength [m]		0.0309	
Pulse repetition frequency [Hz]		3004.8	
Total observation time along azimuth [s]	70	270	210
Mean terrain height above ellipsoid [m]		39.96	

Table B.3: AIS-based specifications of the ships present in the multichannel radar data acquired in the North Sea, Germany during the 2019 DBFSAR flight campaign. In the table, SOG (speed over ground) is the absolute speed of the ship over the ground and MMSI (Maritime Mobile Service Identity) is the unique 9-digit ship identification number.

Ship Name	MMSI	SOG [m/s]	Ship Length/Beam [m]	Ship Moving Direction w.r.t. the Aircraft [°]
		Data Set I		
LANGELAND	211204290	2.72	82/12	-8.35
LONGDUIN	246484000	6.94	112/15	195.93
HAM 316	244521000	3.96	129/22	-1.23
		Data Set II		
CHARISMA	211327400	4.47	12/4	7.67
HOFFNUNG CUX10	211458000	1.64	15/5	-0.32
SAPHIR	211476000	1.85	17/6	1.59
GEO GRAPH	218084000	1.18	18/6	-150.48
UTHOERN	211216410	3.75	31/9	-182.02
WANGEROOGE	211211960	1.38	52/13	20.14
FAIR LADY	211208430	9.82	68/10	4.39
MT BLUE STAR	215691000	7.76	126/18	23.31
VEGA GRANAT	636091919	4.73	180/20	-169.94
		Dataset III		
GEO GRAPH	218084000	3.34	18/6	-11.81
TINA CUX-5	211721570	2.21	19/5	-173.52
AURORA	211552000	4.06	20/6	-104.68
PILOTVESSEL HANSE	211324470	4.83	49/21	-182.36
RMS RATINGEN	304346000	4.27	88/11	-185.16
LONGDUIN	246484000	6.07	112/15	-3.75

B.2.2 2020 Ammersee Flight Campaign

In October 2020 another multichannel flight campaign using again the DBFSAR radar system was carried out over the lake Ammersee located in southern Germany. The goal of this campaign was to detect slowly moving small controlled boats (cf. Figure 6.9 bottom in page 117).

During the campaign several flight tracks were flown around the lake region. Figure B.6 shows the entire trajectory of the DLR's Dornier 228-212 aircraft which was used for acquiring the multichannel radar data sets. For the investigations, three radar data sets from this campaign were considered and they are shown in Figure 6.9 top (cf. page 117). Their corresponding acquisition geometry parameters are listed in Table B.4.

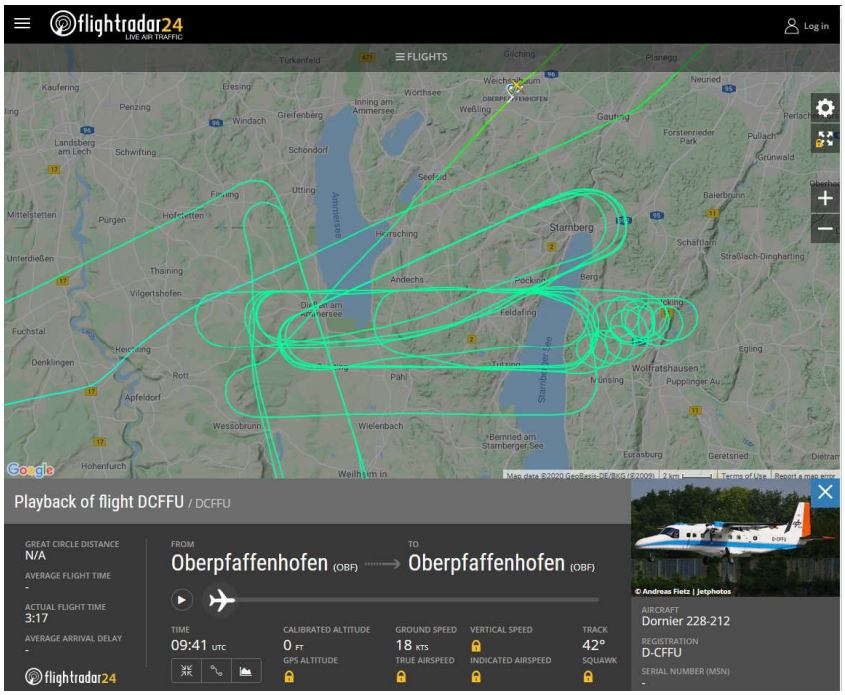

Figure B.6: Several flight tracks of the aircraft containing the DBFSAR antenna flown over the lake Ammersee in Germany (screenshot from flightradar24.com).

Table B.4: Radar system and acquisition geometry parameters of the real X-band multichannel DBFSAR airborne radar data for the 2020 Ammersee campaign. Data sets IV-VI in the table are shown in Figure 6.9 top (page 117).

Parameters	Values		
	Data Set IV	Data Set V	Data Set VI
Average platform velocity [m/s]	90.3	90.5	90.5
Average platform altitude over ground [m]	2499.6	2500.2	2947.4
Aircraft course angle [°]	269	269	245
Maximum squint angle [°]		5	
Number of TX/RX channels		1/6	
Physical antenna separation [m]		0.2	
Polarization		VV	
Chirp bandwidth [MHz]		500	
Range resolution [m]		0.3	
Incidence angle range [°]	21.7-59.8	22.1-59.8	21.7-59.8
Radar wavelength [m]		0.0315	
Pulse repetition frequency [Hz]		3004.8	
Total observation time along azimuth [s]	85	85	100
Mean terrain height above ellipsoid [m]		579	

C Geocoding Results for Multichannel Flight Campaigns

In Figures C.1 and C.2 detection, tracking and geocoding results obtained from the multichannel data sets I and II from the 2019 North Sea campaign (cf. Figure 6.8 in page 117) are shown.

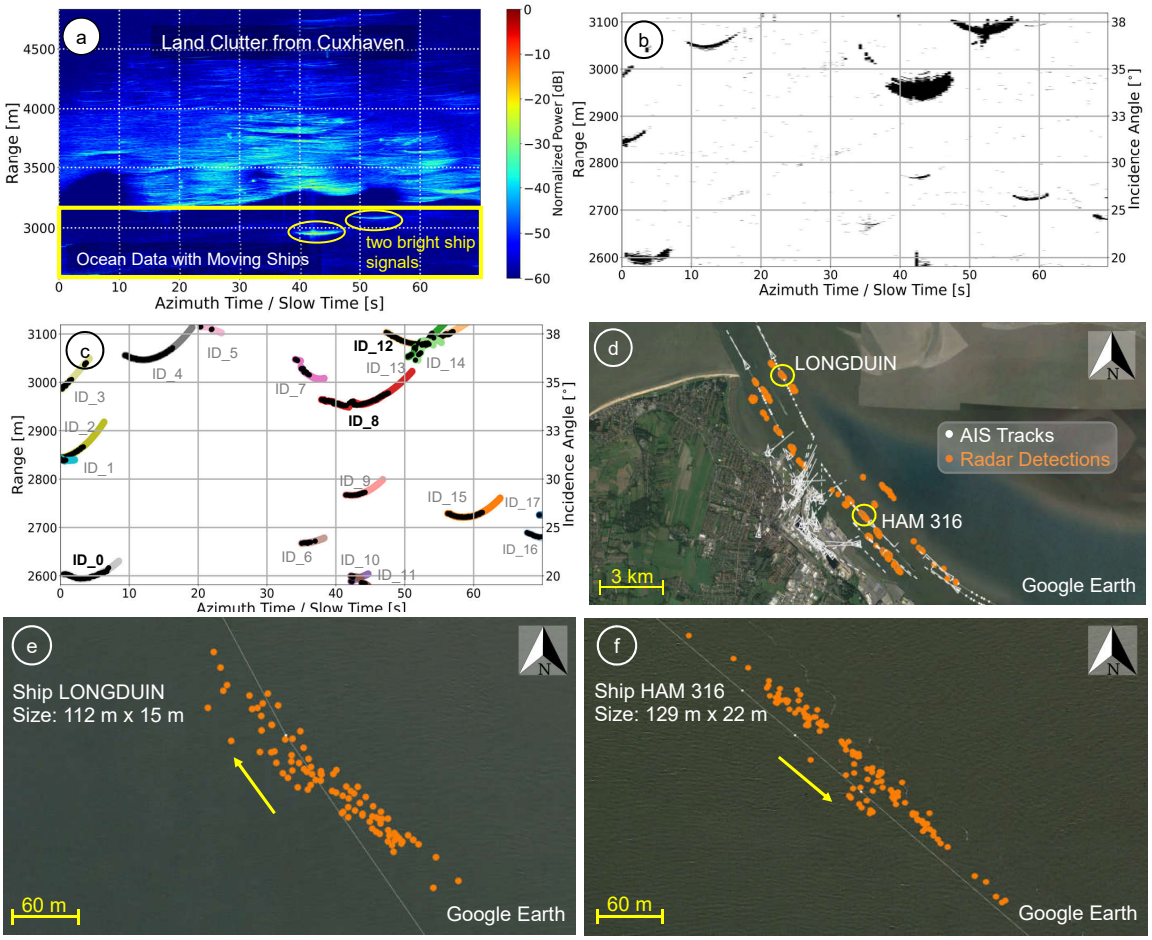

Figure C.1: Geocoding results for multichannel radar data set I. (a) Real RC X-band VV polarized airborne radar data. In the data land clutter from town Cuxhaven and ocean clutter with two bright ship signals can clearly be seen. (b) Binary target detection map of the data from the yellow box in (a). (c) Ship tracking results. Tracked ships with their individual IDs are marked in the figure. Targets with ID_0, ID_8 and ID_12 in the figure corresponds to ships LONGDUIN, HAM 316 and LANGELAND, respectively (cf. Data Set I in Table B.3). (d) Google Earth visualization of the geocoded radar-based detections of all the tracked ships in the data. Detailed view of the mapped detections from (e) ship LONGDUIN and (f) ship HAM 316. Ship dimensions are shown in the figure. Arrows indicate the ships' moving direction.

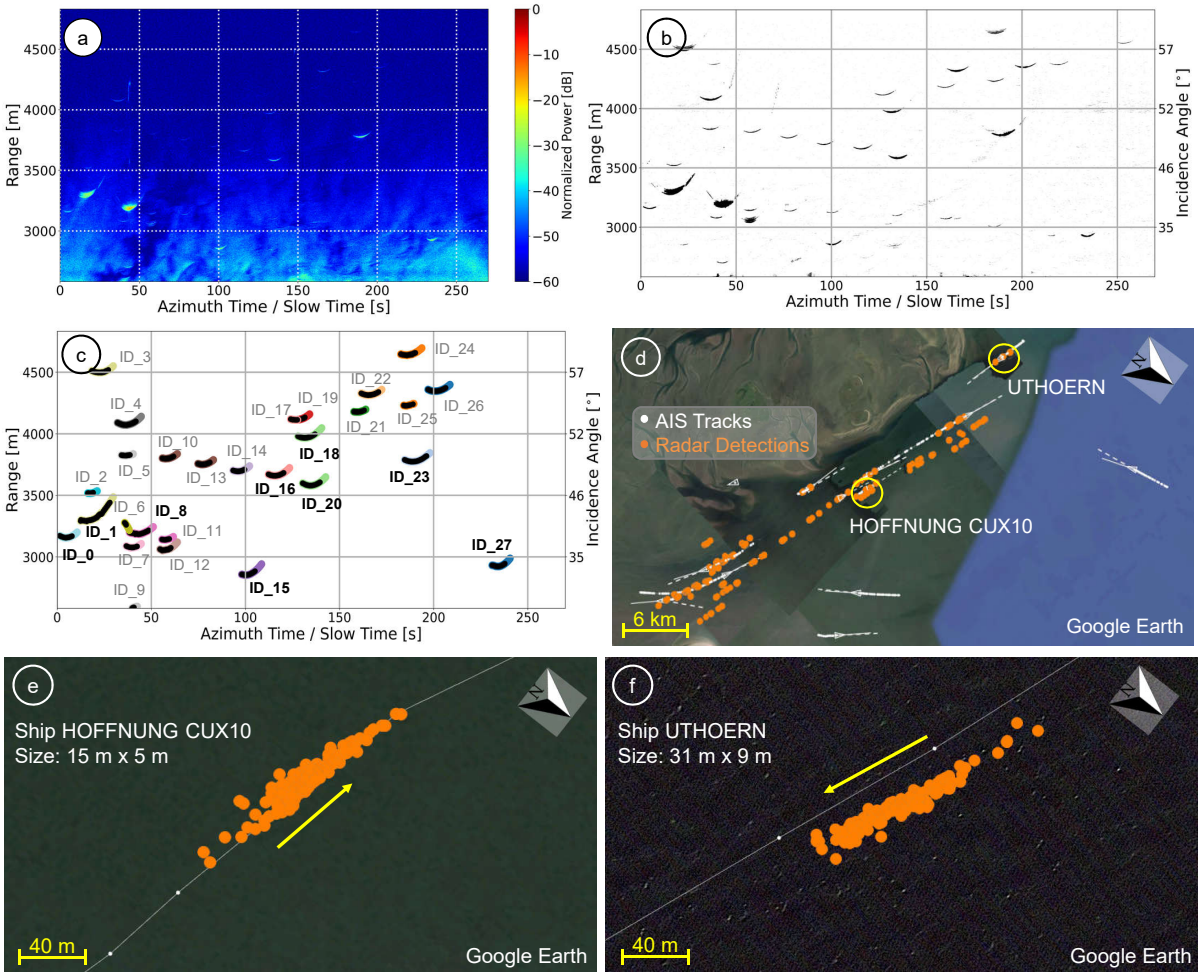

Figure C.2: Geocoding results for multichannel radar data set II. (a) Real RC X-band VV polarized airborne radar data. (b) Binary target detection map of the data. (c) Ship tracking results. Tracked ships with their individual IDs are marked in the figure. Targets with ID_0, ID_1, ID_8, ID_15, ID_16, ID_18, ID_20, ID_23 and ID_27 in the figure corresponds to ships GEO GRAPH, MT BLUE STAR, VEGA GRANAT, WANGEROOGE, CHARISMA, HOFFNUNG CUX10, SAPHIR, FAIR LADY and UTHOERN, respectively (cf. Data Set II in Table B.3). (d) Google Earth visualization of the geocoded radar-based detections of all the tracked ships in the data. Detailed view of the mapped detections from (e) ship HOFFNUNG CUX10 and (f) ship UTHOERN. Ship dimensions are shown in the figure. Arrows indicate the ships' moving direction.

In Figures C.3 and C.4 detection, tracking and geocoding results obtained from the multichannel data sets IV and V from the 2020 Ammersee campaign (cf. Figure 6.9 top in page 117) are shown.

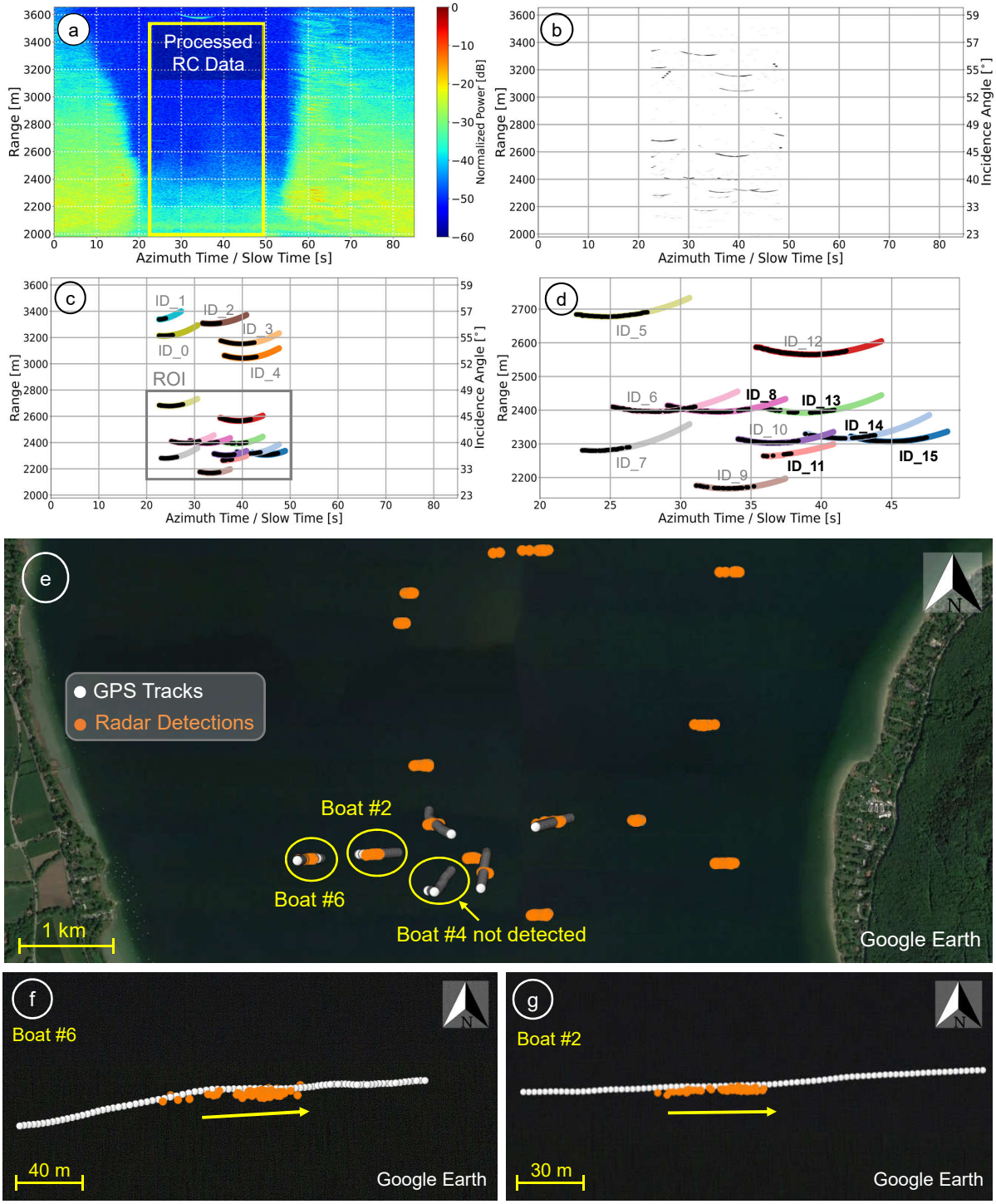

Figure C.3: Geocoding results for multichannel radar data set IV. (a) Real RC X-band VV polarized airborne radar data. Data containing the radar backscatter from the lake region is shown within the yellow box in the figure. (b) Binary target detection map of the processed RC data shown in (a). (c) Tracking results. Tracked targets with their individual IDs are marked in the figure. (d) Zoom in detail of the ROI shown in (c). The ROI contains the controlled boats used for the experiments. Boat #4 is not detected in this data set. Targets with ID_8, ID_11, ID_13, ID_14 and ID_15 corresponds to boat numbers 1, 3, 5, 2 and 6, respectively (cf. Data Set IV in Table 6.3 in page 127). (e) Google Earth visualization of the geocoded radar-based detections of all the tracked targets in the data. Detailed view of the mapped detections from (f) Boat #6 and (g) Boat #2. Arrows indicate the boats' moving direction.

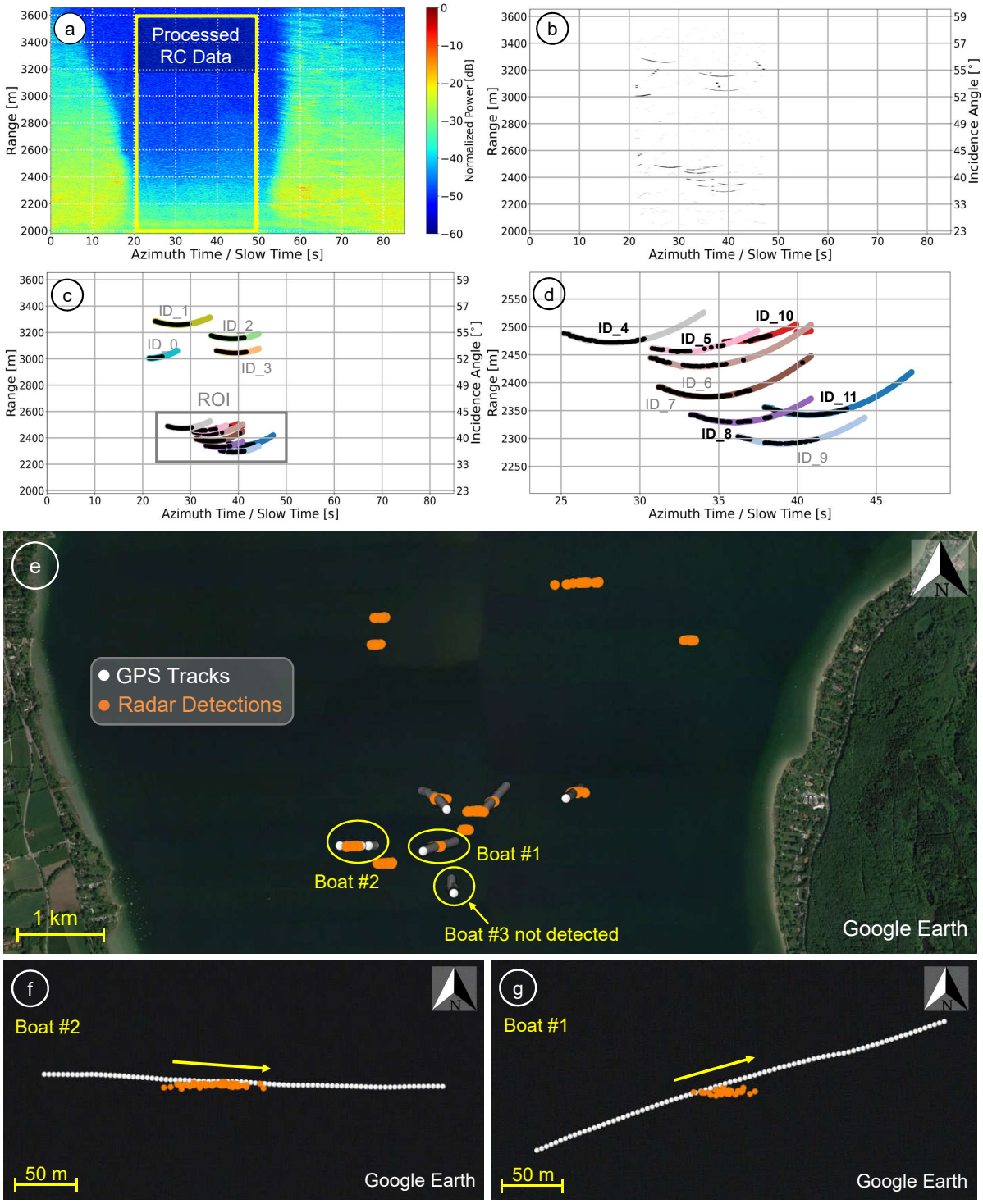

Figure C.4: Geocoding results for multichannel radar data set V. (a) Real RC X-band VV polarized airborne radar data. Data containing the radar backscatter from the lake region is shown within the yellow box in the figure. (b) Binary target detection map of the processed RC data shown in (a). (c) Tracking results. Tracked targets with their individual IDs are marked in the figure. (d) Zoom in detail of the ROI shown in (c). The ROI contains the controlled boats used for the experiments. Boat #3 is not detected in this data set. Targets with ID_4, ID_5, ID_8, ID_10 and ID_11 corresponds to Boat numbers 6, 4, 1, 5 and 2, respectively (cf. Data set V in Table 6.3 in page 127). (e) Google Earth visualization of the geocoded radar-based detections of all the tracked targets in the data. Detailed view of the mapped detections from (f) Boat #2 and (g) Boat #1. Arrows indicate the boats' moving direction.